2022

Biased Constitutive Activity in the Uveal Melanoma Oncogene CYSLTR2 is Unique in CYSLTR2 Germline and Pan-Cancer Human Variome

Mizuho Horioka-Duplix

BIASED CONSTITUTIVE ACTIVITY IN THE UVEAL MELANOMA ONCOGENE *CYSLTR2* IS UNIQUE IN THE *CYSLTR2* GERMLINE AND PAN-CANCER HUMAN VARIOME

A Thesis Presented to the Faculty of
The Rockefeller University
in Partial Fulfillment of the Requirements for
the degree of Doctor of Philosophy

by
Mizuho Horioka-Duplix
June 2022

BIASED CONSTITUTIVE ACTIVITY IN THE UVEAL MELANOMA ONCOGENE *CYSLTR2* IS UNIQUE IN THE *CYSLTR2* GERMLINE AND PAN-CANCER HUMAN VARIOME

Mizuho Horioka-Duplix, Ph.D.

The Rockefeller University 2022

Uveal melanoma is the most common eye cancer in adults and is clinically and genetically distinct from skin cutaneous melanoma. In a subset of cases, the oncogenic driver is an activating mutation in *CYSLTR2*, the gene encoding the G protein-coupled receptor (GPCR) cysteinyl-leukotriene receptor 2. The mutant *CYSLTR2* encodes for CysLTR2-L129Q receptor, with the substitution of Leu to Gln at position 129 (3.43). The ability of CysLTR2-L129Q to cause malignant transformation has been hypothesized to result from constitutive activity, but how the receptor could escape desensitization is unknown. In this work, we characterized the functional properties of CysLTR2-L129Q. CysLTR2 signals through the Gq/11/PLC-β pathways, so using a homogenous time resolved fluorescence (HTRF) IP1 accumulation assay, we show that CysLTR2-L129Q is a constitutively active mutant that strongly drives Gq/11 signaling pathways. However, CysLTR2-L129Q only poorly recruits β-arrestin as shown by a bioluminescence resonance energy transfer 2 (BRET2) based β-arrestin recruitment assay. Using a modified Slack-Hall operational model, we quantified the constitutive activity for both pathways and conclude that CysLTR2-L129Q displays profound signaling bias for Gq/11 signaling pathways while escaping β-arrestin-mediated downregulation. *CYSLTR2* is the first known example of a GPCR driver oncogene that encodes a highly biased constitutively active mutant receptor. These results provide new insights into the mechanism of CysLTR2-L129Q oncoprotein signaling and suggest *CYSLTR2* as a promising potential therapeutic target in uveal melanoma.

Furthermore, we learned that CysLTR2 is a significantly mutated GPCR in several other cancers as well. We identified >100 *CYSLTR2* missense variants of unknown significance (VUS) in human cancer genomes from available cancer databases, as well as another >100 *CYSLTR2* single-nucleotide polymorphisms (SNPs) from exome sequence data. Here, we introduce a proof-of-concept, experimental, activity-based profiling pipeline to systematically assess the mutational landscape of *CYSLTR2*. We use a single transfection mixture of receptor-encoding DNA and HEK293T cells is used to characterize all variants for expression level, basal and agonist-stimulated G protein signaling, and basal and agonist-stimulated β-arrestin recruitment. The CysLTR2-L129Q mutation causing uveal melanoma has a unique phenotype among all cancer-associated variants. It is highly constitutively active with gain-of-function (GoF) in basal Gq/11-PLC-β signaling and loss-of-function (LoF) in agonist-dependent signaling, while only poorly recruiting β-arrestin. Furthermore, we found that about 21% of the variants show no detectable activity and are basically indistinguishable from mock-transfected controls, suggesting that a large portion of these mutations are damaging. A further 21% lose 50% of activity as normalized to WT (100%), and another ten percent are nonsense and frameshift variants. This means that about 50% of total somatic mutations of *CYSLTR2* have a LoF phenotype, which points to a tumor suppressor function following the famous “20/20” rule. While a sizable number of these mutations is located at canonical functional sites (G protein or β-arrestin binding interfaces, ligand binding sites, and microswitch regions), there were some that were in

previously unknown sites, suggesting that predicting damaging sites for GPCRs is difficult bioinformatically. This highlights the importance of empirical investigations such as this work, which introduces a scalable pipeline for a rapid, high throughput characterization of the landscape of cancer-associated mutations in any GPCR.

ACKNOWLEDGMENTS

I would like to thank my advisor, Dr. Thomas Sakmar, for giving me the opportunity to conduct research, gain many important technical skills, and to complete my PhD in his lab. In my time here, he has helped me to become a resilient and independent researcher. It has been an unforgettable experience and I truly learned the importance of good communication, a supportive environment, and constructive mentorship.

The daily advice from my colleague and mentor, Dr. Thomas Huber, has been instrumental in my growth. From day one, he has challenged me to be extremely meticulous and analytical in my experimental design, thinking critically about every step and never settling for the status quo. I firmly believe I have become a skilled assay scientist thanks to his guidance, and I cannot thank him enough. Dr. Emilie Ceraudo, who started the CysLTR2 project before I joined this lab, contributed greatly to this body of work and helped me to develop the impressive activity-based profiling workflow. I thank my close friend and colleague, Jordan Mattheisen, who joined the lab a year after I did, but has taught me many things and contributed to many of my projects. She was always ready for a discussion and made every day in this lab enjoyable. I thank Manija Kazmi for her ever positive attitude and for checking in occasionally to make sure everything was going okay. I must thank Dr. Emily Lorenzen and Dr. Carlos Rico, who were both my mentors as I was starting up my scientific career in the Sakmar lab. They helped me to get oriented and set up good foundations for my graduate work and have continued to support me, long after their own graduations. I also thank the younger graduate students of the Sakmar lab, Ilana Kotliar and Tori Rasmussen, for being eager to learn from me and for developing my projects after my departure.

The Tri-Institutional PhD Program in Chemical Biology (TPCB) and its members have been a wonderful community for me. The director of the program, Dr. Derek Tan, has been an encouraging presence throughout the years and I appreciate the program for providing a social outlet outside of our labs. I especially would like to thank my cohort, the entering class of 2016, who have continued to be my supportive family from the first day of my graduate career! Thank you to Margie Hinonangan-Mendoza and Francine Collazo-Espinell for jumping in and helping me with often daunting administrative tasks.

Thank you very much to my committee members, Drs Jue Chen, Shixin Liu, and Daniel Heller for their tireless encouragement of my scientific endeavors each year! I am also grateful to our collaborators, Drs Ping Chi and Yu Chen for introducing our lab to CysLTR2, for the ongoing meetings and discussions, and for allowing us access to the MSK-IMPACT database.

Lastly, I would like to thank my friends and therapist who have been most supportive and essential in giving me some much-needed perspective at times. Thank you for always being willing to lend an ear, for grounding me, and for helping me make the most of my time in New York City. My family have been my rocks and cheerleaders from afar and I am so thankful for their confidence and belief in me. A special mention goes to my husband, whose love, support, and constant reassurance helped me through the many tough days. I am ever grateful to everyone who helped me in this journey.

TABLE OF CONTENTS

TABLE OF CONTENTS ..... **iv**
LIST OF FIGURES ..... **vi**
LIST OF TABLES ..... **vii**
LIST OF ABBREVIATIONS ..... **viii**

CHAPTER 1. INTRODUCTION **1**
1.1 The discovery of G protein-coupled receptors 1
1.2 Intracellular signaling through G proteins 3
1.3 The role of arrestins 6
1.4 GPCRs in cancer 6
1.5 Uveal melanoma 8
1.6 Cysteinyl leukotrienes and the uveal melanoma driver mutation in *CYSLTR2* 12

CHAPTER 2. MATERIALS AND METHODS **17**
2.1 Materials 17
2.1.1 Reagents *17*
2.1.2 Instruments *17*
2.2 DNA constructs and molecular biology 18
2.2.1 CysLTR2-1D4 expression constructs *18*
2.2.2 CysLTR2-GFP10 fusion protein construct *18*
2.2.3 CysLTR2-V2 and CysLTR2-V2(A)$_6$ constructs *22*
2.2.4 Library construction for CysLTR2 activity-based profiling *22*
2.2.5 SP-FLAG-OLLAS-HT7-NLuc-CysLTR2-GFP10-1D4 constructs in Tet-On inducible gene expression vector *24*
2.3 Cell culture and transfections 26
2.3.1 Transfection for BRET2 assays *26*
2.3.2 Transfection for IP1 assays *29*
2.3.3 Combined transfection for second generation workflow *29*
2.3.4 Transfection of doxycycline-inducible construct for surface expression assays *30*
2.4 BRET2 assays 31
2.4.1 Saturation-binding assays *31*
2.4.2 Time-course assays *31*
2.4.3 Agonist dose-response assays *34*
2.4.4 Activity-based profiling of CYSLTR2 variants *34*
2.5 IP1 assays 34
2.5.1 Agonist dose-response of CysLTR2 DNA titration assays *35*
2.5.2 Time-course assays *35*
2.5.3 Activity-based profiling of CYSLTR2 variants *35*
2.6 Surface expression assays 36
2.7 Plotting binding interfaces 36
2.7.1 Ligand-interacting sites *37*
2.7.2 Arrestin binding interface *37*
2.7.3 G protein binding interface *37*
2.7.4 GRK binding interface *37*

2.7.5 Activating sites *37*
2.8 Quantification and data reduction 45
2.8.1 Data reduction for BRET2 assays *45*
2.8.2 Data reduction, standard calibration and transformation of HTRF data from IP1 assays *45*
2.8.3 Data reduction for nanoBRET surface expression assays *45*

CHAPTER 3. RESULTS AND DISCUSSION 48
3.1 The uveal melanoma oncoprotein CysLTR2-L129Q constitutively activates Gq and escapes β-arrestin down-regulation 48
3.1.1 CysLTR2-L129Q mutation is a CAM that signals through Gq *48*
3.1.2 CysLTR2-L129Q poorly recruits β-arrestins *52*
3.1.3 CysLTR2-L129Q is a Gq-biased CAM that escapes β-arrestin-mediated downregulation *54*
3.1.4 Enhanced recruitment of β-arrestin has only a small effect on basal Gq activation in CysLTR2-L129Q *61*
3.1.5 Data fitting for the IP1 and BRET2 assays *63*
3.2 Activity-based profiling of *CYSLTR2* in the germline and pan-cancer human variome 70
3.2.1 The importance of functionally annotating GPCR VUS in cancer *70*
3.2.2 Development and optimization of activity-based profiling of CYSLTR2 ..... *70*
3.2.3 Prediction of deleterious variants without functional data does not capture the full picture *76*
3.2.4 Frequency distributions and phenotypes of CYSLTR2 variants *78*
3.2.5 Agonist dose-response and surface expression experiments of recurrent variants *83*
3.2.6 Third-generation workflow *86*
3.2.7 The tumor suppressive mechanism of CYSLTR2 and the role of LTC4 ..... *87*
3.3 The activation mechanism of the 3.43 mutant CysLTR2-L129Q 92
3.3.1 Site-saturation mutagenesis of CysLTR2-L129$^{3.43}$ *93*
3.3.2 The noncanonical VRF motif only slightly contributes to the Gq biased constitutive signaling of CysLTR2-L129Q *95*
3.3.3 The L129Q mutation stabilizes the receptor in a partially activated intermediate state. *95*

CHAPTER 4. CONCLUSIONS AND FUTURE WORK 104
4.1 Conclusions 104
4.2 Future directions 105

APPENDIX 107
REFERENCES 108

LIST OF FIGURES

Figure 1-1 GPCR signaling pathways 5
Figure 1-2 CysLTR2-Gq/11 signaling pathways in uveal melanoma 11
Figure 1-3 Key metabolites and enzymes in the synthesis of leukotrienes 14
Figure 2-1 Selection of *CYSLTR2* variants and assay formats in the activity-based screening pipeline 23
Figure 2-2 Transient transfection strategy 27
Figure 2-3 Principle of the functional assays 32
Figure 2-4 Surface expression of recurrent *CYSLTR2* VUS 47
Scheme 3-1 Modeling the pharmacology of constitutively active receptors 49
Figure 3-1 Development of the CysLTR2 functional assay for Gq signaling pathway 50
Figure 3-2 Oncoprotein CysLTR2-L129Q is a Gq-biased CAM that only weakly recruits β-arrestin2 51
Figure 3-3 Time-course of LTD4-stimulated β-arrestin-recruitment measured by the BRET2 assay with CysLTR2-GFP10 and β-arrestin-RLuc3 53
Figure 3-4 β-arrestin-recruitment BRET2 assay with CysLTR2-GFP10 and β-arrestin-RLuc3 .. 55
Figure 3-5 Gene dosage-dependent receptor expression 57
Figure 3-6 Basal and agonist-dependent receptor activity for Gq pathway as function of receptor expression 58
Figure 3-7 Basal and agonist-dependent receptor activity for β-Arrestin2 pathway as function of receptor expression 59
Figure 3-8 Recruitment of β-arrestin has only a small effect on basal Gq activation in CysLTR2-L129Q 62
Figure 3-9 Venn diagrams showing the overlaps of variants in the databases used and the number of recurrent VUS cases in the cancer databases 72
Figure 3-10 Activity-based functional profile of 214 CysLTR2 variants 74
Figure 3-11 Functional sites on CysLTR2 annotated on 2D snake plots 77
Figure 3-12 Landscape of nonsynonymous *CYSLTR2* variants 80
Figure 3-13 Development of frequencies of recurrent *CYSLTR2* variants and their significances 81
Figure 3-14 Functional validation assays of the four recurrent *CYSLTR2* variants 85
Figure 3-15 Preliminary BRET2 and IP1 assays using the tet-inducible FLAG-OLLAS-NLuc-HT7-CysLTR2-GFP10-1D4 88
Figure 3-16 High levels of CysLTR2-L129Q result in cell death 89
Figure 3-17 Role of intracrine signaling of CysLTR2 in stress-activated LTC4 biosynthesis 91
Figure 3-18 Site-saturation mutagenesis of CysLTR2-L129Q$^{3.43}$ 94
Figure 3-19 Known CysLTR2 antagonists have limited efficacy as inverse agonists 96
Figure 3-20 The noncanonical VRF motif only slightly contributes to the Gq biased constitutive signaling of CysLTR2-L129Q 97
Figure 3-21 The L129Q mutation stabilizes the receptor in a partially activated intermediate state 98
Figure 3-22 Characterization of the role of residues in the NPXXY motif 101
Figure 3-23 Hydrogen bond network stabilizes activated state in CysLTR2-L129Q$^{3.43}$ 103

LIST OF TABLES

Table 2. All oligonucleotides used to generate the various constructs used in this thesis..... 19
Table 2-1 Primers for deletion of FLAG epitope tag from FLAG-CysLTR2-1D4 19
Table 2-2 NEBuilder HiFi DNA Assembly primers used in building BRET2 acceptors (CysLTR2-GFP10) 19
Table 2-3 NEBuilder HiFi DNA Assembly primers and oligos used for CysLTR2-V2-GFP10 and CysLTR2-V2$(A)_6$-GFP10 20
Table 2-4 NEBuilder HiFi DNA Assembly primers and oligos used for SP-FLAG-OLLAS-HT7-NLuc-CysLTR2-GFP10-1D4 21
Table 2-5 Table showing CysLTR2 residues involved in G protein, GRK, arrestin, and ligand binding as well as activation as plotted on snake plot in Fig. 3-11B..... 38
Table 3-1 Parameters obtained from fitting experimental data to pharmacological models 66
Table 3-1A Sigmoidal *versus* horizontal line model 66
Table 3-1B Slack-Hall operational model 67
Table 3-1C Two-phase decay model for time-courses 69

LIST OF ABBREVIATIONS

GPCR, G protein-coupled receptors;
β_2AR, β_2-adrenergic receptor;
TM, transmembrane;
G proteins, guanine nucleotide-binding proteins;
GTP, guanosine triphosphate;
GDP, guanosine diphosphate;
ATP, adenosine triphosphate;
ADP, adenosine diphosphate;
cAMP, cyclic adenosine monophosphate;
PKA, protein kinase A;
PKC, protein kinase C;
PLC-β, phospholipase C-β;
IP1, D-myo-inositol-1-phosphate;
IP2, D-myo-inositol-1,4-bisphosphate;
IP3, D-myo-inositol-1,4,5-trisphosphate;
PIP4, phosphatidylinositol-4-phosphate;
PIP2, phosphatidylinositol-4,5-phosphate;
DAG, diacylglycerol;
GEF, guanine nucleotide exchange factor;
GRK, G protein-coupled receptor kinase;
MAP, mitogen-activated protein;
MAPK, mitogen-activated protein kinase;
TEAD, TEA domain transcription factor;
MEK, mitogen-activated protein kinase;
ERK, extracellular signal-regulated kinase;
RGS, regulators of G protein signaling;
AP2, adaptor protein 2;
CPP, clathrin-coated pit;
FDA, Food and Drug Administration;
SBDD, structure-based drug design;
TSHR, thyrotropin receptor gene;
MV, missense variant;
SNP, single nucleotide polymorphism;
VUS, variants of unknown significance;
GoF, gain-of-function;
LoF, loss-of-function;
AltF, altered function;
UM, uveal melanoma;
CysLTR2, cysteinyl leukotriene receptor 2;
CysLTR1, Cysteinyl leukotriene receptor 1;
YAP, yes-associated protein;
TAZ, transcriptional co-activator with PDZ-binding motif;
AP-1, activated protein 1;
PARP, poly (ADP-ribose) polymerase;

DNA, deoxyribonucleic acid;
mRNA, messenger ribonucleic acid;
YM, YM-254890;
BAP1, BRCA1-associated protein 1;
SF3B1, splicing factor 3B1;
EIF1AX, eukaryotic translation initiation factor 1A X-linked;
MSKCC, Memorial Sloan Kettering Cancer Center;
MSK-IMPACT, Memorial Sloan Kettering-Integrated Mutation Profiling of Actionable Cancer Targets;
TCGA, The Cancer Genome Atlas;
CRUK, Cancer Research UK;
QIMR, QIMR Berghofer Medical Research Institute;
UNI-UDE, University of Duisburg-Essen;
ExAC, Exome Aggregation Consortium;
CysLTs, Cysteinyl leukotrienes;
AA, arachidonic acid;
cPLA2, cytosolic phospholipase A_2;
5-HPETE, 5-hydroperoxy-eicosatetraenoic acid;
5-LO, 5-lipoxygenase;
FLAP, 5-LO activating protein;
GSH, glutathione;
LTC4S, LTC4 synthase;
MRP1/4, multidrug resistance-associated proteins 1 and 4;
PTX, pertussis toxin;
MS, multiple sclerosis;
GGT, gamma-glutamyl transpeptidase;
DPEP, dipeptidase;
FACS, fluorescence activated cell sorting;
TPA, 12-*O*-tetradecanoylphorbol-13-acetate;
wt, wild-type;
HTSRC, high throughput and spectroscopy resource center;
BRET2, bioluminescent resonance energy transfer 2;
CMV, cytomegalovirus;
RLuc3, *renilla* luciferase 3;
TRE, tetracycline-responsive element;
tTS, tetracycline transcriptional silencer;
rtTA, reverse tetracycline responsive transcriptional activator M2;
HEK, human embryonic kidney;
ATCC, American type culture collection;
DMEM, Dulbecco's modified Eagle's medium;
DPBS, Dulbecco's phosphate-buffered saline;
FBS, fetal bovine serum;
BSA, bovine serum albumin;
LiCl, lithium chloride;
PCR, polymerase chain reaction;
Me-O-e-CTZ/Prolume Purple, methoxy e-coelenterazine;

HTRF, homogeneous time-resolved fluorescence;
IMPase, inositolmonophosphatase;
mAb, monoclonal antibody;
RT, room temperature;
GRK1, rhodopsin kinase;
RRCS, residue-residue contact score;
GFP10, green fluorescent protein 10;
YFP, yellow fluorescent protein;
C.I., confidence interval;
SEM, standard error of the mean;
ANOVA, analysis of variance;
IC_{50}, half-maximal inhibitory concentration;
EC_{50}, half-maximal effective concentration
GVar, geometric variance;
EPAC, exchange protein activated by cAMP;
CAM, constitutively active mutant;
CA, constitutive activity;
COAD, colorectal adenocarcinoma;
MC4R, melanocortin 4 receptor;
RGS, regulators of G protein signaling;
nLuc, nanoLuciferase;
HT7, HaloTag;
SBS, single base substitutions;
CDS, coding sequence;
AltF, altered function;
ELISA, enzyme-linked immunosorbent assay;
UPR, unfolded protein response;
ISR, integrated stress response;
ER, endoplasmic reticulum;
PC, phosphatidylcholine;
MGST2, microsomal glutathione S-transferase 2;
CHOP, C/EBPbeta homologous protein;
DDIT3, DNA damage-induced transcript 3;
COTL1, coactosin like F-actin binding protein 1;
ROS, reactive oxygen species;
NOX, NADPH oxidase ;
JNK, c-Jun N-terminal kinase;
NAM, negative allosteric modulatory;
hr, hour;
min, minute;
s, second;
χ, chi;
τ, tau;
ε, epsilon;
ex, excitation;
em, emission.

CHAPTER 1. INTRODUCTION

1.1 The discovery of G protein-coupled receptors

The superfamily of G protein-coupled receptors (GPCRs) is the largest gene family encoding cell signaling transmembrane proteins, with ~800 individual GPCRs identified in the human genome. Today, they are recognized as an important class of drug targets that bind to a large diversity of ligands, mediating physiological responses to metabolites, hormones, neurotransmitters, and environmental stimulants.

However, GPCRs and receptors in general, were not well understood and were widely met with skepticism until the last forty years. The discovery and understanding of GPCRs really took off when the study of the visual photoreceptor, rhodopsin, came together with the study of the β_2-adrenergic receptor (β_2AR). Rhodopsin is the prototypical GPCR, activated by light photons and involved in visual signal transmission. It was the first receptor for which a structure was obtained, and it remains one of the most thoroughly studied and characterized (Costanzi et al., 2009). In the 1980s, Paul Hargrave determined the N- and C-terminal sequences of rhodopsin (Wang et al., 1980). Sequencing a highly hydrophobic molecule such as rhodopsin is extremely difficult. A couple of year later, one of the greatest advances in rhodopsin research was made when the complete amino acid sequence of bovine rhodopsin was determined by the laboratories of Ovchinnikov and Hargrave, independently (Hargrave et al., 1983; Ovchinnikov, 1982). At the same time, the complete gene encoding bovine rhodopsin was isolated, allowing the analysis of its full sequence and secondary structure, which revealed that the bovine rhodopsin chain, like that of bacteriorhodopsin, contains seven transmembrane segments (Nathans and Hogness, 1983). Previously, a seven transmembrane (7TM) structure for bacteriorhodopsin was observed by electron microscopy, although this is a light-driven proton pump with limited similarity to rhodopsin otherwise (Henderson and Unwin, 1975). This led to the first bi-dimensional model of rhodopsin, with the extracellular N-terminus followed by a serpentine sequence consisting of seven helices that span the membrane. These seven helices are connected by three external and three intracellular loops, leaving the C-terminus inside the cell. Much biochemical work was conducted on rhodopsin that amounted to insights on its structural and mechanistical features (Sakmar et al., 1989). In 1993, over ten years after the sequence of rhodopsin was determined, Schertler and his coworkers published the first experimental insight into its 3D structure; a 9Å projection map obtained through electron crystallography (Schertler et al., 1993). Palczewski and his coworkers followed with a high-resolution X-ray crystal structure in 2000, which revealed the geometry of the 7TMs and the loop domains almost in their entirety, to reveal many important intramolecular interactions (Palczewski et al., 2000).

While studies of rhodopsin were progressing, Kobilka and Lefkowitz cloned the first ligand-binding GPCR, β_2AR, in 1986 (Dixon et al., 1986). This data showed a significant sequence similarity with bovine rhodopsin and that this receptor also had a seven transmembrane spanning topology. This was the first time that the common structural identity of the GPCR superfamily was recognized. It was only until 20 year later, in 2007, that Kobilka and his coworkers published the crystal structure of the human β_2AR and solidified the long suspected structural homology of these receptors (Rasmussen et al., 2007). Careful comparisons revealed a

good similarity in the topology of the helical bundles as well as the ligand binding pockets, albeit some key differences in the second extracellular loop. It hovers above the ligand binding pocket and closes access from the extracellular side in rhodopsin, while its distinct topology makes the ligand pocket readily accessible in the β_2AR (Cherezov et al., 2007). In 2008, the fourth GPCR structure of the A_{2A} adenosine receptor was published by the Stevens group, which confirmed the structural homology of the GPCRs, particularly the helical bundles, while also highlighting the unique position that the second extracellular loop assumes (Jaakola et al., 2008).

Since then, due to rapid advances in genome sequencing and cryo-electron microscopy, there have been over 450 structures of 82 different receptors that have been determined (Yang et al., 2021). GPCRs are broadly divided into six classes (A-F), based on sequence homology and functional similarity. These classes are class A (rhodopsin-like), B (secretion and adhesion), C (metabotropic glutamate/pheromone), D (fungal mating pheromone), E (cAMP receptors), and F (frizzled/smoothened) (Hu et al., 2017). The class A or "rhodopsin-like family" is the largest of the classes and consists of 719 members divided into subgroups: aminergic, peptide, protein, lipid, melatonin, nucleotide, steroid, hydroxy-carboxylic acid, sensory, and orphan (Foster et al., 2019). These GPCRs show extensive sequence diversity but all share the conserved 7TM motif.

The conserved 7TM core allows for the alignment of GPCR sequences and structures, and to facilitate comparisons of corresponding residues between receptors, generic residue numbering systems have been developed. In particular, the Ballesteros and Weinstein numbering system is commonly used for the class A GPCRs, and will be used extensively in this thesis (Ballesteros and Weinstein, 1995). There is a highly conserved, so-called fingerprint residue in each of the 7TM helices, which fold each segment into its characteristic seven helical bundle. The Ballesteros-Weinstein system labels positions with two numbers: the first is the helix number (1-7) and the second is the residue position relative to the fingerprint residue, which is defined as number 50. For example, the most conserved residue in TM5 is P5.50, and so 5.42 would denote the residue located in TM5, eight residues before P5.50. The residue numbers can be counted directly within the receptor protein sequence but the reference residues can differ slightly between receptors (conservation N1.50: 98%, D2.50: 90%, R3.50: 95%, W4.50: 97%, P5.50: 78%, P6.50: 99%, P7.50: 88%) (Isberg et al., 2015). Most of these conserved residues are part of important microswitch regions. Despite being activated by a diverse set of ligands, the class A GPCRs share their overall activation mechanism, and microswitch regions are residues that have been highly conserved during evolution and undergo rotamer changes between active and inactive states in all receptors (Nygaard et al., 2009). These changes stabilize the global movements of helices and prime the receptor for guanine nucleotide-binding proteins (G proteins) binding (Katritch et al., 2013). The most conserved motif is the D[E]RY motif in helix III, where $R^{3.50}$ forms a salt bridge to the neighboring acidic $D(E)^{3.49}$ in the inactive state (Vogel et al., 2008). In the active state, this salt bridge is broken and $R^{3.50}$ interacts with the Gα subunit (Scheerer et al., 2008). Another conserved motif is the NPXXY motif, located near the intracellular end of helix VII. Here, the $Y^{7.53}$ points towards helices I, II, or VIII in the inactive state but changes its rotamer to interact with side chains of helices III and VI in the active state (Katritch *et al.*, 2013). Lastly, residues $W^{6.48}$, $Y^{7.53}$, $N^{1.50}$, $D^{2.50}$, $S^{3.39}$, $N^{7.45}$, and $N^{7.49}$ make up the sodium binding pocket, in which a Na^+ ion binds and allosterically stabilizes the inactive receptor (Liu et al., 2012; Nygaard *et al.*, 2009).

The rapid speed at which GPCR structures are being published is allowing further studies into commonalities between the receptors and it is now possible to pinpoint the most important, conserved residues for function. Babu and his coworkers have been pushing this field forward by aligning and comparing known structures of GPCRs and discovering molecular signatures of the GPCR fold as well as conserved activation mechanisms of the class A GPCRs (Venkatakrishnan et al., 2016; Venkatakrishnan et al., 2013). Here, it was revealed that there is a consensus network of 24 inter-TM contacts mediated by 36 topological equivalent amino acids. The contacts in the consensus network were found in all the structures, irrespective of their conformational state. Mutations of 14 of the 36 amino acids have been shown to result in modified receptor activity (loss or gain of function) and many of the residues are the highly conserved fingerprint residues mentioned earlier (e.g., $N^{1.50}$, $D^{2.50}$, $W^{4.50}$, $P^{7.50}$). It seems that this consensus network made up of covalent contacts between residues on the TM helices provides an evolutionarily conserved structural scaffold to allow the GPCR to fold into its canonical shape. They further showed that almost every residue in TM3 seems to be important for maintaining either the structure or function of GPCRs (Venkatakrishnan *et al.*, 2013). GPCRs are activated by a diverse set of ligands which trigger structural rearrangements of residue contacts in the TM in an "activation pathway" that connects the ligand-binding pocket to the G-protein-coupling site in order to activate the bound G protein. Although there seem to be distinct activation pathways for the receptors, the pathways converge at the G-protein coupling site, and there is a highly conserved structural rearrangement of residue contacts between TM3, TM6, and TM7 that releases G-protein-contacting residues (Venkatakrishnan *et al.*, 2016). This finding helps to explain how this large family of receptors can all recognize and activate a limited, common repertoire of G proteins.

1.2 Intracellular signaling through G proteins

GPCRs are activated when ligands bind on its extracellular side, which initiate conformational changes within the receptor, which in turn allows it to activate G proteins, which interact with the intracellular side of the receptor. GPCRs bind to a large diversity of ligands, mediating physiological responses to metabolites, hormones, neurotransmitters, and environmental stimulants through activation of G proteins. When activated, the G proteins initiate a series of biochemical reactions and activate signaling pathways within the cells. Each of these pathways are responsible for a wide range of important physiological functions from smell, taste, and vision, to neurotransmission, cell differentiation, inflammatory and immune responses, and metabolism, to name just a few (Hauser et al., 2018b; Lefkowitz, 2000). The study of G proteins was pioneered by Martin Rodbell, who demonstrated that signal transduction in cells required three different components: a discriminator (the receptor) that recognizes extracellular signals, the transducer that utilizes guanosine triphosphate (GTP) (the G protein), and an amplifier that generates large amounts of second messenger (Pohl et al., 1971). Alfred G. Gilman and his coworkers identified the nature of the transducer and purified the protein (Ross and Gilman, 1977). They received the Nobel Prize in Physiology or Medicine in 1994.

G proteins are heteromeric trimers, composed of a Gα subunit and a Gβγ dimer subunit. The Gα and Gγ subunits are attached to the plasma membrane by lipid anchors, and the Gα subunit binds to both guanosine diphosphate (GDP) and GTP. In its inactive state, G proteins

bind to GDP and a nearby GPCR. When an extracellular activating ligand binds to and activates the GPCR, the GPCR undergoes a conformational change, which in turn activates the G protein. This activation causes a GTP to replace the GDP bound to the Gα subunit. The subsequent conformation change in the Gα subunit causes the G protein subunits to dissociate into the Gα subunit and the Gβγ dimer and detach from the GPCR. The two parts remain anchored to the plasma membrane but diffuse laterally and can both interact with and activate downstream effectors, which are often other enzymes or proteins bound to the plasma membrane. In many cases, activating these enzymes gives rise to the production of second messengers. The G protein is inactivated when the GTP on the Gα subunit is hydrolyzed back to GDP, and the three subunits reassemble and reassociate with an inactive GPCR once more.

The Gα subunits are divided into four families based on sequence similarity: Gs, Gi, Gq, and G12 (Neves et al., 2002). GPCRs canonically couple to specific Gα families and each family signals through canonical effectors downstream (**Fig. 1-1**). Members of the Gs family activate adenylyl cyclase (Neves *et al.*, 2002). When adenylyl cyclase is activated, it catalyzes the conversion of adenosine triphosphate (ATP) to cyclic adenosine 3',5'-monophosphates (cAMP), which activates protein kinase A (PKA). cAMP was the first second messenger to be identified and plays many essential roles in regulating physiological responses from hormones to neurotransmitters (Sutherland and Rall, 1958). PKA phosphorylates various metabolic enzymes, such as glycogen synthase, acetyl CoA, and phospholipase C-β (PLC-β) (Sassone-Corsi, 2012). It also activates mitogen-activated protein (MAP) kinases and decreases the activities of Raf and Rho (Sassone-Corsi, 2012). On the other hand, members of the Gi family primarily inhibit adenylyl cyclase, causing an inhibition of the production of cAMP. Both the Gα and Gβγ can activate downstream signaling pathways, and the Gβγ subunits regulate specific isoforms of phospholipases and phosphodiesterases as well as promote the opening of some ion channels (Neves *et al.*, 2002). The Gq family signals through PLC-β, which hydrolyzes phosphatidylinositol biphosphate (PIP2) to produce the second messengers, inositol triphosphate (IP3) and diacylglycerol (DAG). IP3 activates intracellular calcium mobilization and DAG activates protein kinase C (PKC) and Ras guanine nucleotide exchange factors (GEFs) (Mizuno and Itoh, 2009). Members of the Gq family are also known to activate Rho GEFs to stimulate Rho GTPases in a noncanonical fashion (Vaqué et al., 2013). Similarly, members of the G12 family interact with the regulators of G protein signaling (RGS) domains of a family of Rho GEFs to regulate the activity of the Rho GTPases, which are involved in regulating cell migration and formation of actin stress fibers, amongst other processes (Dhanasekaran and Dermott, 1996). A summary schematic of the canonical pathways of the four Gα subunits is shown in **Figure 1-1**.

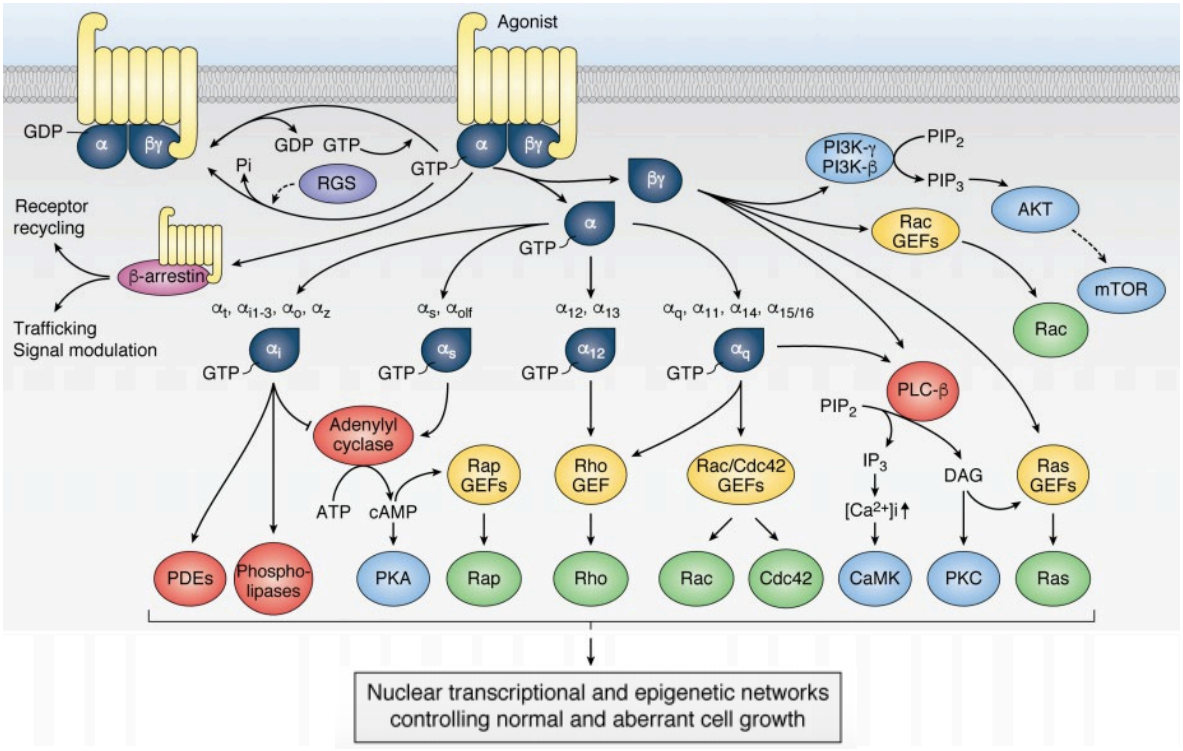

Figure 1-1 GPCR signaling pathways
Schematic of canonical GPCR signaling through heterotrimeric G proteins (navy). Receptor (yellow) activation by an extracellular agonist leads to nucleotide exchange from GDP to GTP in the Gα subunit. The Gα and Gβγ subunits dissociate from the receptor and go on to interact with various downstream effectors. There are four subfamilies of Gα proteins (Gi, Gs, G12, and Gq), which interact with canonical effectors and result in activation and regulation of signaling pathways. These networks all eventually control many cellular functions and nuclear transcription, and irregular activity can cause aberrant cell growth which may lead to disease and cancer. Figure adapted from (Wu et al., 2019).

1.3 The role of arrestins

In the 1970s, activation-induced rhodopsin phosphorylation was first discovered, followed by the discovery of a kinase that specifically phosphorylated activated β_2AR (Benovic et al., 1986; Kühn and Dreyer, 1972). This led to the study of a family of kinases, G protein-coupled receptor kinases (GRKs), which specifically phosphorylate various GPCRs. When GRKs bind to a GPCR, it is activated by it and subsequently phosphorylates residues in the C-terminal tail of the receptor (Gurevich and Gurevich, 2019). As GRKs are soluble proteins, they need to be able to localize near GPCRs. GRK2/3 have a pleckstrin homology domain, which binds the Gβγ subunit (Koch et al., 1993). This means that when the Gβγ subunit is released upon G protein activation, it can help recruit GRKs to the activated receptor to eventually shut it off (Haga and Haga, 1992).

In early experiments, phosphorylation of rhodopsin and β_2AR reduced signaling via G proteins, but it did not completely abort it, suggesting another key player in GPCR downregulation (Arshavsky et al., 1985; Benovic et al., 1989). These were the arrestins. Arrestin-1 was established to have a role in preventing the coupling of phosphorylated rhodopsin to transducin by competing with the transducin for the activated receptor (Wilden et al., 1986). A couple of years later, the first non-visual arrestin was cloned and termed β-arrestin, as they preferred β_2AR over rhodopsin (Lohse et al., 1990). Only two additional arrestins were discovered in the following years, so fascinatingly, there are only four arrestins that bind to and desensitize the hundreds of GPCR subtypes. Two (arrestin-1 and -4) are specific for visual, expressed in photoreceptor cells in the retina, and two are for the non-visual subtypes (arrestin-2 and -3 or β-arrestin1 and 2) (Lohse *et al.*; Wilden, 1995). As predicted in early experiments, recent structural data has revealed that arrestins and G proteins compete for the same inter-helical cavity on the cytoplasmic side of an active receptor (Zhou et al., 2017a). G proteins readily dissociate from the GPCR in the presence of GTP, whereas arrestins bind to phosphorylated GPCRs with a high affinity and easily win the competition to physically block the binding of a G protein.

On top of this, the β-arrestins bind clathrin and adaptor protein 2 (AP2), the major clathrin adaptor protein (Goodman et al., 1996; Laporte et al., 1999). Thus, not only do the β-arrestins physically block G proteins from binding to GPCRs, they facilitate their internalization by targeting the receptor to clathrin-coated pits (CCP) to facilitate endocytosis and further downregulate their cell signaling (Luttrell and Lefkowitz, 2002). Although not covered in this thesis, arrestins can serve as signals transducers in non-canonical signaling pathways as well. In particular, the non-visual arrestins have been shown to scaffold the MAP kinase cascade, c-Raf1-mitogen-activated protein kinase (MEK)1- extracellular signal-regulated kinase (ERK)1/2 (Luttrell et al., 2001).

1.4 GPCRs in cancer

The primary role of GPCRs in physiology is to recognize various ligands, such as peptides, amies, lipids, and nucleotides, and generate cellular responses as a response to these ligands through the activation of different G proteins and the production of second messengers. Of the

826 human GPCRs, ~400 non-olfactory membranes are regarded as druggable, and 165 are validated drug targets (Hauser *et al.*, 2018b). Their transmembrane location allows them easy access and the diverse downstream signaling pathways make them important for drug development. Currently, there are 527 Food and Drug Administration (FDA)-approved drugs and ~60 drug candidates in clinical trials, which target GPCRs (Hauser *et al.*, 2018b; Shimada et al., 2019). Now, over 450 structures of 82 different receptors are available, offering many opportunities for structure-based drug design (SBDD) (Yang *et al.*, 2021). Furthermore, with robust pharmacological assays to measure second messenger accumulation as well as G protein and arrestin interactions, our understanding of the molecular mechanisms of GPCRs and the ability to evaluate the pharmacological outputs of drug hits are greater than ever.

Interestingly, only a handful of these drugs are oncology drugs. Currently, there are only eight FDA-approved anti-cancer drugs that target GPCRs (Wu *et al.*, 2019). However, GPCRs have been shown to be associated with tumor growth and metastasis in various ways. The first example was demonstrated in 1986, when studies showed that the GPCR encoded by the *Mas1* gene produced tumors in mice (Young et al., 1986). A couple of years later, it was discovered that GPCRs can become tumorigenic in a ligand-dependent fashion, when studies showed that muscarinic acetylcholine receptors could only transform NIH3T3 cells in the presence of its agonist, carbachol (Gutkind et al., 1991). This illuminated the possibility of GPCRs having oncogenic roles by harboring activating mutations themselves, or via activation of oncogenic G proteins. For example, there are activating mutations in the thyrotropin receptor gene (*TSHR*) in hyperfunctioning thyroid adenomas, where the mutated GPCRs become constitutively active and initiate neoplastic disease (Parma et al., 1993). Furthermore, downstream of the thyrotropin receptor, somatic mutations were discovered in the Gs protein that impairs its GTPase activity, leading to a constitutively active Gs which in turn leads to constitutively active adenylyl cyclase, leading to development of hyperfunctioning thyroid adenomas and pituitary tumor (Lyons et al., 1990). These mutations have also been seen in pancreatic and colorectal cancers as well (Parish et al., 2018). Since then, there have been many examples of activating mutations in genes encoding GPCRs as well as G proteins, *GNAQ, GNA11, GNA12* and *GNA13*.

Large-scale genomic analysis has revealed that one in five individuals carries a missense variant (MV) in a clinically-relevant GPCR gene. The rate of *de novo* germline MVs in a GPCR gene is one in every 300 newborns, and one in seven MVs is observed at a potential functionally relevant site (Hauser et al., 2018a). To date, there have been over 600 inactivating and 100 activating mutations identified in GPCRs, and these are all responsible for over 30 different kinds of human disease (Thompson et al., 2014). Genetic variants, such as the exchange of a single nucleotide, i.e., a single nucleotide polymorphism (SNP), account for ~80% of all sequence variations. A polymorphism is defined as a genetic variant that occurs at a locus with an allelic frequency of greater than or equal to 1%. This is in contrast to a mutation, which is a germline-transmitted change in an individual or a somatic variation identified in isolated tissues, and is therefore, a rarer genetic variant (Insel et al., 2007). Most SNPs seem to have little effect on receptor function, and it is often difficult to establish the specific consequences of the polymorphism, especially in relation to disease. However, recent studies have shown that asthmatic patients with the Arg16 in the β_2AR shows less response to β_2AR agonists than do patients with Gly16 β_2AR (Tattersfield and Harrison, 2006). Furthermore, it seems that the SNP A1166C in the AT_1 receptor enhances the response to AT_1 antagonists, which can lower blood

pressure, increase glomerular filtration rate, and decrease cardiac hypertrophy in patients with high blood pressure (Kurland et al., 2002).

In addition, GPCR genes are commonly mutated in cancer. Somatic mutations in GPCR-encoding genes are found in 20% of tumor samples, but the lack of specific "hotspot" variants makes it difficult to identify and validate individual receptors as driver oncogenes (Moore et al., 2016). In other words, because each tumor exhibits different sets of mutated GPCRs and further, these do not occur with high frequency in a single or limited number of codons, it is hard to identify and target these GPCR variants. Most of these mutations are also variants of unknown significance (VUS) and their physiological phenotype (gain-of-function, (GoF), loss-of-function (LoF), or a wildtype-like passenger mutation) have yet to be determined. Furthermore, with the increased accessibility of whole exome or genome sequencing, molecular tumor diagnostics are rapidly becoming the standard of care in oncology. An unmet need is to develop a generalizable and scalable strategy to enable the functional classification of GPCR VUS to aid in clinical interpretations of these data. Pursuing GPCRs in oncology has been relatively overlooked for some time. Through better understanding of the mechanisms and roles of GPCRs in tumor progression and metastasis, as well as new methods to uncover the relevance of GPCR VUS, we should be able to study GPCRs as potential oncogenic therapeutic targets.

1.5 Uveal melanoma

Melanoma is a type of skin cancer, which develops from melanocytes, or pigment-containing skin cells. Uveal melanoma (UM) is the most common primary malignant tumor of the eye in adults, representing about 3-5% of all melanoma diagnoses (Chua et al., 2021; Singh et al.). It has an incidence of approximately 2,000 cases per year and affects a quarter of a million individuals in the United States (Katopodis et al., 2021). UM arises from the proliferation of atypical melanocytes in the choroid (85-90%), ciliary body (5-8%) or the iris (5-8%) (Krantz et al., 2017). As UM occurs in one of the most capillary-rich tissues of the body, it spreads solely through the blood stream (Slater et al., 2020). While the primary tumor can be successfully treated with local surgery or radiotherapy, ~50% of all cases lead to metastatic disease, which commonly occurs in the liver (60.5%), lung (24.4%), skin (11%) and bone (8.4%) (Katopodis *et al.*, 2021). Although many advances have been made in the understanding of the pathophysiology of UM, improvements in overall survival have not been seen and remain at 4-18 months for those with metastatic UM (Diener-West et al., 2005). With no therapies available to stop the spread of UM, patients still face an extremely poor prognosis and there is a critically unmet need for new targets and therapeutic agents for UM (Elubous et al., 2021). UM has a low mutational burden, unlike cutaneous melanoma, which makes it difficult to target with immune checkpoint inhibitors (Helgadottir and Höiom, 2016).

Unlike cutaneous melanoma, uveal melanoma lacks the signature mutations in *BRAF*, *NRAS*, or *KIT* (Davies et al., 2002). In fact, over 80% of all UM cases are characterized by mutually exclusive mutations in the genes *GNAQ* and *GNA11*, which encode the Gα subunits Gαq and Gα11 (Van Raamsdonk et al., 2009; Van Raamsdonk et al., 2010). *GNAQ* and *GNA11* are highly conserved and show two hotspot mutations: R183 and Q209 (Van Raamsdonk *et al.*, 2010). These arginine and glutamine residues in the Gα subunits are known to contact the GTP

molecule, and thus mutations at these positions disturb the GTPase function, conferring them to remain locked in an active, signal transducing conformation (Van Raamsdonk *et al.*, 2010). Interestingly, mutations at the homologous position (R201 and Q227) in the Gα subunit in Gs proteins are found in pituitary and thyroid tumors (Landis et al., 1989). It seems then, that the Gαq and Gα11 pathways is the predominant route to the development of uveal melanoma. This is further supported by the fact that *PLCB4*, the gene encoding PLC-β 4, also carries activating mutations in 4% of UM (Amaro et al., 2017). PLC-β is the canonical downstream effector of activated Gq/11 proteins, and these mutations occur in a mutually exclusive manner in UM.

The constitutively active Gq/11 proteins and PLC-β result in the upregulation of downstream signaling pathways, which are implicated in the regulation of cell growth, proliferation, and survival (**Fig. 1-2**). For example, IP3 activates PKC, which begins a cascade of phosphorylation of Raf, MEK, and ERK (mitogen-activated protein kinase (MAPK) pathway), which translocate to the nucleus to regulate cell proliferation and apoptosis (Cobb and Goldsmith, 1995). Yes-associated protein (YAP) is a co-transcriptional regulator involved in the Hippo pathway. When dephosphorylated, it is translocated from the cytoplasm into the nucleus where it activates TEA domain transcription factor (TEAD), which regulates cell proliferation and apoptosis and promotes transcription of growth promoting genes (Amaro *et al.*, 2017). Constitutively active Gq/11 have been shown to increase YAP and transcriptional co-activator with PDZ-binding motif (TAZ) activation through a GEF, TRIO, and the GTPases, Rho and Rac, independent of the Hippo pathway (Feng et al., 2014). Rho and Rac activate c-Jun N-terminal kinase (JNK) and p38, which control nuclear activated protein 1 (AP-1) activity, which in turn promotes cell growth. Lastly, the PI3K-Akt-mTOR pathway is a key pathway for growth and homeostasis and is shown to be upregulated in UM as well (Pópulo et al., 2010). As these pathways are all upregulated when Gq/11 proteins are constitutively active, there are a multitude of targets along each pathway for therapeutic intervention.

As mentioned earlier, response rates with checkpoint inhibitor therapy with anti-CTLA4 (ipilimumab) or anti-PD1 (nivolumab) or combination anti-CTLA4/anti-PD1 inhibition, have proven disappointing (Sussman et al., 2020). This has led to different approaches in targeting the aforementioned pathways. One example is to use MEK inhibitors, such as selumetinib, to target the upregulated MAPK pathway (Carvajal et al., 2014). Although a modest effect was seen when compared to chemotherapy in metastatic UM patients, there were adverse events observed in 97% of patients treated with selumetinib (Carvajal *et al.*, 2014). Another promising candidate is PKC, and a recent phase I study of PKC inhibitor LXS196 has shown encouraging clinical activity with manageable toxicity (Kapiteijn et al., 2019). There has also been promising preclinical activity of natural compounds YM-254890 (YM) and FR900359 that inhibit the α subunit of Gq/11 by stabilizing the inactive, GDP-bound form (Annala et al.; Lapadula et al., 2019). However, their clinical potential is limited from the lack of specificity towards the constitutively active Gq/11, which may lead to adverse effects when normal Gq/11 is blocked. It seems that novel, synergistic combinations of inhibitors may be an important avenue to pursue to broaden therapeutic efficacy. For example, cell-growth inhibition and apoptosis have been observed when inhibitors for MEK and mTOR were combined (Ho et al., 2012). Interestingly, pre-clinical studies have shown that YM alone slowed tumor growth but did not cause regression in human uveal xenografts, and it inhibited MAPK signaling pathways but there was a rebound after 24 hours (Hitchman et al., 2020). However, when combined with a MEK inhibitor,

sustained MAP inhibition as well as tumor shrinkage was seen, adding evidence to the strength of using a combination of therapies (Hitchman *et al.*, 2020). Our group has also shown the promising effects of Arf6 inhibitor, NAV-2729. Inhibition of Arf6 resulted in almost complete inhibition of IP1 accumulation in the Gq/11-dependent signaling (Ceraudo et al., 2019). Although there are various novel therapeutic targets and combination strategies being investigated, there remains a lack of standard of care therapy for metastatic UM and there is an unmet need to improve outcomes for these patients.

Lastly, there are driver mutations in BRCA1-associated protein 1 (*BAP1*), splicing factor 3B1 (*SF3B1*), and eukaryotic translation initiation factor 1A X-linked (*EIF1AX*) that contribute to UM as well (Harbour et al., 2010; Harbour et al., 2013; Martin et al., 2013). These mutations are found in genes whose products are directly involved in transcription and translation. Furthermore, while the mutations described earlier are thought to be tumor initiating mutations, these mutations are linked to tumor progression and occur in concomitance to the initiating mutations (Martin *et al.*, 2013). *BAP1* is a nuclear deubiquitinase, which functions as a tumor suppressor and has an important role in transcription and double-stranded deoxyribonucleic acid (DNA)-damage response. Unsurprisingly, *BAP1* has inactivating mutations in ~50% of primary UM and ~80% of metastatic UM, consistent with its role as a tumor suppressor and the presence of these mutations leading to a poor prognosis (Harbour *et al.*, 2010). *SF3B1* is involved in pre-messenger ribonucleic acid (mRNA) spicing, and alterations are associated with some favorable prognostic features like younger age at diagnosis, fewer undifferentiated epithelioid cells and an inverse correlation with *BAP1* mutations (Harbour *et al.*, 2013). *EIF1AX* and *SF3B1* are both associated with disomy 3, which correlates with a favorable prognosis as opposed to monosomy 3, which is often found in metastatic UM and therefore a poor prognosis (Martin *et al.*, 2013). However, the exact role of *EIF1AX* is not yet known. Once again, these are all targets for therapeutic intervention. For example, there is a current clinical trial evaluating a poly (ADP-ribosse) polymerase (PARP) inhibitor, niraparib, in *BAP1* and other DNA damage response deficient neoplasms in metastatic UM, mesothelioma, and renal cell carcinoma (Sussman *et al.*, 2020). PARP enzymes are responsible for repairing single-stranded DNA breaks, so inhibiting these, while there is an inactivating mutation on the *BAP1* DNA damage repair gene, ultimately leads to truncation of DNA replication, transcription, and cell death, also known as synthetic lethality (Murai et al., 2012).

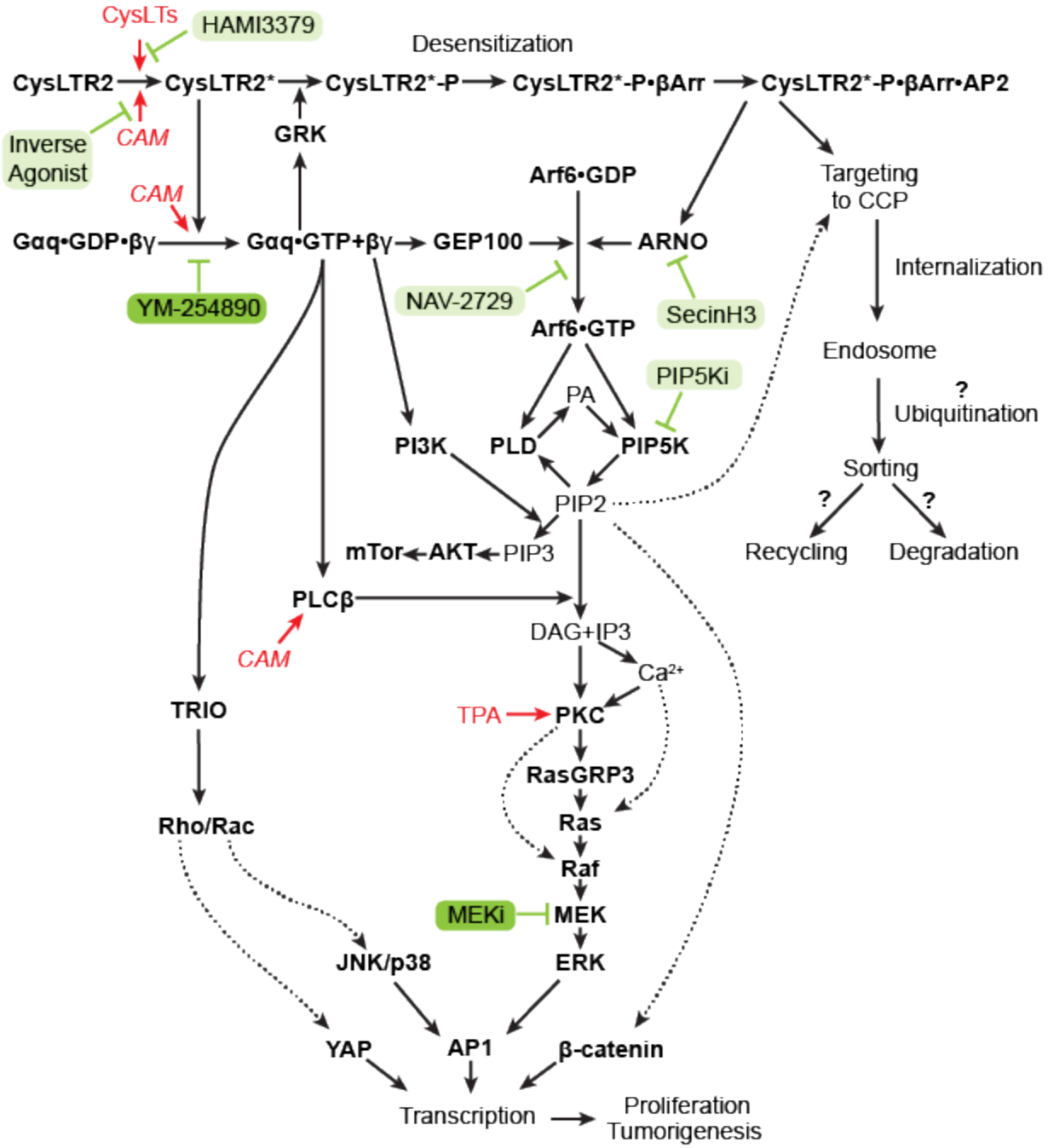

Figure 1-2 CysLTR2-Gq/11 signaling pathways in uveal melanoma
The main downstream signaling pathways of CysLTR2 include PKC/MAPK/MEK/ERK, TRIO/Rho/Rac/YAP, PI3K/Akt/mTOR, and ARF6/GEP100. The constitutively active mutants (CAM) of uveal melanoma driver oncogenes *GNAQ/GNA11*, *PLCB4* and *CYSLTR2* have been identified and labeled with a red arrow. Potential therapeutic targets for uveal melanoma along the pathway are identified with their known inhibitors indicated in green. The β-arrestin dependent desensitization pathway is also shown, where the receptor-arrestin complex is targeted to clathrin-coated pits (CCP) for internalization.

1.6 Cysteinyl leukotrienes and the uveal melanoma driver mutation in *CYSLTR2*

The most common driver mutations in UM were introduced in the previous section, but to identify additional oncogenic drivers in UM, our lab, in collaboration with the laboratories of Ping Chi and Yu Chen at Memorial Sloan Kettering Cancer Center (MSKCC), curated whole-genome or whole-exome sequencing data for 136 UM patients from The Cancer Genome Atlas (TCGA), Cancer Research UK (CRUK), QIMR Berghofer Medical Research Institute (QIMR), and University of Duisburg-Essen (UNI-UDE) cohorts (Moore *et al.*, 2016). A mutational analysis was performed using an algorithm that is highly sensitive in detecting rare hotspot mutations found in oncogenes (Chang et al., 2016). From this, seven significantly mutated ($q<0.05$) codons were found across six genes. Most were already known mutations in *GNAQ, GNA11, PLCB4, SF3B1*, and *EIF1AX* that were introduced in the previous section. However, a novel mutation was found in four samples, in the gene *CYSLTR2*, which encodes a Leu129Gln substitution in the GPCR, cysteinyl leukotriene receptor 2 (CysLTR2) (Moore *et al.*, 2016). Oftentimes, mutations that activate the same pathway tend to be mutually exclusive. We used an algorithm called CoMEt to identify mutually exclusive mutational modules *de novo* in the data set with the 136 UM samples and found that mutations in *GNAQ, GNA11, PLCB4*, and *CYSLTR2* formed a highly significantly mutually exclusive module ($P – 4.2 \times 10^{-33}$) (Leiserson et al., 2015). This suggests that these genes are in the same pathway and that CysLTR2 signals through Gq/11, which then activates PLC-β.

Cysteinyl leukotrienes (CysLTs) are an important group of peptide-conjugated lipids that are a constituent of the eicosanoid family and synthesized from membrane-bound arachidonic acid (AA) (Albert et al., 2003). They are potent inflammatory mediators, which play a role in initiating and propagating a diverse array of biological responses (Kanaoka and Boyce, 2004). CysLTs are produced in stimulated leukocytes, which express the necessary enzymes required for their synthesis (**Fig. 1-3A**). When cells are activated during inflammation, cytosolic phospholipase A_2 (cPLA2) liberates phospholipid-associated AA (Saier and Peyruchaud, 2021). The liberated AA is sequentially lipoxygenated to 5-hydroperoxy-eicosatetraenoic acid (5-HPETE) then dehydrated to the unstable intermediate LTA4 by the enzyme 5-lipoxygenase (5-LO) in concert with 5-LO activating protein (FLAP) (Saier and Peyruchaud, 2021). In neutrophils, LTA4 is preferentially hydrolyzed to the dihydroxy leukotriene, LTB4, by the enzyme LTA4 hydrolase (Kanaoka and Boyce, 2004). In eosinophils, basophils, mast cells, and macrophages, LTA4 is conjugated to a reduced glutathione (GSH) to form LTC4 by LTC4 synthase (LTC4S) (Welsch et al., 1994). 5-LO translocates from its cytosolic or nucleoplasmic location to the perinuclear envelope, while both FLAP and LTC4S constitutively localize there, where CysLT synthesis occurs (Reid et al., 1990). LTC4 is then exported from the cell via multidrug resistance-associated proteins 1 and 4 (MRP1/4) and extracellularly converted into LTD4 via glutamic acid cleave by γ-glutamyl transpeptidase (Anderson et al.; Rius et al., 2008). Lastly, the glycine moiety is cleaved through dipeptidase activity to form LTE4, which is excreted in the urine without further chemical modification (Lee et al., 1983). An overview of the changes in chemical structures AA undergoes is show in **Figure. 1-3B**.

CysLTs signal through specific GPCRs, termed the type 1 and type 2 CysLT receptors (CysLTR1 and CysLTR2). However, recently, the orphan receptors GPR99 and GPR17 have also been implicated as responders to CysLTs as well (Ciana et al., 2006; Kanaoka et al., 2013).

CysLTR1 and CysLTR2 are highly divergent, with only 38% amino acid similarity, as well as incompletely overlapping tissue distributions, suggesting that they serve different functions *in vivo* (Kanaoka and Boyce, 2004). CysLTR1 binds to LTD4 with high affinity (Kd ~ 1nM) and binds LTC4 and LTE4 with progressively lower affinities (LTD4 > LTC4 >> LTE4) (Lynch et al., 1999). On the other hand, CysLTR2 binds LTC4 and LTD4 with equally low affinity (Kd ~ 10 nM, LTC4 = LTD4 >> LTE4) (Heise et al., 2000). GPR99 only exhibits substantial affinity for LTE4, while GPR17 shows substantial affinity for LTD4 (Ciana *et al.*, 2006; Kanaoka *et al.*, 2013). These CysLT receptors all signal through Gi/o, as shown through pertussis toxin (PTX) sensitivity, and Gq/11, and mediate Ca^{2+} mobilization through activation of PLC-β.

Historically, the CysLT receptors have been recognized for their roles in chronic inflammatory diseases, such as asthma, pulmonary fibrosis, atherosclerosis, and inflammatory bowel disease (Bäck and Hansson, 2006; Kanaoka and Boyce, 2004; Samuelsson, 1983). Perhaps most studied, are their powerful broncho-constricting effects, leading to their roles in asthma. Several CysLTR1 specific antagonists like montelukast, zafirlukast, and pranlukast, that show clinical efficacy in asthma treatment by reducing broncho-constrictive response, have been available for more than two decades (Hamilton et al., 1998; Jones et al., 1995; Wenzel and Kamada, 1996). Interestingly, GPR17 has been recently identified as a potential target for neurodegenerative diseases, such as multiple sclerosis (MS), for its role as a modulator of the central nervous system myelination (Dziedzic et al., 2020).

CysLT receptors are also known to play a significant role in some cancers, particularly colorectal cancer (Burke et al., 2016). Elevated levels of inflammatory mediators, such as CysLTs, are found in patients with ulcerative colitis as well as inflammatory bowel disease (Stenson, 1990). As prolonged inflammation is known to increase the risk of developing cancer, it comes as no surprise that these patients display a 30-50% increased risk of developing colon cancer, and that in general, dysregulated CysLT signaling has been implicated in colorectal cancers (Coussens and Werb, 2002; Magnusson et al., 2007). Interestingly, unlike the majority of GPCRs, the CysLT receptors are located both at the plasma membrane and the nuclear membrane (Nielsen et al., 2005). Interestingly, it seems that colon tumors generally have an increased expression of nuclear CysLTR1 as compared with cytoplasmic CysLTR1 (Magnusson et al., 2010). As mentioned previously, the two CysLT receptors do not appear to be functionally interchangeable, and they may even antagonize each other's actions. For example, expression of CysLTR1 is correlated with a poor prognosis for not only colon, but also prostate and breast cancers (Magnusson et al., 2011). High nuclear expression of CysLTR2, on the other hand, is associate with a better overall survival expectancy (Magnusson *et al.*, 2010). CysLTR2 has also been shown to be involved in the differentiation of Caco-2 cells as well as vascular permeability, indicating its potentially protective role in cancer, as compared with CysLTR1, which seems to be important in tumor progression (Hui et al., 2004).

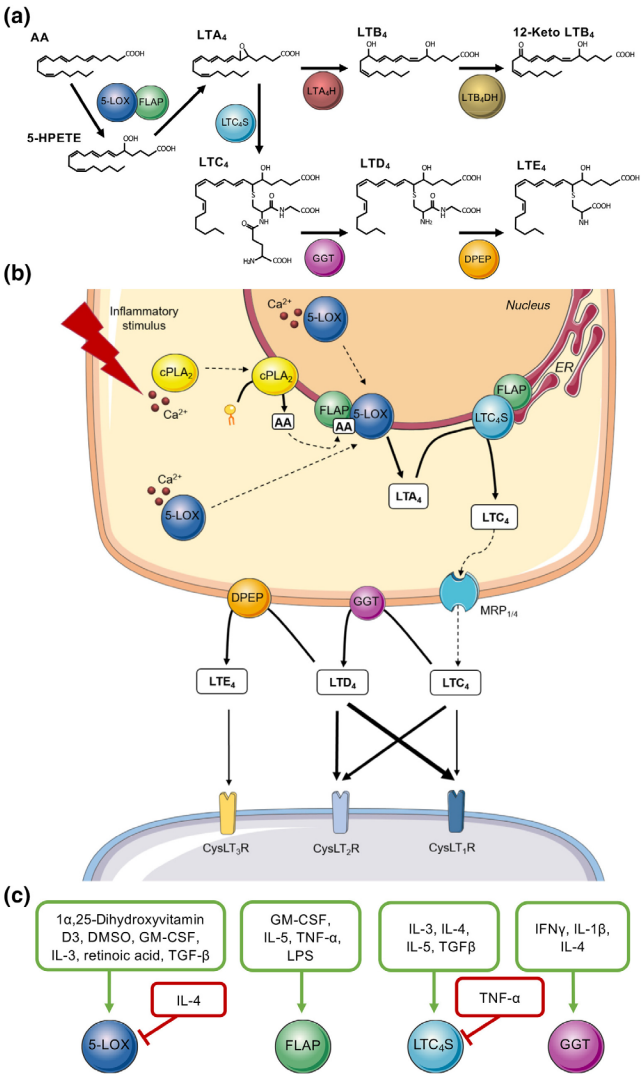

Figure 1-3 Key metabolites and enzymes in the synthesis of leukotrienes
(a) Arachidonic acid (AA) is converted by arachidonate 5-lipoxygenase (5-LO) in concert with 5-LO activating protein (FLAP) into unstable intermediate LTA4 through arachidonic acid 5-hydroperoxide (5-HPETE). The leukotrienes (LTs) are divided into two classes, leukotriene-A4 hydrolase (LTA4H) metabolites such as LTB4, and LTC4 synthetase (LTC4S) metabolites, which are the cysteinyl LTs. **(b)** Upon cellular stimulation, intracellular Ca^{2+} is increased leading to translocation of cytosolic phospholipase A2 (cPLA2) and 5-LO to the nuclear membrane. Phosphorylated cPLA2 is responsible for generating AA by hydrolysis of membrane-associated phosphatidylcholine (PC), which is presented to 5-LO by FLAP and further converted to LTA4. LTA4 is conjugated to reduced glutathione (GSH) by LTC4S to form LTC4, which is exported by multidrug resistance protein (MRP) 1 and 4. In the extracellular space, LTC4 is converted to LTD4 by gamma-glutamyl transpeptidase (GGT) and LTD4 to LTE4 by dipeptidase (DPEP). LTC4 and LTD4 bind to CysLTR1 and CysLTR2, whereas LTE4 binds GPR99, or CysLTR3, with high affinity for LTE4. Figure taken from (Saier and Peyruchaud, 2021).

CysLTR1 antagonists inhibit tumor growth and induce apoptosis in many human cancer cell lines, including those from prostate, breast, and colon cancers (Matsuyama et al., 2007; Savari et al., 2013; Suknuntha et al., 2018). They also significantly reduced cell proliferation and survival in colon cancer cells (Saier and Peyruchaud, 2021). LTD4-CysLTR1 signaling promotes cell proliferation by inducing translocation of β-catenin to the nucleus to promote MYC and CCND1 transcription, which activate expression of many pro-proliferative genes (Salim et al., 2014). Nuclear accumulation of β-catenin has also been linked to colon cancer cells developing resistance to uracil-based drugs such as 5-FU (Satapathy and Sjölander, 2020). Interestingly, treating with a combination of 5-FU and montelukast sensitized these cells to 5-FU and decreased stemness, implicating CysLTR1 in chemotherapeutic drug resistance as well (Satapathy and Sjölander, 2020). Moreover, β-catenin can also be translocated to the mitochondria, where it can interact with anti-apoptotic protein, Bcl-2 (Salim *et al.*, 2014). Interestingly, a retrospective study performed on more than 25,000 asthmatic patients treated with CysLTR1 antagonists (zafirlukast or montelukast) showed that blocking CysLTR1 significantly prevented risk of cancer development, especially breast, colorectal, liver, and lung cancers (Tsai et al., 2016). Although the exact roles of each receptor in cancer is not yet clear, their involvement in cell proliferation, inflammation, and tumor development in cancer is compelling.

In this way, the family of CysLTs, as well as the GPCRs that they activate, are already known to be important targets of disease and cancer and are of high importance to study. But what about in UM? The recurrent mutation was found at position 129, which is located in TM3 at position 3.43 (Ballesteros-Weinstein numbering) in a conserved functional site (Ballesteros and Weinstein, 1995). At this position, the Leu129 interacts with other transmembrane helices within the membrane in the hydrophobic core of the GPCR, and these interactions are implicated in the conformational change the receptor makes upon activation (Moore *et al.*, 2016). A mutation to a more hydrophilic Gln can be speculated to disrupt important contacts and structural organization. Perhaps unsurprisingly, altering residues at the 3.43 position has been shown to confer constitutive activity in a number of GPCRs, including the β-adrenergic, luteinizing hormone, and thyroid-stimulating hormone receptors (Tao, 2008). When wildtype (WT) CysLTR2 was transiently transfected into HEK293T cells, they mobilized Ca^{2+} in a LTD4-dose-dependent manner, confirming the earlier hypothesis that CysLTR2 signals through Gq/11 to activate PLC-β and initiate Ca^{2+} mobilization (Moore *et al.*, 2016). Interestingly, when CysLTR2-L129Q was assayed in the same manner, the cells exhibited high basal Ca^{2+} levels that were not affected by LTD4, indicating that this mutant is constitutively active (Moore *et al.*, 2016). The WT and mutant receptors expressed similarly as determined by western blot analysis, demonstrated similar cellular localizations as demonstrated by immunofluorescence, and showed similar cell surface expression as determined by fluorescence activated cell sorting (FACS) analysis, which all suggests that the functionally different behavior is not due to differences in expression or localization. Further, both WT and mutant receptors were not shown to couple to Gs or Gi, as cells expressing the receptors showed no effect on basal cAMP levels or LTD4-stimulated cAMP levels, indicative of adenylyl cyclase activation via Gs activation, and they further showed negligible inhibitory effects on forskolin-induced cAMP levels. L129Q is a GoF mutation that couples through Gq.

Furthermore, CysLTR2 L129Q, but not WT, was shown to have oncogenic activities and was able to form tumors *in vivo* in immortalized mouse NIH3T3 fibroblasts. To look at melanocyte-lineage-specific effects, CysLTR2 WT and L129Q were stably expressed in melan-a cells, an immortalized mouse melanocytic cell line. Melan-a cells require phorbol esters such as 12-*O*-tetradecanoylphorbol-13-acetate (TPA) for growth and for promoting melanocyte-lineage specification as well as pigmentation (Bennett et al., 1987). CysLTR2 L129Q, but not WT, expressing melan-a cells conferred TPA-independent growth, and augmented pigmentation in melan-a cells cultured in TPA-containing medium. These results were corroborated in MEL290 cells, a human uveal melanoma cell line that is wildtype for *GNA11* and *GNAQ,* where expression of CysLTR2 L129Q increased melanocyte specific genes. To our knowledge, no single GPCR-encoding gene has been identified and validated as a driver oncogene for a malignant tumor type, making CysLTR2 L129Q the first example of a cancer mutation in a GPCR that has been validated as a driver oncogene. The mutation in *CYSLTR2* is a novel driver oncogene that needs to be carefully considered along with previously known driver oncogenes, *GNAQ, GNA11, PLCB4, SF3B1*, and *EIF1AX.* CysLTR2 L129Q exhibits constitutive activity and couples through Gq/11, essentially conferring the same constitutively active phenotype as the mutant Gq/11 proteins and activating the same downstream pathway. As mentioned above, the CysLT receptors have been implicated and targeted in several other diseases, and there are several specific inhibitors for these receptors. It would be of great interest to see if these antagonists could be repurposed to serve as an inhibitor for the constitutively active CysLTR2 L129Q mutant. Ideally, we would develop high-affinity inverse agonists that stabilize the inactive state and switch off the high basal activity (Bond and Ijzerman, 2006). There is hope that development of such drugs will have a massive therapeutic potential in UM, a disease that currently has no effective therapy.

CHAPTER 2. MATERIALS AND METHODS

2.1 Materials

2.1.1 Reagents

LTD4 was obtained from Cayman Chemical (Ann Arbor, MI). YM-254890 was obtained from Wako Pure Chemical Industries (Richmond, VA). BRET2 substrate, methoxy e-Coelenterazine was from NanoLight Technology (Pinetop, AZ). The IP-One HTRF kit was from CisBio (Codolet, France). The NanoBRET substrate, Nano-Glo Luciferase Assay System as well as the two HaloTag ligands, HaloTag NanoBRET 618 Ligand and HaloTag Alexa Fluor 660 Fluorescent Ligand, were purchased from Promega (Madison, WI). Bovine serum albumin (BSA) fraction V fatty acid-frees was from Roche (Basel, Switzerland). Poly-D-lysine and lithium chloride (LiCl) were from Sigma-Aldrich (St. Louis, MO). HEK293T cells were from American Type Culture Collection (ATCC) (Manassas, VA). Dulbecco's Modified Eagle's Medium (DMEM) GlutaMAX, FluoroBrite DMEM, Dulbecco's phosphate-buffered saline without calcium and magnesium (DPBS) and HEPES buffer were from Thermo Fisher Scientific (Waltham, MA). L-glutamine, Lipofectamine 2000, and Trypsin-EDTA (0.25%, phenol red) were from Thermo Fisher Scientific (Waltham, MA). Fetal bovine serum (FBS) was from Gemini Bio-Products (West Sacramento, CA). Doxycycline was from Clontech (Mountainview, CA). Black and white low volume 384-well microplates, and black CELLSTAR 96-well microplates (polystyrene wells flat bottom) were from Greiner (Monroe, NC). NEBuilder Hifi DNA Assembler, Dpn1, T4 DNA Ligase, Q5 Hot Start High-Fidelity DNA Polymerase, and dNTPs were from New England BioLabs (Ipswich, MA). Quikchange Lightning Site-Directed Mutagenesis Kit was from Agilent Technologies (Santa Clara, CA) and TagMaster Site-Directed Mutagenesis Kit was from GM Biosciences Inc. (Frederick, MD). DNA Clean and Concentrator was from Zymo Research (Irvine, CA). Oligonucleotides which are listed in **Tables 2-1 to 2-4** were purchased at the standard desalting grade from Integrated DNA Technology (IDT, Coralville, IA). QIAGEN Plasmid Maxi Kits and QIAprep Spin Miniprep Kit were from QIAGEN (Germantown, MD). Custom plasmid, SP-FLAG-OLLAS-NLuc-HT7-CCR5-SNAP-1D4 with a TRE promoter in the Mammalian Tet-On Inducible Gene Expression Vector was designed and purchased from VectorBuilder (Chicago, IL).

2.1.2 Instruments

Time-resolved fluorescence signals for the CisBio IP1 assays were read on the BioTek Synergy NEO plate reader (for first generation assays) or the BioTek Synergy NEO2-TRF Hybrid multi-mode reader (for second generation assays) from BioTek Instruments (Winooski, VT) in the Rockefeller University's High Throughput and Spectroscopy Resource Center (HTSRC). All BRET2 β-arrestin recruitment assays were read on the BioTek Synergy NEO2 plate reader from BioTek Instruments in the HTSRC as well. NanoBRET Surface Expression Assays were read on the SpectraMax i3x multi-mode microplate reader from Molecular Devices (San Jose, CA).

2.2 DNA constructs and molecular biology

2.2.1 CysLTR2-1D4 expression constructs

The synthetic vector encodes human CysLTR2 cDNA in pcDNA3.1(+) with a cytomegalovirus (CMV) promoter fused to an N-terminal FLAG tag (DYKDDDDK) and a C-terminal 1D4 epitope tag (TETSQVAPA) (Moore *et al.*, 2016). The FLAG tag was then deleted by site-directed mutagenesis using TagMaster Site-Directed Mutagenesis Kit according to the manufacturer's instructions to generate CysLTR2-1D4. TagMaster primers that were used to generate the 1D4 constructs are listed in **Table 2-1** and were purchased from Integrated DNA Technology (IDT). All constructs were confirmed by sequencing (Genewiz, South Plainfield, NJ).

2.2.2 CysLTR2-GFP10 fusion protein construct

The NEBuilder HiFi DNA Assembly Tool was used to assemble the bioluminescence resonance energy transfer 2 (BRET2) acceptor construct CysLTR2-GFP10-1D4 (CysLTR2-GFP10 for simplicity). We assembled the construct from three parts: pcDNA3.1(+) backbone from construct HA-CLIP-CLR (Lorenzen et al., 2019), CysLTR2 and full-length C-terminal 1D4 epitope tag from FLAG-CysLTR2-1D4 mentioned above, and GFP10 from YB124_CXCR4-GFP10 (Berchiche and Sakmar, 2016). The primers (**Table 2-2**) were designed using the NEBuilder Assembly Tool on the NEB website with a specific sequence to prime to the gene of interest for template priming (3' end), as well as an overlap sequence to aid in assembly (5' end).

The fragments introduced above were polymerase chain reaction (PCR) amplified using Q5 Hot Start High-Fidelity DNA Polymerase and fresh dNTPs purchased from NEB. Briefly, the PCR reactions were performed in 25 µL total volume containing: 1× Q5 Reaction Buffer, 0.2 mM dNTPs, 0.5 µM of the forward primer, 0.5 µM of the reverse primer, 1 ng template DNA, and 1 unit of Q5 Hot Start High-Fidelity DNA Polymerase. The PCR thermocycle was as follows: initial denaturation at 98 °C for 30 s, followed by 25 cycles of denaturation (98 °C, 10s), annealing (varied from 50–70 °C, 30 s), and elongation (72 °C, 3 min), and ending with a final elongation (72 °C, 2 min). The recommended annealing temperature calculated on the NEBuilder Assembly Tool was used for each primer pair. Following PCR, 1 unit of DpnI was added and the mixture was incubated at 37 °C for 30 min to digest any remaining template DNA. This was cleaned up, and any enzymes were removed using a DNA Clean and Concentrator. The concentrations of all PCR-amplified fragments were determined using a NanoDrop.

The NEBuilder Hifi DNA Assembler includes three enzymes; the exonuclease to create 3' overhangs to aid annealing of neighboring fragments sharing a complimentary overlap region, the polymerase to fill the gaps of each annealed fragment and the DNA ligase to seal nicks in the assembled DNA. The assembly reaction was performed in 20 µL total volume, with 50 ng of vector, 100 ng of insert(s), and 10 µL of the NEBuilder HiFi DNA Assembly Master Mix. This was incubated at 50 °C for 60 min, and 2 µL of the assembled product was used to transform NEB 5-alpha Competent *E. coli* cells. Cells were spread on LB-Amp plates and colonies were picked and confirmed by sequencing.

Table 2. All oligonucleotides used to generate the various constructs used in this thesis

(**2-1**) TagMaster site-directed mutagenesis primers used in deleting FLAG epitope tag from FLAG-CysLTR2-1D4. (**2-2**) NEBuilder HiFi DNA Assembly primers used to amplify fragments and build CysLTR2-GFP10. (**2-3**) Top: Gene optimized 27 amino acid sequence from C-terminal tail of vasopressin V2 receptor and its hexa-Ala version. Bottom: NEBuilder HiFi DNA Assembly primers used to generate CysLTR2-V2-GFP10 and CysLTR2-V2$(A)_6$-GFP10. All oligonucleotides were ordered from IDT at the standard desalting grade. (**2-4**) NEBuilder HiFi DNA Assembly primers used to amplify fragments and build SP-FLAG-OLLAS-HT7-NLuc-CysLTR2-GFP10-1D4.

Table 2-1 Primers for deletion of FLAG epitope tag from FLAG-CysLTR2-1D4

Purpose of Primer	Oligonucleotide Sequence of Primers
FLAG-deletion-Fwd	5' TCT GCA GAT ATC GCC ACC ATG GAG AGG AAG TTC ATG TCC CTG 3'
FLAG-deletion-Rev	3' CAG GGA CAT GAA CTT CCT CTC CAT GGT GGC GAT ATC TGC AGA G 5'

Table 2-2 NEBuilder HiFi DNA Assembly primers used in building BRET2 acceptors (CysLTR2-GFP10)

Name	Sequence of Primers (5' to 3') w/ overlaps underlined	Purpose
TH1700_1	GGT GGC GGC GGT ATC ATC TCG TGC AGG GCG GCC GCT AAG CTT AAG TTT AAA CGC TAG CCA GC	Anneals to FLAG-CysLTR2-1D4 and overlaps with HA-CLIP-CLR
TH1700_2	TAG CGT TTA AAC TTA AGC TTA GCG GCC GCC CTG CAC GAG ATG ATA CCG CCG CCA CCA TGT CCC TGC AGC CCA GC	Anneals to HA-CLIP-CLR and overlaps with FLAG-CysLTR2-1D4
TH1700_3	CGA ATT CAC CGG TAC CCA CCC TTG TCT CTT TTC TGA GC	Anneals to CXCR4-GFP10, and overlaps with FLAG-CysLTR2-1D4
TH1700_4	GAC AAG GGT GGG TAC CGG TGA ATT CGT GAG CAA GGG CGA GGA G	Anneals to FLAG-CysLTR2-1D4, and overlaps with CXCR4-GFP10
TH1700_5	ACG GTG GTG CTG GCC TCA TCG GAT CCG CCT GCA GGC TTG TAC AGC TCG TCC ATG C	Anneals to HA-CLIP-CLR, and overlaps with CXCR4-GFP10
TH1700_6	CCT GCA GGC GGA TCC GAT GAG GCC AGC ACC ACC	Anneals to CXCR4-GFP10, and overlaps with HA-CLIP-CLR
1740_FLAG-CysLTR2_fwd	ATG ATA CCG CCG CCA CCA TGG AGA GGA AGT TCA TGT CC	Anneals to FLAG-CysLTR2-1D4, and overlaps with

1740_FLAG-CysLTR2_rev	CTC ACG AAT TCA CCG GTA CCC ACC CTT GTC TCT TTT CTG	TH1705 (CLTR2-GFP10-1D4) Anneals to FLAG-CysLTR2-1D4, and overlaps with TH1705 (CLTR2-GFP10-1D4)
1720_TH1705_fwd	GGT ACC GGT GAA TTC GTG AG	Anneals to TH1705 (CLTR2-GFP10-1D4)
1720_TH1705_rev	CAT GGT GGC GGC GGT ATC	Anneals to TH1705 (CLTR2-GFP10-1D4)

Table 2-3 NEBuilder HiFi DNA Assembly primers and oligos used for CysLTR2-V2-GFP10 and CysLTR2-V2(A)$_6$-GFP10

Name	Sequence of Oligonucleotides	Purpose
V2 Tail	GGC AGA ACA CCT CCA TCT CTG GGA CCT CAG GAT GAG AGC TGT ACC ACA GCC TCT AGC AGC CTG GCC AAG GAT ACA AGC TCT	Gene optimized 27 amino acid sequence from C-terminal tail of vasopressin V2 receptor
V2(A)$_6$ Tail	GGC AGA ACA CCT CCA TCT CTG GGA CCT CAG GAT GAG AGC TGT ACC ACA GCT GCT GCC GCT CTG GCC AAA GAT GCT GCT GCT	Gene optimized, phosphorylation-resistant (A)$_6$ 27 amino acid sequence from C-terminal tail of vasopressin V2 receptor
Name	Sequence of Primers (5' to 3') w/ overlaps underlined	Purpose
CysLTR2(1-346)V2-GFP10-1D4_fwd	TGG CCA AGG ATA CAA GCT CTG GTA CCG GTG AAT TCG TG	Anneals to CysLTR2-GFP10 after the full length CysLTR2, and overlaps with V2 tail
CysLTR2(1-346)V2-GFP10-1D4_rev	AGA GAT GGA GGT GTT CTG CCC ACC CTT GTC TCT TTT CTG	Anneals to CysLTR2-GFP10 after the full length CysLTR2, and overlaps with V2 tail
CysLTR2(1-346)V2(A)$_6$-GFP10-1D4_fwd	TGG CCA AAG ATG CTG CTG CTG GTA CCG GTG AAT TCG TG	Anneals to CysLTR2-GFP10 after the full length CysLTR2, and overlaps with V2(A)$_6$ tail
CysLTR2(1-346) V2(A)$_6$-GFP10-1D4_rev	AGA GAT GGA GGT GTT CTG CCC ACC CTT GTC TCT TTT CTG	Anneals to CysLTR2-GFP10 after the full length CysLTR2, and overlaps with V2(A)$_6$ tail

Table 2-4 NEBuilder HiFi DNA Assembly primers and oligos used for SP-FLAG-OLLAS-HT7-NLuc-CysLTR2-GFP10-1D4

Name	Sequence of Primers (5' to 3') w/ overlaps underlined	Purpose
TH1086_fwd	ACCCAGCTTTCTTGTACAAAG	Anneals to TH1086 (SP-FLAG-OLLAS-NLuc-HT7-CCR5-SNAP-1D4) after the 1D4 until HT7 to make backbone with N-terminal tags (SP-FLAG-OLLAS-HT7-NLuc)
TH1086_rev	GGTGTCATCTCCTGCAGG	Anneals to TH1086 after the 1D4 until HT7 to make backbone with N-terminal tags
TH1740_fwd	CCCCTGCAGGAGATGACACC ATGGAGAGGAAGTTCATGTCCC	Anneals to CysLTR2-GFP10 after the GFP10-1D4 and overlaps with TH1086 backbone and N-terminal tags
TH1740_rev	TTTGTACAAGAAAGCTGGGT TTAGGCAGGGGCCACCTG	Anneals to CysLTR2-GFP10 after the GFP10-1D4 and overlaps with TH1086 backbone and N-terminal tags

After the assembled product was confirmed by sequencing, the second *NotI* site that is flanked by two *XhoI* sites, which had been part of the pcDNA3.1(+) backbone in HA-CLR-CLIP, was removed. This was simply done by digesting at the *XhoI* sites and self-ligating the vector using T4 DNA Ligase. We then sequenced the *NotI*-removed CysLTR2-GFP10 in its entirety to check for any erroneous modifications or linkages.

The β-arrestin2-RLuc3 BRET2 donor was constructed previously by fusing the coding sequence of *Renilla* luciferase 3 (RLuc3) to the C-terminus of β-arrestin2 (Berchiche and Sakmar, 2016).

2.2.3 CysLTR2-V2 and CysLTR2-V2(A)$_6$ constructs

The cDNA encoding the 27 amino acids from the C-terminal tail of the vasopressin V2 receptor, GRTPPSLGPQDESCTTASSSLAKDTSS, was fused to the end of the full-length CysLTR2 receptor in the CysLTR2-GFP10 construct introduced above. As a negative control, we also fused a hexa-Ala variant (Oakley et al., 1999) of the 27 amino acids with the phosphorylation sites (Ser and Thr) replaced with Ala (GRTPPSLGPQDESCTTAAAALAKDAAA, Ala substitutions underlined) to the full-length CysLTR2 receptor. For both amino acid sequences, we used the GeneOptimizer algorithm in GeneArt (ThermoFisher Scientific, Waltham, MA) to get a DNA sequence optimized for humans and avoiding major restriction sites. The NEBuilder HiFi DNA Assembly Tool was used to assemble these constructs from two parts: the single-stranded oligonucleotide of the V2 receptor tail sequence and the linearized CysLTR2-GFP10 construct cut after the full-length receptor and before the GFP10. The primers were designed using the NEBuilder Assembly Tool on the NEB website and their sequences are shown in **Table 2-3**. The PCR amplification of the CysLTR2-GFP10 fragment, and the isothermal assembly of these two parts were performed as outlined above. Note that the NEBuilder HiFi DNA Assembly method allows the assembly of a single-stranded oligonucleotide to a double-stranded DNA strand. All constructs were prepared from the QIAGEN Plasmid Maxi Kits and confirmed by Sanger sequencing using standard BGH reverse sequencing primers.

2.2.4 Library construction for CysLTR2 activity-based profiling

First, we identified 120 unique *CYSLTR2* variants from the TCGA and COSMIC databases, plus four additional germline variants from GPCRdb/Exome Aggregation Consortium (ExAC) that were located at sites with a high likelihood of functional impact e.g., Na binding sites, microswitch sites, and G protein and β-arrestin interaction sites (**Fig. 2-1**). These were generated by site-directed mutagenesis using the QuikChange Lightning Site-Directed Mutagenesis Kit and the aforementioned *NotI*-removed CysLTR2-GFP10 construct as the template. The QuikChange Primer Design web tool (Agilent, Santa Clara, CA) was used to design primers to introduce all mutations. For each mutated codon, we used the most frequently used triplet encoding for a particular amino acid in humans. The PCR reactions were performed based on the manufacturer's instructions with slight modifications using half-volume reactions (total of 25 µL) using 25 ng of template DNA. All constructs were prepared from QIAprep Spin Miniprep Kit and confirmed by Sanger sequencing using standard CMV forward and BGH reverse sequencing primers.

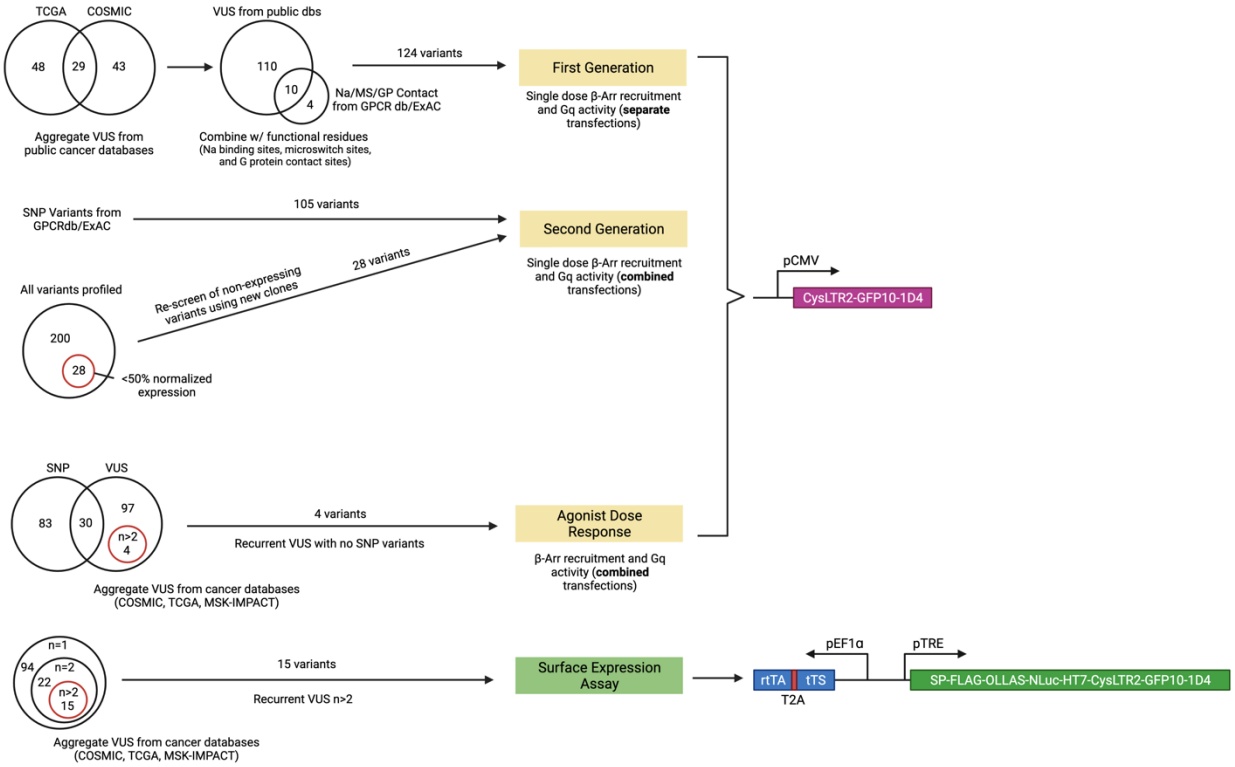

Figure 2-1 Selection of *CYSLTR2* variants and assay formats in the activity-based screening pipeline

In the "First Generation" screen, we identified 120 unique *CYSLTR2* variants from public cancer databases, TCGA and COSMIC, plus four additional germline variants from ExAC that were located at sites with a high likelihood of functional impact e.g., Na binding sites, microswitch sites, and G protein and β-arrestin interaction sites. This led to a total of 124 variants that we screened using the CysLTR2-GFP10-1D4 construct in pcDNA3.1(+) with a CMV promoter, where we conducted single-dose BRET2 β-arrestin recruitment assays and IP1 assays where each assay was conducted with a separate transfection. We used the "Second Generation" workflow to screen 105 variants from ExAC with unknown relevance in cancer, and also to re-screen 28 variants that showed poor expression in the initial screen (<50% normalized expression). For the re-screen, we made new clones for all variants in the same CysLTR2-GFP10-1D4 plasmid, which recovered expression in all cases. In this screen, we conducted single-dose BRET2 assays and IP1 assays and both assays were conducted using the same transfection. We next aggregated the variants found as SNP and VUS in the cancer databases, COSMIC, TCGA, and MSK-IMPACT. We found four variants that were recurrent VUS but with no SNP cases and performed a detailed agonist dose-response assay for these, using the same transfection mixture for both BRET2 assays and IP1 assays. For the last generation of optimization, we took 15 recurrent VUS (n>2) and introduced them into a doxycycline-inducible expression system to enable controlled expression of a new construct carrying Nano luciferase (NLuc) and HaloTag (HT7) as an additional N-terminal fusion (Freundlieb et al., 1999; Machleidt et al., 2015). These allowed for a novel high-throughput capable surface expression assay to be developed using a nanoBRET pulse-chase experiment.

After the initial screen, we identified another 105 variants from GPCRdb/ExAC with unknown relevance in cancer (**Fig. 2-1**). We also decided to re-screen 28 variants that showed poor expression in the initial screen (<50% normalized expression). These SNP mutants were generated in the same manner as the CysLTR2 MVs, with site-directed mutagenesis using the QuikChange Lightning Site-Directed Mutagenesis Kit on the CysLTR2-GFP10 template. Again, the QuikChange Primer Design web tool was used to design primers to introduce all mutations. For the re-screen, we used the same primers to redo the site-directed mutagenesis and made new clones for all poorly expressing variants, which recovered expression in all cases. Since all the clones had the correct coding sequence using Sanger sequencing, we concluded that the poorly expressing clones were likely due to sporadic errors introduced into the plasmid backbone by the QuikChange site-directed mutagenesis method. All constructs were prepared from QIAprep Spin Miniprep Kit and confirmed by Sanger sequencing using standard CMV forward and BGH reverse sequencing primers.

2.2.5 SP-FLAG-OLLAS-HT7-NLuc-CysLTR2-GFP10-1D4 constructs in Tet-On inducible gene expression vector

Custom plasmid, SP-FLAG-OLLAS-NLuc-HT7-CCR5-SNAP-1D4 with a TRE promoter in the mammalian Tet-On inducible gene expression vector was designed and purchased from VectorBuilder (Chicago, IL) for a different project in the lab. We wanted to work with a doxycycline-inducible system that is compatible with transient expression, to allow for compatibility with highly toxic proteins in the future. As such, we decided to switch our constructs from the constitutive CMV promoter in pcDNA3.1(+) to the tetracycline-responsive element (TRE) promoter, which is regulated by a class of transcription factors that are activated by tetracycline or its analogs (Freundlieb *et al.*, 1999). In this system, we use a combination of the Tet-Off and Tet-On technologies to prevent any leaky expression and allow for precise control of our expression. The Tet-Off system utilizes the tetracycline transcriptional silencer (tTS), which binds to the TRE promoter to suppress gene transcription. On the other hand, the Tet-On system utilizes the reverse tetracycline responsive transcriptional activator M2 (rtTA), which is a transcriptional activator that binds to the TRE promoter in a doxycycline-dependent manner.

The NEBuilder HiFi DNA Assembly Tool was used to assemble the SP-FLAG-OLLAS-HT7-NLuc-CysLTR2-GFP10-1D4 construct that will be used for the surface expression assay. We assembled the construct from two parts: the Tet-On inducible gene expression vector backbone with N-terminal tags (SP-FLAG-OLLAS-HT7-NLuc) from SP-FLAG-OLLAS-NLuc-HT7-CCR5-SNAP-1D4 with a TRE promoter in the mammalian Tet-On inducible gene expression and CysLTR2, full-length C-terminal 1D4 epitope tag, and GFP10 from our CysLTR2-GFP10 construct. The primers (**Table 2-4**) were designed using the NEBuilder Assembly Tool on the NEB website with a specific sequence to prime to the gene of interest for template priming (3' end), as well as an overlap sequence to aid in assembly (5' end).

As before, the two fragments introduced above were PCR amplified using Q5 Hot Start High-Fidelity DNA Polymerase and fresh dNTPs purchased from NEB. Briefly, the PCR reactions were performed in 50 µL total volume containing: 1× Q5 Reaction Buffer, 0.2 mM dNTPs, 0.5 µM of the forward primer, 0.5 µM of the reverse primer, 1 ng template DNA, and 1

unit of Q5 Hot Start High-Fidelity DNA Polymerase. The PCR thermocycle was as follows: initial denaturation at 98 °C for 30 s, followed by 30 cycles of denaturation (98 °C, 10s), annealing (63.4 °C for vector, 67.3 °C for insert, 30 s), and elongation (72 °C, 3.5 min), and ending with a final elongation (72 °C, 2 min). The recommended annealing temperature calculated on the NEBuilder Assembly Tool was used for each primer pair. Following PCR, 1 unit of DpnI was added and the mixture was incubated at 37 °C for 30 min to digest any remaining template DNA. This was cleaned up, and any enzymes were removed using a DNA Clean and Concentrator. The concentrations of all PCR-amplified fragments were determined using a NanoDrop.

The assembly reaction was performed as before, in 20 µL total volume. We added vector and insert in a 1:2 ratio according to DNA mass. This was calculated to be 100 ng of vector and 50 ng of insert. Lastly, 10 µL of the NEBuilder HiFi DNA Assembly Master Mix is added, and this was incubated at 50 °C for 60 min. Then, 2 µL of the assembled product was used to transform NEB 5-alpha Competent *E. coli* cells. Cells were spread on LB-Amp plates and colonies were picked and confirmed by sequencing.

We aggregated the case numbers for each variant from the COSMIC, TCGA, and Memorial Sloan Kettering-Integrated Mutation Profiling of Actionable Cancer Targets (MSK-IMPACT) databases and identified 15 cancer VUS (14 variants + L129Q) that had n>2 recorded cases (**Fig. 2-1**). We generated these variants in the doxycycline-inducible SP-FLAG-OLLAS-HT7-NLuc-CysLTR2-GFP10-1D4 construct to conduct the pilot surface expression assay. The NEBuilder Assembly primers to amplify the CysLTR2-GFP10-1D4 insert, designed as described above, can be used on the variants in the CysLTR2-GFP10 construct from our previous screens. This is because none of the mutations overlap with the priming region, so the base pairs should be identical and allow for insert amplification of the receptor with the mutation in place already.

As such, we used the same procedure as described above to PCR amplify the fragments, with some minor changes. For the inserts, we used Q5 Hot Start High-Fidelity DNA Polymerase and performed the PCR reactions in 50 µL total volume with 10 ng template DNA, while for the vector we performed the PCR reactions in 100 µL total volume with 20 ng template DNA. The PCR thermocycle was as follows: initial denaturation at 98 °C for 30 s, followed by 30 cycles of denaturation (98 °C, 10s), annealing (varied from 55–70 °C, 30 s), and elongation (72 °C, 3.5 min), and ending with a final elongation (72 °C, 2 min). The recommended annealing temperature calculated on the NEBuilder Assembly Tool was used for each primer pair. Following PCR, 1 unit of DpnI was added and the mixture was incubated at 37 °C for 30 min to digest any remaining template DNA. This was cleaned up, and any enzymes were removed using a DNA Clean and Concentrator. The concentrations of all PCR-amplified fragments were determined using a NanoDrop. The assembly reaction was performed as before, in 20 µL total volume, with 2 µL of the assembled product used to transform NEB 5-alpha Competent *E. coli* cells. Cells were spread on LB-Amp plates, and colonies were picked and confirmed by sequencing after preparing the DNA with a QIAprep Spin Miniprep Kit. As universal primers used in our pcDNA3.1(+) constructs (T7 forward and BGH reverse) do not prime to the doxycycline-inducible constructs, we generated custom primers using MacVector (version 18) and ordered and purchased the oligonucleotides from IDT at the standard desalting grade.

On the other hand, it is possible to generate these variants using site-directed mutagenesis with the QuikChange Lightning Site-Directed Mutagenesis Kit and WT SP-FLAG-OLLAS-HT7-NLuc-CysLTR2-GFP10-1D4 as a template. Again, the same primers designed for variant generation in the CysLTR2-GFP10 construct can be used. The PCR reactions were performed based on the manufacturer's instructions with slight modifications using half-volume reactions (total of 25 μL) using 25 ng of template DNA, as above.

QuikChange was used as a secondary option for generating the doxycycline-inducible variants if we did not get the correctly assembled construct upon sequence verification. Furthermore, informed from our previous experience in which some of our clones showed poor expression due to sporadic errors introduced into the plasmid backbone by our mutagenesis method, we first tested the variants for their expression level before performing the assay. For those that showed poor expression, new clones were generated using the QuikChange Lightning Site-Directed Mutagenesis Kit. Of the constructs ultimately used for the surface expression nanoBRET assay, WT, L129Q, R136C, S236L, and V131M were generated by NEBuilder Assembly and E343K, G55E, L147Q, M114I, R136H, R226W, R239W, T272M, V14I, V75I, and V269I were generated by QuikChange. All constructs were prepared from QIAprep Spin Miniprep Kit and confirmed by Sanger sequencing using the custom primers mentioned above.

2.3 Cell culture and transfections

All experiments were conducted using human embryonic kidney (HEK) 293T cells purchased from ATCC. These were maintained in Dulbecco's Modified Eagle Medium (DMEM) GlutaMAX supplemented with 10% fetal bovine serum (FBS) at 37 °C under 5% CO_2. All cells used in these experiments were between passage number 5 and 20.

In general, we transiently transfected HEK293T cells with our receptor-encoding plasmid DNA. Our strategy combines transfection and cell plating as a single operation. As outlined in **Figure 2-2**, we first form complexes of Lipofectamine 2000 with plasmid DNA encoding a subset of variants and controls (WT, mock, and L129Q), combine them with a defined number of freshly suspended HEK293T cells, and plate the mixtures in the 96- and 384-well microtiter plates for the assays. Each assay in the two generations of screen had a slightly different transfection, and the details for each are outlined below.

2.3.1 Transfection for BRET2 assays

HEK293T cells were transiently co-transfected with β-arrestin2-RLuc3 and CysLTR2-GFP10 directly 'in-plate' in 96-well plates using Lipofectamine 2000 according to manufacturer's instructions with some modifications. The total DNA amount was kept constant at 205 ng per well using empty vector pcDNA3.1(+). Briefly, a master-mix of the β-arrestin2-RLuc3 was made in FluoroBrite DMEM (DMEM without phenol red and suitable for fluorescence experiments) and the CysLTR2-GFP10 DNA were added to these after appropriate distribution. In a separate mixture, the total Lipofectamine 2000 was mixed in FluoroBrite DMEM and incubated for 5 min. The appropriate amount of Lipofectamine 2000/FluoroBrite DMEM mixture was mixed with the DNA/FluoroBrite DMEM and incubated for 20 min. Cells were then trypsinized,

Figure 2-2 Transient transfection strategy
In general, this workflow first forms complexes of Lipofectamine 2000 with plasmid DNA encoding a subset of variants and controls, combine them with a defined number of freshly suspended human embryonic kidney 293T (HEK293T) cells, and plate the mixtures in microtiter plates for the assays. This combines the transfection and plating procedures into one "in-plate" transfection. Between the first and second-generation transfections, we updated the protocol such that we can use the same transfection mixture to plate both the 96-well plates (BRET2) and low volume 384-well plates (IP1). In the first-generation screen, we transfected 11 ng of receptor-encoding DNA per 7,000 cells (1.57 pg receptor/cell) per well for the IP1 assay. Separately, we transfected 80 ng of receptor-encoding DNA per 40,000 cells (2 pg receptor/cell) per well for the BRET2 assays. For the combined transfection protocol, we took the average of these two values and transfected 1.785 pg receptor/cell and 0.112 pg β-arrestin2-RLuc3/cell. As we measure GFP10 fluorescence in the BRET2 assays, the first-generation BRET2 and combined transfections were conducted in DMEM FluoroBrite which does not contain phenol red. The first-generation IP1 transfection was conducted in our regular culturing media, DMEM GlutaMax, which contains phenol red. In the first generation, each BRET2 transfection included β-arrestin2 only (mock), CysLTR2-GFP10 WT, L129Q, and seven unique mutants. On the other hand, each IP1 transfection included pcDNA 3.1(+) (mock), CysLTR2-GFP10 WT, L129Q, and 11 unique mutants. For the combined protocol, each transfection included β-arrestin2 only (mock), CysLTR2-GFP10 WT, L129Q and 21 unique mutants. This fills three 96-well plates (7 x 3) and two 384-well plates (11 x 2, 1 row extra). This was repeated with five different sets of variant groups, with three replicates of each plate. In the combined transfection, the mock control is consistent between the assays and is β-arrestin2-RLuc3 only. Lastly, for the surface expression assay, we used the doxycycline-inducible SP-FLAG-OLLAS-NLuc-HT7-CysLTR2-GFP10-1D4, transiently transfected into HEK293T cells. The major difference is that 24 hours after plating the transfection mixture, 3300 ng/mL (final) doxycycline is added to each well to induce expression of this receptor. The surface expression assays were conducted 24 hours after induction, or 48 hours after transfection.

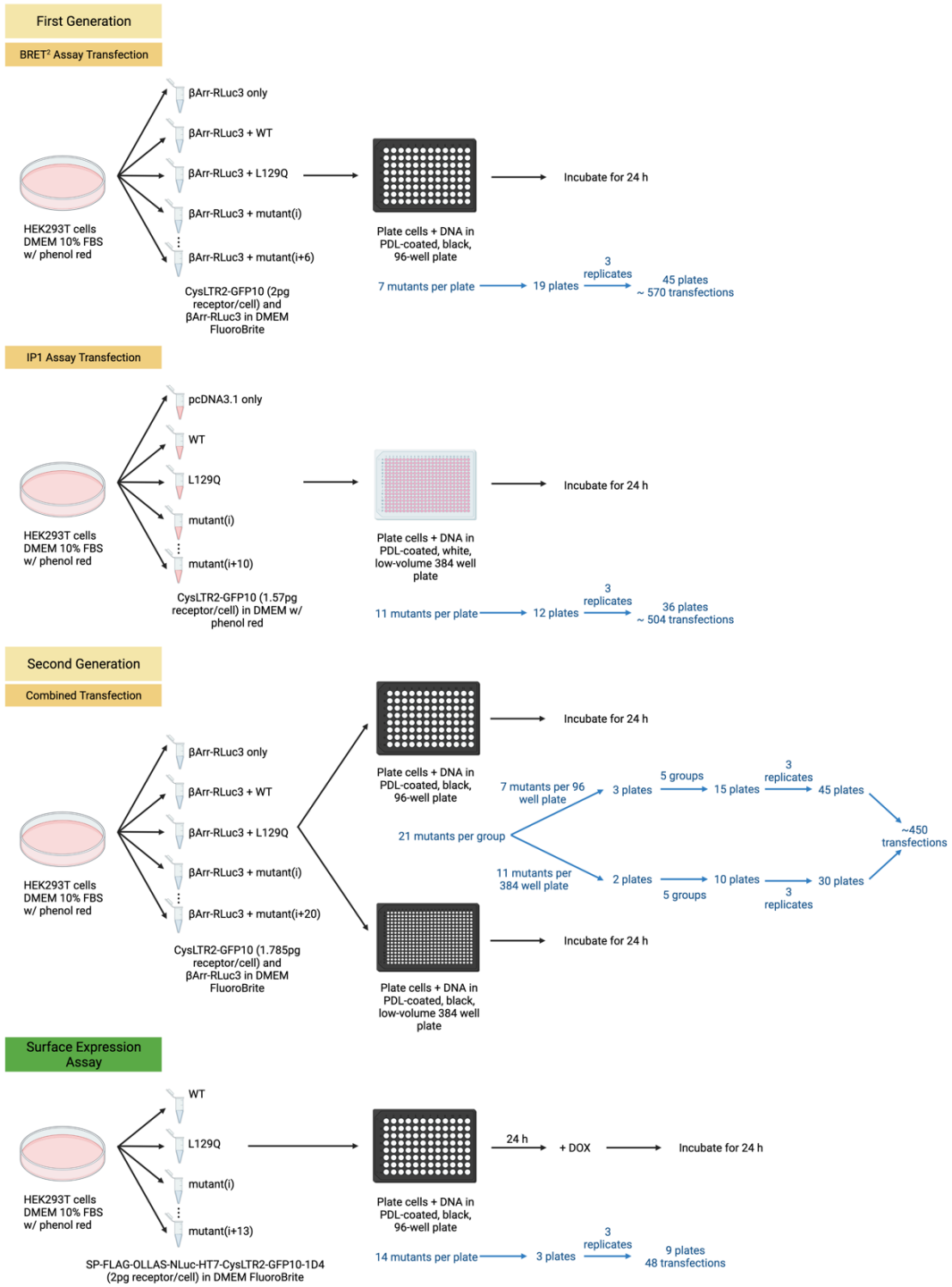
First Generation
BRET² Assay Transfection
βArr-RLuc3 only
βArr-RLuc3 + WT
βArr-RLuc3 + L129Q
βArr-RLuc3 + mutant(i)
βArr-RLuc3 + mutant(i+6)
HEK293T cells
DMEM 10% FBS
w/ phenol red
CysLTR2-GFP10 (2pg receptor/cell) and βArr-RLuc3 in DMEM FluoroBrite
Plate cells + DNA in PDL-coated, black, 96-well plate
Incubate for 24 h
7 mutants per plate
19 plates
3 replicates
45 plates
~ 570 transfections
IP1 Assay Transfection
pcDNA3.1 only
WT
L129Q
mutant(i)
mutant(i+10)
HEK293T cells
DMEM 10% FBS
w/ phenol red
CysLTR2-GFP10 (1.57pg receptor/cell) in DMEM w/ phenol red
Plate cells + DNA in PDL-coated, white, low-volume 384 well plate
Incubate for 24 h
11 mutants per plate
12 plates
3 replicates
36 plates
~ 504 transfections
Second Generation
Combined Transfection
βArr-RLuc3 only
βArr-RLuc3 + WT
βArr-RLuc3 + L129Q
βArr-RLuc3 + mutant(i)
βArr-RLuc3 + mutant(i+20)
HEK293T cells
DMEM 10% FBS
w/ phenol red
CysLTR2-GFP10 (1.785pg receptor/cell) and βArr-RLuc3 in DMEM FluoroBrite
Plate cells + DNA in PDL-coated, black, 96-well plate
Incubate for 24 h
7 mutants per 96 well plate
3 plates
5 groups
15 plates
3 replicates
45 plates
21 mutants per group
11 mutants per 384 well plate
2 plates
5 groups
10 plates
3 replicates
30 plates
~450 transfections
Plate cells + DNA in PDL-coated, black, low-volume 384 well plate
Incubate for 24 h
Surface Expression Assay
WT
L129Q
mutant(i)
mutant(i+13)
HEK293T cells
DMEM 10% FBS
w/ phenol red
SP-FLAG-OLLAS-NLuc-HT7-CysLTR2-GFP10-1D4 (2pg receptor/cell) in DMEM FluoroBrite
Plate cells + DNA in PDL-coated, black, 96-well plate
24 h
+ DOX
Incubate for 24 h
14 mutants per plate
3 plates
3 replicates
9 plates
48 transfections

re-suspended in FluoroBrite DMEM, 20% FBS, 30 mM HEPES, 8 mM glutamine and counted. Cells were mixed with the DNA/Lipofectamine 2000/FluoroBrite DMEM mixture and directly plated onto 0.01% poly-D-lysine coated, black, clear-bottom, tissue culture treated 96-well plates at a density of 40,000 cells per well in 100 µL FluoroBrite DMEM 10% FBS, 15 mM HEPES, 4 mM glutamine. All assays were conducted 24 hrs after the transfection.

2.3.2 Transfection for IP1 assays

HEK293T cells were transiently transfected directly 'in-plate' in low-volume 384-well plates using Lipofectamine 2000 as described above with slight modifications to account for the smaller well volume. The total DNA amount was kept constant at 11 ng per well using empty vector pcDNA3.1(+). All transfection reagents mixes were performed in DMEM GlutaMAX, unless specifically noted as being performed in FluoroBrite DMEM. Briefly, the appropriate amount of plasmid DNA was mixed with DMEM (no FBS). In a separate mixture, the total Lipofectamine 2000 (2.5 µL per µg DNA) was mixed in DMEM (no FBS) and incubated for 5 min. The appropriate amount of Lipofectamine 2000/DMEM mixture was mixed with the DNA/DMEM and incubated for 20 min. Cells were then trypsinized, re-suspended in DMEM supplemented with 20% FBS and counted. Cells were mixed with the DNA/Lipofectamine 2000/DMEM mixture, and directly plated onto 0.01% poly-D-lysine coated, white, clear-bottom, tissue culture treated low-volume 384-well plates at a density of 7,000 cells per well in 7 µL. All assays were conducted 24 hrs after the transfection.

2.3.3 Combined transfection for second generation workflow

After completing our initial screen, we streamlined the workflow as the "second generation" pipeline by using a combined transfection for both G protein activation and β-arrestin recruitment assays. As outlined in **Fig. 2-2**, we updated the protocol such that we can use the same transfection mixture to plate assay plates used for the BRET2 assay (96-well plates) and the IP1 assay (low volume 384-well plates). In the first-generation screen, we transfected 11 ng of receptor-encoding DNA per 7,000 cells (1.57 pg receptor/cell) per well for the IP1 assay. On the other hand, we transfected 80 ng of receptor-encoding DNA per 40,000 cells (2 pg receptor/cell) per well for the BRET2 assays. For the combined transfection protocol, we took the average of these two values and transfected 1.785 pg receptor/cell. Taking the original ratio of 5ng β-arrestin2-RLuc3 to 80ng CysLTR2-GFP10, we transfected 0.112 pg β-arrestin2-RLuc3 /cell.

In the first generation, each BRET2 transfection included β-arrestin2 only (mock), CysLTR2-GFP10 WT, L129Q (the three controls), and seven unique mutants. This is because the 96-well plates allow for seven variants plus the three controls (10 of 12 columns occupied, leaving the outside wells empty). This was repeated ~19 times to cover each variant, with three technical replicates of each plate (**Fig. 2-2**). On the other hand, each IP1 transfection included pcDNA 3.1(+) only (mock), CysLTR2-GFP10 WT, L129Q, and 11 unique mutants. The 384-well plates allow for 11 variants plus the three controls (14 of 16 columns occupied, leaving the outside wells empty). Similarly, this was repeated ~12 times to cover each variant, with three technical replicates of each plate (**Fig. 2-2**). For the combined protocol, each transfection

included β-arrestin2 only (mock), CysLTR2-GFP10 WT, L129Q and 21 unique mutants. This nicely fills three 96-well plates (7 x 3) and two 384-well plates (11 x 2, 1 row extra). This was repeated with five different sets of variant groups, with three technical replicates of each plate (**Fig. 2-2**). Furthermore, with the combined transfection, the mock controls are consistent between the assays and is β-arrestin2-RLuc3 only. The β-arrestin2 only control will not cause the accumulation of IP1, so can be effectively used as the control.

As before, HEK293T cells were transiently co-transfected with 0.112 pg β-arrestin2-RLuc3 /cell and 1.785 pg CysLTR2-GFP10 SNPs/cell directly 'in-plate' using Lipofectamine 2000 as described above. Again, a master-mix of the β-arrestin2-RLuc3 was made in FluoroBrite DMEM and the CysLTR2-GFP10 DNA were added to these after appropriate distribution. In a separate mixture, the total Lipofectamine 2000 was mixed in FluoroBrite DMEM and incubated for 5 min. The appropriate amount of Lipofectamine 2000/FluoroBrite DMEM mixture was mixed with the DNA/FluoroBrite DMEM and incubated for 20 min. Cells were then trypsinized, re-suspended in FluoroBrite DMEM, 20% FBS, 30 mM HEPES, 8 mM glutamine and counted. Cells were mixed with the DNA/Lipofectamine 2000/FluoroBrite DMEM mixture, so the final cell concertation is $1x10^6$ cells/mL. Then, 50 µL of this mixture is directly plated onto 0.01% poly-D-lysine coated, black, clear-bottom, tissue culture treated 96-well plates for BRET2 assays, and 7 µL is directly plated on 0.01% poly-D-lysine coated, black, clear-bottom, tissue culture treated low volume 384-well plates for IP1 assays. Each 96-well contains 89.25 ng CysLTR2-GFP10 (1.785 pg/cell) and 5.58 ng bArr2-Rluc3 (0.112 pg/cell) DNA in 50,000 cells in 50 µL FluoroBrite DMEM 10% FBS, 15 mM HEPES, and 4 mM glutamine. Similarly, each low-volume 384-well contains 12.5 ng receptor-GFP10 (1.785 pg/cell) and 0.78 ng bArr2-Rluc3 (0.112 pg/cell) DNA in 7,000 cells in 7 µL media. Assay plates were returned to the incubator and the cells were left to express for 24 hrs at 37 °C under 5% CO_2.

Then, 24 hrs after the transfection, the respective preparations were performed on each assay plates to conduct the BRET2 assays and IP1 assays, exactly as described above, but now performing the assays on cells plated from the same transfection mixture to allow for a more direct comparison.

2.3.4 Transfection of doxycycline-inducible construct for surface expression assays

The doxycycline-inducible SP-FLAG-OLLAS-NLuc-HT7-CysLTR2-GFP10-1D4 can be transiently transfected into HEK293T cells as well, so a very similar protocol as above was followed, with some modifications. HEK293T cells were transiently transfected with 2 pg/cell of the receptor-encoding DNA directly 'in-plate' using Lipofectamine 2000. The appropriate amount of Lipofectamine 2000/FluoroBrite DMEM mixture was mixed with the DNA/FluoroBrite DMEM and incubated for 20 min. Cells were trypsinized, re-suspended in FluoroBrite DMEM, 20% FBS, 30 mM HEPES, 8 mM glutamine and counted. Cells were mixed with the DNA/Lipofectamine 2000/FluoroBrite DMEM mixture, so the final cell concertation is $1x10^6$ cells/mL. Then, 50 µL of this transfection mixture was plated in 96-well plates (50,000 cells) and returned to the incubator for 24 hrs at 37 °C under 5% CO_2. After 24 hours, 10 µL of 3300 ng/mL (final) doxycycline is added to each well to induce expression of this receptor. The surface expression assays were conducted 24 hours after induction, or 48 hours after transfection.

2.4 BRET2 assays

We designed a BRET2 experiment to quantify the basal and agonist-dependent recruitment of β-arrestins to CysLTR2 variants. The BRET2 experiments are performed on HEK293T cells expressing CysLTR2-GFP10 fusion construct, which acts as the fluorescent acceptor, in combination with β-arrestins fused to an engineered variant of *Renilla* luciferase (RLuc3), β-arrestin2-RLuc3 (Berchiche and Sakmar, 2016). The β-arrestin2-RLuc3 acts as a bioluminescent donor when a coelenterazine substrate is added.

BRET2 assays are performed 24 hrs after transfection (**Fig. 2-3**). Generally, the 96-well assay plate is removed from the incubator, and the media are aspirated carefully from all wells. Then, 30 µL of pre-warmed BRET buffer (DMEM FluoroBrite, 15 mM HEPES, 0.1% (w/v) BSA, 4 mM glutamine) are added to each well. Some wells are stimulated with LTD4, so 10 µL of LTD4 in BRET buffer are added to these, while 10 µL of just BRET buffer are added to all other wells. Cells are incubated for 10 min at room temperature (RT). Following the incubation, BRET2 measurements are taken on the BioTek Synergy NEO2 microplate reader using filter set 109 (center wavelength/band width) of 410/80 nm (donor) and 515/30 nm (acceptor). First, the GFP fluorescence is read using the monochromator (ex: 395 nm, em: 510 nm +/- 20 nm from bottom, auto gain) to quantify total expression levels. Following this, the cell-permeable substrate methoxy e-Coelenterazine (Me-O-e-CTZ/Prolume Purple) is added to each well at a final concentration of 5 µM, and the luminescence at the two wavelengths are read simultaneously to calculate the BRET2 ratio. Each experiment has slight adjustments and these are detailed below.

2.4.1 Saturation-binding assays

HEK293T cells were transiently transfected with 5 ng of β-arrestin2-RLuc3 and 0, 12.8, 32, 80, or 200 ng of CysLTR2-GFP10 WT/-L129Q, CysLTR2-V2 WT/-L129Q or CysLTR2-V2$(A)_6$ WT/-L129Q per well. Then, 24 hrs after transfection, media were aspirated carefully from all wells and 30 µL of pre-warmed BRET buffer was added to each well. Half of the WT wells were stimulated with LTD4, so 10 µL of LTD4 in BRET buffer (final concentration 1 µM) was added to these and 10 µL of BRET buffer was added to all other wells. Cells were incubated for 10 min at RT. Following the incubation, GFP signals were measured, the substrate was added and the BRET2 signals were obtained.

2.4.2 Time-course assays

For the time-course assay, HEK293T cells were transiently transfected with 5 ng of β-arrestin2-RLuc3 and 80 ng of CysLTR2-GFP10 WT, CysLTR2-V2 WT or CysLTR2-V2$(A)_6$ WT per well. Then, 24 hrs after transfection, media were aspirated and 30 µL of pre-warmed BRET buffer was added to each well and the GFP fluorescence was read. Methoxy e-Coelenterazine was added to three columns at 5 µM final concentration followed by addition of 0 nM, 30 nM, and 1000 nM of LTD4 to appropriate wells in the three columns. The plate was quickly placed into the microplate reader so that there was as little lag time between addition of the ligand and BRET2 readings as possible. The three columns take about 60 s to read, and this was repeated 24 times such that a BRET2 reading was recorded every 60 s for about 24 min.

Figure 2-3 Principle of the functional assays
Top: BRET2 assays are performed 24 h after transfection. First, the GFP10 fluorescence is read using the monochromator (ex: 395 nm, em: 510 nm) to quantify total expression levels. Half of the wells are stimulated with LTD4, and cells are incubated for 10 min at room temperature (RT). Following the incubation, the cell-permeable substrate methoxy e-Coelenterazine (Prolume Purple) is added to each well and BRET2 measurements are taken on the BioTek Synergy NEO2 microplate reader. The BRET2 ratio is calculated as acceptor over donor luminescence (515 nm/410 nm). **Middle:** The IP1 assays are performed 24 h after transfection. Cells are first treated with YM-254890 (YM) or vehicle. Following 1 h incubation, LTD4 and LiCl are added for 2 h at 37 °C. Cells are then lysed by addition of d2-labeled IP1 analog and terbium cryptate-labeled anti-IP1 mAb diluted in the lysis and detection buffer. Time-resolved fluorescence signals are read on the BioTek Synergy NEO plate reader (for first-generation cells transfected in DMEM Glutamax and assayed in white microplates) or the BioTek Synergy NEO2-TRF Hybrid multi-mode reader (for second-generation cells transfected in FluoroBrite DMEM and assayed in black microplates). The plate is first subjected to flash lamp excitation at 320 nm (BioTek Synergy NEO) or to laser excitation (BioTek Synergy NEO2-TRF) at 337 nm, and then the fluorescence is measured simultaneously. The HTRF ratio is calculated as acceptor over donor fluorescence (665 nm/620 nm) and is converted into concentration of IP1 (nM) using a standard curve. **Bottom:** The surface expression assays were conducted 24 hours after doxycycline-induction, or 48 hours after transfection. We then label HaloTag (HT7) with HaloTag Ligand AlexaFluor 660 at 0 or 100 nM for 2 h at 16 ℃ to minimize membrane turnover. The AlexaFluor is cell impermeable, so this first step labels all receptors on the cell surface. After the 2 h incubation, we "chase" by adding 100 nM HaloTag Ligand nanoBRET 618 for 2 h at 16 ℃. This dye is cell permeable and should label all receptors left unlabeled inside and outside of the cell. After this incubation, we add Nano-Glo Luciferase Assay Substrate to lyse the cells and release all receptors for luminescence detection. We monitor the luminescence at the three wavelengths on the SpectraMax i3x multi-mode microplate to quantify the fraction of surface receptor (see **Fig. 2-4**).

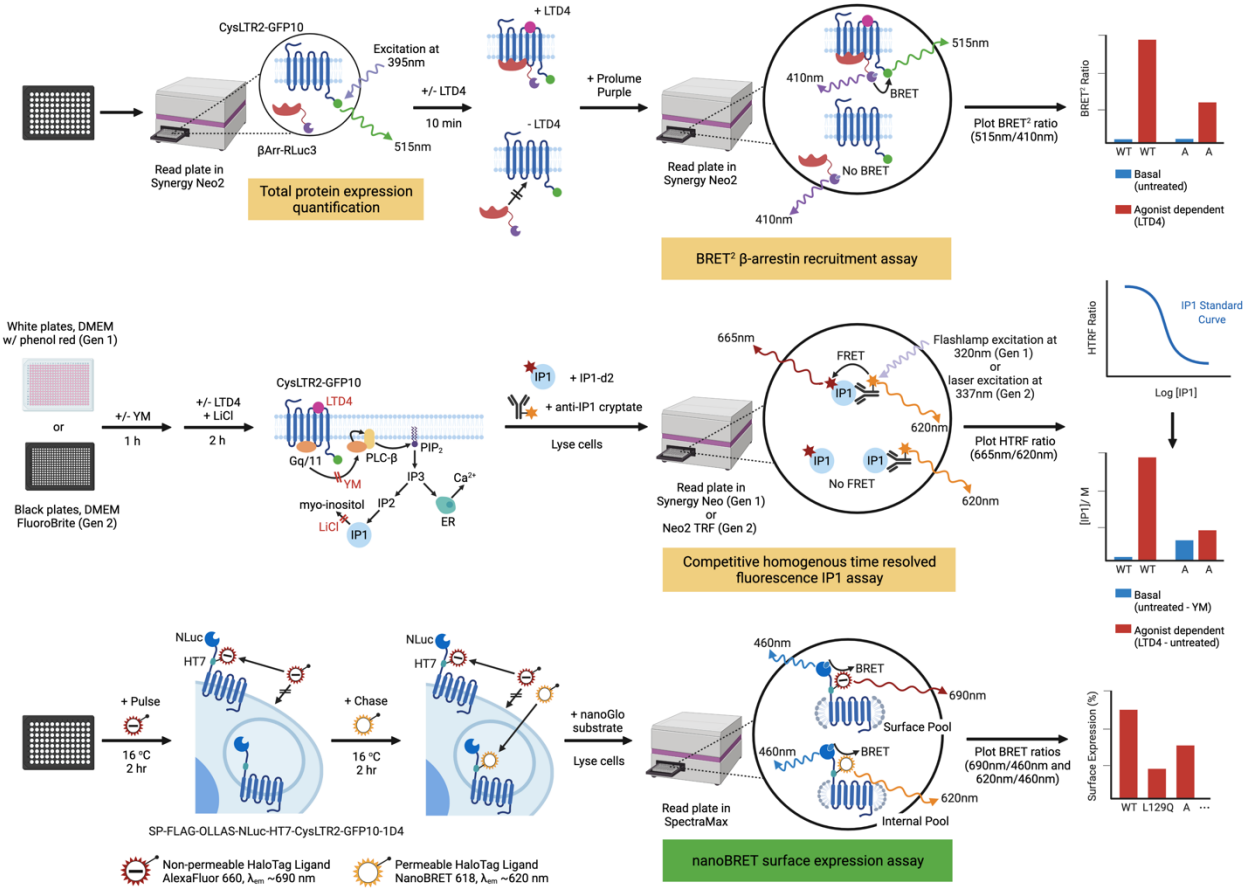
CysLTR2-GFP10
Excitation at 395nm
515nm
βArr-RLuc3
Read plate in Synergy Neo2
Total protein expression quantification
+/- LTD4
10 min
+ LTD4
- LTD4
+ Prolume Purple
Read plate in Synergy Neo2
410nm
BRET
515nm
No BRET
410nm
BRET² β-arrestin recruitment assay
Plot BRET² ratio (515nm/410nm)
BRET² Ratio
WT WT A A
Basal (untreated)
Agonist dependent (LTD4)
White plates, DMEM w/ phenol red (Gen 1)
or
Black plates, DMEM FluoroBrite (Gen 2)
+/- YM
1 h
+/- LTD4
+ LiCl
2 h
CysLTR2-GFP10
LTD4
Gq/11
PLC-β
PIP2
YM
IP3
Ca2+
myo-inositol
IP2
LiCl
IP1
IP1
+ IP1-d2
+ anti-IP1 cryptate
Lyse cells
665nm
FRET
IP1
Flashlamp excitation at 320nm (Gen 1)
or
laser excitation at 337nm (Gen 2)
620nm
IP1
IP1
No FRET
620nm
Read plate in Synergy Neo (Gen 1)
or
Neo2 TRF (Gen 2)
Competitive homogenous time resolved fluorescence IP1 assay
Plot HTRF ratio (665nm/620nm)
HTRF Ratio
IP1 Standard Curve
Log [IP1]
[IP1]/ M
WT WT A A
Basal (untreated - YM)
Agonist dependent (LTD4 - untreated)
NLuc
HT7
+ Pulse
16 °C
2 hr
+ Chase
16 °C
2 hr
+ nanoGlo substrate
Lyse cells
SP-FLAG-OLLAS-NLuc-HT7-CysLTR2-GFP10-1D4
Non-permeable HaloTag Ligand AlexaFluor 660, λem ~690 nm
Permeable HaloTag Ligand NanoBRET 618, λem ~620 nm
460nm
BRET
690nm
Surface Pool
460nm
BRET
620nm
Internal Pool
Read plate in SpectraMax
nanoBRET surface expression assay
Plot BRET ratios (690nm/460nm and 620nm/460nm)
Surface Expression (%)
WT L129Q A ...

2.4.3 Agonist dose-response assays

HEK293T cells were transiently transfected with 5 ng of β-arrestin2-RLuc3 and 80 ng of CysLTR2-GFP10 WT/-L129Q, CysLTR2-V2 WT/-L129Q or CysLTR2-V2$(A)_6$ WT/-L129Q per well. Then, 24 hrs after transfection, media were aspirated and 30 µL of pre-warmed BRET buffer was added to each well. Various concentrations of LTD4 (final concentrations from 1 µM to 10 pM) were added to appropriate wells and incubated for 10 min at RT. Following the incubation, GFP signals were measured, the substrate was added and the BRET2 signals were obtained.

2.4.4 Activity-based profiling of *CYSLTR2* variants

The two generations of workflow had slightly different transfection procedures and amounts of the receptor-encoding DNA, as outlined above, but 24 hrs after transfection, on the day of the BRET2 assay, identical protocols were followed for both (**Fig. 2-3**). As mentioned previously, 24 hrs after transfection, media were aspirated and 30 µL of pre-warmed BRET buffer was added to each well. To half of the wells, 10 µL of LTD4 in BRET buffer was added (final concentration 1 µM) and to the other half, 10 µL of BRET buffer only was added. Cells were incubated for 10 min at RT. Following the incubation, GFP signals were measured, the substrate was added and the BRET2 signals were obtained.

2.5 IP1 assays

The CisBio IP-One HTRF Immunoassay quantifies d-myo-inositol-1-phosphate (IP1). The IP1 assay is a competitive HTRF assay where the d2-labeled IP1 analogue acts as the fluorescence acceptor and the Terbium cryptate-labeled anti-IP1 monoclonal antibody (mAb) acts as the fluorescence donor (**Fig. 2-3**). The Terbium-cryptate is a long-lifetime fluorescence donor that can be excited by ultraviolet (UV) light. Lithium chloride (LiCl) is added during the stimulation period of the assay to block further degradation of IP1 by the enzyme inositolmonophosphatase (IMPase).

The IP1 assays are performed 24 hrs after transfection and outlined in **Fig. 2-3**. The assay plate is taken out of the incubator and placed on an aluminum heating block maintained at 37 °C. Cells are first treated with 3.5 µL/well of YM (final concentration 1 µM) or vehicle diluted in pre-warmed DMEM GlutaMAX for 1 hr at 37 °C. Following 1 hr incubation, 3.5 µL/well of LTD4 (final concentration 100 nM) or vehicle, diluted in pre-warmed stimulation assay buffer provided by the manufacturer (10 mM HEPES, 1 mM $CaCl_2$, 0.5 mM $MgCl_2$, 4.2 mM KCl, 146 mM NaCl, 5.5 mM glucose, 50 mM LiCl, pH 7.4) supplemented with 0.2% (w/v) BSA and 50 mM LiCl, are added for 2 hrs at 37 °C. Following incubation, cells are lysed by addition of 3 µL/well of d2-labeled IP1 analog and 3 µL/well of terbium cryptate-labeled anti-IP1 mAb diluted in the lysis and detection buffer. The plates are incubated overnight, in the dark, at RT. Time-resolved fluorescence signals are read on the BioTek Synergy NEO plate reader (for cells transfected in DMEM Glutamax and assayed in white microplates) or the BioTek Synergy NEO2-TRF Hybrid multi-mode reader (for cells transfected in FluoroBrite DMEM and assayed in black microplates). The plate is first subjected to flash lamp excitation at 320 nm (BioTek

Synergy NEO) or to laser excitation (BioTek Synergy NEO2-TRF) at 337 nm, and then the fluorescence is measured at wavelengths centered at 620 nm and 665 nm simultaneously.

2.5.1 Agonist dose-response of CysLTR2 DNA titration assays

HEK293T cells were transiently transfected with a serial dilution of 11, 3.6, 1.2, 0.4, and 0.1 ng of CysLTR2-GFP10 wt/-L129Q, CysLTR2-V2 wt/-L129Q or CysLTR2-V2$(A)_6$ wt/-L129Q per well as described above. Then, 24 hrs after transfection, the assay plate was placed on an aluminum heating block maintained at 37 °C, and cells were treated with 7 µL/well of various concentrations of LTD4 (final concentrations from 1 µM to 10 pM) diluted in pre-warmed stimulation assay buffer supplemented with 0.2% (w/v) BSA and 50 mM LiCl to prevent IP1 degradation. The plate was incubated at 37 °C for 2 hrs. Following incubation, cells were lysed by addition of 3 µL/well of d2-labeled IP1 analogue and 3 µL/well of terbium cryptate-labeled anti-IP1 mAb diluted in the lysis and detection buffer. Time-resolved fluorescence signals were measured as mentioned above.

2.5.2 Time-course assays

We obtained a time-course of basal and LTD4-dependent IP1 accumulation in HEK293T cells transiently transfected with plasmids for CysLTR2 WT, CysLTR2-L129Q, and mock-transfected control. HEK293T cells were transiently transfected with 11 ng of CysLTR2-1D4 (wt and L129Q) per well. Then, 24 hrs after transfection, the assay plate was placed on an aluminum heating block as described above, and the cells were treated every 20 min over 180 min with 3.5 µL/well of LiCl diluted in pre-warmed stimulation assay buffer at a final concentration of 50 mM. Cells were incubated at 37 °C. At 1 hr after the start point, 3.5 µL/well of LTD4 diluted in pre-warmed DMEM GlutaMAX at a final concentration of 100 nM (agonist stimulated) or 3.5 µL/well of DMEM GlutaMAX alone (basal) were added in appropriate wells and incubated for 2 hrs. The reaction was then stopped by successively adding 3 µL/well of the IP1 analogue and the anti-IP1 mAb in reverse chronological order. Time-resolved fluorescence signals were measured as mentioned above.

2.5.3 Activity-based profiling of *CYSLTR2* variants

The two generations of IP1 assay workflows had slightly different transfection procedures and amounts of the receptor-encoding DNA, as outlined above. However, 24 hrs after transfection, the assay procedures were, for the most part, identical with a few key differences (**Fig. 2-3**). Again, cells were first treated with 3.5 µL/well of YM (final concentration 1 µM) or vehicle diluted in pre-warmed DMEM GlutaMAX for 1 hr at 37 °C. Following 1 hr incubation, 3.5 µL/well of LTD4 (final concentration 100 nM) or vehicle, diluted in pre-warmed stimulation assay buffer supplemented with 0.2% (w/v) BSA and 50 mM LiCl, were added for 2 hrs at 37 °C. Then cells were lysed by addition of 3 µL/well of d2-labeled IP1 analog and 3 µL/well of terbium cryptate-labeled anti-IP1 mAb diluted in the lysis and detection buffer. The minor differences lie in which plate reader was used. For the first-generation screen, where white microplates were used and cells were transfected and seeded in DMEM Glutamax, time-resolved fluorescence signals were read on the BioTek Synergy NEO plate reader. This plate reader excites the donor with a flash lamp excitation at 320 nm. On the other hand, for the second-generation screen, cells were transfected and seeded in FluoroBrite DMEM in white assay plates.

These plates were read on the BioTek Synergy NEO2-TRF Hybrid multi-mode reader where excitation occurs by laser excitation at 337 nm.

2.6 Surface expression assays

Our aim was to develop a cell surface expression assay that would allow us to distinguish between the pool of receptors at the surface and those inside the cell. To achieve this, we decided to use a pulse-chase assay, in which we first label all cell surface receptors with a cell impermeable HaloTag ligand and follow, or chase, with a cell permeable HaloTag ligand, which would label all remaining receptors. We identified two HaloTag ligands that are efficiently excited by nLuc to serve as acceptor fluorophores, that also have a large enough spectral distance between them. Importantly, these two ligands had distinctive cell permeability properties. Our pulse is the cell impermeable HaloTag Ligand AlexaFluor 660 (λ_{max} ~ 690 nm). Our chase is the cell permeable HaloTag Ligand nanoBRET 618 (λ_{max} ~ 620 nm). To detect the two distinctly labeled pools of receptor, the cells are lysed and the nLuc substrate is added. The nLuc will then emit luminescence at ~ 460 nm, and the transfer of energy will allow us to monitor fluorescence at the two red wavelength to quantify the fraction of surface receptor (**Fig. 2-3**).

After the transfection and induction steps outlined in section **2.3.4**, we first aspirated the media carefully from all wells. Then, 30 µL of pre-warmed BRET buffer are added to each well. We then label the HEK293T cells expressing SP-FLAG-OLLAS-nLuc-HT7-CysLTR2-GFP10-1D4 with HaloTag Ligand AlexaFluor 660 at 0 or 100 nM (final) in 10 µL BRET buffer for 2 hrs at 16 ℃. The AlexaFluor is cell impermeable, so this first step labels all receptors on the cell surface. We decided to label at this lower temperature to minimize membrane turnover. After the 2-hr incubation, we "chase" by adding 100 nM (final) of HaloTag Ligand nanoBRET 618 in 10 µL BRET buffer. We incubate again for 2 hrs at 16 ℃, to label all receptors left unlabeled inside and outside of the cell. After this incubation, we mix the Nano-Glo Luciferase Assay Substrate with the Nano-Glo Luciferase Assay Buffer, which is a lysis buffer that solubilizes the cells and releases all receptors for luminescence detection. We let the assay plate come to RT for about 10 mins, and then add 50 µL of the Nano-Glo Luciferase Assay Substrate in Assay Buffer, to each well. We monitor the luminescence at the three wavelengths (nLuc λ_{em} ~460 nm, HaloTag Ligand nanoBRET 618 λ_{em} ~620 nm, HaloTag Ligand AlexaFluor 660 λ_{em} ~690 nm) on the SpectraMax i3x multi-mode microplate to quantify the fraction of surface receptor.

2.7 Plotting binding interfaces

Known structures were compared to those of CysLTR2 and residues involved in ligand binding, arrestin binding, G protein binding, and activating sites were marked on the snake plot shown in **Fig. 3-11**. An interaction is defined as residues that are within <3.9 Å of each other. All corresponding sites in the helices were assigned to the structure of CysLTR2 based on generic numbering positions as described in the GPCRdb. For sites in segments that did not have generic residue number positions, we used class-specific multiple sequence alignments to designate the appropriate corresponding residues in CysLTR2 (**Table 2-5**).

2.7.1 Ligand-interacting sites

Ligand-interacting sites were obtained from the recent structure of CysLTR2 in complex with ONO-2570366, an antagonist for CysLTR1 and CysLTR2 (Gusach et al., 2019b). We defined ligand-interacting sites as those residues which were within 3.9 Å of the antagonist atoms.

2.7.2 Arrestin binding interface

Arrestin binding sites were obtained from neurotensin receptor type 1 in complex with β-arrestin1 (Huang et al., 2020), muscarinic acetylcholine receptor M_2 in complex with β-arrestin1 (Staus et al., 2020), β-1 adrenergic receptor in complex with β-arrestin1 (Lee et al., 2020), and rhodopsin in complex with visual arrestin (Zhou *et al.*, 2017a). We defined arrestin binding sites as those residues in the receptors which were within 3.9 Å of the arrestin atoms.

2.7.3 G protein binding interface

G protein binding sites were obtained from structures of receptors in complex with Gq proteins, as CysLTR2 canonically binds to Gq. These receptors were the 5-HT_{2A} receptor (Kim et al., 2020), histamine H1 receptor (Xia et al., 2021), muscarinic acetylcholine receptor M1 (Maeda et al., 2019), and cholecystokinin A receptor (Mobbs et al., 2021). We defined G protein binding sites as those residues in the receptors which were within 3.9 Å of the Gq protein atoms.

2.7.4 GRK binding interface

G protein kinase binding sites were obtained from the recent structure of rhodopsin kinase (GRK1) in complex with rhodopsin (Chen et al., 2021). We defined GRK binding sites as those residues in the receptors which were within 3.9 Å of the GRK atoms.

2.7.5 Activating sites

Activating sites were taken from work by Zhou et al., which analyzed 234 structures of 45 class A GPCRs and determined the existence of a common activation pathway (i.e., a common set of residue contact changes) across class A GPCRs (Zhou et al., 2019). To capture conformational changes between active and inactive structure, they defined a residue-residue contact score (RRCS) which is an atomic distance-based calculation that quantifies the strength of contact between residue pairs to analyze these structures. The pathway is comprised of 34 residue pairs (formed by 35 residues), which connect several well-known motifs like the Na^+ pocket, NPXXY and DRY, from the extracellular side to the intracellular side. These conformational changes occur in four layers. The first layer is the signal initiation layer, the second is the signal propagation layer, the third is the microswitches rewiring layer and the fourth is the G-protein coupling layer.

Table 2-5 Table showing CysLTR2 residues involved in G protein, GRK, arrestin, and ligand binding as well as activation as plotted on snake plot in Fig. 3-11B

All interactions are defined as residues that are <3.9 Å of the interacting partner in complex with CysLTR2. Ligand-interacting sites were obtained from the recent structure of CysLTR2 in complex with ONO-2570366 (Gusach *et al.*, 2019b). Arrestin binding sites, G protein binding sites, G protein kinase (GRK) binding sites, were all obtained from structures of GPCRs in complex with arrestins, Gq/11 proteins, or GRKs. All corresponding sites in the helices were assigned to the structure of CysLTR2 based on generic numbering positions as described in the GPCRdb. For sites in segments that did not have generic residue number positions, we used class-specific multiple sequence alignments to designate the appropriate corresponding residues in CysLTR2. Lastly, activation sites were taken from work by Zhou et al., which determined the existence of a common activation pathway across class A GPCRs, connecting well-known motifs like the Na^+ pocket, NPXXY and DRY, from the extracellular side to the intracellular side (Zhou *et al.*, 2019). There is the signal initiation layer (layer 1), signal propagation layer (layer 2), microswitches rewiring layer (layer 3), and G-protein coupling layer (layer 4).

Generic Position (CysLTR2)	Residue Number (CysLTR2)	Residue (CysLTR2)	Type of interface	Original Structure	Residue w/ generic position
1x31	37	K	Ligand	CLTR2/ONO-2570366	K37(1x31)
1x49	55	G	Layer 2	Class A GPCRs	1x49
1x53	59	S	Layer 3	Class A GPCRs	1x53
1x58	64	L	GRK	Rho/GRK	V63(1x58)
1x60	66	P	GRK	Rho/GRK	H65(1x60)
12x48	67	Y	G protein	Beta-1/Gs, Rho/Gt, HRH1/Gq, ACM1/Gq, CCK1/Gq	Q70(12x48), K66(12x48), R56(12x48), T54(12x48), K70(12x48)
12x48	67	Y	GRK	Rho/GRK	K66(12x48)
12x49, 2x34	68	K	Arr	Beta-1/bArr1, NTS1/bArr1	R71(12x49), S96(2x34)
12x49	68	K	G protein	Beta-1/Gs, HRH1/Gq	R71(12x49), K57(12x49)
12x49	68	K	GRK	Rho/GRK	K67(12x49)
2x35	69	K	Arr	NTS1/bArr1	L97(2x35)
12x51, 2x36	70	S	Arr	Beta-1/bArr1, NTS1/bArr1	Q73(12x51), Q98(2x36)
12x51, 2x36	70	S	G protein	HRH1/Gq, NTS1/Gi	H59(12x51), Q98(2x36)
12x51	70	S	GRK	Rho/GRK	R69(12x51)
2x37	71	T	Arr	Beta-1/bArr1, Rho/Arr	T74(2x37), T70(2x37)
2x37	71	T	G protein	5HT2A/Gq, CCK1/Gq	N107(2x37), T74(2x37)
2x38	72	S	Arr	Beta-1/bArr1	L75(2x38)

2x38	72	S	G protein	CCK1/Gq	V75(2x38)
2x39	73	V	Arr	M2/bArr1, Beta-/bArr1, Rho/Arr	N58(2x39), T76(2x39), L72(2x39)
2x39	73	V	G protein	NTS1/Gi, Rho/Gt, ACM1/Gq, CCK1/Gq	V101(2x39), L72(2x39), N60(2x39), T76(2x39)
2x40	74	N	Arr	Rho/Arr	N73(2x40)
2x40	74	N	G protein	CCK1/Gq	N77(2x40)
2x43	77	M	Arr	Beta-1/bArr1	I80(2x43)
2x43	77	M	Layer 3	Class A GPCRs	2x43
2x46	80	L	Layer 2	Class A GPCRs	2x46
2x50	84	D	Layer 1	Class A GPCRs	2x50
3x29	115	S	Ligand	CLTR2/ONO-2570366	S115(3x29)
3x33	119	Y	Ligand	CLTR2/ONO-2570366	Y119(3x33)
3x37	123	Y	Ligand	CLTR2/ONO-2570366	Y123(3x37)
3x39	125	S	Layer 1	Class A GPCRs	3x39
3x40	126	I	Layer 1	Class A GPCRs	3x40
3x41	127	Y	Ligand	CLTR2/ONO-2570366	Y127(3x41)
3x43	129	L	Layer 2	Class A GPCRs	3x43
3x46	132	L	Layer 3	Class A GPCRs	3x46
3x49	135	V	G protein	5HT2A/Gq, HRH1/Gq	D172(3x49), D124(3x49)
3x49	135	V	Layer 4	Class A GPCRs	3x49
3x50	136	R	Arr	Beta-1/bArr1	R139(3x50)
3x50	136	R	G protein	Beta-1/Gs, Rho/Gt, ACM1/Gq, CCK1/Gq, NTS1/Gi, M2/Go	R139(3x50), R135(3x50), R123(3x50), R139(3x50), R166(3x50), R121(3x50)
3x50	136	R	GRK	Rho/GRK	R135(3x50)
3x50	136	R	Layer 4	Class A GPCRs	3x50
3x51	137	F	Layer 4	Class A GPCRs	3x51
3x53	139	A	Arr	Beta-1/bArr1	A142(3x53)
3x53	139	A	G protein	NTS1/Gi, M2/Go, Beta-1/Gs, Rho/Gt, 5HT2A/Gq, HRH1/Gq, ACM1/Gq, CCK1/Gq	A169(3x53), R121(3x53), A142(3x53), V138(3x53), A176(3x53), S128(3x53), S126(3x53), A142(3x53)
3x53	139	A	GRK	Rho/GRK	V138(3x53)

3x53	139	A	Layer 4	Class A GPCRs	3x53
3x54	140	M	Arr	NTS1/bArr1, Rho/Arr	I170(3x54), V139(3x54)
3x54	140	M	G protein	NTS1/Gi, M2/Go, Beta-1/Gs, Rho/Gt, 5HT2A/Gq, HRH1/Gq, ACM1/Gq, CCK1/Gq	I170(3x54), V125(3x54), I143(3x54), V139(3x54), I177(3x54), V129(3x54), V127(3x54), I143(3x54)
3x54	140	M	GRK	Rho/GRK	V139(3x54)
3x54	140	M	Layer 4	Class A GPCRs	3x54
3x55	141	V	Arr	Rho/Arr	C140(3x55)
3x56	142	H	Arr	Rho/Arr	K141(3x56)
3x56	142	H	GRK	Rho/GRK	K141(3x56)
34x50	143	P	Arr	NTS1/bArr1, Rho/Arr, Beta-1/bArr1	P173(34x50), P142(34x50), P146(34x50)
34x50	143	P	G protein	5HT2A/Gq, HRH1/Gq, ACM1/Gq, CCK1/Gq, NTS1/Gi, M2/Go, Beta-1/Gs	P180(34x50), P132(34x50), P130(34x50), P146(34x50), P173(34x50), P128(34x50), P146(34x50)
34x51	144	F	Arr	M2/bArr1, Beta-1/bArr1, Rho/Arr	L129(34x51), F174(34x51), M143(34x51)
34x51	144	F	G protein	5HT2A/Gq, HRH1/Gq, ACM1/Gq, CCK1/Gq, NTS1/Gi, Beta-1/Gs	I181(34x51), L133(34x51), L131(34x51), L147(34x51), F174(34x51), F147(34x51)
34x51	144	F	GRK	Rho/GRK	M143(34x51)
34x52	145	R	Arr	M2/bArr1, Beta-1/bArr1	T130(34x52), R148(34x52)
34x52	145	R	GRK	Rho/GRK	S144(34x52)
34x53	146	L	Arr	Rho/Arr	N145(34x53)
34x53	146	L	G protein	HRH1/Gq, Beta-1/Gs, Rho/Gt	Y135(34x53), Y149(34x53), N145(34x53)
34x53	146	L	GRK	Rho/GRK	N145(34x53)
34x54	147	L	Arr	NTS1/bArr1, Beta1-bArr1, Rho/Arr	K177(34x54), Q150(34x54), F146(34x54)
34x54	147	L	G protein	5HT2A/Gq, HRH1/Gq, ACM1/Gq, CCK1/Gq, NTS1/Gi,	S184(34x54), L136(34x54), R134(34x54), R150(34x54), I143(34x54),

				Beta-1/Gs, Rho/Gt	K177(34x54), F146(34x54)
34x54	147	L	GRK	Rho/GRK	F146(34x54)
34x55	148	H	Arr	Beta-1/bArr1	S151(34x55)
34x55	148	H	G protein	5HT2A/Gq, HRH1/Gq, ACM1/Gq, CCK1/Gq, NTS1/Gi, Beta-1/Gs, Rho/Gt	R185(34x55), K137(34x55), A135(34x55), P146(34x55), T178(34x55), S151(34x55), R147(34x55)
34x55	148	H	GRK	Rho/GRK	R147(34x55)
34x56	149	V	Arr	Rho/Arr	F148(34x56)
34x56	149	V	GRK	Rho/GRK	F148(34x56)
34x57	150	T	Arr	Beta-1/bArr1	M153(34x57)
34x57	150	T	G protein	5HT2A/Gq, HRH1/Gq, ACM1/Gq, CCK1/Gq, NTS1/Gi,	N187(34x57), R139(34x57), R137(34x57), Q153(34x57), M180(34x57)
4x38	151	S	Arr	Beta-1/bArr1, Rho/Arr	T154(4x38), G149(4x38)
4x38	151	S	G protein	CCK1/Gq, NTS1/Gi, Beta-1/Gs	T154(4x38), S181(4x38), T154(4x38)
4x38	151	S	GRK	Rho/GRK	G149(4x38)
4x39	152	I	Arr	Beta-1/bArr1	R155(4x39)
4x39	152	I	GRK	Rho/GRK	E150(4x39)
4x40	153	R	GRK	Rho/GRK	N151(4x40)
4x41	154	S	GRK	Rho/GRK	H152(4x41)
4x56	169	S	Ligand	CLTR2/ONO-2570366	S169(4x56)
4x57	170	S	Ligand	CLTR2/ONO-2570366	S170(4x57)
45x51	188	L	Ligand	CLTR2/ONO-2570366	L188(45x51)
45x52	189	E	Ligand	CLTR2/ONO-2570366	E189(45x52)
ECL2	190	L	Ligand	CLTR2/ONO-2570366	L190
ECL2	194	K	Ligand	CLTR2/ONO-2570366	K194
5x36	198	L	Ligand	CLTR2/ONO-2570366	L198(5x36)
5x39	201	M	Ligand	CLTR2/ONO-2570366	M201(5x39)
5x40	202	N	Ligand	CLTR2/ONO-2570366	N202(5x40)
5x42	204	I	Ligand	CLTR2/ONO-2570366	I204(5x42)

5x43	205	A	Ligand	CLTR2/ONO-2570366	A205(5x43)
5x461	209	G	Ligand	CLTR2/ONO-2570366	G209(5x461)
5x51	214	F	Layer 1	Class A GPCRs	5x51
5x55	218	S	Layer 2	Class A GPCRs	5x55
5x57	220	C	Layer 3	Class A GPCRs	5x57
5x58	221	Y	Layer 3	Class A GPCRs	5x58
5x61	224	I	G protein	ACM1/Gq, Beta-1/Gs	I211(5x61), V230(5x61)
5x61	224	I	Layer 4	Class A GPCRs	5x61
5x62	225	I	Layer 4	Class A GPCRs	5x62
5x64	227	V	Arr	Rho/Arr	T229(5x64)
5x65	228	L	Arr	Beta-1/bArr1	A234(5x65)
5x65	228	L	G protein	HRH1/Gq, ACM1/Gq, M2/Go, Beta-1/Gs	V217(5x65), T215(5x65), S213(5x65), A234(5x65)
5x65	228	L	GRK	Rho/GRK	V230(5x65)
5x67	230	K	G protein	HRH1/Gq, M2/Go	Q219(5x67), S215(5x67)
5x68	231	V	Arr	Beta-1/bArr1, Rho/Arr	Q237(5x68), A233(5x68)
5x68	231	V	G protein	ACM1/Gq, NTS1/Gi, Beta-1/Gs	R218(5x68), M266(5x68), Q237(5x68)
5x68	231	V	GRK	Rho/GRK	A233(5x68)
5x71	234	P	Arr	Beta-1/bArr1, Rho/Arr	K240(5x71), Q236(5x71)
5x71	234	P	GRK	Rho/GRK	Q236(5x71)
5x72	235	E	Arr	Beta-1/bArr1, Rho/Arr	I241(5x72), Q237(5x72)
5x72	235	E	G protein	ACM1/Gq, Beta-1/Gs, Rho/Gt	L222(5x72), I241(5x72), Q237(5x72)
5x72	235	E	GRK	Rho/GRK	Q237(5x72)
6x25	236	S	Arr	Rho/Arr	T242(6x25)
6x25	236	S	G protein	HRH1/Gq, Rho/Gt	L405(6x25), T242(6x25)
6x26	237	G	GRK	Rho/GRK	T242(6x25)
6x27	238	L	GRK	Rho/GRK	T243(6x26)
6x28	239	R	Arr	Rho/Arr	K245(6x28)
6x29	240	V	Arr	NTS1/bArr1	A297(6x29)
6x29	240	V	G protein	5HT2A/Gq, HRH1/Gq, NTS1/Gi, M2/Go, Beta-1/Gs, Rho/Gt	N317(6x29), R409(6x29), A297(6x29), R381(6x29), R284(6x29), A246(6x29)

6x30	241	S	Arr	NTS1/bArr1	L298(6x30)
6x30	241	S	GRK	Rho/GRK	A246(6x29)
6x32	243	R	Arr	Rho/Arr	E249(6x32)
6x32	243	R	G protein	HRH1/Gq, ACM1/Gq, M2/Go, Beta-1/Gs	K412(6x32), K362(6x32), K384(6x32), K287(6x32)
6x33	244	K	Arr	NTS1/bArr1, Beta1-bArr1	G301(6x33), A288(6x33)
6x33	244	K	G protein	ACM1/Gq, CCK1/Gq	A363(6x33), V311(6x33)
6x33	244	K	GRK	Rho/GRK	E249(6x32)
6x33	244	K	Layer 4	Class A GPCRs	6x33
6x34	245	A	GRK	Rho/GRK	V250(6x33)
6x36	247	T	Arr	Beta-1/bArr1, Rho/Arr	T291(6x36), M253(6x36)
6x36	247	T	G protein	HRH1/Gq, ACM1/Gq, M2/Go, Beta-1/Gs	Q416(6x36), T366(6x36), T388(6x36), T291(6x36)
6x37	248	T	Arr	Beta-1/bArr1	L292(6x37)
6x37	248	T	Layer 3	Class A GPCRs	6x37
6x40	251	I	Arr	Beta-1/bArr1	I295(6x40)
6x40	251	I	Layer 2	Class A GPCRs	6x40
6x41	252	T	Layer 2	Class A GPCRs	6x41
6x44	255	I	Layer 1	Class A GPCRs	6x44
6x48	260	F	Layer 1	Class A GPCRs	6x48
6x55	267	R	Ligand	CLTR2/ONO-2570366	R267(6x55)
6x58	270	H	Ligand	CLTR2/ONO-2570366	H270(6x58)
6x59	271	L	Ligand	CLTR2/ONO-2570366	L271(6x59)
7x31	284	H	Ligand	CLTR2/ONO-2570366	H284(7x31)
7x34	287	L	Ligand	CLTR2/ONO-2570366	L287(7x34)
7x45	297	N	Layer 1	Class A GPCRs	7x45
7x49	301	N	Layer 2	Class A GPCRs	7x49
7x50	302	P	Layer 2	Class A GPCRs	7x50
7x52	304	L	Layer 3	Class A GPCRs	7x52
7x53	305	Y	Arr	Beta-1/bArr1	Y343(7x53)
7x53	305	Y	G protein	5HT2A/Gq	Y380(7x53)
7x53	305	Y	Layer 3	Class A GPCRs	7x53
7x54	306	Y	Layer 3	Class A GPCRs	7x54
7x55	307	F	Layer 3	Class A GPCRs	7x55

7x56	308	A	G protein	5HT2A/Gq, HRH1/Gq, ACM1/Gq, M2/Go	F383(7x56), C471(7x56), C421(7x56), C443(7x56)
7x56	308	A	GRK	Rho/GRK	M309(7x56)
8x47	309	G	Arr	Beta-1/bArr1, Rho/Arr, NTS1/bArr1	S346(8x47), N310(8x47), S368(8x47)
8x47	309	G	G protein	5HT2A/Gq, HRH1/Gq, ACM1/Gq, CCK1/Gq, Rho/Gt, NTS1/Gi	N384(8x47), N472(8x47), N422(8x47), N374(8x47), N310(8x47), S368(8x47)
8x47	309	G	GRK	Rho/GRK	N310(8x47)
8x48	310	E	Arr	Beta-1/bArr1, Rho/Arr	P347(8x48), K311(8x48)
8x48	310	E	G protein	HRH1/Gq, Rho/Gt	E473(8x48), K311(8x48)
8x48	310	E	GRK	Rho/GRK	K311(8x48)
8x49	311	N	Arr	NTS1/bArr1, Rho/Arr	N370(8x49), Q312(8x49)
8x49	311	N	G protein	HRH1/Gq, CCK1/Gq, Rho/Gt	N474(8x49), R376(8x49), Q312(8x49)
8x49	311	N	GRK	Rho/GRK	Q312(8x49)
8x50	312	F	Arr	Rho/Arr	F313(8x50)
8x50	312	F	Layer 3	Class A GPCRs	8x50
8x51	313	K	GRK	Rho/GRK	R314(8x51)
8x51	313	K	Layer 3	Class A GPCRs	8x51
8x52	314	D	GRK	Rho/GRK	N315(8x52)

2.8 Quantification and data reduction

2.8.1 Data reduction for BRET2 assays

Raw BRET2 ratios were determined by calculating the ratio of the light intensity emitted by the acceptor GFP10 (515 nm) over the light intensity emitted by the donor RLuc3 (410 nm). The BRET2 signals minus the basal BRET2 signals (β-arrestin-RLuc3 only signals) give the net BRET2 values.

2.8.2 Data reduction, standard calibration and transformation of HTRF data from IP1 assays

The raw signals from the IP1 assay were transformed into a fluorescence ratio (665 nm/620 nm) and IP1 concentrations were interpolated from a standard curve prepared using the supplied IP1 calibrator. The IP1 standard curve was fit to a sigmoidal curve using the equation,

$$y = Bottom + \frac{(Top - Bottom)}{1+10^{(x - logIC_{50})}}$$

The *Bottom* and *Top* parameters are the minimum and maximum fluorescence ratios obtained from the standard curve, and the IC_{50} as well as concentration of IP1 in nM (x) are calculated as logarithmic values.

The fluorescence ratios obtained from individual experiments were then converted into the corresponding IP1 concentration (nM, linear) using the equation,

$$IP1 = \frac{IC_{50}(y - Top)}{Bottom - y},$$

and the standard curve. The IC_{50} and IP1 concentrations are now calculated as linear values, and not logarithmic values. In some cases, these concentrations were further analyzed to obtain normalized IP1 values relative to the unstimulated mock-transfected cells (set to 0%) and to the fully stimulated WT receptor (set to 100%).

2.8.3 Data reduction for nanoBRET surface expression assays

To calculate the fraction of labeled surface receptors, we must first account for the spectral overlap between the two HaloTag ligand fluorophores and correct for the bleed through fluorescence of HaloTag Ligand nanoBRET 618 (λ_{em} ~620 nm) into the light intensity reading at 690 nm, meant to capture fluorescence of HaloTag Ligand AlexaFluor 660 (λ_{em} ~690 nm). The bleed through luminescence is calculated as using the equation,

$$Lum_{690}(Bleed\ through) = Lum_{620}(sample) \times \left(\frac{Lum_{690}(sample, 0nM\ Halo\ AF660)}{Lum_{620}(sample, 0nM\ Halo\ AF660)}\right)$$

The correction constant can be calculated as the ratio of the luminescence at 690 nm over the luminescence at 620 nm for those wells that were not treated with HaloTag Ligand AlexaFluor 660. The bleed through luminescence of nanoBRET618 is calculated by multiplying the correction constant to the luminescence obtained at 620 nm for each sample. Lastly, the corrected luminescence reading for AlexaFluor 660 at 690 nm is obtained by subtracting the bleed through value of nanoBRET618 from the observed luminescence value at 690 nm.

To convert these readings into fraction of surface receptor, we must first plot the corrected and normalized BRET ratios against each other. The BRET 690 ratio is calculated as the ratio of the light intensity emitted by acceptor AlexaFluor 660 (corrected 690 nm value from above) over the light intensity emitted by the donor nLuc (460 nm). The normalized BRET 620 ratio (acceptor nanoBRET 618 (620 nm) over donor nLuc (460 nm)), is obtained using the equation,

$$Normalized\ BRET_{620} = 1 - \frac{BRET_{620}(sample, 100nM\ Halo\ AF660)}{BRET_{620}(sample, 0nM\ Halo\ AF660)}$$

When we plot the normalized BRET 620 on the x-axis and the BRET 690 on the y-axis, the gradient of this line becomes the scaling factor, which indicates the value of the BRET 690 ratio if we had 100% surface labeling (**Fig. 2-4**). This scaling factor can be used to convert the BRET 690 ratios into percent surface labeling.

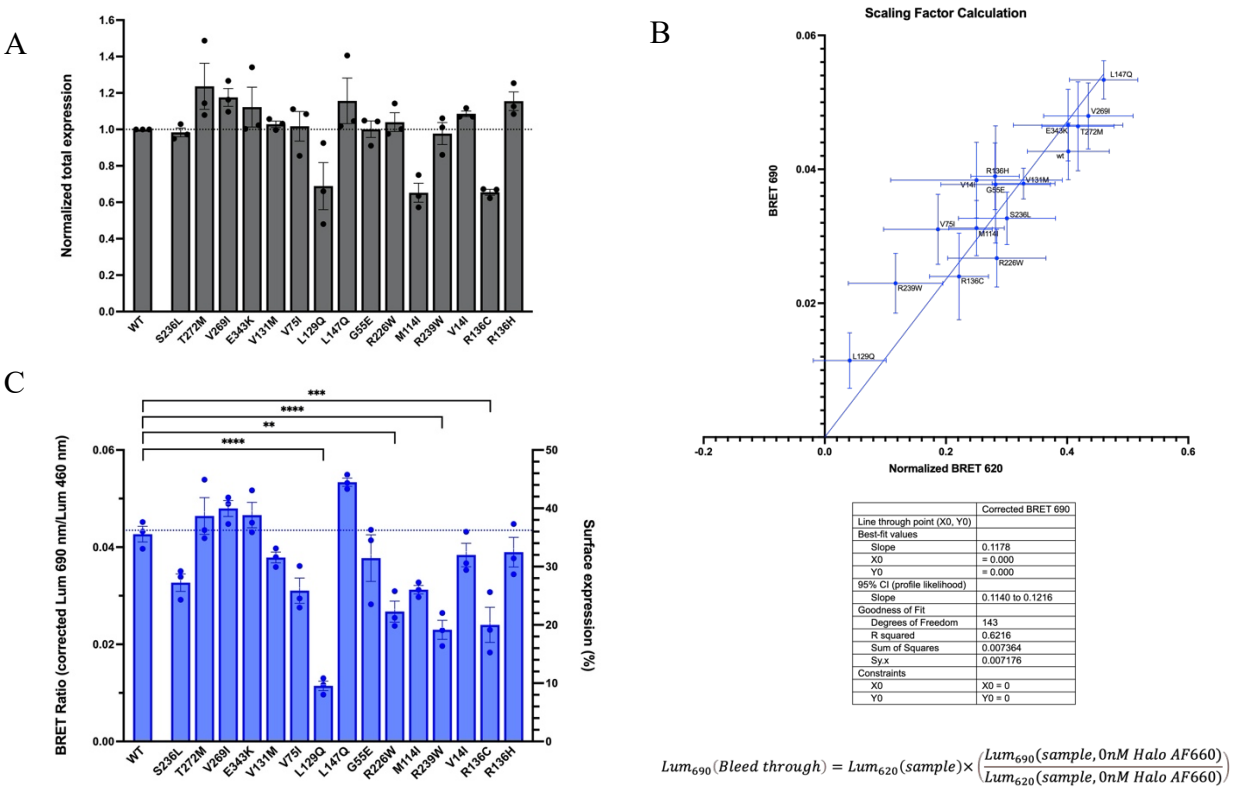

	Corrected BRET 690
Line through point (X0, Y0)	
Best-fit values	
Slope	0.1178
X0	= 0.000
Y0	= 0.000
95% CI (profile likelihood)	
Slope	0.1140 to 0.1216
Goodness of Fit	
Degrees of Freedom	143
R squared	0.6216
Sum of Squares	0.007364
Sy.x	0.007176
Constraints	
X0	X0 = 0
Y0	Y0 = 0

$$Lum_{690}(Bleed\ through) = Lum_{620}(sample) \times \left(\frac{Lum_{690}(sample, 0nM\ Halo\ AF660)}{Lum_{620}(sample, 0nM\ Halo\ AF660)}\right)$$

Figure 2-4 Surface expression of recurrent *CYSLTR2* VUS

A) The total protein expression is obtained from the luminescence reading (nLuc λ_{em} ~460 nm) and is normalized to the total expression of CysLTR2 WT. The data are the mean±SEM from three independent experiments with three technical replicates each. The dotted line is set at 1.0. All receptor variants express just as well, if not slightly better than the wildtype receptor. The lowest expressing receptors still show an expression of over 50% of WT. **B)** In order to convert the nanoBRET ratio of the surface labeling into percentage surface expression, we must first account for the spectral overlap between the two HaloTag ligand fluorophores. We must correct for the bleed through fluorescence of HaloTag Ligand nanoBRET 618 (λ_{em} ~620 nm) into the light intensity reading at 690 nm, meant to capture fluorescence of HaloTag Ligand AlexaFluor 660 (λ_{em} ~690 nm). The bleed through luminescence, Lum_{690}(bleed through), is calculated using the equation shown above. The corrected light intensity reading for AlexaFluor 660 at 690 nm is obtained by subtracting the Lum_{690}(bleed through) from the observed light intensity value at 690 nm. To convert these readings into fraction of surface receptor, we plot normalized BRET 620 on the x-axis and the corrected BRET 690 on the y-axis. The gradient of this line (0.1178 from best-fit value for "Slope" in table) becomes the scaling factor, which indicates the value of the BRET 690 if we had 100% surface labeling. This scaling factor can be used to convert the BRET 690 ratios into percent surface labeling. **C)** The scaling factor was used to plot the percentage surface expression for each variant. CysLTR2 WT has a surface expression of about 36%, and most variants are not statistically significantly different from these when compared using a one-way ANOVA. Notably, the UM mutant L129Q has a very low surface expression of ~10%. Three other recurrent variants, R226W, R239W, and R136C show a significantly lower surface expression of about 20%.

CHAPTER 3. RESULTS AND DISCUSSION

3.1 The uveal melanoma oncoprotein CysLTR2-L129Q constitutively activates Gq and escapes β-arrestin down-regulation

3.1.1 CysLTR2-L129Q mutation is a CAM that signals through Gq

To characterize the functional phenotype of CysLTR2-L129Q, we first determined the agonist-dependent signaling for CysLTR2-L129Q and CysLTR2 wild-type (CysLTR2 WT). CysLTR2 predominantly couples to Gq/11 when treated with the agonist LTD4 (Heise *et al.*, 2000). PLC-β is the classical effector of Gq/11 and results in receptor-stimulated phosphoinositide hydrolysis (de Rubio et al., 2018). The CisBio IP-One HTRF Immunoassay allows us to quantify IP1, a degradation product of the second messenger IP3, to measure activation of PLC-β by Gq-coupled GPCRs (Trinquet et al., 2006). The IP1 assay is a competitive HTRF assay where the d2-labeled IP1 analogue acts as the fluorescence acceptor and the terbium cryptate-labeled anti-IP1 mAb acts as the fluorescence donor. The terbium-cryptate is a long-lifetime fluorescence donor that can be excited by UV light. LiCl is added during the stimulation period of the assay to block further degradation of IP1 by the enzyme IMPase. It has been suggested that PLC-β-dependent IP1 accumulation also includes contributions from the d-myo-inositol-1,4-bisphosphate (IP2) formed by direct hydrolysis of phosphatidylinositol-4-phosphate (PI4P), instead of IP2 formed by the dephosphorylation of IP3 formed by hydrolysis of PIP2 (de Rubio *et al.*, 2018). Since this novel pathway does not depend on PIP2, which is predominantly found at the plasma membrane, the PI4P-dependent IP1 accumulation could have a substantial contribution to PLC-β signaling from the endosomal compartment.

We first obtained a time-course of basal and LTD4-dependent IP1 accumulation in HEK293T cells transiently transfected with plasmids for CysLTR2 WT, CysLTR2-L129Q, and mock controls. LTD4-stimulated CysLTR2 WT showed increasing IP1 accumulation over the first 100 min before reaching a plateau (**Fig. 3-1A**), whereas the unstimulated CysLTR2 WT samples were indistinguishable from mock-transfected controls with and without LTD4 treatment. The samples transfected with the same amount of DNA encoding for the CysLTR2-L129Q mutant showed ligand-independent IP1 accumulation of comparable magnitude as LTD4-treated CysLTR2 WT. After 100 min, the basal IP1 accumulation of CysLTR2-L129Q kept increasing while the ligand-dependent signaling of the wt receptor reached a plateau (**Fig. 3-1B**).

We generated fusion constructs of CysLTR2 WT and CysLTR2-L129Q, with a version of green fluorescent protein (GFP10) at the C-terminus. These fusion constructs enable quantification of basal and agonist-dependent Gq/11 cellular signaling as well as β-arrestin recruitment activity under comparable conditions. The agonist LTD4 induces a dose-dependent increase in IP1 accumulation for CysLTR2 WT (**Fig. 3-2A**) that scales as expected with the receptor density controlled by the gene dosage as described by a modified Slack-Hall operational model (**Scheme 3-1, Table 3-1B**). In contrast, the CysLTR2-L129Q mutant shows little or no response to treatment with LTD4, but the ligand-independent basal IP1 accumulation dramatically increases with increasing gene dosage (**Fig. 3-2B**). Therefore, the mutation is

A - Sigmoidal dose-response function:

$$E = bottom + \frac{top - bottom}{1 + \left(\frac{[A]}{EC50}\right)^{-n}}$$

B - Operational model (Black-Leff):

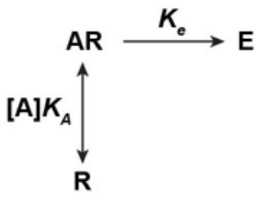

$$E = \frac{E_{max}}{1 + \left(\frac{[R]_t}{K_e}\frac{[A]K_A}{1 + [A]K_A}\right)^{-n}}$$

C - Operational model (Slack-Hall):

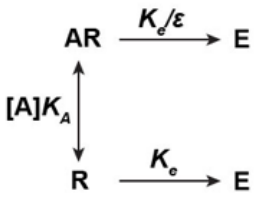

$$E = \frac{E_{max}}{1 + \left(\frac{[R]_t}{K_e}\frac{1 + \varepsilon[A]K_A}{1 + [A]K_A}\right)^{-n}}$$

Scheme 3-1 Modeling the pharmacology of constitutively active receptors
The different models and corresponding equations proposed to describe the pharmacology of the constitutively active CysLTR2-L129Q receptor are described here. (**A**) The sigmoidal dose-response model, (**B**) the Black-Leff operational model, and (**C**) the Slack-Hall operational model.

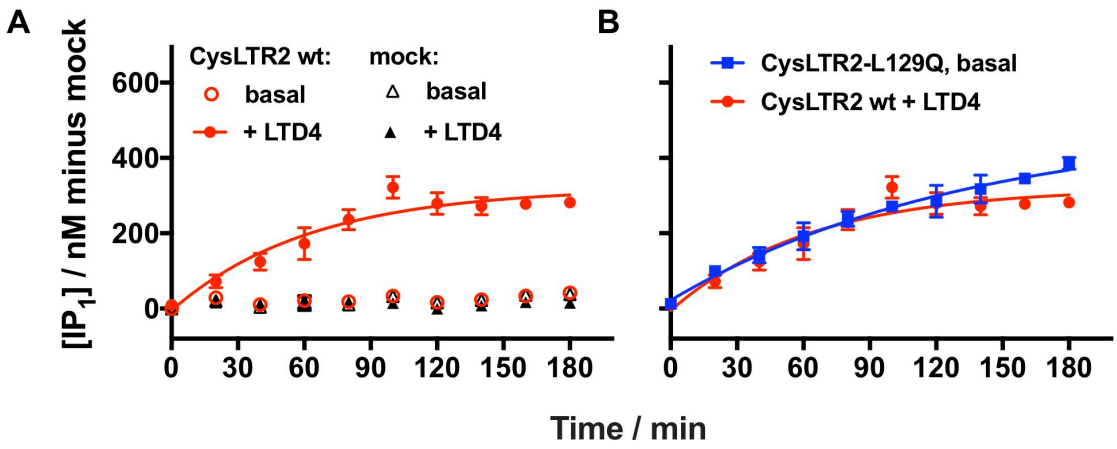

Figure 3-1 Development of the CysLTR2 functional assay for Gq signaling pathway
Lithium chloride-dependent accumulation of IP1 differs for agonist-induced and constitutive receptor activity. Lithium chloride (LiCl) is added during the stimulation period of the assay to block further degradation of IP1. Time-course of the effect of 50 mM LiCl on the basal and LTD4-induced IP1 accumulation for CysLTR2 WT (**A**) and -L129Q (**B**) transfected HEK293T cells over 180 min. **(A)** Basal IP_1 accumulation of CysLTR2 WT (open red circles) is comparable to mock-transfected cells with (solid black triangles) or without (open black triangles) LTD4 stimulation and is not affected by the addition of LiCl. CysLTR2 WT stimulated by LTD4 exhibits an increasing IP1 accumulation over 100 min after addition of LiCl, before reaching a plateau (solid red circles). **(B)** CysLTR2-L129Q (blue squares) shows a LTD4-independent IP1 accumulation similar to the WT receptor that continues to increase over 180 min. The data are expressed as the mean ± SEM of IP1 (nM) minus mock and result from one experiment performed in four technical replicates.

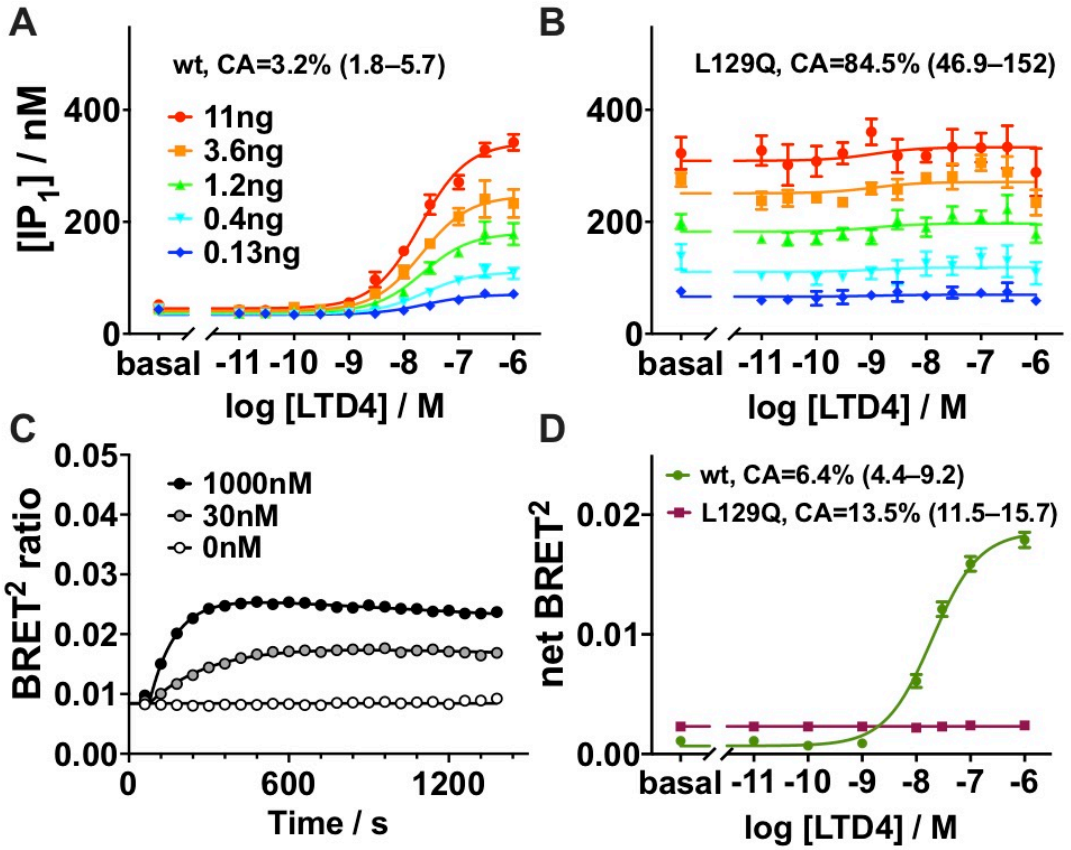

Figure 3-2 Oncoprotein CysLTR2-L129Q is a Gq-biased CAM that only weakly recruits β-arrestin2

(A,B) Gq second messenger IP1 accumulation assay. **(A)** Agonist LTD4 leads to dose-dependent IP1 accumulation in HEK293T cells transfected with different amounts (0.13 to 11 ng DNA, blue to red) of CysLTR2-GFP10 wt. **(B)** The corresponding experiment with CysLTR2-L129Q shows dramatic agonist-independent basal IP1 accumulation that scales with the amount of CysLTR2-L129Q-encoding DNA. Only a very small agonist-dependent response to LTD4 can be detected. The results show that CysLTR2-L129Q is a CAM with 85% constitutive activity relative to fully agonist-stimulated wt receptor. Data points are mean±SEM of the accumulated IP1 concentration and from one experiment with four replicates each. The set of curves are fits to the Slack-Hall operational model (**Table 3-1B, Scheme 3-1**). **(C,D)** β-arrestin2-recruitment BRET2 assays. **(C)** Time-course of LTD4-stimulated β-arrestin2-recruitment for three LTD4 concentrations (0 nM, 30 nM, and 1000 nM). β-arrestin2 recruitment exhibits a biphasic time-course, increasing for about ten min after LTD4 addition before slowly decreasing. The data points are mean±SEM from three independent experiments with eight replicates each. Curves are double exponential fits (**Table 3-1C**). **(D)** The LTD4 dose-dependent β-arrestin2 recruitment to CysLTR2 wt (dark green; EC_{50} is 30 nM (95% C.I. 25 to 36 nM)). In comparison, CysLTR2-L129Q (maroon) shows higher basal β-arrestin2 recruitment, corresponding to 13.5% constitutive activity, and no response to agonist. The data points are the mean±SEM from three independent experiments with three replicates each.

meeting the essential criteria for a constitutively active mutant (CAM), since the hallmark of CAM receptors is agonist-independent signaling that scales with receptor density. The results also show that under the experimental conditions, the Gq signaling pathway is not saturated, which suggests that the high basal receptor activation of Gq for CysLTR2-L129Q is not due to a high amplification of the Gq signaling pathway.

3.1.2 CysLTR2-L129Q poorly recruits β-arrestins

Signals from active GPCRs are normally terminated by β-arrestin-dependent mechanisms, including desensitization, sequestration, and downregulation. To follow up on this, we next asked the question, how is CysLTR2-L129Q capable of sustained strong signaling at a level comparable to the fully agonist-stimulated wt receptor? CysLTR2 has been shown to bind β-arrestin2 in response to several agonists (Yan et al., 2011). However, little is known about the β-arrestin-dependent desensitization, trafficking and downregulation of CysLTR2 and CysLTR2-L129Q.

We designed a bioluminescence resonance energy transfer 2 (BRET2) experiment to quantify the basal and agonist-dependent binding of β-arrestins to CysLTR2 variants. The BRET2 experiments are performed on HEK293T cells expressing CysLTR2-GFP10 fusion construct in combination with β-arrestins fused to an engineered variant of *Renilla* luciferase (RLuc3), β-arrestin-RLuc3 (Berchiche and Sakmar, 2016). The first BRET system, BRET[1], involved the bioluminescence generated by the enzyme Rluc and the luciferin substrate coelenterazine-h, and a yellow fluorescent protein (YFP) as the resonance energy transfer acceptor (Xu et al., 1999). However, the BRET1 assay suffered from a poor signal-to-background ratio due to the small Stokes' shift of the YFP fluorescence spectra and the significant overlap of the luminescence and acceptor fluorescence emission spectra. This led to the development of the BRET2 assay that uses Rluc with the substrate DeepBlueC and GFP2 or GFP10 as the acceptor (Bertrand et al., 2002). DeepBlueC is an analog of the natural substrate with emission maxima at 410 nm. GFP2 and GFP10 are UV-excitable versions of GFP, which allow for a much larger Stokes' shift compared to YFP (~90 nm as compared with 15 nm for YFP) (Kobayashi et al., 2019). Together with the blue-shifted emission of DeepBlueC, BRET2 results in a superior signal-to-background performance. Today, there are other blue-shifted substrates available, such as Me-O-e-CTZ (also known as Prolume Purple, used in our experiments), which are much brighter than the original DeepBlueC (Zhang et al., 2013). BRET was developed and first applied to GPCRs 20 years ago and has been refined and extended since then to address key questions in GPCR biology such as G protein activation, β-arrestin recruitment, cell trafficking, and receptor dimerization (Angers et al., 2000; Stoddart et al., 2015).

We first performed a time-course experiment to characterize the agonist-dependent β-arrestin-recruitment. The BRET2 ratio shows an agonist concentration-dependent increase for approximately 10 min after the addition of the agonist LTD4, before starting to decrease again slowly (**Fig. 3-2C**). The initial increase in the slope increases with higher concentrations of the agonist. The shapes of the time-courses were similar when comparing samples expressing β-arrestin1-RLuc3 and β-arrestin2-RLuc3, but the peak increase seen for β-arrestin2-RLuc3 was almost twice that of β-arrestin1-RLuc3 (**Fig. 3-3**). Such a biphasic BRET2 β-arrestin-recruitment time-course is typical for GPCRs with "class A" β-arrestin-recruitment phenotype that have

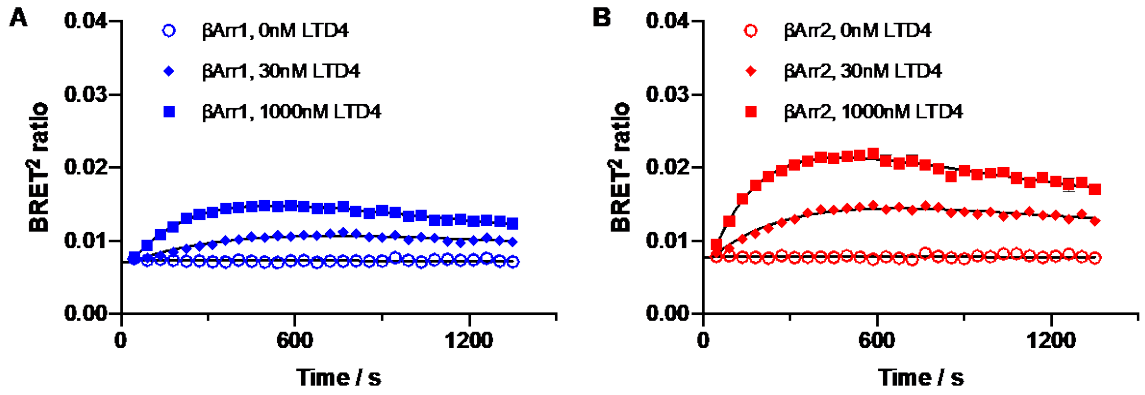

Figure 3-3 Time-course of LTD4-stimulated β-arrestin-recruitment measured by the BRET2 assay with CysLTR2-GFP10 and β-arrestin-RLuc3

(**A**) The time-dependent increase of net BRET2 demonstrates recruitment of β-arrestin1 (βArr1) and was measured for two LTD4 concentrations (30 nM, blue diamond; 1000 nM, blue square) and vehicle (0 nM, blue open circle). (**B**) Time-course of β-arrestin2 (βArr2) recruitment for two LTD4 concentrations (30 nM, red diamond; 1000 nM, red square) and vehicle (0 nM, red open circle). The time-dependent data in (**A**,**B**) were globally fitted with a double exponential function using shared slow kinetic rates and starting values. They are the mean ± SEM from two independent experiments, with two sets of four technical replicates.

transient, weak interactions with β-arrestins. These class A receptors rapidly recycle after internalization (DeWire et al., 2007).

The LTD4 dose-dependent increase of the BRET2 ratio for samples transfected with CysLTR2-GFP10 wt and β-arrestin-RLuc3 substantiate the finding from the time-course assay that the agonist-dependent increase of BRET2 is larger for β-arrestin2-RLuc3 as compared with β-arrestin1-RLuc3 (**Fig. 3-4A**). Even though the agonist-dependent increase was different, the midpoints of the sigmoidal fits of the agonist dose-dependent data for both β-arrestins were identical (**Fig. 3-4B**). From these findings, we decided to proceed with the subsequent experiments using only β-arrestin2, which gave the larger BRET2 ratios.

To characterize the effect of the L129Q mutation on β-arrestin-recruitment, we included a set of samples expressing CysLTR2-L129Q in the BRET2 experiments. The results from the LTD4 dose-response experiment show a basal, ligand-independent net BRET2 ratio of 0.0028±0.00007 with no ligand dose-dependence (**Fig. 3-2D**). In comparison, the basal net BRET2 ratio for the wt receptor is 0.0007±0.0002 that increases to 0.0186±0.0004 at saturating LTD4 concentrations (**Table 3-1A**).

3.1.3 CysLTR2-L129Q is a Gq-biased CAM that escapes β-arrestin-mediated downregulation

We next quantified the constitutive activity for both Gq/11 signaling and β-arrestin-recruitment using the modified Slack-Hall operational model to enable the calculation of *receptor bias* between Gq/11 and β-arrestin pathways (Zhou *et al.*, 2019) for L129Q relative to wt. The term *receptor bias* was introduced to describe the pathway preference of the basal signaling activity of a receptor (Zhou *et al.*, 2019), in contrast to the term *agonist bias* that describes ligand-dependent pathway preferences of a receptor (Kenakin et al., 2012).

Scheme 3-1 introduces two operational models: the Black-Leff and Slack-Hall models. The key insight of Zhou *et al.* is that the Slack-Hall model can be used to quantify the inherent agonist-independent pathway bias of the constitutive signaling of a receptor referred to as *receptor bias* (Slack and Hall, 2012; Zhou *et al.*, 2019). The Slack-Hall model is an expansion of the classical Black-Leff operational model, which underlies methods to calculate functional selectivity or agonist bias (Kenakin *et al.*, 2012). In the Slack-Hall model, both the free receptor [R] and agonist bound receptor [AR] can produce a stimulus, $S = \varepsilon[AR] + [R]$. The parameter ε describes the efficacy of an agonist (A), to produce a stimulus. The Slack-Hall model splits the τ parameter of the Black-Leff model into a product of two parameters, χ and ε. The basal response is determined by χ and is defined as the ratio of $[R]_t$, the total receptor concentration, and K_e, the receptor concentration producing half-maximal effect in the *absence* of an agonist. In contrast, the τ parameter in the Black-Leff model is the ratio of $[R]_t$ and a different K_e, which is defined as the receptor concentration producing half-maximal effect in the *presence* of a saturating agonist concentration. The ε parameter measures the *intrinsic efficacy* of the ligand. We slightly modified the original form of this equation to account for fitting problems for χ, the basal response parameter, in cases where the constitutive activity is very low. Taking the $log\ \tau$ parameter from the Black-Leff model, we implicitly calculate $log\ \chi$ from $log\ \tau – log\ \varepsilon$. The final equation of our modified Slack-Hall model is:

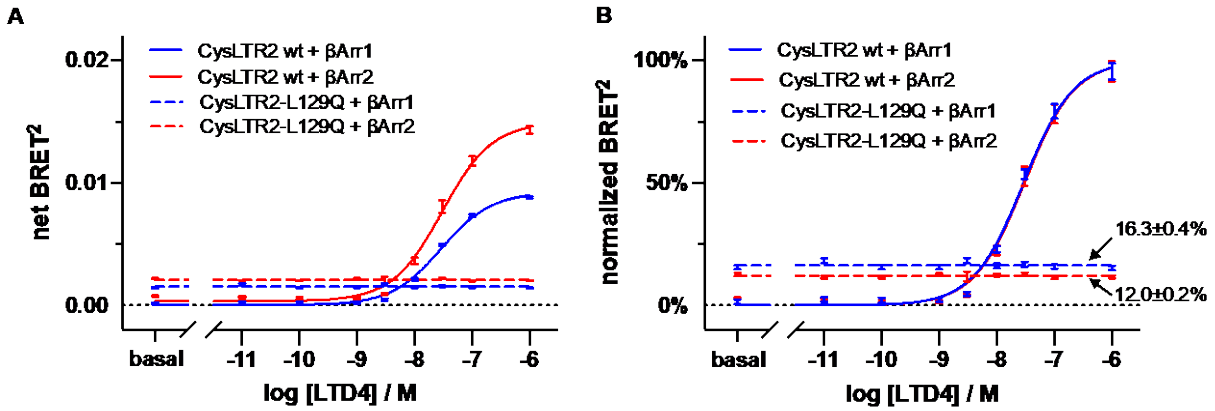

Figure 3-4 β-arrestin-recruitment BRET2 assay with CysLTR2-GFP10 and β-arrestin-RLuc3

(**A**) The LTD4 dose-dependent increase of net BRET2 demonstrates the recruitment of β-arrestin1 (βArr1, solid red line and points; EC_{50} is 29 nM (95% C.I. 25 to 34 nM)) and β-arrestin2 (βArr2, solid blue line and points; EC_{50} is 30 nM (95% C.I. 25 to 36 nM)) to CysLTR2 wt. In comparison, the data for CysLTR2-L129Q indicate ligand-independent recruitment of β-arrestin1 (blue dashed line and open points) and β-arrestin2 (red dashed line and open points) to CysLTR2-L129Q. (**B**) The BRET2 data were independently normalized for either β-arrestin1 or 2 using the asymptotic endpoints of the sigmoidal fits for the wt receptor. The normalized data show a nearly perfect overlap of the fitted curves for both β-arrestins binding the wt receptor. The ligand-independent β-arrestin recruitment for CysLTR2-L129Q is 16.3±0.4% and 12.0±0.2% for β-arrestin1 and 2, respectively. The dose-response data are the mean ± SEM from three independent experiments, with nine concentrations and three technical replicates each.

$$y = Basal + \frac{E_{max}(10^{log\tau - log\varepsilon} + 10^{log\tau + x + logK_A})^n}{(10^{log\tau - log\varepsilon} + 10^{log\tau + x + logK_A})^n + (1 + 10^{x + logK_A})^n}$$

The parameter χ determines the value of the basal response. The challenge is that χ is proportional to the receptor density, which requires standardization for the comparison of receptor mutants with potential impact on receptor expression levels. In our experiments, we control the receptor density by the gene dosage and measure the fluorescence from the GFP10 fusion to calibrate the relative expression levels (**Fig. 3-5**). The GFP10 readings were first normalized by dividing the sample GFP10 fluorescence by the basal GFP10 fluorescence (β-arrestin2-RLuc3 only), and then further dividing this by the normalized GFP10 fluorescence of the exchange protein activated by cAMP (EPAC) BRET2 biosensor (RLuc3-EPAC-GFP10 (Berchiche and Sakmar, 2016) developed from the guanine nucleotide exchange protein activated by cAMP that acts as the positive control) to give,

$$GFP_{norm} = \langle \frac{\langle \frac{GFP(sample)}{GFP(RLuc)} - 1 \rangle}{\langle \frac{GFP(EPAC)}{GFP(RLuc)} - 1 \rangle} \rangle$$

The inner averages are for technical replicates per experiment, and the outer averages are for all experiments. These data are fit to a sigmoidal model, where GFP10 fluorescence is the response as a function of DNA dosage. The log EC_{50} parameter is shared in the global fit, the bottom parameter is set to zero, while the top parameter is left unconstrained to capture the different expression levels of each variant. We used the sigmoidal fits of the GFP10 fluorescence to adjust for lower DNA/cell levels used in the Gq second messenger IP1 assays, and thus the interpolated GFP10 fluorescence values were plotted against *log* τ values and *log* χ values from fitting the data to the modified Slack-Hall model (**Fig. 3-6, Table 3-1B**). Assuming the GFP10 fluorescence (GFP10 F) is proportional to the total receptor concentration by some scaling constant, *c*, and rearranging $\chi = \frac{[R]_T}{K_e}$ gives,

$$log\chi = logc + log(GFP10\ F) - logK_e$$

Thus, plotting *log* χ against *log (GFP10 F)* and fitting to a line with a slope of 1 gives y-intercept of *log c – log* K_e. We can similarly plot *log* τ against *log (GFP10 F)* to get a y-intercept of *log c – log* K_e + *log* ε. These allow for an accurate quantification of *log* ε and of differences of *log* K_e for different receptor constructs at a standard density.

We noticed that in the absence of a ligand, the Slack-Hall model reduces to the mathematical form of a one-site saturation-binding function (Hulme and Trevethick, 2010). We plotted the BRET2 ratios against normalized GFP10 fluorescence readings for each CysLTR2 variant and fit the data to a one-site saturation-binding isotherm using the equation below (**Fig. 3-7**).

$$y = \frac{10^{logB_{max}}}{x + 10^{logK_d}} x + background.$$

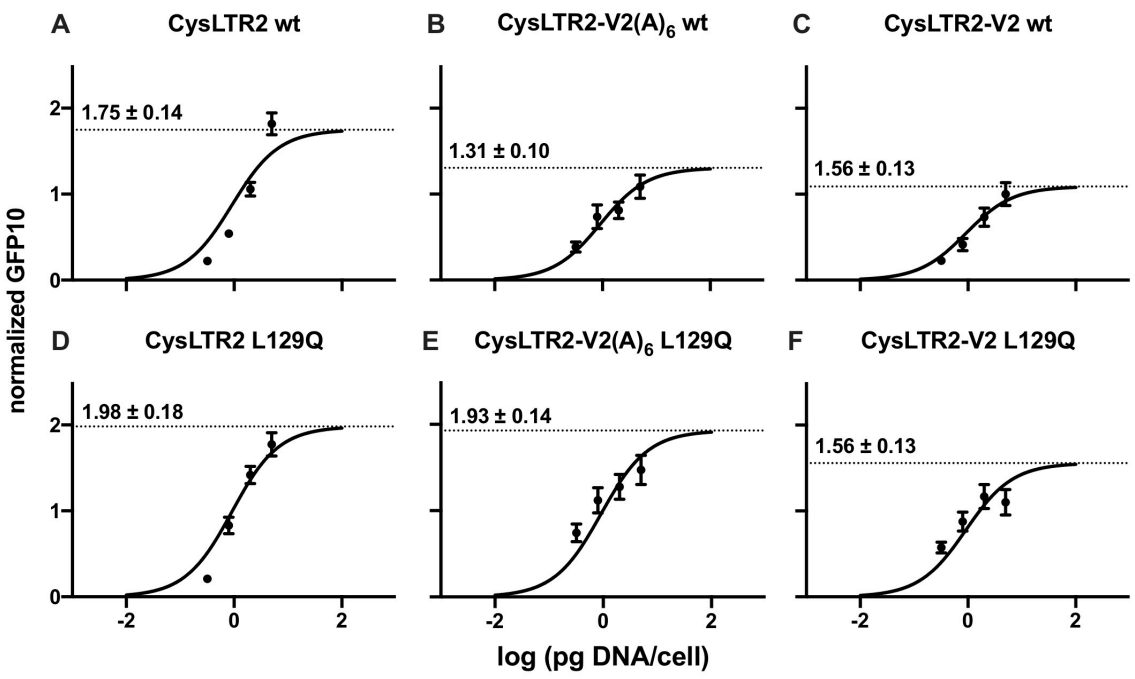

Figure 3-5 Gene dosage-dependent receptor expression

Normalized GFP10 fluorescence of HEK293T cells transfected with varying amounts of receptor-encoding plasmid are fit to a sigmoidal model, where GFP10 fluorescence is the output as a function of DNA dosage. 40,000 cells were transfected with 12.5, 32, 80, and 200 ng of receptor-encoding plasmid, to yield 0.3125, 0.8, 2, and 5 pg/cell of DNA. The log EC50 value (log EC50 = −0.038 ±0.072) is shared for all CysLTR2 wt (**A**, normal; **B**, V2(A)6 tail; **C**, V2 tail) and L129Q (**D**, normal; **E**, V2(A)6 tail; **F**, V2 tail) variants. The bottom parameter is set to zero, while the top parameter is left free to capture the different expression levels of each variant and is indicated on the graphs. These sigmoidal fits are used to interpolate GFP10 fluorescence for subsequent plots (**Fig. 3-6**), because the GFP10 fluorescence is not strong enough to reliably measure the total receptor concentrations, especially at lower DNA/cell levels used in the Gq second messenger IP1 assays.

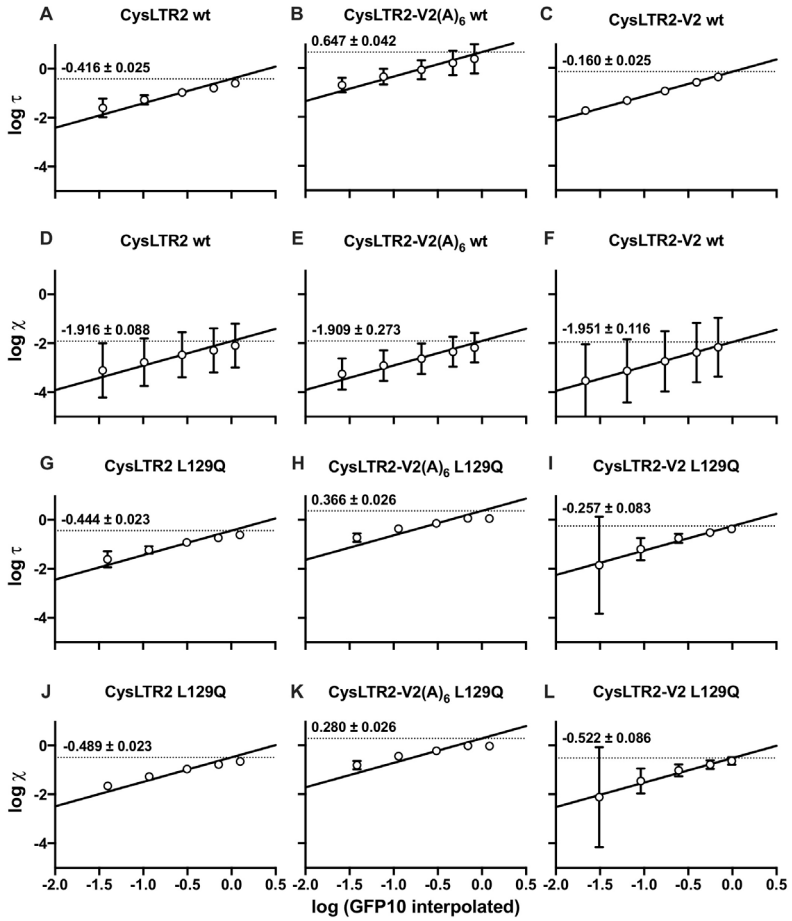

Figure 3-6 Basal and agonist-dependent receptor activity for Gq pathway as function of receptor expression

The GFP10 readings for HEK293T cells transfected with varying amounts of receptor-encoding plasmid from the Gq second messenger IP1 assays (**Fig. 3-2A,B, Fig. 3-8A-D**) were interpolated from the sigmoidal fits in **Fig. 3-5**. 7,000 cells were transfected with 0.1, 0.4, 1.2, 3.6, and 11 ng of receptor-encoding plasmid, to yield 0.019, 0.057, 0.17, 0.51, and 1.57 pg/cell of DNA. These were plotted against log τ values (wt, **A-C**; L129Q, **G-I**) and log χ values (wt, **D-F**; L129Q, **J-L**) obtained from fitting the data to the modified Slack-Hall model (**Table 3-1B**). Assuming the GFP10 fluorescence is proportional to the total receptor concentration by some scaling constant, c, and rearranging $\chi = \frac{[R]_T}{K_e}$ gives $log\chi = logc + \log(GFP10) - logK_e$, plotting $log\,\chi$ against *log (GFP10)* and fitting to a line with a slope of 1 gives y-intercept of $log\ c - log\ K_e$. We can similarly plot $log\ \tau$ against *log (GFP10)* to get a y-intercept of $log\ c - log\ K_e + log\ \varepsilon$. The y_0 values are indicated on graphs and allow for an accurate quantification of $log\ K_e$ and $log\ \varepsilon$, of different receptor constructs at standard density.

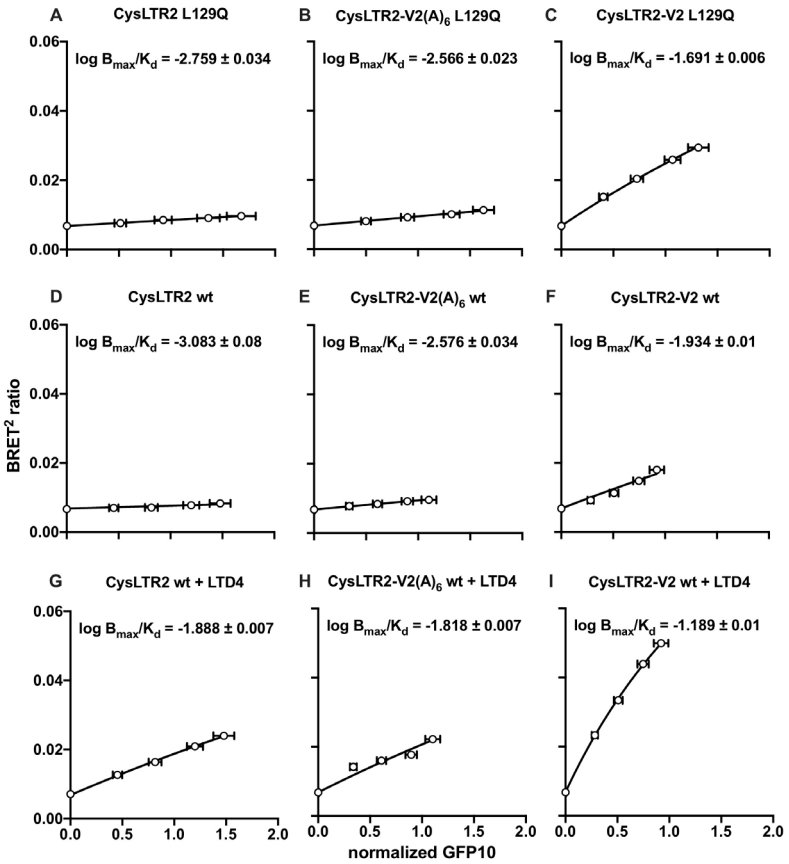

Figure 3-7 Basal and agonist-dependent receptor activity for β-Arrestin2 pathway as function of receptor expression

Saturation-binding BRET2 experiment with CysLTR2-L129Q (**A-C**), unstimulated wt (**D-F**) and wt stimulated with 1000 nM LTD4 (**G-I**). The data are fit to a one-site saturation binding function. Tight independent estimates of K_d and B_{max} are not required, because at low concentrations, only the ratio B_{max}/K_d determines the concentration-dependent binding, which can be estimated from the initial slope. The initial slopes are well defined by samples even at low expression levels of receptors and avoid the need for very high receptor concentrations to reach saturation. All data are fit with a shared *log* B_{max}, and *log* B_{max}/K_d are indicated on the graphs. This enables direct comparison of the slopes for unstimulated CysLTR2 wt and CysLTR2-L129Q to subsequently calculate the constitutive activity values in **Fig. 3-2D, 3-8E,F**.

The logarithmic fitting parameters, $logB_{max}$ and $logK_d$, ensure positive fitting solutions for B_{max} and K_d. B_{max} is the maximal increase of the BRET2 ratio due to β-arrestin binding. $logB_{max}$ is a shared value for the global fits of all variants. K_d is the equilibrium dissociation of the GFP10 fluorescence, which gives half-maximal β-arrestin binding. The $logK_d$ varied independently for each curve. The parameter *background* is constrained to 0.0068, the BRET2 ratio for the β-arrestin2-RLuc3 sample without receptor.

Tight independent estimates of K_d and B_{max} are not required, because at low concentrations, only the ratio B_{max}/K_d determines the concentration-dependent binding, which can be estimated from the initial slope. The initial slopes are well defined by samples even at low expression levels of receptors and avoid the need for very high receptor concentrations to reach saturation. The initial slope of a saturation binding experiment as a function of total receptor concentration is B_{max}/K_d. The Initial slope of the Slack-Hall model as function of total receptor concentration is E_{max}/K_e. The equivalence of B_{max}/K_d and E_{max}/K_e enables subsequent calculations of $\Delta\log\chi$, the differences of $\log\chi$ for the wt and mutant receptors that determine changes in the constitutive activity and the double difference $\Delta\Delta\log\chi$ that determines the receptor bias. Those differences eliminate the constant B_{max} and E_{max} terms and focus on changes of the bias-relevant terms K_d and K_e.

Using the values obtained from the fits in **Figs. 3-6** and **3-7,** we are finally able to compare constitutive activities for the different receptor constructs at a standard density. The constitutive activities are normalized relative to the fully agonist-stimulated wt receptor. The ligand-independent constitutive activity of CysLTR2-L129Q corresponds to 84.5% (95% confidence interval (C.I.) 46.9%–152%) of the maximally LTD4-stimulated CysLTR2 wt at a comparable total receptor concentration. The constitutive activity of the wt receptor is 3.2% (95% C.I. 1.8%–5.7%). Therefore, the L129Q mutation results in a 26-fold increase of the constitutive activity in the Gq pathway. The ligand-dependent increase in IP1 signaling of CysLTR2-L129Q is statistically insignificant as reflected by the efficacy parameter ε of 1.11 (95% C.I. 1.03–1.19) close to unity (**Table 3-1B**). Overall, the results suggest that CysLTR2-L129Q displays a GoF phenotype for ligand-independent basal signaling and a LoF phenotype for agonist-dependent signaling in the Gq/11 signaling pathway. Compared to the agonist-dependent β-arrestin-recruitment of the wt receptor (set to 100%), the constitutive activity of the wt receptor is 6.4% and of the L129Q mutant is 13.5%. Therefore, the effect of the L129Q mutation on the constitutive activity in the β-arrestin pathway is a 2-fold increase, which is much smaller than the 26-fold increase in the Gq pathway. Therefore, the L129Q mutation introduces a strong bias of the constitutive signaling ("receptor bias") towards Gq and away from β-arrestins.

It is challenging to quantify receptor bias. Although ligand bias or biased agonism has been studied for many GPCR-agonist pairs with well-developed mathematical approaches, the concept of receptor bias is still a relatively underexplored area. To our knowledge, this is the first time a rigorous mathematical method has been developed for the detailed analysis of receptor bias. The method described here is generalizable and can be used to study mutations that might cause receptor bias in any GPCR.

3.1.4 Enhanced recruitment of β-arrestin has only a small effect on basal Gq activation in CysLTR2-L129Q

We speculated that the receptor bias away from β-arrestins may be due to a lack of phosphorylation sites in the C-terminal tail of the receptor. When a GPCR is activated, GRKs phosphorylate the serine and threonine-rich carboxyl terminus. The CysLTR2 C-terminal tail sequence is SVWLRKE, which has been predicted to have a partial phosphorylation code characteristic of a class A β-arrestin-recruitment phenotype (Zhou et al., 2017b). Class A GPCRs are typified by the β_2AR, bind preferentially to β-arrestin2, and have transient and weak interactions with β-arrestins and dissociate from it before internalization (Luttrell and Lefkowitz, 2002). This is consistent with our findings of a biphasic β-arrestin2-recruitment time-course. On the other hand, class B GPCRs, such as the V2 vasopressin receptor, bind equally well to β-arrestins1 and 2 and bind to them more tightly and stably, which leads to the GPCR-β-arrestin complex being sustained for a longer time, even after internalization (DeWire *et al.*, 2007). When the GPCR dissociates from the β-arrestins before endocytosis, dephosphorylation and recycling to the plasma membrane is favored. Meanwhile, persistent binding to β-arrestins favors receptor degradation (Spiegel, 2003).

We hypothesized that adding the tail sequence of the vasopressin V2 receptor, which carries a strong phosphorylation code, would enhance the recruitment of β-arrestins and switch the receptor to a class B β-arrestin-recruitment phenotype. It has been reported previously that modifying the C-terminal tail, namely with the tail of the vasopressin V2 receptor, dictates the β-arrestin-recruitment phenotype (Oakley *et al.*, 1999). We used a hexa-alanine variant (V2(A)$_6$) as a negative control in which we replaced six Ser and Thr residues with Ala residues. In order to explore the strong bias of CysLTR2-L129Q towards Gq, we must investigate the relationship between β-arrestin and Gq binding to CysLTR2. To this end, we enhanced the β-arrestin recruitment to CysLTR2 through the addition of a strong phosphorylation code and observed the corresponding effects on Gq binding and activation. By enhancing the β-arrestin binding to CysLTR2-L129Q, is it possible to observe a shift in the bias?

The results from IP1 and BRET2 assays of the V2 and V2(A)$_6$ tail variants for CysLTR2 wt and L129Q are shown in **Fig. 3-8**. The V2 tail reduces the agonist-dependent signaling at comparable gene dosage for wt as compared to the V2(A)$_6$ tail variant (**Fig. 3-8A,B**). Similarly, the basal signaling of the L129Q mutant is reduced for V2 as compared with V2(A)$_6$ (**Fig. 3-8C,D**). Once more, **Figs. 3-5 to 3-7** were used in order to compare the constitutive activities for the different receptor constructs at a standard density. The constitutive activity values of the L129Q mutants are comparable with 43.5% for the -V2 tail and 43.0% for the V2(A)$_6$ tail variant. Surprisingly, the V2 tail restores some of the agonist-dependent signaling of L129Q as indicated by an efficacy parameter ε of 1.84 (95% C.I. 1.70–1.99) different from unity (**Table 3-1B**). The V2 tail enhances both basal and agonist-dependent increase of BRET2 for CysLTR2 wt (**Fig. 3-8E,F**). Interestingly, the enhancement of basal, agonist-independent β-arrestin-recruitment to CysLTR2-L129Q was much more pronounced for the V2 tail variant as compared with the V2(A)$_6$ control, which showed only weak β-arrestin-recruitment similar to that of CysLTR2-L129Q without the added sequences. We also determined the agonist-dependent β-arrestin-recruitment time-course for CysLTR2 wt that showed a biphasic time-course for the V2(A)$_6$ control and a monophasic increase for the V2 construct, which is consistent with a class

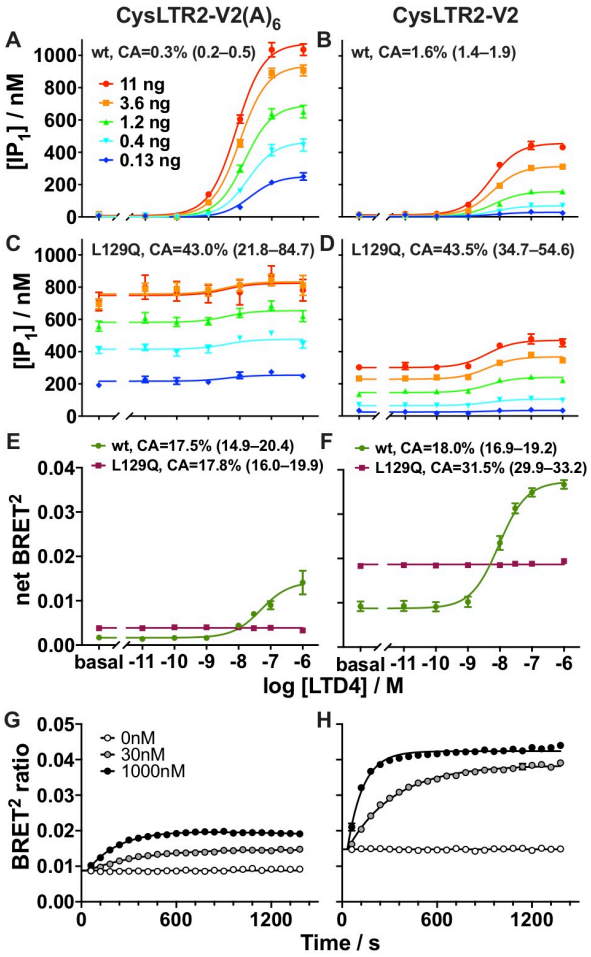

Figure 3-8 Recruitment of β-arrestin has only a small effect on basal Gq activation in CysLTR2-L129Q

We added the C-terminal 27 residues of the vasopressin V2 receptor to full-length CysLTR2 to promote high-affinity interactions with β-arrestins (construct CysLTR2-V2). Construct CysLTR2-V2(A)$_6$ is the corresponding phosphorylation-resistant control. (**A-D**) Gq second messenger IP1 accumulation assay. (**E-H**) β-arrestin2-recruitment BRET2 assay. (**A,B**) Agonist-stimulated Gq signaling is reduced by the addition of the V2 sequence as compared to the addition of V2(A)$_6$ sequences at comparable gene dosages. (**C,D**) Similarly, basal Gq signaling of L129Q is reduced by half in CysLTR2-V2 as compared to -V2(A)$_6$. Data points are mean±SEM from three independent experiments with six replicates each. Sets of curves are fits to the Slack-Hall operational model (**Table 3-1B**). (**E,F**) Agonist-stimulated β-arrestin-recruitment is enhanced by the V2 sequence and reduced by the V2(A)$_6$ sequence. Basal, agonist-independent β-arrestin-recruitment of L129Q is 5-fold stronger for CysLTR2-V2 as compared to -V2(A)$_6$. Data points are mean±SEM from three independent experiments with three replicates each. (**G,H**) Time-course of LTD4-stimulated β-arrestin2-recruitment for three LTD4 concentrations (0 nM, white circles; 30 nM, grey circles; 1000 nM, black circles). While the CysLTR2-V2(A)$_6$ wt exhibited a biphasic time-course, CysLTR2-V2 wt reached a plateau after about eight min. Data are fit to double exponential curves (**Table 3-1C**) and points are mean±SEM from three independent experiments with eight replicates.

B β-arrestin-recruitment phenotype and with tightly bound β-arrestin (**Fig. 3-8G,H**). The constitutive activity significantly increases from 18.0% for wt to 31.5% for L129Q in the -V2 tail variant, whereas the V2(A)$_6$ variants have comparable constitutive activity values or 17.5% (wt) and 17.8% (L129Q). Therefore, the V2 tail reduces the receptor bias of L129Q away from β-arrestins. We conclude that the receptor bias of the L129Q CAM towards Gq and away from β-arrestins is due to the C-terminal sequence of the receptor.

Why does the enhanced β-arrestin-recruitment not interfere more strongly with the Gq-activation-dependent IP1 accumulation? The binding of β-arrestins with an activated receptor includes two interaction modes, one mode that pre-activates β-arrestin, with interactions only with the phosphorylated tail of the receptor, and a second fully activated mode, with simultaneous interactions with the core and the phosphorylated tail of the receptor blocking G protein signaling (Kang et al., 2015). The recent structure of a GPCR–G protein–β-arrestin megacomplex demonstrates how one receptor can simultaneously interact with a G protein, bound to the transmembrane core, and with β-arrestin, bound to the tail, without blocking G protein signaling (Nguyen et al., 2019).

Based upon the available structural and biochemical data, we conclude that with CysLTR2-L129Q the β-arrestin is unable to compete strongly with the G protein for the core binding site. Even by adding the V2 tail sequence to the mutant, where the β-arrestin is forced to interact strongly with the phosphorylated tail of the receptor, the β-arrestin is unable to simultaneously interact with the core to enter the fully activated mode. This is why a marked decrease in Gq activity is not observed. It is possible that this weak competition with the G protein is due to a receptor core conformation that is incompatible with β-arrestin-binding, but suitable, and even favorable for G protein binding and activation. We speculate that the strong receptor bias of CysLTR2-L129Q towards Gq signaling is due to a selective stabilization of an intermediate state which is partially activated, perhaps facilitated by the L129Q mutation. In the intermediate state, G protein binding is promoted by the open pocket at the core. Catalytic activation of the nucleotide exchange in the G protein only transiently requires a fully active receptor state, whereas the stable interaction of β-arrestins with the receptor core requires a fully active state, consistent with our findings. We plan to investigate further the mechanisms behind the receptor bias in CysLTR2-L129Q.

3.1.5 Data fitting for the IP1 and BRET2 assays

IP1 concentrations or normalized IP1 data were fitted to specific models summarized in **Scheme 3-1** and introduced below.

Sigmoidal dose-response

For the LTD4 dose-response of HEK293T cells transfected with varying amounts of CysLTR2 encoding plasmid DNA, the IP1 concentrations in nM were plotted against the logarithmic concentration of LTD4. These data were first fit to three-parameter sigmoidal dose-response function described below:

$$y = Bottom + \frac{(Top - Bottom)}{1+10^{(logEC_{50}-x)}}$$

The *Bottom* and *Top* parameters describe the lower and upper asymptotic values, respectively. The logarithmic form of the $logEC_{50}$ parameter ensures positive solution for the half maximal effective concentration EC_{50}. Moreover, the logarithmic fitting parameters account for the fact that the solutions for EC_{50} should be log-normally distributed. We use an alternative form for dose-response experiments with competitors or inverse agonists, where the $logIC_{50}$ parameter replaces $logEC_{50}$ and ensures positive fitting solutions for the half maximal inhibitory concentration IC_{50}.

$$y = Bottom + \frac{(Top - Bottom)}{1 + 10^{(x - logIC_{50})}}$$

To account for data sets that show no significant dose-response, we also fit each data set with a horizonal line function as an alternative hypothesis. We chose the best model, either sigmoidal curve or horizontal line, by the Akaike Information Criterion (**Table 3-1A**). Note that the horizontal line fitting function in the GraphPad Prism 8 software has the form $y = \text{Mean} + 0(x)$, since the software requires the use of the independent variable *x*, which is multiplied by zero to negate its influence. Effectively, this fit is a horizontal line plotting the mean IP1 concentrations for all LTD4 doses.

Slack-Hall operational model

In the Slack-Hall model, the basal response is determined by χ and is defined as the ratio of $[R]_t$, the total receptor concentration, and K_e, the receptor concentration producing half-maximal effect in the *absence* of an agonist. The ε parameter measures the *intrinsic efficacy* of the ligand. We slightly modified the original form of this equation to account for fitting problems for χ, the basal response parameter, in cases where the constitutive activity is very low. Taking the *log* τ parameter from the Black-Leff model, we implicitly calculate *log* χ from *log* τ*–log* ε. The final equation of our modified Slack-Hall model is:

$$y = Basal + \frac{E_{max}\left(10^{log\tau - log\varepsilon} + 10^{log\tau + x + logK_A}\right)^n}{\left(10^{log\tau - log\varepsilon} + 10^{log\tau + x + logK_A}\right)^n + \left(1 + 10^{x + logK_A}\right)^n}$$

Table 3-1B shows the parameters for the Slack-Hall operational model fitted to the experiments shown in **Fig. 3-2A,B, 3-8A-D**. In these fits, *x* is the log of the agonist concentration and *y* is the response to the agonist. E_{max}, maximal IP1 concentration for the system, was first fit individually for each condition, and then highest E_{max} value from this was used as a shared, fixed value for all final fits. The parameter *log* K_A is the logarithm of the agonist-receptor association constant, K_A. Note that K_A is the inverse of the dissociation constant K_a. The fitting parameters *log* ε and *log* K_A were shared for all conditions, while *log* τ was left free to give an independent value for each condition. The optimal value and error for *log* χ was separately calculated from the difference *log* τ*–log* ε.

Modeling the time-course of IP1 accumulation using IP1 assays

For the IP1 accumulation time-course (**Fig. 3-1**), the corrected IP1 concentrations, in nM, were plotted against time in minutes. These data are then fitted to a one-phase decay model using the equation,

$$y = (y_0 - Plateau)e^{-kx} + Plateau.$$

Here y_0 is the IP1 concentration at time zero while *Plateau* is the IP1 concentration at infinite time, k is the rate constant of the decay, x is the time of incubation, and y is the IP1 concentration.

Data reduction for BRET2 assays

Two-phase decay model for time-course

For all time-course assays, the BRET2 ratios (y) were plotted against time (x), in seconds, to assess the time-dependence of the LTD4 stimulated β-arrestin recruitment (**Fig. 3-2C, 3-8G,H**). These data were fitted to a two-phase decay model using the equation,

$$y = \begin{cases} \left(-e^{-\left(10^{logk_{fast}}\right)(x-x_0)} + e^{-\left(10^{logk_{slow}}\right)(x-x_0)}\right) \\ \quad \frac{Plateau \cdot 10^{logk_{fast}}}{10^{logK_{fast}} - 10^{logk_{slow}}} + y_0, \text{ for } x > x_0 \\ \\ \qquad\qquad y_0 \text{ otherwise} \end{cases}$$

This model is the sum of two decay processes, one fast and the other slow. The fast process describes the rise of the curve, whereas the slow process determines the subsequent decay. We use logarithmic fitting parameters, $logk_{fast}$ and $logk_{slow}$, to constrain the fitting space to positive values of the rate constants, k_{fast} and k_{slow}, which are rate constants for the two decay processes. The *Plateau* parameter scales the peak height, and y_0 is the β-arrestin recruitment at time zero. k_{fast} describes the initial recruitment of β-arrestin which is dependent on the concentration of active receptor and is represented as the initial increase in signal. k_{slow} describes the disassembly of the receptor–β-arrestin complex and is represented by the decay of the signal over time. For this fit, x_0 and $log\ k_{slow}$ are shared for all three curves (0 nM, 30 nM, and 1000 nM LTD4). The y_0 is determined by first fitting the 0 nM LTD4 curve to a horizontal line, and then using this constant as the fixed y_0 value for the fits of the 30 nM and 1000 nM LTD4 data where $log\ k_{fast}$ is varied independently for each condition. The data for the fits are provided in **Table 3-1C**.

Sigmoidal dose-response and normalization

For the agonist dose-response assays, the BRET2 ratios were plotted against logarithmic concentrations of LTD4 (**Fig. 3-2D, 3-8E,F**). The data were fit to a sigmoidal curve with an alternative model as a horizontal line, $y = Mean + 0(x)$, as described above. **Table 3-1A** summarizes the fitting parameters.

Table 3-1 Parameters obtained from fitting experimental data to pharmacological models
The different models introduced in **Scheme 3-1** were used to fit the experimental data shown in **Fig. 3-2 and 3-8**. (**A**) Parameters for sigmoidal *versus* horizontal line model used in LTD4 dose-response experiments. The horizontal line accounts for data that show no significant dose-response and are represented by Mean, only. The Akaike Information Criterion were used to determine which model fit the data set best (**bold**). (**B**) Parameters for the modified Slack-Hall model. Shared parameters are indicated in respective rows, and E_{max} is fixed for all data sets. The global, fixed E_{max} was determined by first fitting all CysLTR2-GFP10 dose-responses individually to find the largest E_{max} (*). ε and its C.I.s were later calculated from *log* ε fit parameters. (**C**) Parameters for two-phase decay model for the CysLTR2-GFP10 BRET2 time-courses. The time-course for the unstimulated (0 nM) cells were fit to a horizontal line, to determine y_0. This y_0 was used as a fixed value when fitting the stimulated (30, 1000 nM) cells to the two-phase decay model.

Table 3-1A Sigmoidal *versus* horizontal line model

	Bottom	Top	log EC_{50}	Amplitude	Mean	Dof [a]
CysLTR2-GFP10 BRET2 Dose-Response (**Fig. 3-2D**)						
WT	**0.000679 ± 0.000227**	**0.0186 ± 0.0004**	**-7.708 ± 0.043**	**0.0179 ± 0.0004**	0.00698 ± 0.00059	143
L129Q	0.00228 ± 0.0000664	0.00243 ± 0.00019	-7.015 ± 1.978	0.000144 ± 0.000188	**0.00231 ± 0.00005**	95
CysLTR2-V2$(A)_6$-GFP10 BRET2 Dose-Response (**Fig. 3-8E**)						
WT	**0.00165 ± 0.00051**	**0.0143 ± 0.0012**	**-7.305 ± 0.151**	**0.0126 ± 0.0012**	0.00510 ± 0.00057	95
L129Q	0.00391 ± 0.00009	N.C.	N.C.	N.C.	**0.00387 ± 0.00007**	63
CysLTR2-V2-GFP10 BRET2 Dose-Response (**Fig. 3-8F**)						
WT	**0.00874 ± 0.00061**	**0.0374 ± 0.0009**	**-8.031 ± 0.0743**	**0.0286 ± 0.0011**	0.0205 ± 0.0013	95
L129Q	0.0184 ± 0.0002	0.0195 ± 0.0007	-6.894 ± 0.964	0.00106 ± 0.00068	**0.0187 ± 0.0002**	69

Bold = Indicates the parameters of the preferred model (either sigmoidal dose-response or horizontal line). Normal = Parameters of the rejected model.
a) Degrees of Freedom, N.C. = Non-converging

Table 3-1B Slack-Hall operational model

	log K_A	log χ	log ε	Basal	E_{max}	log τ	Dof [a)]	ε
CysLTR2-GFP10 WT (**Fig. 3-2A**)								
11ng		-2.098 ± 0.182				-0.5979 ± 0.01157		
3.6ng		-2.291 ± 0.185				-0.7904 ± 0.01511		
1.21ng		-2.474 ± 0.188				-0.9739 ± 0.02083		
0.4ng		-2.776 ± 0.199				-1.275 ± 0.03822		
0.1ng		-3.106 ± 0.226				-1.605 ± 0.07844		
Global (fixed)					= 1531			
Global (shared)	7.607 ± 0.038		1.501 ± 0.178	33.22 ± 2.88			232	31.70 (95% C.I. 14.19–70.78)
CysLTR2-GFP10-L129Q (**Fig. 3-2B**)								
11ng		-0.658 ± 0.0148				-0.6129 ± 0.0131		
3.6ng		-0.7802 ± 0.0162				-0.7351 ± 0.0146		
1.21ng		-0.9665 ± 0.0197				-0.9214 ± 0.0184		
0.4ng		-1.274 ± 0.032				-1.229 ± 0.031		
0.1ng		-1.656 ± 0.068				-1.610 ± 0.067		
Global (fixed)				= 33.22	= 1531			
Global (shared)	8.955 ± 0.774		0.04507 ± 0.01596				233	1.109 (95% C.I. 1.032–1.192)
CysLTR2-V2$(A)_6$-GFP10 WT (**Fig. 3-8A**)								
11ng		-3.257 ± 0.637				-0.7007 ± 0.0608		
3.6ng		-2.914 ± 0.627				-0.3576 ± 0.0655		
1.21ng		-2.635 ± 0.620				-0.07933 ± 0.07907		
0.4ng		-2.355 ± 0.612				0.2011 ± 0.1027		
0.1ng		-2.182 ± 0.606				0.3744 ± 0.1226		
Global (shared)	7.596 ± 0.069		2.556 ± 0.642	-2.169 ± 7.923	1531 ± 142*		411	359.7 (95% C.I. 19.8–6521.1)
CysLTR2-V2$(A)_6$-GFP10-L129Q (**Fig. 3-8C**)								
11ng		-0.8145 ± 0.0350				-0.7290 ± 0.0358		
3.6ng		-0.4482 ± 0.0228				-0.3627 ± 0.0244		

1.21ng		-0.2283 ± 0.0200			-0.1428 ± 0.0221		
0.4ng		-0.02402 ± 0.01916			0.0615 ± 0.0216		
0.1ng		-0.03373 ± 0.01917			0.05179 ± 0.02163		
Global (fixed)				= 13.44	= 1531		
Global (shared)	8.402 ± 0.562		0.08552 ± 0.01980			410	1.218 (95% C.I. 1.114–1.331)
CysLTR2-V2-GFP10 WT (**Fig. 3-8B**)							
11ng		-3.538 ± 0.305			-1.747 ± 0.113		
3.6ng		-3.129 ± 0.264			-1.338 ± 0.046		
1.21ng		-2.736 ± 0.251			-0.9453 ± 0.0210		
0.4ng		-2.382 ± 0.247			-0.591 ± 0.012		
0.1ng		-2.163 ± 0.246			-0.3724 ± 0.0092		
Global (fixed)					= 1531		
Global (shared)	8.121 ± 0.032		1.791 ± 0.243	1.355 ± 3.069		411	61.80 (95% C.I. 20.64–185.0)
CysLTR2-V2-GFP10-L129Q (**Fig. 3-8D**)							
11ng		-2.119 ± 0.416			-1.855 ± 0.405		
3.6ng		-1.460 ± 0.105			-1.196 ± 0.093		
1.21ng		-1.024 ± 0.050			-0.7589 ± 0.0384		
0.4ng		-0.7854 ± 0.0366			-0.5208 ± 0.0253		
0.1ng		-0.6355 ± 0.0314			-0.3709 ± 0.0203		
Global (fixed)					= 1531		
Global (shared)	8.332 ± 0.109		0.2647 ± 0.0171	13.44 ± 14.51		411	1.840 (95% C.I. 1.703–1.987)

a) Degrees of Freedom, N.C. = Non-converging

* The data for all CysLTR2-GFP10 dose-responses were first fit individually to determine the largest E_{max}, indicated here with the asterisk. All fits to the Slack-Hall model shown in this table share this E_{max} value as a global, fixed value

Table 3-1C Two-phase decay model for time-courses

	y_0	x_0	Plateau	log K_{fast}	log K_{slow}	Dof [a)]	K_{fast}	K_{slow}
CysLTR2-GFP10 BRET2 time-course (**Fig. 3-2C**)								
0 nM*	0.00842 ± 0.00004					551		
30 nM			0.0101 ± 0.0003	-2.373 ± 0.037		1098	0.00424 (95% C.I. 0.00359-0.00501)	
1000 nM			0.0180 ± 0.0004	-1.992 ± 0.042		1098	0.0102 (95% C.I. 0.0084-0.0123)	
Global (fixed)	= 0.00842							
Global (shared)		75.78 ± 5.86			-3.821 ± 0.074			0.000151 (95% C.I. 0.000108-0.000211)
CysLTR2-V2$(A)_6$-GFP10 BRET2 time-course (**Fig. 3-8G**)								
0 nM*	0.00880 ± 0.00004					551		
30 nM			0.00663 ± 0.00027	-2.590 ± 0.035		1098	0.00257 (95% C.I. 0.00220-0.003003)	
1000 nM			0.0118 ± 0.0004	-2.318 ± 0.031		1098	0.00481 (95% C.I. 0.0042-0.0055)	
Global (fixed)	= 0.00880							
Global (shared)		37.90 ± 4.30			-3.957 ± 0.137			1.00 (95% C.I. 0.54-1.85)
CysLTR2-V2-GFP10 BRET2 time-course (**Fig. 3-8H**)								
0 nM*	0.0148 ± 0.0001					551		
30 nM			0.0237 ± 0.0003	-2.471 ± 0.019		1098	0.00338 (95% C.I. 0.00311-0.00368)	
1000 nM			0.0276 ± 0.0002	-1.996 ± 0.0243		1098	0.0101 (95% C.I. 0.0090-0.0113)	
Global (fixed)	= 0.0148							
Global (shared)		32.58 ± 3.45			$-\infty$			0

a) Degrees of Freedom

* These data are fit to a horizontal line, not the two-phase decay model, so the other parameters listed are not applicable.

3.2 Activity-based profiling of *CYSLTR2* in the germline and pan-cancer human variome

3.2.1 The importance of functionally annotating GPCR VUS in cancer

In the previous chapter, we thoroughly characterized the oncogenic driver in UM, CysLTR2-L129Q, and showed that it is a CAM biased towards Gq/11 signaling that recruits β-arrestins very weakly. *CYSLTR2* is significantly mutated in several other cancers, including colorectal adenocarcinoma (COAD) (Wu *et al.*, 2019). It is, however, difficult to assign the role of those *CYSLTR2* variants, as the majority of nonsynonymous *CYSLTR2* mutations are VUS. Molecular tumor diagnostics are rapidly becoming the standard of care in oncology, but the large number of VUS present a challenge for clinical interpretations. The need for high throughput pipelines for assigning functional phenotypes to these VUS so that they can be correlated with disease outcomes is being quickly recognized. For example, earlier work functionally characterized 61 melanocortin 4 receptor (MC4R) variants found in the UK Biobank (Lotta et al., 2019). MC4R is implicated in obesity, and this work identified that GoF mutants were associated with lower BMI and lower odds of developing obesity and type 2 diabetes. Another group conducted a pan-cancer analysis of 20 regulators of G protein signaling (RGS) proteins and found a large subset of LoF variants (DiGiacomo et al., 2020). Following this, our goal is to develop a generalizable and scalable strategy to enable the functional classification of GPCRs, which are exquisitely druggable and actionable targets. By developing a platform to functionally annotate GPCR VUS, we aim to aid association with clinical pathologies and to identify their role in pathogenic pathways to fulfil a critical unmet need. Here, our focus is on *CYSLTR2*, which carries an oncogenic driver mutation in UM but appears to function as a tumor suppressor in other cancers.

3.2.2 Development and optimization of activity-based profiling of *CYSLTR2*

Our goal was to devise a platform which would be scalable and high throughput to allow the functional annotation of *CYSLTR2* VUS and SNP variants. In the development of this platform, we went through four generations of pilot screens, as illustrated in **Fig. 2-1**. In the "First Generation" screen, we identified 120 unique *CYSLTR2* variants from public cancer databases, TCGA and COSMIC, plus four additional germline variants from GPCRdb/ExAC that were located at sites with a high likelihood of functional impact e.g., Na binding sites, microswitch sites, and G protein and β-arrestin interaction sites. The variants were generated by site-directed mutagenesis using the QuikChange Lightning Site-Directed Mutagenesis Kit with a fusion protein of CYSLTR2 and GFP10 with a C-terminal rhodopsin 1D4 epitope tag as the template. Informed by the experience from the first screen, we streamlined the workflow as the "Second Generation" pipeline by using one transfection for both the G protein activation and β-arrestin recruitment assays (**see Methods 2.3.3 for details**). As outlined in **Fig. 2-2**, we updated the protocol such that we can use the same transfection mixture to plate microtiter assay plates used for the BRET2 assay (96-well plates) and the IP1 assay (low volume 384-well plates). This updated workflow is advantageous as we can directly correlate the G protein and β-arrestin recruitment activity and get rid of cell-to-cell variabilities as well as systematic errors in the transfection procedures. We used the Second-Generation workflow to screen 105 variants from ExAC with unknown relevance in cancer, and also to re-screen 28 variants that showed poor

expression in the initial screen (<50% normalized expression). For the re-screen, we made new clones for all variants, which recovered expression in all cases. Since all clones had the correct coding sequence as verified by Sanger sequencing, we concluded that the poorly expressing clones were likely due to sporadic errors introduced into the plasmid backbone by the QuikChange site-directed mutagenesis method.

We followed up with a detailed agonist dose-response for somatic variants that were highly recurrent with three or more recorded cases combined from COSMIC, TCGA and MSK-IMPACT, which have not been observed as germline variants in ExAC/gnomAD or TOPMed (G55E, L129Q, L147Q and E343K). All screens mentioned above were conducted with a construct with a CMV promoter expressing CYSLTR2-GFP10-1D4. For the last generation of optimization, we introduced a doxycycline-inducible expression system to enable controlled expression of a new construct carrying nano luciferase (NLuc) and HaloTag (HT7) as an additional N-terminal fusion (Freundlieb *et al.*, 1999; Machleidt *et al.*, 2015). These allowed for a novel high-throughput capable surface expression assay to be developed using a nanoBRET pulse-chase experiment, where we pulse with a membrane-impermeable fluorescent HaloTag ligand and chase with a permeable, blue-shifted HaloTag ligand.

Our transfection screens use transiently transfected plasmid DNA with human embryonic kidney 293T (HEK293T) cells (**Fig. 2-2**). Our strategy combines transfection and cell plating as a single operation. Briefly, we form complexes of Lipofectamine 2000 with plasmid DNA encoding a subset of CysLTR2 variants together with controls (wildtype, mock, and L129Q), combine them with a defined number of freshly suspended HEK293T cells, and plate the mixtures in the 96- and 384-well microtiter plates for the assays. Detailed methods can be read in the methods section in the previous chapter.

We perform cell-based functional assays previously developed, on each of the 200+ variants in a high throughput manner, to characterize their functional phenotypes (Ceraudo et al., 2021). We measured five different functional readouts, (i) basal Gq signaling, (ii) agonist-dependent Gq-signaling, (iii) basal β-arrestin recruitment, (iv) agonist-dependent β-arrestin recruitment, and (v) receptor protein expression. The CysLTR2-GFP10 fusion construct enables both the β-arrestin recruitment BRET2 assay and the quantification of the receptor expression level by quantifying the GFP10 fluorescence, while leaving the IP1 accumulation unaffected by the C-terminal tags. To determine basal β-arrestin recruitment, we calculated the net BRET2 as the difference of BRET2 ratios for the unstimulated mutant receptor sample and the β-arrestin2-RLuc3-only sample. To determine agonist-dependent β-arrestin recruitment, we calculated the difference of BRET2 ratios with and without agonist stimulation. We then normalize all data to the difference in BRET2 ratio of the agonist-treated WT sample and the β-arrestin2-only sample per assay plate to facilitate comparison with the Gq activation assay. We calculated the basal Gq activation as the difference of the IP1 accumulation in the untreated sample and the sample containing the Gq-inhibitor, YM. Agonist-dependent Gq activation is the difference between IP1 accumulation with and without agonist-stimulation. Again, we normalize all data to the difference of IP1 accumulation of agonist-treated and YM-treated WT samples per assay plate.

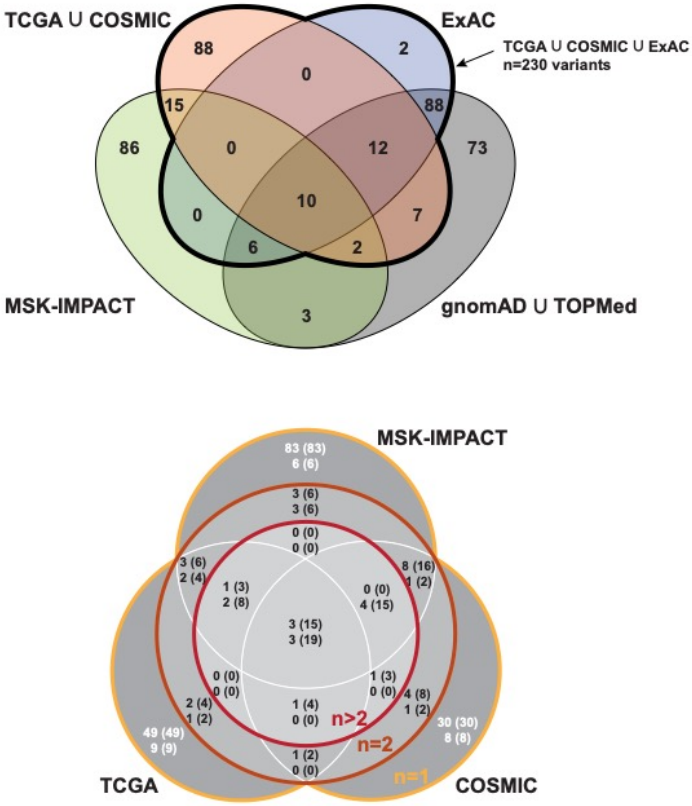

Figure 3-9 Venn diagrams showing the overlaps of variants in the databases used and the number of recurrent VUS cases in the cancer databases

(A) The variants tested were identified from the TCGA, COSMIC, and ExAC databases (orange and blue sectors of Venn diagram, outlined in **bold**). We identified 134 unique *CYSLTR2* variants from the TCGA and COSMIC databases, and 118 in the ExAC database. Of these, 22 were overlapping and found in both sets. Later, additional variants from the MSK-IMPACT (green) and gnomAD and TOPMed (grey) were identified and used in our bioinformatics analysis (**Fig. 3-12**) but not the activity-based profiling (**Fig. 3-10**) so these do not have corresponding phenotypic information. **(B)** The recurrencies for VUS cancer cases were calculated using the three cancer databases, TCGA, COSMIC, and MSK-IMPACT. The outer layer, in yellow, are the number of variants that occurred once (n=1), the mid layer, in orange, are the number of variants that occurred twice (n=2), and the inner layer, in red, are the number of variants that occurred more than twice (n>2). Each sector has a set of four numbers. The numbers on the top are the number of variants only found in somatic mutations and the numbers on the bottom are those with a known SNP. The numbers on the left-hand side are the number of variants and the numbers on the right-hand side, in the parentheses, are the number of cases.

We then compiled the data for all *CYSLTR2* variants that we profiled from both the first- and second-generation screens. The Venn diagrams in **Fig. 3-9** show the overlaps of variants in the databases used and the number of recurrent VUS cases in the cancer databases. The variants tested were identified from the TCGA, COSMIC, and ExAC databases (orange and blue sectors of Venn diagram, outlined in **bold**). We identified 134 unique *CYSLTR2* variants from the TCGA and COSMIC databases, and 118 in the ExAC database. Of these, 22 were overlapping and found in both sets. Later, additional variants from the MSK-IMPACT (green) and gnomAD and TOPMed (grey) were identified and used in our bioinformatics analysis (**Fig. 3-12**) but not the activity-based profiling (**Fig. 3-10**) so these do not have corresponding phenotypic information. The recurrencies for VUS cancer cases were calculated using the three cancer databases, TCGA, COSMIC, and MSK-IMPACT. The outer layer, in yellow, are the number of variants that occurred once (n=1), the mid layer, in orange, are the number of variants that occurred twice (n=2), and the inner layer, in red, are the number of variants that occurred more than twice (n>2). Each sector has a set of four numbers. The numbers on the top are the number of variants only found in somatic mutations and the numbers on the bottom are those with a known SNP. The numbers on the left-hand side are the number of variants and the numbers on the right-hand side, in the parentheses, are the number of cases.

We grouped the *CYSLTR2* variants by the number of VUS cases (n =0, 1, 2 or >2) and sorted the variants by average total signaling, where the basal and agonist-dependent activities of each pathway are added together, and then the mean of these totals are calculated (**Fig. 3-10**). The first column (x_1) shows the total receptor protein expression as measured by GFP10 fluorescence, normalized to WT expression (1, dashed line). The average values across three experimental replicates are shown in the green bars and the average of the technical replicates per experiment are shown in the yellow circles. In the second column, the blue bars and orange circles show the normalized average agonist-dependent β-arrestin recruitment (x_2), and the red bars and green dots show the normalized average agonist-dependent Gq-signaling (x_3). In the third column, we have the blue bars and orange circles showing the normalized average basal β-arrestin recruitment (x_4), and the red bars and green dots showing the normalized average basal Gq-signaling (x_5).

We used a chi-squared test on the four signaling observables (basal and ligand-dependent signaling from Gq and β-arrestin) with a family-wise type 1 error rate of 0.05 to analyze the dataset. The open diamonds (◇) show the -log p values for the null hypothesis (H_0)= wildtype-like and the plus signs (+) show the -log p values for H_0= mock-like. The threshold to reject H_0 is -log p > -log 0.05/214= 3.64 and is depicted as a light blue line. In the circles, we show the phenotype of each variant. First, those that were functionally indistinguishable from mock were designated as “deleterious” LoF phenotype (purple). We then performed a second chi-squared test comparing the four signaling observables plus the expression with wildtype CysLTR2. Using the same family-wise error rate, we identified variants that are indistinguishable from wildtype and designated these as “benign” (green). The remaining variants show an “altered” function (AltF) phenotype and we designate variants with an averaged LTD4-dependent Gq and β-arrestin signaling that is less than 50% as “likely deleterious” (red), and otherwise they are designated as “likely benign” (orange).

Figure 3-10 Activity-based functional profile of 214 CysLTR2 variants
Results from an activity-based profiling of 214 CysLTR2 variants assayed for five functional readouts; (i) total protein expression (x_1, average in green bars, replicates in yellow circles), (ii) agonist-dependent β-arrestin recruitment (x_2, average in blue bars, replicates in orange circles), (iii) agonist-dependent Gq activation (x_3, average in red bars, replicates in green circles), (iv) basal β-arrestin recruitment (x_4, average in blue bars, replicates in orange circles), (v) basal Gq activation (x_5, average in red bars, replicates in green circles). These activities are normalized to the activity of WT (1, dashed lines) and the variants are sorted by average total signaling. We grouped the CysLTR2 variants by the number of VUS cases; **a**, n=0; **b**, n=1; **c**, n=2; **d**, n>2. We used a chi-squared test on the four signaling observables (x_2, x_3, x_4, x_5) with a family-wise type 1 error rate of 0.05 to analyze the dataset. The open diamonds (◇) show the -log p values for the null hypothesis (H_0)= wildtype-like and the plus signs (+) show the -log p values for H_0= mock-like. The threshold to reject H_0 is -log p= 3.64 and is depicted as a light blue line. In the circles, we show the phenotype where those that were functionally indistinguishable from mock were designated as "deleterious" LoF phenotype (purple). We then performed a second chi-squared test comparing the four signaling observables plus the expression with wildtype CysLTR2. Using the same family-wise error rate, we identified variants that are indistinguishable from wildtype and designated these as "benign" (green). The remaining variants show an "altered" function (AltF) phenotype and we designate variants with an averaged LTD4-dependent Gq and β-arrestin signaling that is less than 50% as "likely deleterious" (red), and otherwise they are designated as "likely benign" (orange). The data points are the mean from three or more independent experimental replicates with three to seven technical replicates each.

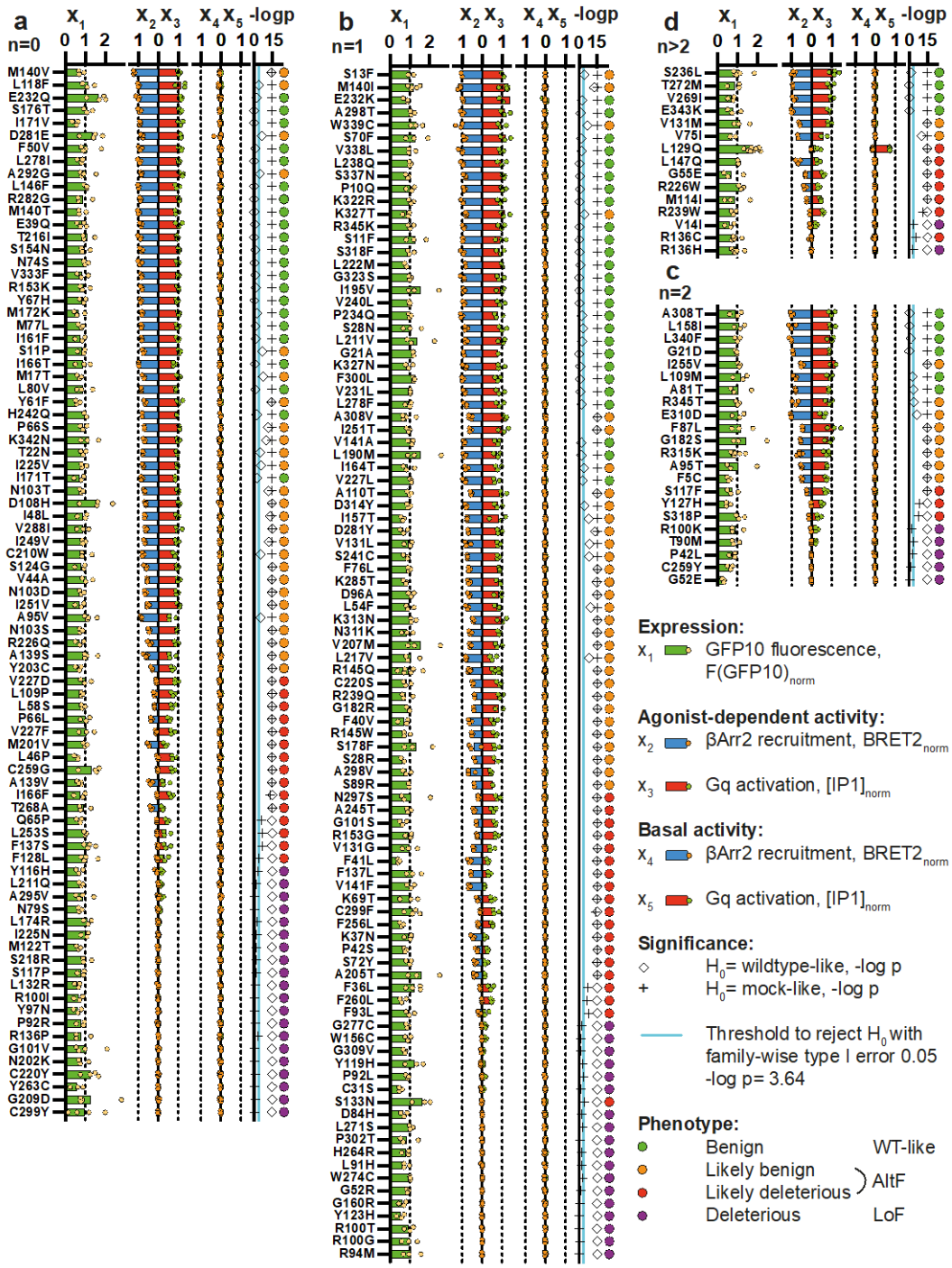
a
n=0
b
n=1
d
n>2
c
n=2
x1
x2 x3
x4 x5
-logp
Expression:
x1 GFP10 fluorescence, F(GFP10)norm
Agonist-dependent activity:
x2 βArr2 recruitment, BRET2norm
x3 Gq activation, [IP1]norm
Basal activity:
x4 βArr2 recruitment, BRET2norm
x5 Gq activation, [IP1]norm
Significance:
H0= wildtype-like, -log p
H0= mock-like, -log p
Threshold to reject H0 with family-wise type I error 0.05
-log p= 3.64
Phenotype:
Benign
Likely benign
Likely deleterious
Deleterious
WT-like
AltF
LoF

Ultimately, we found that the only mutant showing any basal GoF activity is the uveal melanoma, p.L129Q mutant. Furthermore, we calculated that 27% (58 of 214) of variants had benign WT-like phenotype, 21% (45 of 214) were deleterious total LoF phenotype, 52% (111 of 214) showed altered function (21% (44 of 214) were likely deleterious with < 50% WT signaling activity and 31% (67 of 214) were likely benign, with > 50% activity). Taking this together it seems that ~42% of variants tested showed a deleterious phenotype. In other words, a large portion of non-L129Q missense variants of CysLTR2 have a LoF phenotype. What was further surprising was that this distribution was the same in all four groups of variants with VUS cases (n =0, 1, 2 or >2). This suggests that the large fraction of variants that showed a LoF phenotype was not unique to those with recurrent VUS cases, nor were they enhanced in these groups. These data also suggest that recurrency of VUS cases does not necessarily correlate to a deleterious phenotype. On the flipside, the data also suggest that the assumption that germline variants, variants that have n=0 VUS, are benign is not accurate, as we see an equal share of deleterious phenotypes in this group as well.

3.2.3 Prediction of deleterious variants without functional data does not capture the full picture

With our large functional data set, we have shown that it is difficult to reliably predict the phenotype of a variant in a GPCR. For example, PolyPhen2 has at best about 77% accuracy when comparing its benign or deleterious classification of variants with either more or less than 50% of wildtype activity in the functional assays. The performance is worse trying to predict the severe LoF variants. The location of the mutation in the 3D structural elements of CysLTR2, like functional microdomains or binding-sites for ligand, G protein, or β-arrestin as inferred from the X-ray structure of CysLTR2 in complex with small-molecule antagonists or from X-ray or cryo-EM structures of homologous GPCR in complex with G proteins or β-arrestins, also only incompletely predict residues vulnerable to mutations (Gusach *et al.*, 2019b).

In **Figure 3-11A**, we show a snake plot of CysLTR2 annotated with the functional phenotype from our activity-based profiling screen. We grouped the variants according to their phenotype using the chi-squared test on the four signaling observables (basal and ligand-dependent signaling from Gq and β-arrestin) from the activity-based profiling of CysLTR2 variants, with a family-wise type 1 error rate of 0.05. As before, those that were functionally indistinguishable from mock were designated as “deleterious” LoF phenotype (purple), variants that are indistinguishable from wildtype were designated as “benign” (green) and the remaining variants were designated as AltF phenotype. Variants with an averaged LTD4-dependent Gq and β-arrestin signaling that is less than 50% are designated “likely deleterious” (red), and otherwise they are designated as “likely benign” (orange). In **Figure 3-11B**, we show a snake plot of CysLTR2 annotated with known interacting sites, where interactions are defined as residues that are <3.9 Å of the interacting partner in complex with CysLTR2. Ligand-interacting sites (orange) were obtained from the recent structure of CysLTR2 in complex with ONO-2570366, an antagonist for CysLTR1 and CysLTR2 (Gusach *et al.*, 2019b). Arrestin binding sites (red) were obtained from neurotensin receptor type 1 in complex with β-arrestin1 (Huang *et al.*, 2020), muscarinic acetylcholine receptor M_2 in complex with β-arrestin1 (Staus *et al.*, 2020), β-1 adrenergic receptor in complex with β-arrestin1 (Lee *et al.*, 2020), and rhodopsin in complex with visual arrestin (Zhou *et al.*, 2017a). G protein binding sites (blue) were obtained from structures of receptors in complex with Gq proteins. These receptors were the 5-HT_{2A} receptor (Kim *et al.*, 2020), histamine H1 receptor (Xia *et al.*, 2021), muscarinic acetylcholine receptor

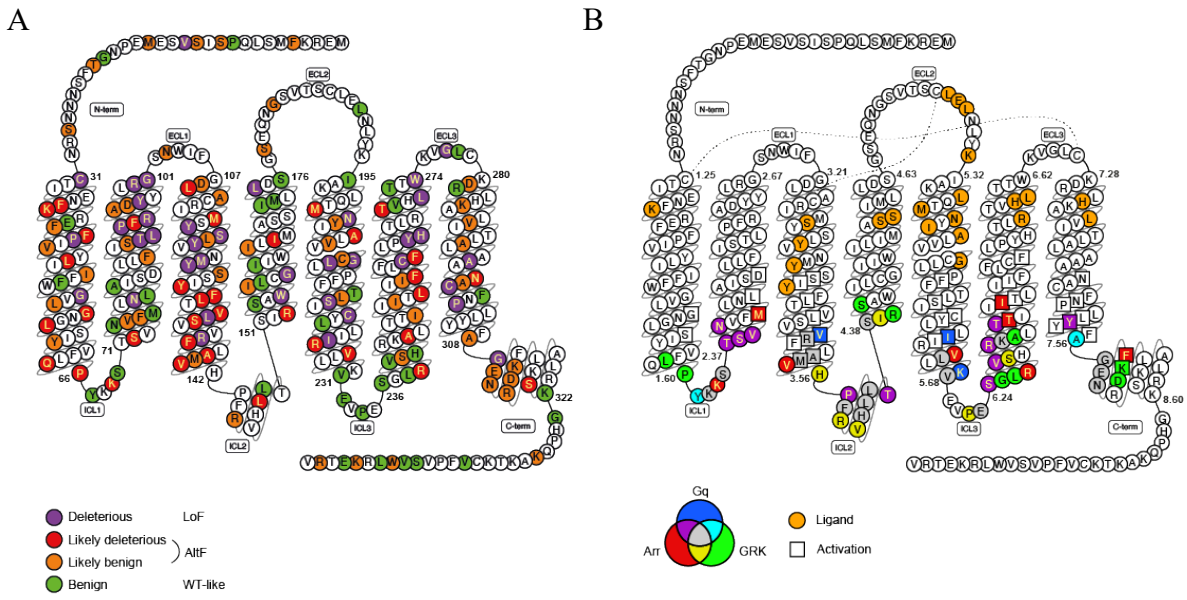

Figure 3-11 Functional sites on CysLTR2 annotated on 2D snake plots
(A) Snake plot of CysLTR2 annotated with the functional phenotype from activity-based profiling. We grouped the variants according to their phenotype using the chi-squared test on the four signaling observables in the activity-based profiling of CysLTR2 variants (**Fig. 3-10**), with a family-wise type 1 error rate of 0.05. Those that were functionally indistinguishable from mock were designated as "deleterious" LoF phenotype (purple), those indistinguishable from wildtype and designated these as "benign" (green). The remaining variants show AltF phenotype and we designate variants with an averaged LTD4-dependent Gq and β-arrestin signaling that is less than 50% as "likely deleterious" (red), and otherwise they are designated as "likely benign" (orange). **(B)** Snake plot annotated with known interaction sites. All interactions are defined as residues that are <3.9 Å of the interacting partner in complex with CysLTR2. Ligand-interacting sites (orange) were obtained from the recent structure of CysLTR2 in complex with ONO-2570366 (Gusach *et al.*, 2019b). Arrestin binding sites (red), G protein binding sites (blue), G protein kinase (GRK) binding sites (green), were all obtained from structures of GPCRs in complex with arrestins, Gq/11 proteins, or GRKs. Those residues that are involved in interactions with more than one interactor are colored in the overlapping colors shown in the Venn diagram. Lastly, activation sites (square) were taken from work by Zhou et al., which determined the existence of a common activation pathway across class A GPCRs, connecting well-known motifs like the Na^+ pocket, NPXXY and DRY, from the extracellular side to the intracellular side (Zhou *et al.*, 2019).

M1 (Maeda *et al.*, 2019), and cholecystokinin A receptor (Mobbs *et al.*, 2021). G protein kinase (GRK) binding sites (green) were obtained from the recent structure of rhodopsin kinase (GRK1) in complex with rhodopsin (Chen *et al.*, 2021). Those residues that are involved in interactions with more than one interactor are colored in the overlapping colors shown in the Venn diagram. Lastly, activation sites (square) were taken from work by Zhou et al., which analyzed 234 structures of 45 class A GPCRs and determined the existence of a common activation pathway across class A GPCRs (Zhou *et al.*, 2019). The pathway is comprised of 34 residue pairs (formed by 35 residues), which connect several well-known motifs like the Na^+ pocket, NPXXY and DRY, from the extracellular side to the intracellular side. All corresponding sites in the helices were assigned to the structure of CysLTR2 based on generic numbering positions as described in the GPCRdb. For sites in segments that did not have generic residue number positions, we used class-specific multiple sequence alignments to designate the appropriate corresponding residues in CysLTR2.

Comparing these two snake plots, we see that some deleterious sites are in functionally important sites, such as ligand-binding sites (e.g., Y119, Y123, G160, N202, L271), activation sites (e.g., L132, S218, I225, P302), or those involved in all three (Gq, arrestin, and GRK) interaction sites like R136 and G309. However, other than these, the deleterious sites are mostly in sites that are not functionally important. In fact, of the ~70 residues that show a LoF or AltF phenotype (less than 50% activity) only about 40% (30 of 73) occurred in known interface and functional sites. The other ~60% (43 of 73) were found in previously unknown or unpredicted sites, in areas that have not been known to be necessary for CysLTR2 function, highlighting the need for phenotypic evaluation of GPCR VUS and SNPs in human cancers.

3.2.4 Frequency distributions and phenotypes of *CYSLTR2* variants

Intrigued by our findings that some recurrent mutations had a benign phenotype and that recurrency was not a good predictor of function, we focused our attention to the mutational signatures for each variant. One of the major insights derived from the cancer genome project was the identification of mutational signatures characteristic for selected cancer types (Alexandrov et al., 2020; Alexandrov et al., 2013a; Alexandrov et al., 2013b). There a six subtypes of single base substitutions (SBS), C:G>A:T, C:G>G:C, C:G>T:A, T:A>A:T, T:A>C:G, and T:A>G:C. They are usually abbreviated to the pyrimidine of the mutated Watson-Crick base pair, C>A, C>G, C>T, T>A, T>C, and T>G. For example, C>T substitutions are most frequent due to endogenous mutational processes and carry a clock-like signature. The different mutational processes strongly depend on the flanking nucleotides immediately 5' and 3' of each mutated base. Therefore, it is customary to denote the nucleotide context of a SBS, for example, "ACG>ATG" is represented as "A[C>T]G" or as "C>T at ACG" to aid graphical representation. There are 96 SBS types considering such triplets.

Recurrency of VUS in cancer genomes could arise for two reasons. The first could indicate that this position is a particularly vulnerable site for mutations to occur, leading to frequent base changes. This does not necessarily correlate with a disease-causing mutation. The second possibility is that the mutation is recurrent due to its phenotype, which has a high biological fitness for tumor formation. To better understand which of these categories the recurrent *CYSLTR2* VUS fell in, we analyzed the relevance of the mutational signatures in the

CYSLTR2 variants. The two-dimensional map in **Figure 3-12** shows the location of each variant sorted according to its SBS type. All possible single base substitutions in the *CYSLTR2* coding sequence (CDS) were enumerated and the base positions of each variant are shown on the y-axis. On the x-axis, we show the number of MV observed as germline or somatic variants (black bars) and those that are not observed in the databases as of now (light grey bars). The data are divided into the six subtypes of SBS, abbreviated as C>A, C>G, C>T, T>A, T>C, and T>G. Within each subtype, there are 16 SBS when accounting for the flanking nucleotides on the 5' and 3' end, which are shown within the larger bracket of the six main subtypes. Each symbol is labeled with the encoding protein variant and its size is proportional to the number of somatic cases of a particular variant. The color corresponds to the functional phenotype from our screen (purple, deleterious, LoF; green, benign, WT-like; orange, likely benign, AltF; red, likely deleterious; AltF, white, new variant without functional data). White circles with italicized label are novel germline variants without functional phenotype. Unlabeled dots are variants currently not observed. Furthermore, the cancer case counts, N(cancer cases), for somatic variants and the allele counts, N(alleles), for germline variants are projected as a function of the amino acid (AA) residue as plots parallel to the ordinate. The thresholds separate AA residues with more than 2 cancer cases or 100 alleles, respectively. The total number of cancer cases used for the analysis is about 20,000. The allele count corresponds to the number of carriers in germline sequences from about 200,000 individuals. Note that the allele count is shown on a log scale. The results illustrate that many observed variants have C>T type SBS, including the most highly recurrent T272M with a benign phenotype at a ACG triplet with the A[C>T]G type SBS.

The results illustrate that many observed variants have the C>T type SBS, including the most highly recurrent variant, T272M. This variant has a benign phenotype and a mutation in the ACG triplet with the A[C>T]G type SBS. All other possible variants with the A[C>T]G SBS are present in our dataset, which indicates a sufficient sample size for this SBS. From this result, it seems that recurrent variants with benign or WT-like phenotypes are due to high mutation rates of functionally unimportant sites, as we had predicted. However, other than this SBS, we noticed that many other SBS types have few or no observed cases, which prompted us to predict the mutation frequencies.

Analysis of a large number of mutations from ~7000 cancers has shown that there is a high overlap of mutational signatures for different cancer types (Alexandrov *et al.*, 2020). We calculated the raw frequency distribution of SBS types from the COSMIC mutation dataset, normalized them to the frequency distribution of nucleotide triplets in the human genome, and calculated the expected frequency for each of 2269 total missense variants of *CYSLTR2* (**Fig. 3-13**). The first sixteen variants have an expected frequency of about 1%, that is, there is a one in one hundred chance of observing these variants when observing any MV for this gene. Most of them were observed more than once as somatic case, except for one that was only observed as a germline variant. The remaining variants are in the "long tail" of the distribution, starting at about 0.2% and ending at about 0.01%. A distribution with a long tail has a tail that tapers off gradually, instead of a sharp drop and this tail contains occurrences far from the "head" or the central part of the distribution. Interestingly, there are many more germline variants in the long tail, which suggests that the mutational processes in cancer do not reliably predict their occurrence. We used a Poisson distribution to calculate the negative decadic logarithm of the probability (-log p) of observing the particular number of cases for one variant, given the

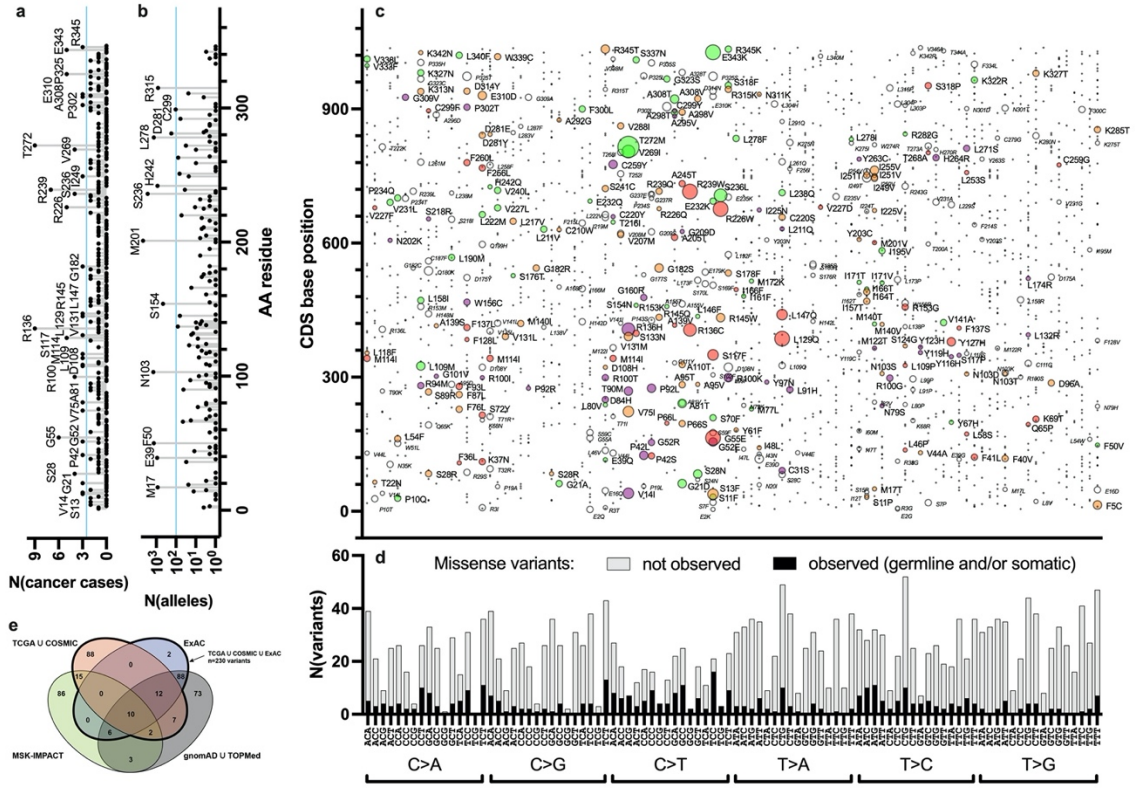

Figure 3-12 Landscape of nonsynonymous *CYSLTR2* variants

In this two-dimensional map, all possible single base substitutions (SBS) in the *CYSLTR2* coding sequence (CDS) were enumerated, and the base positions of each variant are shown on the y-axis. The variants are sorted in the six main SBS subtypes in the x-axis (C>A, C>G, C>T, T>A, T>C, and T>G). We show the cancer case counts, N(cancer cases) **(a)**, for somatic variants and the allele counts, N(alleles) **(b)**, for germline variants are projected as a function of the amino acid (AA) residue as plots parallel to the ordinate. The thresholds separate AA residues with more than two cancer cases or 100 alleles, respectively. The total number of cancer cases used for the analysis is about 20,000. The allele count corresponds to the number of carriers in germline sequences from about 200,000 individuals and is shown on a log scale. In the 2D map in **(c)**, each symbol is labeled with the encoding protein variant and its size is proportional to the number of somatic cases of a particular variant. The color corresponds to the functional phenotype from our screen (purple, LoF; green, benign, WT-like; orange, AltF, likely benign; red, AltF, likely deleterious; white, new variant without functional data). In **(d)**, we list the 16 SBS that arise when accounting for the flanking nucleotides within the larger brackets of the main subtypes. For each of the 96 SBS, we show the number of missense variants (MVs) observed as germline or somatic variants (black bars) and those that are not observed in the databases as of now (light grey bars). The results illustrate that many observed variants have C>T type SBS, including the most highly recurrent p.T272M with a benign phenotype. **(e)** The variants tested were identified from the TCGA, COSMIC, and ExAC databases (orange and blue sectors of Venn diagram, outlined in bold). Later, additional variants from the MSK-IMPACT (green) and gnomAD and TOPMed (grey) were identified and used in our bioinformatics analysis but not the activity-based profiling (**Fig. 3-10**) so these do not have corresponding phenotypic information.

Figure 3-13 Development of frequencies of recurrent *CYSLTR2* variants and their significances

(a) This graph depicts the normalized expected frequency distribution of each SBS type from the COSMIC dataset. They are normalized to the frequency of each trinucleotide triplet in the human genome to get a percentage frequency. We then used this to calculate the expected frequency for each of the 2269 missense variants (MV) of *CYSLTR2*. **(b)** The number of cancer cases found for each MV in the COSMIC database, where each variant is annotated with the functional phenotype from our screen (purple, LoF; green, benign, WT-like; orange, likely benign; red, likely deleterious), is shown here. **(c)** We depict the negative decadic logarithm of the probability (-log p) using the Poisson distribution for observing a particular number of cases for one variant, given the expected frequencies multiplied by 297 cases total. The blue line indicates the significance threshold using a family-wise type 1 error rate of 0.05. Four recurrent variants stand out in our pan-cancer significance analysis, G55E, L129Q, L147Q and E343K. The magenta line indicates an error rate of 0.05 without multiple comparisons correction, and indicates that number of hits is much larger, with essentially all of the recurrent variants in the long tail reaching the threshold. **(d)** Recurrently mutated residues at the amino acid level were calculated by summing the *CYSLTR2* variants that occurred at the same position. Some residues had multiple variants occurring at that position (N(cases), **(e)**), but after all calculations were complete, the results suggest that the overall significances (-log p, **(d)**) in the recurrency are similar to the results in **(c)** when looking at the recurrency of variants at the DNA level. We depict the annotated C-terminal tail of CysLTR2 in **(f)**, with the partial long β-arrestin code from residue 337 to 344, and the PDZ ligand motif from residue 343 to 346. There are two kinases that phosphorylate the C-terminal tail of CysLTR2 at S337 and T344. Lastly, in **(g)** we show all PDZ ligands that bind to CysLTR2 WT and mutants at the C-terminal tail. In particular, we see that the recurrent mutant E343K loses interactions with many of the interacting partners.

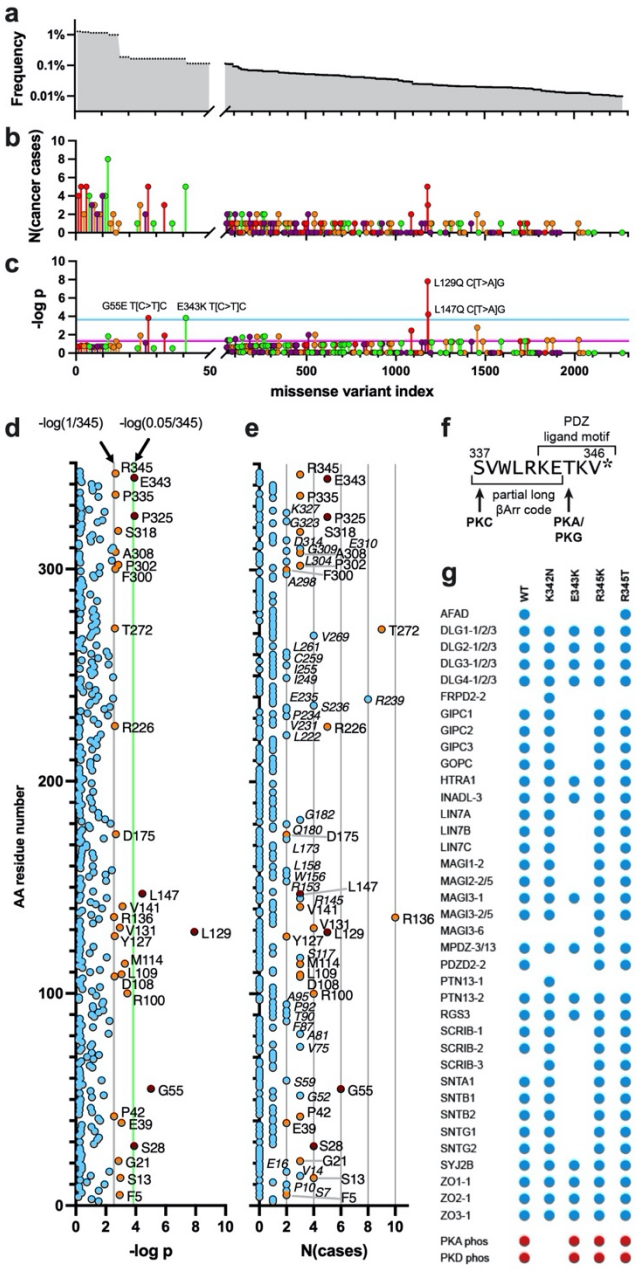
a
Frequency
1%
0.1%
0.01%
b
N(cancer cases)
c
-log p
G55E T[C>T]C
E343K T[C>T]C
L129Q C[T>A]G
L147Q C[T>A]G
missense variant index
d
-log(1/345)
-log(0.05/345)
AA residue number
-log p
e
N(cases)
f
PDZ
ligand motif
337
346
SVWLRKETKV*
partial long
βArr code
PKC
PKA/
PKG
g
WT
K342N
E343K
R345K
R345T
AFAD
DLG1-1/2/3
DLG2-1/2/3
DLG3-1/2/3
DLG4-1/2/3
FRPD2-2
GIPC1
GIPC2
GIPC3
GOPC
HTRA1
INADL-3
LIN7A
LIN7B
LIN7C
MAGI1-2
MAGI2-2/5
MAGI3-1
MAGI3-2/5
MAGI3-6
MPDZ-3/13
PDZD2-2
PTN13-1
PTN13-2
RGS3
SCRIB-1
SCRIB-2
SCRIB-3
SNTA1
SNTB1
SNTB2
SNTG1
SNTG2
SYJ2B
ZO1-1
ZO2-1
ZO3-1
PKA phos
PKD phos

expected frequencies multiplied by 297 cases total. The blue line indicates the significance threshold using a family-wise type 1 error rate of 0.05. Four recurrent variants stand out in our pan-cancer significance analysis, G55E, L129Q, L147Q and E343K. The enriched variants L129Q and L147Q have C[T>A]G mutation type, and variants G55E and E343K have G[C>T]G mutation type (**Fig. 3-13**). From this, we hypothesize these mutations carry a significance in our receptor of interest.

3.2.5 Agonist dose-response and surface expression experiments of recurrent variants

Looking at the phenotypes of the four recurrent mutants (G55E, L129Q, L147Q, and E343K) in **Figure 3-13**, it seems that they lose the agonist-depended β-arrestin recruitment activity before losing the Gq activity. Many of the impaired variants show a modest Gq activity while showing virtually no β-arrestin recruitment activity. We must point out, however, that due to the conditions used in our workflow, it is difficult to conclude that these variants are biased towards the G protein or β-arrestin pathways. During the first and second-generation screens, we used different concentrations of LTD4 for the HTRF IP1 assay and the β-arrestin recruitment BRET2 assay. In the IP1 assay, we were interested in looking for changes in the EC_{50}, so to get the most sensitivity, a concentration of 100 nM of LTD4 was employed for the workflow. In the BRET2 assay, however, we were more interested in seeing if there is an interaction with β-arrestin or not, so we used 1 μM of LTD4, which was at saturation and gave maximum coupling. With only one concentration of agonist, it is impossible to tell whether the shifts we are seeing are due to a shift in potency (EC_{50}) or efficacy (max IP1 or BRET2 ratio) and therefore, we cannot quantitatively conclude that the receptors show bias towards one pathway over the other. To address this question and get the full pharmacological effects of these mutations, a full LTD4-dose response of both assays is required.

On the other hand, one hypothesis for a loss of β-arrestin recruitment is lack of plasma membrane localization of the receptor. Perhaps these mutations were impairing the receptor variants' ability to fold correctly and make it to the plasma membrane at the cell surface. As GRKs act at the plasma membrane, these receptors may not get phosphorylated and therefore remain unable to recruit β-arrestin. Moreover, G proteins are present and able to be activated intracellularly, further adding to the G protein bias of these mutants. To explore this theory, we decided to develop another assay that can be added to this multi-assay workflow, which would allow us to distinguish receptors at the cell surface versus receptors inside the cell. To assay for surface expression of receptors, others have used enzyme-linked immunosorbent assay (ELISA) assays, but we wanted to develop an assay in which we can quantify the percentage of receptors at the cell surface, rather than simply getting a value of how much receptor there is at the surface. We decided to employ a BRET-based assay that uses nanoLuciferase (nLuc) (Machleidt *et al.*, 2015). Our BRET2 assay suffers from limited sensitivity and dynamic range, but nLuc is extremely bright with a narrow spectrum (λ_{max} ~ 460 nm) and is very small (19 kDa). By combining this with an efficient red-emitting fluorophore, attached to the receptor by a HaloTag, we believe the improved spectral resolution will lead to improved sensitivity and robustness of the assay. To this end, we attached a nLuc and a HaloTag, HT7, as well as several other epitope tags, to the extracellular side of the receptor. As described in **chapter 2.6**, we developed a pulse-chase assay, in which we first label all cell surface receptors with a cell impermeable HaloTag Ligand AlexaFluor 660 (λ_{max} ~ 690 nm), and follow, or chase, with a cell permeable HaloTag Ligand nanoBRET 618 (λ_{max} ~ 620 nm), which would label all remaining receptors.

We characterized these variants by detailed agonist dose-response and surface expression experiments (**Figure 3-14**). L129Q is the oncogenic driver in UM with a GoF in basal signaling biased towards Gq, reduced surface expression, and minimal agonist- dependent signaling. The L129Q mutant shows strikingly low surface expression, under 10%, as compared to ~36% for the WT. This suggests that L129Q may be signaling through Gq and generating IP3 intracellularly, without ever reaching the cell membrane. As L129Q is a CAM, no extracellular agonist ligand is needed for signaling. Previously, we had believed that the L129Q mutant was reaching the surface, but due to its very low β-arrestin recruitment, it was unable to get desensitized and downregulated. However, from these results it seems more likely that the L129Q mutant never actually reaches the cells surface, and much of its signaling occurs intracellularly.

G55E shows a dramatic loss in efficacy of β-arrestin recruitment while retaining high abundance of surface receptors. The maximal BRET2 ratio is 0.015 as compared to 0.025 for WT and there is a decrease in potency as indicated by the right shift of the EC_{50} as well (orange line). For the IP1 accumulation, there is a reduction in potency with no change in efficacy. G55E is not in a functionally important site, but our results indicate that a mutation in this site impairs β-arrestin recruitment while affecting Gq activity to a lesser extent. Furthermore, the reduction in β-arrestin recruitment cannot be attributed to the lack of receptors at the plasma membrane.

The L147Q variant causes decrease in potency, as well as a marked decrease in maximal IP1 accumulation and BRET2 ratio (pink line). Interestingly, L147Q has the highest percentage of surface expression at about 45%. L147Q is in TM2, at the interface of the G protein and β-arrestin binding site. As the mutation is most likely interfering with recognition of G protein and β-arrestin, the reduction in both potency and efficacy can be explained.

Lastly, E343K has an interesting phenotype, where the IP1 accumulation is virtually unchanged, and the dose-response curve is very similar to that of the WT, but there is a modest gain in beta-arrestin recruitment (red line). The BRET2 ratio is 0.030 compared to 0.025 for WT, indicating a GoF in the β-arrestin recruitment. Despite wildtype-like functionality in our signaling assay, the E343K variant is likely deleterious, since the mutation affects the C-terminal pentapeptide that is a PDZ ligand as shown in **Figure 3-13G** (Marchese et al., 2008), which confers interaction with several PDZ proteins, CASK, DLG1, LIN7C, MPP7, and PLD3 as a non-PDZ protein (Camp et al., 2015). Bioinformatics tools enable the prediction of PDZ interaction partners (Kundu et al., 2014), and the E343K variants is predicted to abolish interaction with LIN7C, which in turn will result in a loss of the LIN7C-mediated interaction with CASK, a calcium/calmodulin-dependent serine protein kinase (Hata et al., 1996). This is currently being investigated through reporter assays using a plasmid with the native C-terminal, lacking the GFP10-1D4 tags.

In addition, when we apply a threshold indicated by the magenta line set at an error rate of 0.05 without multiple comparisons correction, the results indicate that number of hits is much larger with essentially all the recurrent variants in the long tail reaching the threshold and the single observed cases at the end of the tail also crossing the threshold. This suggests that we should repeat the in-depth functional validation assays for these variants as well.

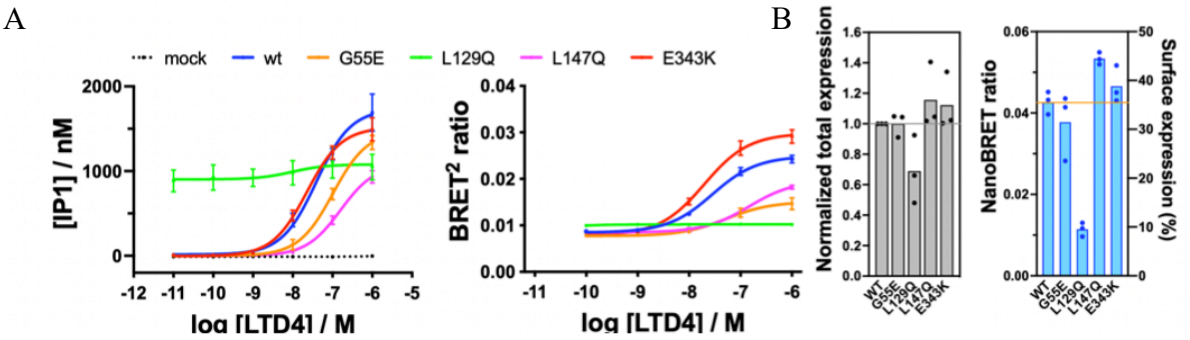

Figure 3-14 Functional validation assays of the four recurrent *CYSLTR2* variants
(A) The four recurrent variants that stood out in our pan-cancer significance analysis, G55E, L129Q, L147Q and E343K, as well as WT were characterized in a detailed agonist dose-response assay. The dose-response curves on the left show the LTD4 dose-dependent IP1 accumulation while those on the right show the β-arrestin recruitment. L147Q (pink) and G55E (orange) show slightly decreased Gq activation and β-arrestin recruitment compared to the WT (blue). The uveal melanoma mutant, L129Q (green), shows basal signaling biased towards Gq and minimal agonist-dependent signaling. E343K (red) suggests a WT-like phenotype and even a slight GoF in the β-arrestin recruitment. The data points are mean±SEM from three independent experiments with three to seven technical replicates each. **(B)** The four recurrent variants plus WT were also characterized in a pulse-chase nanoBRET surface expression experiment. The bars on the left (grey) show total receptor expression as quantified by the total luminescence from nLuc conjugated to each variant. The bars on the right (blue) show the nanoBRET ratio, which can be converted into percentage of surface expression (**Fig. 2-4**). All variants showed a similar surface expression of about 35-45%, except for L129Q, which had a surface expression of about 10%. The data points are mean±SEM from three independent experiments with three technical replicates each.

3.2.6 Third-generation workflow

We wish to deploy our streamlined pipeline for activity-based profiling to characterize the remaining 200 novel *CYSLTR2* variants observed in the MSK-IMPACT, gnomAD and TOPMed cohorts and to add any additional ones from the UK Biobank (**Fig. 3-9A**). We want to identify all carriers of variants with LoF phenotype, either in the germline or as somatic mutations, and correlate the associated pathologies, and test the clinical significance of a LoF phenotype in comparison with matched controls.

In the third-generation screen, we will use the doxycycline-inducible construct with extracellular NLuc and HT7, as well as the original C-terminal GFP-10 and 1D4 (FLAG-OLLAS-NLuc-HT7-CysLTR2-GFP10-1D4). Briefly, we decided to switch our constructs from the constitutive cytomegalovirus (CMV) promoter in the pcDNA to an inducible system, to allow for more controlled expression of the receptors. In this construct, we decided to use the tetracycline-responsive element (TRE) promoter, which is regulated by a class of transcription factors that are activated tetracycline or its analogs (Freundlieb *et al.*, 1999). In this system, we use a combination of the Tet-Off and Tet-On technologies to prevent any leaky expression and allow for precise control of our expression. The Tet-Off system utilizes the tetracycline transcriptional silencer (tTS), which binds to the TRE promoter to suppress gene transcription. Upon addition of tetracycline, this is released from the DNA to allow transcription to begin. On the other hand, the Tet-On system utilizes the reverse tetracycline responsive transcriptional activator M2 (rtTA), which is a transcriptional activator that binds to the TRE promoter in a doxycycline-dependent manner. In the past, some groups reported that some cell lines showed constitutive activity when just using the Tet-On system. However, by combining the transcriptional repressor and activator, we can prevent leaky activity and have the utmost control and sensitivity to tetracycline addition in this two-step initiation of transcription. This system is compatible with highly toxic proteins. Cytotoxicity can lead to a lot more variability in expression and activity, and carefully controlling the transcription and expression times is crucial if we were to work with such proteins in the future.

In preliminary experiments, we tested the expression and compatibility with the IP1 accumulation assay and the BRET2 β-arrestin recruitment assay of WT CysLTR2 in the doxycycline-inducible construct. One of the advantages of using this construct is that we are able to run a "two-dimensional dose response assay". The two dimensions are the doxycycline-dose, which should control the receptor expression in a dose-dependent manner, and the LTD4-dose, which should control the β-arrestin recruitment or IP1 accumulation in a dose-dependent manner (**Fig. 3-15**). These experiments confirmed that the expression was exquisitely controlled by doxycycline concentration, as expected, and that the plasmid is compatible with our previously developed assays with no artefacts caused by the extracellular tags and the change to the doxycycline-inducible system. Furthermore, it is possible to correlate receptor expression and G protein activity or β-arrestin recruitment in a more controlled manner. This is useful in calculating constitutive activity using the operational models and fits introduced in **chapter 3.1.3** and may be an improved way to calculate this for future receptors and variants.

The third-generation screen will be informed from our previous screens and will be developed upon the second-generation workflow with the combined transfection. On top of this,

the agonist-dose responses have shown the importance of surveying the G-protein activity and β-arrestin recruitment at several agonist doses to get a better idea of changes in potency and efficacy of the variants. As the nanoBRET based cell surface expression assay we have developed is easily scalable and has high throughput capability, we believe it can be easily incorporated into the single transfection workflow. Putting this all together, the third-generation screen will have a single transfection of the doxycycline-inducible construct to combine the nanoBRET surface expression assay and the IP1 accumulation and BRET2 β-arrestin recruitment assays at four concentrations of LTD4 (0, 10, 100, and 1000 nM). We will use this to probe variations in the fraction of receptors at the cell surface as well as changes in G-protein and β-arrestin activity of the remaining 200 novel *CYSLTR2* variants observed in the additional cancer databases.

3.2.7 The tumor suppressive mechanism of *CYSLTR2* and the role of LTC4

To our surprise, we found that the recurrent *CYSLTR2* variant, L129Q, observed in UM is the only GoF phenotype and most other cancer types carry a substantial fraction of LoF variants. We found that about 20% of MVs show no detectable activity. About ten percent are nonsense and frameshift variants, so we find that about 30% of somatic mutations of *CYSLTR2* have a LoF phenotype, which points to a tumor suppressor function following the famous "20/20" rule (Vogelstein et al., 2013). As mentioned in the introduction, *CYSLTR2* expression was found to be a good prognostic factor in breast cancer and COAD, but the mechanisms are poorly understood (Magnusson *et al.*, 2007; Magnusson *et al.*, 2011). We had previously noticed that the samples expressing CysLTR2-GFP10-L129Q showed larger GFP10 fluorescence as compared to samples expressing CysLTR2-GFP10 WT, which corresponds to higher levels of expression when transfecting the same amounts of plasmid DNA into HEK293T cells (**Fig. 3-5**). We conducted a separate flow cytometry analysis with increasing gene dosages of CysLTR2-GFP10 WT and -L129Q encoding plasmid and observed the GFP10 fluorescence as well as cell death by propidium iodide (PI)-staining (**Fig. 3-16**). This showed an increasing degree of cell death for the cells transfected with the oncogenic CAM. It seems that L129Q induces apoptosis in a substantial fraction of HEK293T cells after about one day, which is the opposite of the strongly proliferative effect on melanocytes. Intrigued by these observations, we asked the question if programmed cell death due to activation of CysLTR2 could play a role in as a tumor suppressive mechanism, which would give LoF variants of *CYSLTR2* a driver role in the etiology of some cancers?

We propose a new model that reconciles the existing literature and supports the notion of a tumor suppressor function of *CYSLTR2*. The key connector is the identification of LTC4 signaling through CysLTR1 and CysLTR2 as the major trigger of endoplasmic reticulum (ER) stress-induced oxidative DNA damage and cell death (Dvash et al., 2015). ER stress and the unfolded protein response (UPR) are part of a network of signaling pathways called the integrated stress response (ISR) (Pakos-Zebrucka et al., 2016; Wang and Kaufman, 2014). In cancer, the IRS can be activated by oncogene signaling, hypoxia, nutrient starvation, and acidosis, which lead to adaptive responses as well as LTC4 formation and apoptosis (Denoyelle et al., 2006; Liu et al., 2008). Moreover, LTC4 released from the stressed cancer cells will signal

A

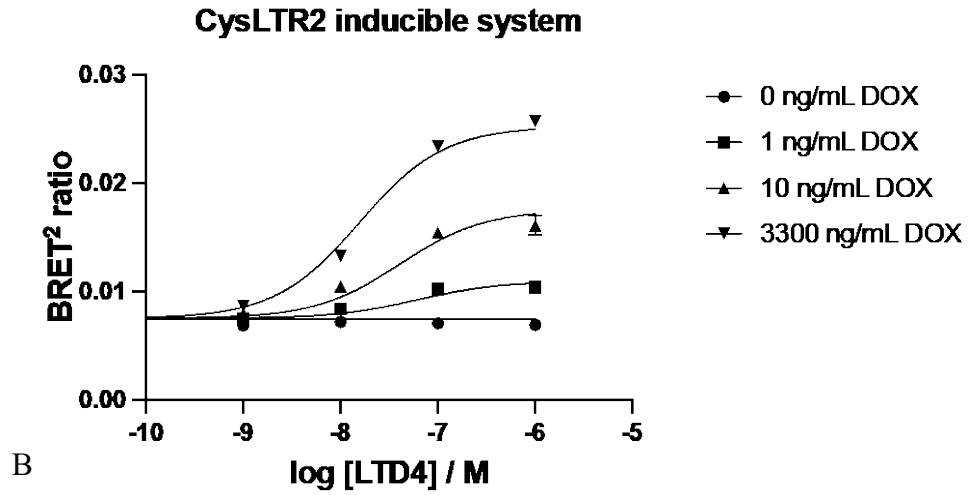

B

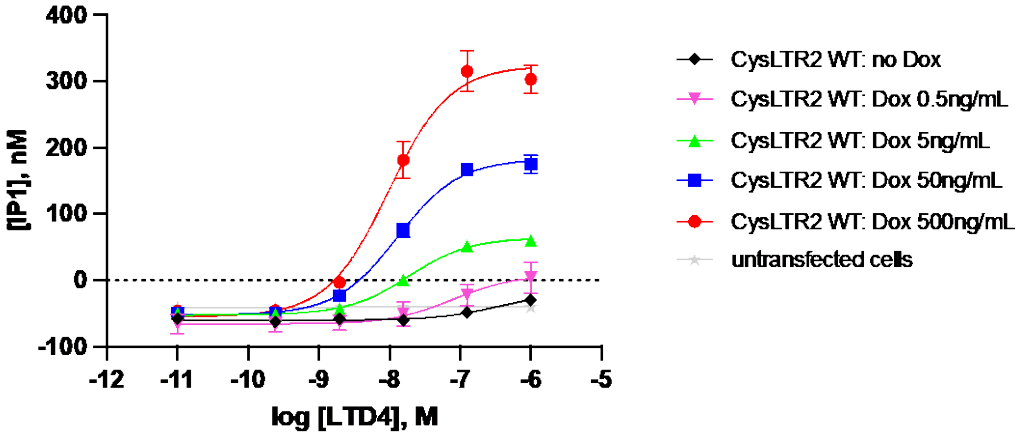

Figure 3-15 Preliminary BRET2 and IP1 assays using the tet-inducible FLAG-OLLAS-NLuc-HT7-CysLTR2-GFP10-1D4

BRET2 β-arrestin recruitment assay **(A)** and IP1 accumulation assay **(B)** of WT CysLTR2 in the tetracycline-inducible construct. The advantage of using this construct is that we are able to run a "two-dimensional dose response assay". The two dimensions are the doxycycline-dose (the various symbols and curves), which control receptor expression in a dose-dependent manner, and the LTD4-dose (x-axis), which should control the β-arrestin recruitment or IP1 accumulation in a dose-dependent manner. These experiments confirmed that the expression was exquisitely controlled by doxycycline concentration, as expected, and that the plasmid is compatible with our previously developed assays with no artefacts caused by the extracellular tags and the change to the doxycycline-inducible system.

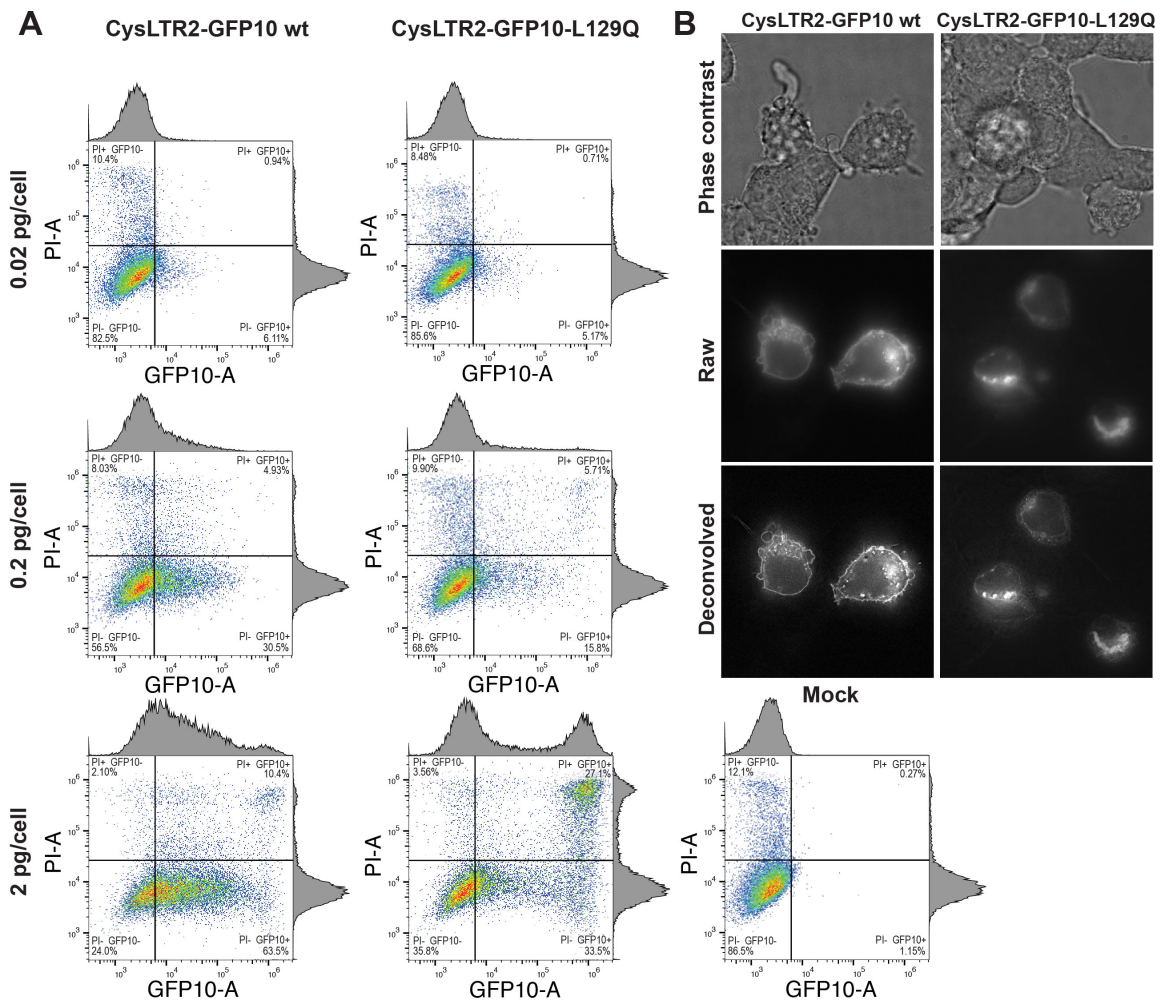

Figure 3-16 High levels of CysLTR2-L129Q result in cell death

(A) The toxicity of CysLTR2 wt and -L129Q was assessed using flow cytometry for GFP10 and the live-dead cell marker propidium iodide (PI). Data shown has been unmixed to correct for spectral overlap between GFP10 and PI. Representative dot plots with gating for HEK293T cells transfected with different amounts of DNA (0.02, 0.2 and 2.0 pg/cell) of CysLTR2 wt and -L129Q, keeping the total DNA fixed at 2 pg/cell, and mock transfected cells, all in the presence of PI staining. Single parameter histograms representing expression of GFP10 and PI are shown above and to the left of each dot plot, respectively. Each plot represents a single replicate where 20,000 events in the SSC singlet gate were collected. Quadrant gating was created using untransfected control cells and single stained sample cells. High levels of receptor expression as monitored by GFP10 intensity correlates with cell death as monitored by PI staining for CysLTR2-L129Q-transfected samples but not for CysLTR2 wt-transfected samples. **(B)** Live cell imaging of CysLTR2 wt and -L129Q transfected cells at 2 pg/cell. Cellular context of cells is shown using phase contrast. Raw and deconvolved images are optical sections extracted from the confocal stacks for CysLTR2 wt and -L129Q receptors, respectively. Images are 64 µm side length, each.

through CysLTR2 expressed in endothelial cells of the tumor microenvironment, which will lead to enhanced endothelial permeability, tumor angiogenesis and metastasis, which are the canonical roles of CysLTR2 (Duah et al., 2019; Moos et al., 2008). *CYSLTR2* might also play an early tumor suppressive role by eliminating precancerous cells, since ER stress triggered by oncogenic stress leads to apoptosis or senescence as a failsafe mechanism to prevent tumorigenesis (Denoyelle *et al.*, 2006; Vanacker et al., 2017).

As outlined in **Fig. 3-17**, the p38 MAPK pathway is activated by stress, whether ER stress, oxidative stress, or stress from chemotherapeutic agents. This pathway phosphorylates cPLA2, which is responsible for generating AA by hydrolysis of membrane-associated phosphatidylcholine (PC). The liberated AA is lipoxygenated and dehydrated sequentially by arachidonate 5-lipoxygenase (ALOX5/5-LO) in concert with FLAP to form the unstable intermediate LTA4. The more broadly expressed coactosin like F-actin binding protein 1 (COTL1) has a similar function to FLAP (Basavarajappa et al., 2014). LTA4 is then conjugated to a reduced GSH to form LTC4 by LTC4S in hematopoietic cells or by microsomal glutathione S-transferase 2 (MGST2), which is ubiquitously expressed. LTC4 can activate CysLTR2, found in all tissues of the body except for the brain, in which GPR17 (shown to respond to CysLTs) is expressed. These receptors couple to and activate the Gq/11/ PLC-β pathway which produces the second messenger, IP3. IP3 then binds to IP3 receptors on the ER and facilitates the release of Ca^{2+} from the ER, giving rise to a cytoplasmic Ca^{2+} flux. As Ca^{2+} is required for translocation of cPLA2 to the plasma membrane, a positive feedback loop is established. On the other hand, Gq/11 signaling also activates TRIO, which is a guanine nucleotide exchange factor (GEF) for Rho and Rac. COTL1 is activated by recruitment to F-actin, which is Rho dependent, forming a second positive feedback loop. Lastly, Rac activates NADPH oxidase (NOX) 1/4, which is turn produces reactive oxygen species (ROS) which lead to oxidative stress to activate p38 MAPK in a third positive feedback loop. This means that there are three positive feedback loops converging and increasing the LTC4 synthesis in concert.

We hypothesize that stress-induced LTC4 results in CysLTR2-dependent apoptosis, which is a tumor suppressive process. Apoptosis effectively acts as negative feedback on LTC4 production. Somatic LoF missense variation or loss of copy number variation of *CYSLTR2* will attenuate the efficiency of the negative feedback mechanism and result in increased production of LTC4 by the tumor. The resulting increase of LTC4 release acting on the tumor microenvironment will promote neovascularization and metastasis. Therefore, the somatic loss of the tumor-suppressive action of *CYSLTR2* will drive tumor growth due to reduced cancer cell apoptosis, increased tumor vascularization, and reduced endothelial barrier function promoting metastasis. It is worth noting that for those cells that don't reach apoptosis, they will stop and exist in a senescent state, in which they can still secrete leukotrienes (Wiley et al., 2019).

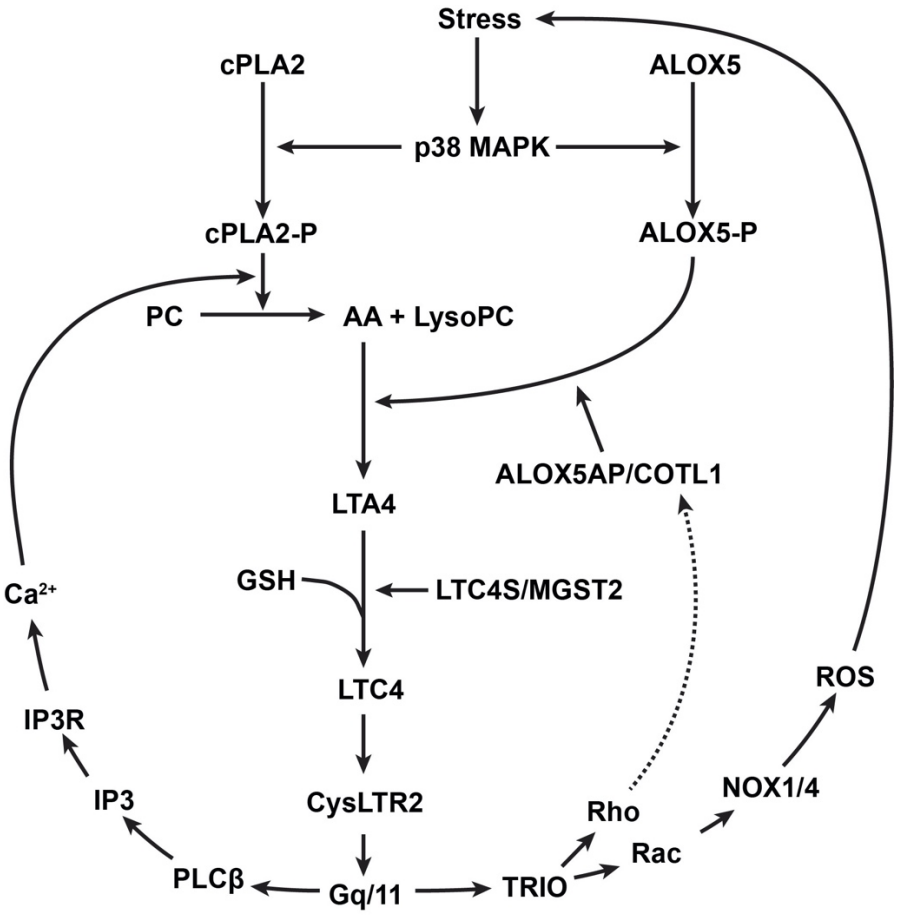

Figure 3-17 Role of intracrine signaling of CysLTR2 in stress-activated LTC4 biosynthesis
The p38 mitogen-activated protein kinase (MAPK) pathway is activated by stress, whether endoplasmic reticulum (ER) stress, oxidative stress, or stress from chemotherapeutic agents. This pathway phosphorylates cytosolic phospholipase A2 (cPLA2), which is responsible for generating arachidonic acid (AA) by hydrolysis of membrane-associated phosphatidylcholine (PC). The liberated AA is lipoxygenated and dehydrated sequentially by arachidonate 5-lipoxygenase (ALOX5/5-LO) in concert with ALOX5 activating protein (ALOX5AP) or more broadly expressed coactosin like F-actin binding protein 1 (COTL1) to form the unstable intermediate LTA4. LTA4 is then conjugated to a reduced glutathione (GSH) to form LTC4 by LTC4 synthase (LTC4S) in hematopoietic cells or by microsomal glutathione S-transferase 2 (MGST2), which is ubiquitously expressed. LTC4 activates CysLTR2, which activates the Gq/11/Phospholipase C-β (PLC-β) pathway to produce the second messenger, inositol triphosphate (IP3). IP3 then binds to IP3 receptors on the ER and facilitates the release of Ca^{2+} from the ER, giving rise to a cytoplasmic Ca^{2+} flux. As Ca^{2+} is required for translocation of cPLA2 to the plasma membrane, a positive feedback loop is established. On the other hand, Gq/11 signaling also activates TRIO, which is a guanine nucleotide exchange factor (GEF) for Rho and Rac. COTL1 is activated by recruitment to F-actin, which is Rho dependent, forming a second positive feedback loop. Lastly, Rac activates NADPH oxidase (NOX) 1/4, which is turn produces reactive oxygen species (ROS) which lead to oxidative stress to activate p38 MAPK in a third positive feedback loop.

The initial phase of the ISR helps cells adapting to stress, whereas severe stress activates the late, cell death-promoting phase of the ISR. The late ISR upregulates the major cell death mediator C/EBPbeta homologous protein (CHOP) also known as the DNA damage-induced transcript 3 (DDIT3) (Hu et al., 2018). CHOP induces LTC4 biosynthesis and signaling by upregulating the key enzymes MGST2 and ALOX5, and the LTC4 receptors CysLTR1 and CysLTR2, which appear to be localized to the nuclear membrane that is continuous with the ER (Bhosle et al., 2019; Mohammad Nezhady et al., 2020; Nielsen *et al.*, 2005). Intracrine signaling of LTC4 results in production of reactive oxygen species (ROS), especially hydrogen peroxide produced by NADPH oxidase 4 (NOX4), which results in oxidative DNA damage and either senescence, or apoptosis (Chen et al., 2012; Hernandez-Segura et al., 2018; Szegezdi et al., 2006). The positive feedback loop between CHOP and the MGST2-LTC4 pathway dependent ROS formation can be interrupted by inhibition of LTC4 biosynthesis by zileuton, or by blocking the LTC4 receptors with montelukast, pranlukast and BayCysLT2 (Dvash *et al.*, 2015).

However, the signaling pathway from CysLTR1 and CysLTR2 to yield NOX4-dependent ROS formation, DNA damage and apoptosis are not well characterized. Intense Gq/11 signaling is known to sometimes cause apoptosis, for example, in apoptotic heart failure (Adams et al., 1998; Althoefer et al., 1997; Narula et al., 1996; Olivetti et al., 1997; Pleskoff et al., 2005; Ueda et al., 2001; Yamauchi et al., 2001; Yamauchi et al., 1997). Gq/11 signals through several MAPK pathways, such as ERK, JNK and p38 MAPK, and Hippo- independent activation of the YAP pathway. A systematic study of these key downstream players is required to thoroughly dissect the role of CysLTR2 signaling in the stress-induced, death-promoting signaling pathway.

It seems that *CYSLTR2* plays three different roles in cancer biology. First, the GoF variant of *CYSLTR2* is an oncogenic driver in UM and other melanocytic neoplasias by constitutively activating the Gq/11 signaling pathway. Second, CysLTs produced by tumor cells or tumor-infiltrating immune cells activate CysLTR2 in endothelial cells and promote vascular permeability and metastasis. Third, the LTC4-CysLTR2 signaling axis mediates oxidative DNA damage and apoptotic cell death due to ER stress or chemotherapeutics. We have described here our reasoning to believe that ER stress and the integrated stress response is the key to understanding why *CYSLTR2* simultaneously can be tumor suppressive and promoting.

3.3 The activation mechanism of the 3.43 mutant CysLTR2-L129Q

In the previous sections, we have shown that CysLTR2-L129Q is a CAM receptor that strongly couples to Gq/11 cellular signaling pathways. However, the receptor only very weakly recruits β-arrestins and thereby avoids cellular down-regulation mechanisms. The L129Q substitution in CysLTR2 is located at the generic position 3.43 according to the GPCRdb/Ballesteros-Weinstein numbering system. Position 3.43 is highly conserved with 96% hydrophobic residues (Leu, Ile, Val, Met, and Phe) in 286 class A GPCRs from the GPCRdb. L(3.43)Q mutations have been shown to induce disease-causing constitutive activity in CysLTR2 (Moore *et al.*, 2016) and thyroid-stimulating hormone receptor (TSHR) (Nishihara et al., 2006). Other constitutively activating mutations of $L^{3.43}$ have been described for the luteinizing hormone (LH)/chorionic gonadotropin (CG) receptor (LHCGR), follicle-stimulating hormone receptor (FSHR), β_2-adrenergic receptor (β_2AR), and M_1 acetylcholine receptor (M_1AChR) (Lu and Hulme, 1999;

Stoy and Gurevich, 2015; Tao et al., 2000). Based on a combination of site-directed mutagenesis and molecular dynamics simulations, we propose a model for the constitutive activation mechanism of CysLTR2-L129Q in which the mutant Q interacts with the highly conserved $Y221^{5.58}$ and $Y305^{7.53}$ and differentially stabilizes a partially activated intermediate state conformation to allow functional selectivity and escape from β-arrestin-dependent down-regulation.

3.3.1 Site-saturation mutagenesis of CysLTR2-$L129^{3.43}$

We focused on understanding the mechanism of GoF underlying the L129Q mutation. We determined the LTD4 dose-response for Gq signaling using the IP1 accumulation assay and β-arrestin recruitment using the BRET2 assay for 19 amino acid substitutions at position 129 in CysLTR2 (**Fig. 3-18**). For the Gq signaling (**Fig. 3-18A**), mutants L129C, L129I, L129K, L129V and L129G were essentially like WT with very little constitutive activity, a similar response to LTD4 (efficacy and potency). All other substitutions resulted in a significantly reduced agonist-dependent activity, where the IP1 accumulation was less than 50% of that of WT. L129W showed no response to the agonist. L129P and L129Y showed significantly lower agonist potencies. Five variants, L129Q, L129E, L129A, L129S, and L129M showed significantly increased basal activity as compared with WT. However, L129Q is the only significant GoF as seen in the site saturation mutagenesis. It seems like there is something specific about the Q that is causing this GoF, and it is not simply due to the position, 3.43. On the other hand, the mutations at position 3.43 decreased LTD4-dependent β-arrestin recruitment much more dramatically (**Fig. 3-18B**). Only L129M had WT-like recruitment and the rest of the mutations resulted in a significantly reduced agonist-dependent activity, where the recruitment was less than 50% of that of WT. In particular, L129P, L129E, L129W, L129Y, L129N, L129G, L129D, L129F, and L129R are indistinguishable from mock-transfected controls and show no discernable recruitment. These mutants show significant receptor expression as seen in **Fig. 3-18C**, so they are being folded and expressed properly and are truly LoF mutants. L129Q and L129A were the only mutants that showed some basal β-arrestin recruitment, and L129E, L129S, and L129M, which showed some constitutive Gq activity, did not show the same constitutive β-arrestin recruitment. The LTD4-dependent β-arrestin recruitment was much more sensitive to mutations at this position, as only L129W was a complete LoF in Gq activity. This suggests that the interactions of $L129^{3.43}$ may be more critical for β-arrestin recruitment.

Furthermore, we tested the two CysLTR2 antagonists HAMI3379 (Wunder et al., 2010) and BayCysLT2 (Ni et al., 2011) on the three mutants with the highest Gq constitutive activity, L129Q/E/A. These antagonists can bring the LTD4-dependent WT Gq activity to levels that are indistinguishable from mock-transfected cells (**Fig. 3-19D**). For the two weaker CAMs, L129E (**Fig. 3-19B**) and L129A (**Fig. 3-19C**), we see a slight reduction in the constitutive IP1 accumulation, but it is not completely abolished. For the UM mutant L129Q (**Fig. 3-19A**), the two antagonists have little to no effect, and the Gq activity is virtually unaffected upon addition of increasing concentrations of both HAMI3379 and BayCYSLT2. Ultimately, they have weak efficacy as inverse agonists on the constitutively active L129Q/E/A, as seen by their limited effects on the basal activity.

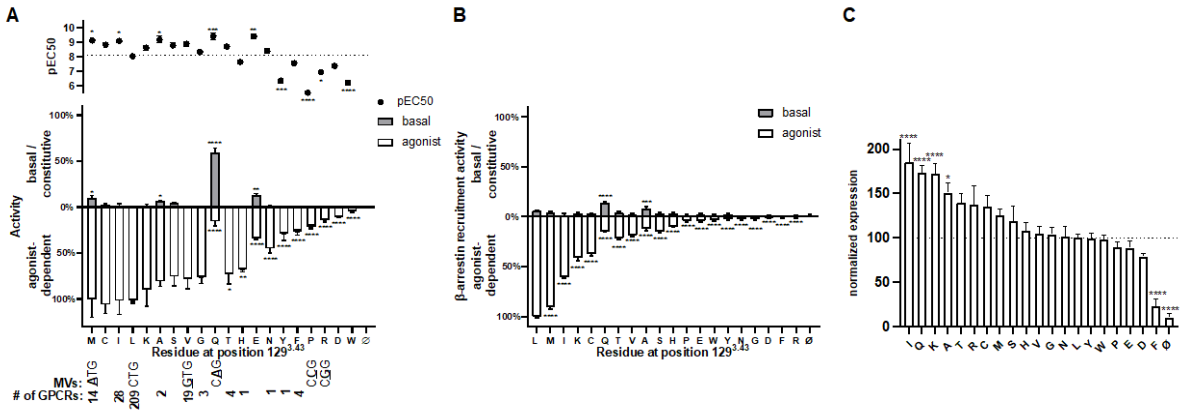

Figure 3-18 Site-saturation mutagenesis of CysLTR2-L129Q$^{3.43}$
(A) The LTD4 dose-dependent IP1 accumulation for each of 19 amino acid substitutions at residue CysLTR2-L129$^{3.43}$ is depicted here. The agonist-dependent activity (white downward bars) is the span between the normalized bottom and top endpoints, and the basal or constitutive activity (grey upward bars) is the normalized bottom endpoint. The pEC_{50} plots (black dots) correspond to the midpoint of the dose-response curve for each mutant. The graph shows the mutants in descending order of total activity defined as the sum of basal and agonist-dependent activity. Ø corresponds to mock-transfected cells. The linear combinations of fitting parameters for each mutant compared to WT were assessed for significant difference using a two-way ANOVA with Dunnett's multiple comparison test. The MVs that can result from single-nucleotide exchange from the WT CTG codon (**bold** and underlined nucleotide) encode for Val, Met, Gln, Pro, and Arg. All other single-nucleotide variants of CTG are synonymous and encode for Leu. Among 286 rhodopsin-like GPCRs in the GPCRdb, 209 have the highly conserved Leu at position 3.43. **(B)** The 1µM LTD4-dependent β-arrestin recruitment was measured for each of 19 amino acid substitutions at residue CysLTR2-L129$^{3.43}$. The agonist-dependent activity (white downward bars) and the basal or constitutive activity (grey upward bars) are normalized relative to maximally stimulated wild-type receptor and mock-transfected control. The graph shows the mutants in in descending order of total activity defined as the sum of basal and agonist-dependent activity. Ø corresponds to mock-transfected cells. The data for each mutant compared to WT were assessed for significant difference using a two-way ANOVA with Dunnett's multiple comparison test. (**C**) The quantification of the total receptor expression was measured for each of 19 amino acid substitutions at residue CysLTR2-L129$^{3.43}$ as normalized GFP10 fluorescence relative to WT expression and mock-transfected cells (white bars). The graph shows the mutants in descending order of total expression. Ø corresponds to mock-transfected cells. The dotted line at 100% expression represents the expression of WT CysLTR2. The data for each mutant compared to WT were assessed for significant difference using a two-way ANOVA with Dunnett's multiple comparison test.

3.3.2 The noncanonical VRF motif only slightly contributes to the Gq biased constitutive signaling of CysLTR2-L129Q

GPCRs have a conserved DRY motif in H3, where $R^{3.50}$ forms a salt bridge to the neighboring acidic $D^{3.49}$ in the inactive state (Vogel *et al.*, 2008). In the active state, this salt bridge is broken and $R^{3.50}$ interacts with the Gα subunit (Scheerer *et al.*, 2008). In CysLTR2, the canonical DRY motif is a noncanonical VRF. As the DRY motif is critical for G protein activation, we wondered whether reverting the VRF back to DRF might affect the constitutive activity of CysLTR2-L129Q. Could it be that the noncanonical VRF motif is what is causing such a high constitutive activity?

To investigate this, we performed a LTD4 dose-dependent IP1 accumulation (**Fig. 3-20A**) and β-arrestin recruitment (**Fig. 3-20B**) assay on combinations of mutations of residue 3.43 ($L129^{3.43}$ or $Q129^{3.43}$) and residue 3.49, the D of the canonical DRY motif ($V135^{3.49}$ or $D135^{3.49}$). When we restore the canonical D to the WT CysLTR2, we see a significant decrease in maximal Gq activity as compared to WT and the response to LTD4 is decreased as well (curve is right shifted). As expected, the UM mutant, L129Q, has a high constitutive activity. Surprisingly, upon introduction of the V135D (L129Q/V135D double mutant) we only see a slight reduction in the constitutive signaling of Gq. Both the single and double mutants of V135D lost β-arrestin recruitment and became indistinguishable from mock-transfected controls. This means that, while important for Gq activation and β-arrestin recruitment, the noncanonical VRF is not sufficient to explain the constitutive activity of CysLTR2-L129Q as restoration to DRF did not significantly reduce the high constitutive Gq activity.

3.3.3 The L129Q mutation stabilizes the receptor in a partially activated intermediate state

The recent crystal structures of CysLTR2 showed the receptor in two distinct conformations (Gusach et al., 2019a). One conformation corresponds to the fully inactive state. The other shows about 5 Å outward movement of the intracellular part of helix H6 and a flip of the $Y221^{5.58}$ microswitch, which are both consistent with a partially activated intermediate state. We used these structures as starting points in all-atom molecular dynamics simulations of the mutant receptor without ligand, embedded in a lipid bilayer membrane to analyze the packing around the L129Q mutation. We obtained three trajectories with about 14 μs length in total. The first trajectory started from the inactive state and relaxed to a stable conformational state. In the two trajectories starting from the intermediate state, one visited the intermediate state for only about 100 ns, before flipping into the inactive state, and the other remained in the intermediate state for the whole duration. Interestingly, the side chain hydrogen bonding interactions of $L129Q^{3.43}$ flip from $N301^{7.49}$ in the inactive state to $Y221^{5.58}$ in the intermediate state (**Fig. 3-21**). This is a key observation for understanding the molecular mechanism of the GoF mutation.

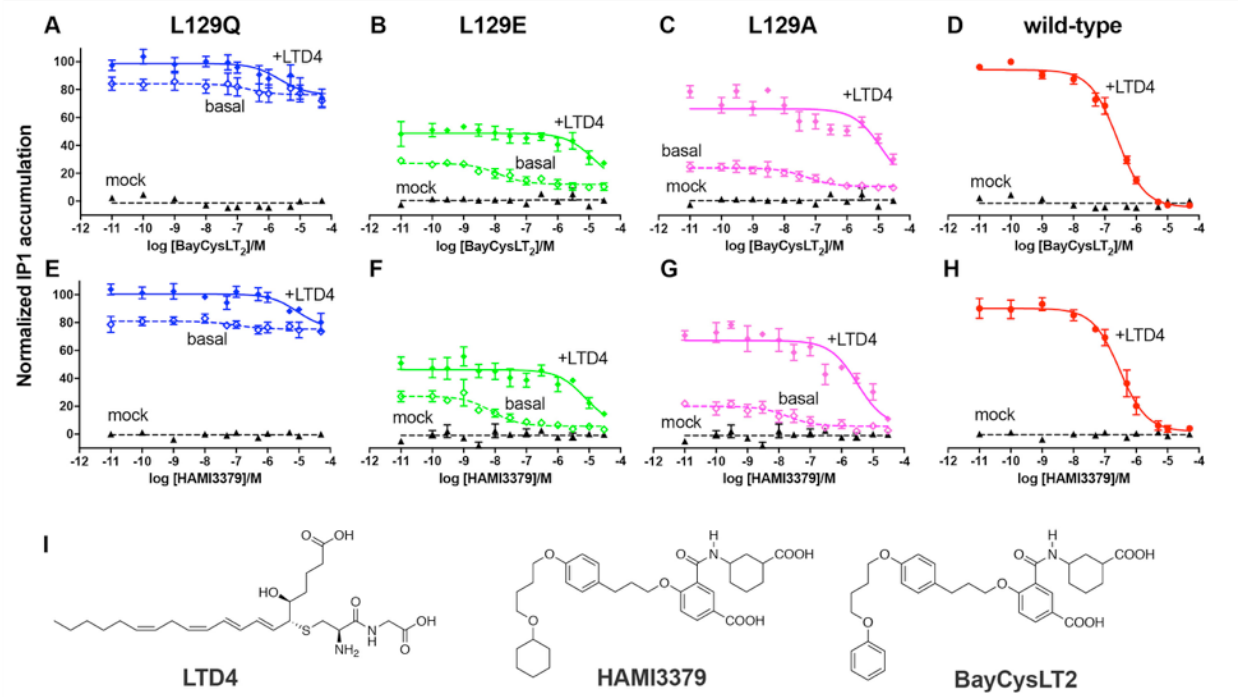

Figure 3-19 Known CysLTR2 antagonists have limited efficacy as inverse agonists
(A-H) IP1 accumulation of CysLTR2$^{3.43}$ mutants in an inverse agonist competition assay. The CysLTR2 antagonists BayCysLT2 **(A-D)** and HAMI3379 **(E-H)** show only minimal reduction of the constitutive IP1 accumulation in cells expressing the three CAMs, CysLTR2-L129Q (blue diamonds), -L129E (green diamonds), and -L129A (pink diamonds) (basal, dashed lines and open symbols), and full inhibition of the LTD4-dependent IP1 stimulation of the CAMs and wt receptor (+LTD4, solid lines and symbols). The data are presented as the percentage of IP1 accumulation minus mock over the maximal response exhibited by CysLTR2 wt following 100 nM LTD4 stimulation and represent the mean ± SEM of at least three independent experiments, each carried out in at least triplicate. These findings suggest that the two CysLTR2 antagonists, HAMI3379 and BayCysLT2, act as neutral antagonists, but they have limited efficacy as inverse agonists targeting the oncogenic CAM CysLTR2-L129Q. **(I)** Molecular structure of the diverse compounds tested for IP1 accumulation studies. Shown (from left to right) are the CysLTR2 agonist Leukotriene D4 (LTD4) and CysLTR2 antagonists HAMI3379 (Wunder *et al.*, 2010) and BayCysLT2 (Ni *et al.*, 2011).

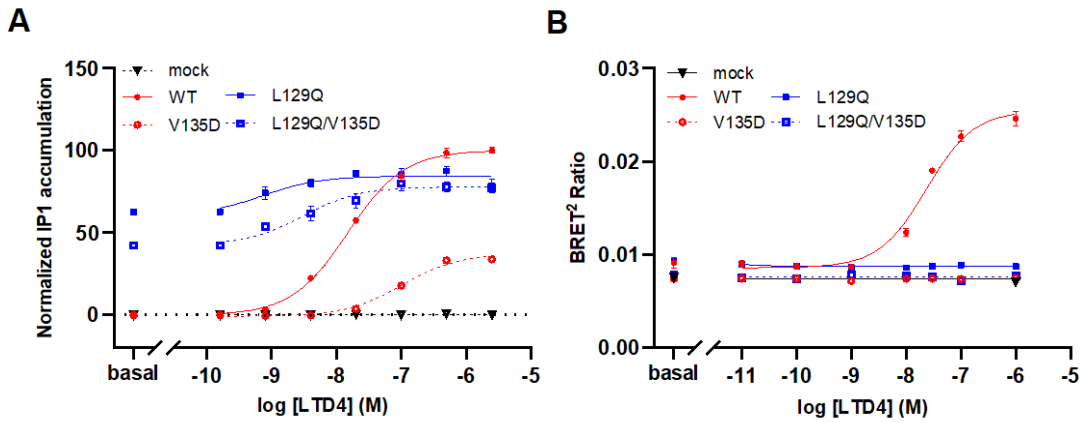

Figure 3-20 The noncanonical VRF motif only slightly contributes to the Gq biased constitutive signaling of CysLTR2-L129Q

We performed LTD4 dose-dependent IP1 accumulation (**A**) and β-arrestin recruitment (**B**) assays on combinations of mutations of residue 3.43 ($L129^{3.43}$ or $Q129^{3.43}$) and residue 3.49, the D of the canonical DRY motif ($V135^{3.49}$ or $D135^{3.49}$). When we restore the canonical Asp to the VRF (V135D, dashed red line) we see a significant decrease in Gq activity for the IP1 assay as compared to WT (solid red line). The UM mutant, L129Q (solid blue line) has a high constitutive activity and upon introduction of the V135D (L129Q/V135D double mutant, dashed blue line) we only see a slight reduction in the constitutive signaling of Gq. Both the single and double mutants of V135D (dashed lines) lost β-arrestin recruitment and became indistinguishable from mock-transfected controls. The data are the mean ± SEM from two independent experiments (for WT) and one experiment (for L129Q) with six concentrations and at least three technical replicates each.

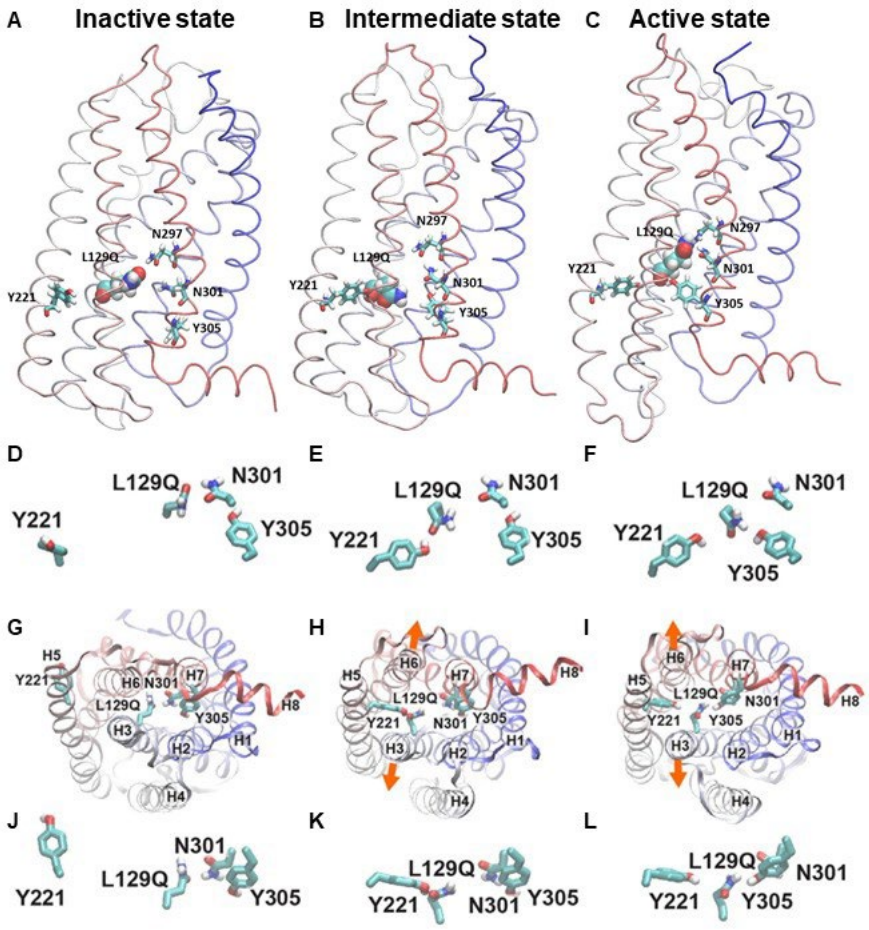

Figure 3-21 The L129Q mutation stabilizes the receptor in a partially activated intermediate state

We carried out molecular dynamics simulations at 14 microsecond timescales of CysLTR2 L129Q. Representative structures of three major conformational clusters starting from inactive state (**A,D,G,J**), intermediate state (**B,E,H,K**) and stable "activated" state (**C,F,I,L**) crystal structures are shown (**B,C,E,F,H,I,K,L**). L129Q$^{3.43}$ binds to N301$^{7.49}$ and N297$^{7.45}$ in the inactive state with Y221$^{5.58}$ rotated out of the TM bundle (**A**). L129Q$^{3.43}$ flips and binds Y221$^{5.58}$ to stabilize the intermediate state of the receptor (**B**) with a concomitant increase in distance between H3 and H6 (orange arrows in **H,I**). The trajectory transiently samples an activated state (**C**) with a change of the conformation of the NPXXY motif resulting in rotation of Y305$^{7.53}$ towards L129Q$^{3.43}$ (**C,F,I,L**). In the stable "activated" state, Y221$^{5.58}$ and Y305$^{7.53}$ are in proximity and L129Q flips to interact with N297$^{7.45}$ and N301$^{7.49}$ (**C**). The role of L129Q is to mediate the interaction of Y221$^{5.58}$ and Y305$^{7.53}$, which is a conserved hallmark of GPCRs in the active state. CysLTR2 receptor backbone is colored from blue to white to red (N- to C-term). L129Q$^{3.43}$ is in space fill. Y221$^{5.58}$, N297$^{7.45}$, N301$^{7.49}$, and Y305$^{7.53}$ are shown as sticks.

It has been suggested that the activation mechanism of GPCRs involves predominantly three states: inactive, intermediate, and active (Dror et al., 2011). The hallmark feature of GPCR activation is the outward movement of the cytoplasmic end of H6. Less prominent features are concomitant changes with an inward movement of the cytoplasmic end of H7. The transition from the inactive state to the intermediate state is characterized by an outward movement of H6 past the $Y^{5.58}$ microswitch, which moves from the lipid-exposed side of H6 to an area between H3 and H6 and opens the G protein-binding site. The transition from the intermediate state to the active state is facilitated by binding of the G protein and involves a conformational change of the conserved NPXXY motif that brings the side chain of $Y^{7.53}$ close to that of $Y^{5.58}$.

We first analyzed the packing around the L129Q mutation. We reasoned that as an activating mutation, L129Q should stabilize the active state, destabilize the inactive state, or both. Previously, we observed that the L(3.43)Q side chain is in hydrogen-bonding distance of the side chains of $N^{7.49}$ or $Y^{7.53}$ in the highly conserved NPXXY motif in models of several GPCRs. We see these interactions in models based on templates in the active state, but not in the inactive state. This finding is highly relevant as a potential mechanism for a CAM. Our simulations suggest that that *intermediate state is stabilized* by the hydrogen bonds between $L129Q^{3.43}$ and $Y221^{5.58}$, which would, in turn, facilitate G protein-binding to the open pocket and, therefore, promote the fully active state. In the inactive state (**Fig 3-21A,D,G,J**) $L129Q^{3.43}$ binds to $N301^{7.49}$ and $N297^{7.45}$ with $Y221^{5.58}$ rotated out of the TM bundle. Then, in the intermediate state $L129Q^{3.43}$ flips and binds $Y221^{5.58}$ to stabilize the intermediate state of the receptor (**Fig. 3-21B,E**) with a concomitant increase in distance between H3 and H6 (orange arrows in **Fig. 3-21H,I**). The trajectory transiently samples an activated state (**Fig. 3-21C**) with a change of the conformation of the NPXXY motif resulting in rotation of $Y305^{7.53}$ towards $L129Q^{3.43}$ (**Fig. 3-21C,F,I,L**). In the stable "activated" state, $Y221^{5.58}$ and $Y305^{7.53}$ are in proximity and L129Q flips to interact with $N297^{7.45}$ and $N301^{7.49}$ (**Fig. 3-21C**). The role of L129Q is to mediate the interaction of $Y221^{5.58}$ and $Y305^{7.53}$, which is a conserved hallmark of GPCRs in the active state.

The Gq-biased constitutive activity in CysLTR2-L129Q may be compared with the β-arrestin-biased agonism observed in the angiotensin II type 1 receptor (AT1R) (Suomivuori et al., 2020; Wingler et al., 2020). The strong receptor bias of CysLTR2-L129Q towards Gq signaling seems consistent with a selective stabilization of the partially activated intermediate state, since the catalytic activation of the nucleotide exchange in the G protein only transiently requires a fully active receptor state, whereas the stable interaction of β-arrestins with the receptor core requires a fully active state (Kang et al., 2015).

Residue $L129^{3.43}$ is part of the allosteric sodium-binding site (Katritch et al., 2014). Negative allosteric modulatory (NAM) effects of sodium ions and amilorides have been observed for some class A GPCRs. Amilorides are analogs of the diuretic amiloride and are small organic cations that can bind in the sodium-binding site (Liu *et al.*, 2012). The sodium-binding site collapses upon receptor activation, and the NAM effect of the sodium ions and amilorides can be explained by selectively stabilizing the inactive state. Our alternative hypothesis is that $L129Q^{3.43}$ blocks sodium binding and destabilizes the inactive state. It is currently unknown whether CysLTR2 is controlled by sodium ions, but the conservation of the residues suggests that the receptor has a functional sodium-binding site. The only crystal

structures of δ-group GPCRs with clear evidence of bound sodium ions are PAR1, PAR2, and CysLTR1 (Cheng et al., 2017; Luginina et al., 2019; Zhang et al., 2012). They all have a type II sodium site with two acidic residues, $D^{2.50}$ and $D^{7.49}$, as exemplified in the PAR1 structure (Zarzycka et al., 2019). Note that CysLTR2 lacks the second acidic site $D^{7.49}$ and has the common $N^{7.49}$. We further speculate that the sodium-binding pocket might accommodate a small molecule drug specific for CysLTR2-L129Q, and virtual screening of compound libraries should be possible once a high-resolution crystal structure of CysLTR2 becomes available. We predict that many class A GPCRs will be activated by the L(3.43)Q mutation, given the high conservation of the conformational change and the residues involved in this interaction. We further note the complete absence of a glutamine residue at the 3.43 position in all known GPCR sequences. However, other receptors might lack the receptor bias away from β-arrestin. The efficiency of β-arrestin-dependent desensitization and downregulation mechanisms will determine the ultimate phenotype of the mutation.

As our molecular dynamics simulations predicted hydrogen-bonding interactions between $L129Q^{3.43}$ and $N301^{7.49}$ and $Y305^{7.53}$ of the NPXXY motif, as well as between $L129Q^{3.43}$ and $Y221^{5.58}$, we investigated these potential interactions by mutagenesis. We conducted LTD4 dose-dependent IP1 accumulation and β-arrestin recruitment assays on single, double, and triple mutants in an effort to disrupt stabilizing interactions and measure the functional outcome for the NPXXY motif (**Figure 3-22**). We used L and Q at position $129^{3.43}$, N and A at position $301^{7.49}$, and Y and F at position $305^{7.53}$. We designate the eight possible combinations by three letters highlighting the mutated residues as LNY, LN**F**, L**A**Y, L**AF**, **Q**NY, **Q**N**F**, **QA**Y, and **QAF**. The LTD4 dose-response of IP1 accumulation in each of these mutants (**Figure 3-22A**) compared to the WT (LNY) sample shows a significant loss of agonist-dependent activity for all mutants, a significant gain of constitutive activity for **Q**N**F**, **QA**Y, and significantly lower pEC50 for **Q**NY. Interestingly, introducing either N301A, Y305F, or N301A/Y305F into the L129Q mutant partially reverts the LoF in agonist-dependent signaling, but without reverting the GoF in the basal activity. The same mutations introduced into the WT receptor led to a LoF in agonist-dependent signaling, which was partial for Y305F and complete for N301A and N301A/Y305F. On the other, hand looking at the β-arrestin recruitment assays (**Figure 3-22B**), we see that introduction of the mutation, N301A, in the WT and L129Q receptor abolishes both basal and LTD4-dependent β-arrestin recruitment. On the other hand, the introduction of Y305F in the WT receptor does not abolish LTD4-dependent β-arrestin recruitment but causes a right shift, with a slight increase in recruitment seen only at the highest concentration of LTD4. Interestingly, the same mutation introduced in the L129Q mutant causes the receptor to regain sensitivity to LTD4. This is the first time we have seen CysLTR2-L129Q show LTD4-dependent β-arrestin recruitment. There is also a slight decrease in basal β-arrestin recruitment leading to an overall more WT-like phenotype for this double mutant. Together, these findings underscore the importance of the highly conserved NPXXY motif for active state formation.

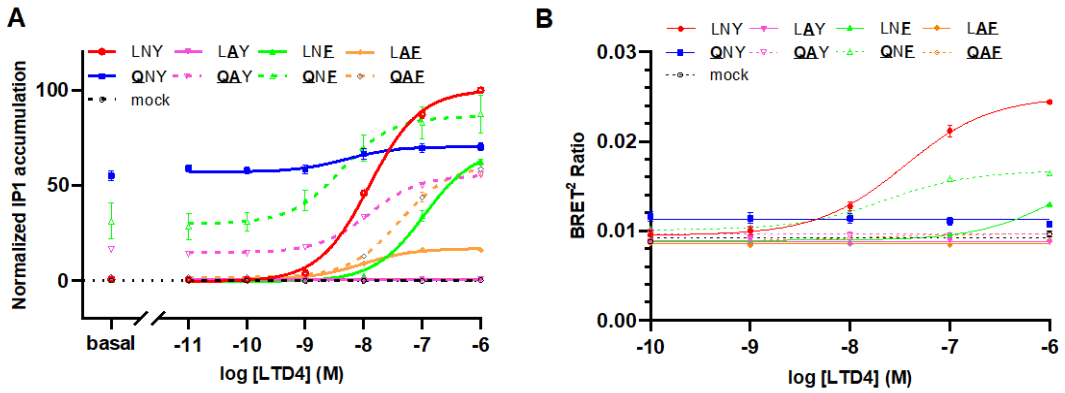

Figure 3-22 Characterization of the role of residues in the NPXXY motif
Characterization of the role of residues in the NPXXY motif (N301$^{7.49}$, Y305$^{7.53}$). The LTD4 dose-dependent IP1 accumulation (**A**) and β-arrestin recruitment (**B**) were assayed for eight combinations of mutations of at 3.43 (L129$^{3.43}$ or Q129$^{3.43}$), 7.49 (N301$^{7.49}$ or A301$^{7.49}$), and 7.53 (Y305$^{7.53}$ or F305$^{7.53}$). The single mutants (L129Q, **Q**NY (blue solid line); N301A, L**A**Y (pink solid line); Y305F, LN**F** (green solid line)), the double mutants (L129Q/N301A, **QA**Y (pink dashed line); L129Q/Y305F, **Q**N**F** (green dashed line); N301A/Y305F, L**AF** (orange solid line)) and the triple mutant (L129Q/N301A/Y305F, **QAF** (orange dashed line)) were compared with WT (LNY, red solid line). Sequential introduction of mutations at N301$^{7.49}$ and Y305$^{7.53}$ in the L129Q mutant shows a corresponding decrease in constitutive IP1 accumulation as well as increased responsiveness to LTD4 (**A**, green and pink dashed lines), with the triple mutant (orange dashed line) showing the lowest constitutive activity and the most WT-like activity. On the other hand, the introduction of the mutations at N301$^{7.49}$ and Y305$^{7.53}$ in the L129Q mutant causes a decrease in basal β-arrestin recruitment (**B**, dashed lines) but only the L129Q/Y305F double mutant (dashed green line) regains the LTD4-dependence. The dose-responses curves were fit with a three-parameter sigmoidal function. The data are the mean ± SEM two independent experiments with at least five concentrations and at least three technical replicates each.

Lastly, the molecular dynamics simulations revealed an important hydrogen bond network involving the NPXXY motif and Y221$^{5.58}$, so we similarly conducted LTD4-dependent IP1 accumulation and β-arrestin recruitment assays on receptors with combinations of mutations at 3.43 and 5.58. We used L and Q at position 129$^{3.43}$ and Y, A, and F at position 221$^{5.58}$. In the LTD4 dose-dependent IP1 accumulation, introduction of both Y221A (L**A**) and Y221F (L**F**) into the WT receptor abolished LTD4-dependent Gq activity completely, and the data are indistinguishable from mock-transfected controls (**Fig. 3-23A**). Interestingly, however, the loss of the Y and hydrogen bond at 5.58 reduces the constitutive IP1 accumulation of the L129Q mutants (L129Q/ Y221A, **QA** and L129Q/ Y221F, **QF**) and they also regain some sensitivity to LTD4 (**QF** responds more weakly to LTD4 compared with **QA**). Interestingly, all mutants seem to abolish the LTD4-dependent β-arrestin recruitment of CysLTR2. Furthermore, the slight constitutive activity of L129Q is decreased upon introduction of both Y221 mutations. Together with the molecular dynamics simulations, these mutagenesis experiments support our hypothesis that the role of L129Q is to mediate the interaction of Y221$^{5.58}$ and Y305$^{7.53}$ and stabilize an active state intermediate of CysLTR2 to allow for constitutive Gq activity. The catalytic activation of the nucleotide exchange in the G protein only transiently requires a fully active receptor state, whereas the β-arrestins require a fully active state to interact with the receptor core, so the stabilization of this partially activated intermediate state can explain the bias towards Gq and the mutant's ability to escape β-arrestin-mediated downregulation.

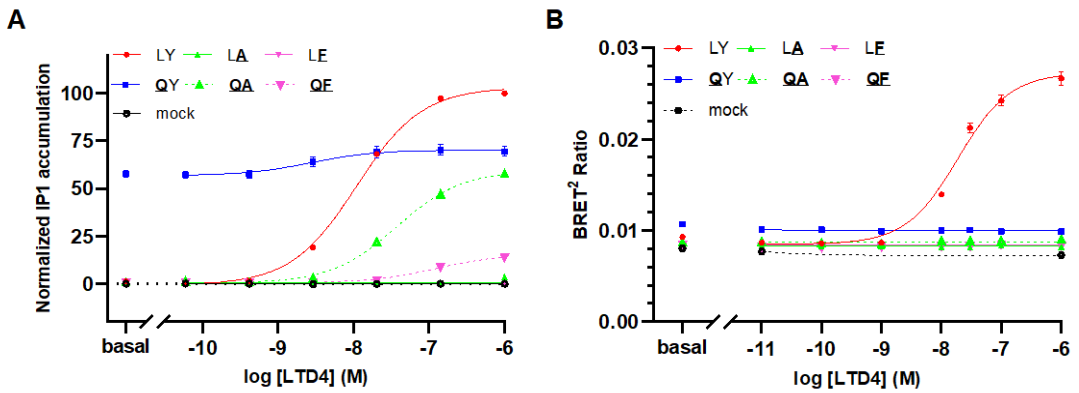

Figure 3-23 Hydrogen bond network stabilizes activated state in CysLTR2-L129Q$^{3.43}$
As the molecular dynamics simulations in **Fig. 3-21** showed a hydrogen bond network involving the NPXXY motif and Y221$^{5.58}$ we made six combinations of mutations at 3.43 (L129$^{3.43}$ or Q129$^{3.43}$) and 5.58 (Y221$^{5.58}$, A221$^{5.58}$ or F221$^{5.58}$). The LTD4 dose-dependent IP1 accumulation (**A**) and β-arrestin recruitment (**B)** were assayed for WT (LY, red solid line), the single mutants (L129Q, **Q**Y (blue solid line); Y221A, L**A** (green solid line); Y221F, L**F** (pink solid line)) and the double mutants (L129Q/ Y221A, **QA** (green dashed line); L129Q/ Y221F, **QF** (pink dashed line)). The loss of the Tyr and hydrogen bond at 5.58 completely abolished the constitutive IP1 accumulation of the L129Q mutants (green and pink dashed lines). Interestingly, all mutants seem to abolish the LTD4-dependent β-arrestin recruitment of CysLTR2. The dose-responses curves were fit with a three-parameter sigmoidal function. The data are the mean ± SEM from three independent experiments with six concentrations and at least three technical replicates each.

CHAPTER 4. CONCLUSIONS AND FUTURE WORK

4.1 Conclusions

In conclusion, we characterized a *CYSLTR2* oncogene in UM and established that CysLTR2-L129Q drives Gq/11 signaling activity in malignant UM and serves as a driver oncogene. The lack of a strong phosphorylation code in the cytoplasmic tail contributes to the extremely high constitutive activity of the mutant receptor. We established that the CysLTR2-L129Q CAM is highly biased toward Gq/11 cellular signaling pathways and fails to recruit β-arrestins significantly. The biased constitutive signaling pattern explains why it can persistently activate Gq and avoid β-arrestin-dependent cellular downregulation mechanisms.

CYSLTR2 was also found to be significantly mutated in the COAD cohort of TCGA. However, it was difficult to assign the role of those variants as the majority of nonsynonymous *CYSLTR2* mutations are VUS. To address this issue, we generated a library with more than two hundred variants of *CYSLTR2*, observed as somatic mutations in COSMIC and TCGA and as germline variants from the ExAC. We performed an activity-based profiling on these 200+ variants and assayed them for total expression, basal and agonist-dependent G protein activation, and basal and agonist-dependent β-arrestin recruitment. We found that about 21% of the variants show no detectable activity and are basically indistinguishable from mock-transfected controls, suggesting that a large portion of these mutations are damaging. A further 21% lose 50% of activity as normalized to WT (100%), and another ten percent are nonsense and frameshift variants. This means that about 50% of total somatic mutations of *CYSLTR2* have a LoF phenotype, which points to a tumor suppressor function following the famous “20/20” rule (Vogelstein *et al.*, 2013).

We aim to elucidate the precise signaling mechanism of *CYSLTR2* in the proposed role as tumor suppressor. Our proposed mechanistic model has LTC4 in the key mediator role, linking the ER stress response, which is triggered by a combination of oncogenic signaling, hypoxia, nutrient deprivation, and acidosis in the growing tumor, to CysLTR2-dependent oxidative DNA damage and apoptotic cell death. The apoptotic response will act as a negative feedback loop that limits the production of the proinflammatory LTC4. Moreover, LTC4 released by the tumor cells signals through CysLTR2 in endothelial cells in the tumor microenvironment and increases endothelial permeability, neovascularization, and metastasis. LoF somatic variants and loss of copy number variants of *CYSLTR2* in the tumor cell will break the negative feedback loop, resulting in increased LTC4 production and amplifying its effect on the tumor microenvironment.

Oftentimes, variant analysis from cancer genomes either lack functional assays and is based on recurrency arguments or are cell-based CRISPR screens of variants of known cancer targets like, BRCA (Kweon et al., 2020; Wu *et al.*, 2019). Deep mutational scanning of GPCRs has been done before: on CCR5 and CXCR4 by (Dunham and Beltrao, 2020) and β2-AR by (Jones et al., 2020). Work by Dunham et al. lacked signaling functional data and interestingly, in Jones et al., they point out that the functional assay measurements of individual mutations are seen to be too noisy and thus present their functional analysis as being best suited as an initial

funnel to guide further characterization. Our work is complementary to this approach, where we have a large amount of high-quality functional data on a clinically-relevant GPCR that can be used on its own to classify functional modifications caused by the missense variants. In conclusion, we optimized an activity-based profiling workflow and learned about the strength of using a bioinformatics filter to focus on fewer variants from more receptors by filtering out the noise of variants and predicting recurrent variants with benign or WT-like phenotypes through calculation of high mutation rates of specific SBS at functionally unimportant sites. Furthermore, by functionally mapping the landscape of naturally occurring variants of *CYSLTR2,* we were able to identify carriers of selected LoF variants from clinical case records to study the impact of *CYSLTR2* variants on the pathophysiology. Our results will motivate the mapping of the sequence-activity landscapes of other GPCRs. Detailed functional annotation maps of GPCR gene variants will help to address the big problem of VUS often encountered in genetic diagnosis and interpretation of somatic and genomic sequencing results. Our future overarching goal is to elucidate the actionable targets in the "GPCRome" relevant to human cancers.

Lastly, based on a combination of site-directed mutagenesis and molecular dynamics simulations, we elucidate the precise activation mechanism for the L129Q oncoprotein, which is constitutively active and biased towards the Gq/11 pathways. We see that in CysLTR2-L129Q, the mutant Q interacts with the highly conserved $Y221^{5.58}$ and $Y305^{7.53}$ (from the highly conserved NPXXY, which is important for activation). When this hydrogen network is broken, we saw the abolishment of the very high constitutive Gq/11 activity of L129Q and saw the return of LTD4-dependence in some cases as well. The role of L129Q is to mediate the interaction of $Y221^{5.58}$ and $Y305^{7.53}$ and stabilize an active state intermediate of CysLTR2 to allow for constitutive Gq activity. This partially activated intermediate state conformation allows functional selectivity and escape from β-arrestin-dependent down-regulation.

4.2 Future directions

From the insight gained from the work in this thesis, we know that CysLTR2-L129Q is an important albeit difficult receptor to target to help increase prognoses for patients with UM. Through the surface expression assays, we have learned that only 10% of the receptors are on the cell surface, posing further challenges in targeting the receptor itself. We have shown that BayCysLT2 and HAMI3379, result only in a small reduction of the constitutive activity of L129Q, although LTD4-dependent WT IP1 accumulation can be fully reduced. This suggests that they are neutral antagonists and have limited efficacy as inverse agonists, unable to bring down the constitutive activity to basal levels of WT. YM is a Gq/11 inhibitor which is able to completely block both LTD4-dependent WT activity and L129Q constitutive activity. However, YM is a potent inhibitor of physiologically active WT Gq/11 as well, which raises concerns about potential side effects. In on going work, we also looked at the inhibition of Arf6 by NAV-2729. Arf6 inhibition has been shown to block all known signaling pathways (PLC/PKC, Rho/Rac, YAP, and β-catenin) of oncogenic Gq/11. This compound results in almost complete inhibition of IP1 accumulation for the CysLTR2-L129Q CAM. Thus, this seems to suggest that Gq/11 and Arf6 are both potential therapeutic targets for the constitutively active UM oncoprotein. Others have shown encouraging clinical activity when targeting PKC (Kapiteijn *et al.*, 2019). Our collaborators have shown that YM combined with a MEK inhibitor, sustained MAP inhibition as well as tumor shrinkage, adding evidence to the strength of using a

combination of therapies (Hitchman *et al.*, 2020). Although there are various novel therapeutic targets and combination strategies being investigated, there remains a lack of standard of care therapy for metastatic UM and we believe this is an important area to research further.

Furthermore, it would be extremely interesting to investigate the tumor-suppressive mechanism of *CYSLTR2*. We plan to characterize the precise role of *CYSLTR2* in the stress-induced, death-promoting signaling pathway using pharmacological and gene editing tools, bioluminescent reporter assays to quantify signaling and trafficking, and live-cell imaging. Lastly, the activity-based phenotype screening platform would allow us to characterize a novel set of variants in different receptors of interest that are clinically-relevant. In particular, with our newly developed and proposed third-generation screen, we have a scalable and robust set of assays resulting in high-quality results, which comes at the cost of being a moderately high-throughput screen. This issue of scalability can be addressed and improved upon in two ways: introducing automated liquid handling in the workflow and adopting an emerging technology known as deep mutational scanning.

APPENDIX

List of published work:

Ceraudo, E.*, Horioka, M.*, Mattheisen, J. M., Hitchman, T. D., Moore, A. R., Kazmi, M. A., Chi, P., Chen, Y., Sakmar, T. P., & Huber, T. (2020). Direct evidence that the GPCR CysLTR2 mutant causative of uveal melanoma is constitutively active with highly biased signaling. *The Journal of biological chemistry*, 296, 100163. https://doi.org/10.1074/jbc.RA120.015352

Horioka, M., Ceraudo, E., Lorenzen, E., Sakmar, T. P., & Huber, T. (2021). Purinergic Receptors Crosstalk with CCR5 to Amplify Ca^{2+} Signaling. *Cellular and molecular neurobiology*, *41*(5), 1085–1101. https://doi.org/10.1007/s10571-020-01002-1

Horioka, M., Huber, T., & Sakmar, T. P. (2020). Playing Tag with Your Favorite GPCR Using CRISPR. *Cell chemical biology*, 27(6), 642–644. https://doi.org/10.1016/j.chembiol.2020.06.001

Rico, C. A., Berchiche, Y. A., Horioka, M., Peeler, J. C., Lorenzen, E., Tian, H., Kazmi, M. A., Fürstenberg, A., Gaertner, H., Hartley, O., Sakmar, T. P., & Huber, T. (2019). High-Affinity Binding of Chemokine Analogs that Display Ligand Bias at the HIV-1 Coreceptor CCR5. *Biophysical journal*, 117(5), 903–919. https://doi.org/10.1016/j.bpj.2019.07.043

Manuscripts in progress:

Horioka, M., Ceraudo, E., Mattheisen, J. M., Rasmussen, V., Chi, P., Chen, Y., Sakmar, T. P., & Huber, T. Activity-based profiling of *CYSLTR2* in the germline and pan-cancer human variome. In progress.

Ceraudo, E.*, Horioka, M.*, Mattheisen, J. M., Chi, P., Chen, Y., Sakmar, T. P., & Huber, T. Activation mechanism of uveal melanoma oncoprotein CysLTR2-L129Q. In progress.

REFERENCES

Adams, J.W., Sakata, Y., Davis, M.G., Sah, V.P., Wang, Y., Liggett, S.B., Chien, K.R., Brown, J.H., and Dorn, G.W., 2nd (1998). Enhanced Galphaq signaling: a common pathway mediates cardiac hypertrophy and apoptotic heart failure. Proc Natl Acad Sci U S A *95*, 10140-10145. 10.1073/pnas.95.17.10140.

Albert, D., Buerkert, E., Steinhilber, D., and Werz, O. (2003). Induction of 5-lipoxygenase activation in polymorphonuclear leukocytes by 1-oleoyl-2-acetylglycerol. Biochim Biophys Acta *1631*, 85-93. 10.1016/s1388-1981(02)00359-1.

Alexandrov, L.B., Kim, J., Haradhvala, N.J., Huang, M.N., Tian Ng, A.W., Wu, Y., Boot, A., Covington, K.R., Gordenin, D.A., Bergstrom, E.N., et al. (2020). The repertoire of mutational signatures in human cancer. Nature *578*, 94-101. 10.1038/s41586-020-1943-3.

Alexandrov, L.B., Nik-Zainal, S., Wedge, D.C., Aparicio, S.A., Behjati, S., Biankin, A.V., Bignell, G.R., Bolli, N., Borg, A., Børresen-Dale, A.L., et al. (2013a). Signatures of mutational processes in human cancer. Nature *500*, 415-421. 10.1038/nature12477.

Alexandrov, L.B., Nik-Zainal, S., Wedge, D.C., Campbell, P.J., and Stratton, M.R. (2013b). Deciphering signatures of mutational processes operative in human cancer. Cell Rep *3*, 246-259. 10.1016/j.celrep.2012.12.008.

Althoefer, H., Eversole-Cire, P., and Simon, M.I. (1997). Constitutively active Galphaq and Galpha13 trigger apoptosis through different pathways. J Biol Chem *272*, 24380-24386. 10.1074/jbc.272.39.24380.

Amaro, A., Gangemi, R., Piaggio, F., Angelini, G., Barisione, G., Ferrini, S., and Pfeffer, U. (2017). The biology of uveal melanoma. Cancer Metastasis Rev *36*, 109-140. 10.1007/s10555-017-9663-3.

Anderson, M.E., Allison, R.D., and Meister, A. (1982). Interconversion of leukotrienes catalyzed by purified gamma-glutamyl transpeptidase: concomitant formation of leukotriene D4 and gamma-glutamyl amino acids. Proc Natl Acad Sci U S A *79*, 1088-1091. 10.1073/pnas.79.4.1088.

Angers, S., Salahpour, A., Joly, E., Hilairet, S., Chelsky, D., Dennis, M., and Bouvier, M. (2000). Detection of beta 2-adrenergic receptor dimerization in living cells using bioluminescence resonance energy transfer (BRET). Proc Natl Acad Sci U S A *97*, 3684-3689. 10.1073/pnas.060590697.

Annala, S., Feng, X., Shridhar, N., Eryilmaz, F., Patt, J., Yang, J., Pfeil, E.M., Cervantes-Villagrana, R.D., Inoue, A., Häberlein, F., et al. (2019). Direct targeting of Gα(q) and Gα(11) oncoproteins in cancer cells. Sci Signal *12*. 10.1126/scisignal.aau5948.

Arshavsky, V.Y., Dizhoor, A.M., Shestakova, I.K., and Philippov, P. (1985). The effect of rhodopsin phosphorylation on the light-dependent activation of phosphodiesterase from bovine rod outer segments. FEBS Lett *181*, 264-266. 10.1016/0014-5793(85)80272-6.

Bäck, M., and Hansson, G.K. (2006). Leukotriene receptors in atherosclerosis. Ann Med *38*, 493-502. 10.1080/07853890600982737.

Ballesteros, J.A., and Weinstein, H. (1995). [19] Integrated methods for the construction of three-dimensional models and computational probing of structure-function relations in G protein-coupled receptors. In Methods in Neurosciences, S.C. Sealfon, ed. (Academic Press), pp. 366-428. https://doi.org/10.1016/S1043-9471(05)80049-7.

Basavarajappa, D., Wan, M., Lukic, A., Steinhilber, D., Samuelsson, B., and Rådmark, O. (2014). Roles of coactosin-like protein (CLP) and 5-lipoxygenase-activating protein (FLAP) in cellular leukotriene biosynthesis. Proc Natl Acad Sci U S A *111*, 11371-11376. 10.1073/pnas.1410983111.

Bennett, D.C., Cooper, P.J., and Hart, I.R. (1987). A line of non-tumorigenic mouse melanocytes, syngeneic with the B16 melanoma and requiring a tumour promoter for growth. Int J Cancer *39*, 414-418. 10.1002/ijc.2910390324.

Benovic, J.L., DeBlasi, A., Stone, W.C., Caron, M.G., and Lefkowitz, R.J. (1989). β-Adrenergic Receptor Kinase: Primary Structure Delineates a Multigene Family. Science *246*, 235-240. doi:10.1126/science.2552582.

Benovic, J.L., Strasser, R.H., Caron, M.G., and Lefkowitz, R.J. (1986). Beta-adrenergic receptor kinase: identification of a novel protein kinase that phosphorylates the agonist-occupied form of the receptor. Proc Natl Acad Sci U S A *83*, 2797-2801. 10.1073/pnas.83.9.2797.

Berchiche, Y.A., and Sakmar, T.P. (2016). CXC Chemokine Receptor 3 Alternative Splice Variants Selectively Activate Different Signaling Pathways. Mol Pharmacol *90*, 483-495. 10.1124/mol.116.105502.

Bertrand, L., Parent, S., Caron, M., Legault, M., Joly, E., Angers, S., Bouvier, M., Brown, M., Houle, B., and Ménard, L. (2002). The BRET2/arrestin assay in stable recombinant cells: a platform to screen for compounds that interact with G protein-coupled receptors (GPCRS). J Recept Signal Transduct Res *22*, 533-541. 10.1081/rrs-120014619.

Bhosle, V.K., Rivera, J.C., and Chemtob, S. (2019). New insights into mechanisms of nuclear translocation of G-protein coupled receptors. Small GTPases *10*, 254-263. 10.1080/21541248.2017.1282402.

Bond, R.A., and Ijzerman, A.P. (2006). Recent developments in constitutive receptor activity and inverse agonism, and their potential for GPCR drug discovery. Trends Pharmacol Sci *27*, 92-96. 10.1016/j.tips.2005.12.007.

Burke, L., Butler, C.T., Murphy, A., Moran, B., Gallagher, W.M., O'Sullivan, J., and Kennedy, B.N. (2016). Evaluation of Cysteinyl Leukotriene Signaling as a Therapeutic Target for Colorectal Cancer. Front Cell Dev Biol *4*, 103. 10.3389/fcell.2016.00103.

Camp, N.D., Lee, K.S., Wacker-Mhyre, J.L., Kountz, T.S., Park, J.M., Harris, D.A., Estrada, M., Stewart, A., Wolf-Yadlin, A., and Hague, C. (2015). Individual protomers of a G protein-coupled

receptor dimer integrate distinct functional modules. Cell Discov *1*, 15011-. 10.1038/celldisc.2015.11.

Carvajal, R.D., Sosman, J.A., Quevedo, J.F., Milhem, M.M., Joshua, A.M., Kudchadkar, R.R., Linette, G.P., Gajewski, T.F., Lutzky, J., Lawson, D.H., et al. (2014). Effect of selumetinib vs chemotherapy on progression-free survival in uveal melanoma: a randomized clinical trial. Jama *311*, 2397-2405. 10.1001/jama.2014.6096.

Ceraudo, E., Horioka, M., Mattheisen, J.M., Hitchman, T.D., Moore, A.R., Kazmi, M.A., Chi, P., Chen, Y., Sakmar, T.P., and Huber, T. (2019). Uveal Melanoma Oncogene CYSLTR2 Encodes a Constitutively Active GPCR Highly Biased Toward Gq Signaling. bioRxiv, 663153. 10.1101/663153.

Ceraudo, E., Horioka, M., Mattheisen, J.M., Hitchman, T.D., Moore, A.R., Kazmi, M.A., Chi, P., Chen, Y., Sakmar, T.P., and Huber, T. (2021). Direct evidence that the GPCR CysLTR2 mutant causative of uveal melanoma is constitutively active with highly biased signaling. J Biol Chem *296*, 100163. 10.1074/jbc.RA120.015352.

Chang, M.T., Asthana, S., Gao, S.P., Lee, B.H., Chapman, J.S., Kandoth, C., Gao, J., Socci, N.D., Solit, D.B., Olshen, A.B., et al. (2016). Identifying recurrent mutations in cancer reveals widespread lineage diversity and mutational specificity. Nat Biotechnol *34*, 155-163. 10.1038/nbt.3391.

Chen, F., Haigh, S., Barman, S., and Fulton, D.J. (2012). From form to function: the role of Nox4 in the cardiovascular system. Front Physiol *3*, 412. 10.3389/fphys.2012.00412.

Chen, Q., Plasencia, M., Li, Z., Mukherjee, S., Patra, D., Chen, C.L., Klose, T., Yao, X.Q., Kossiakoff, A.A., Chang, L., et al. (2021). Structures of rhodopsin in complex with G-protein-coupled receptor kinase 1. Nature *595*, 600-605. 10.1038/s41586-021-03721-x.

Cheng, R.K.Y., Fiez-Vandal, C., Schlenker, O., Edman, K., Aggeler, B., Brown, D.G., Brown, G.A., Cooke, R.M., Dumelin, C.E., Dore, A.S., et al. (2017). Structural insight into allosteric modulation of protease-activated receptor 2. Nature *545*, 112-+. 10.1038/nature22309.

Cherezov, V., Rosenbaum, D.M., Hanson, M.A., Rasmussen, S.G., Thian, F.S., Kobilka, T.S., Choi, H.J., Kuhn, P., Weis, W.I., Kobilka, B.K., and Stevens, R.C. (2007). High-resolution crystal structure of an engineered human beta2-adrenergic G protein-coupled receptor. Science *318*, 1258-1265. 10.1126/science.1150577.

Chua, V., Mattei, J., Han, A., Johnston, L., LiPira, K., Selig, S.M., Carvajal, R.D., Aplin, A.E., and Patel, S.P. (2021). The Latest on Uveal Melanoma Research and Clinical Trials: Updates from the Cure Ocular Melanoma (CURE OM) Science Meeting (2019). Clin Cancer Res *27*, 28-33. 10.1158/1078-0432.Ccr-20-2536.

Ciana, P., Fumagalli, M., Trincavelli, M.L., Verderio, C., Rosa, P., Lecca, D., Ferrario, S., Parravicini, C., Capra, V., Gelosa, P., et al. (2006). The orphan receptor GPR17 identified as a new dual uracil nucleotides/cysteinyl-leukotrienes receptor. Embo j *25*, 4615-4627. 10.1038/sj.emboj.7601341.

Cobb, M.H., and Goldsmith, E.J. (1995). How MAP kinases are regulated. J Biol Chem *270*, 14843-14846. 10.1074/jbc.270.25.14843.

Costanzi, S., Siegel, J., Tikhonova, I.G., and Jacobson, K.A. (2009). Rhodopsin and the others: a historical perspective on structural studies of G protein-coupled receptors. Curr Pharm Des *15*, 3994-4002. 10.2174/138161209789824795.

Coussens, L.M., and Werb, Z. (2002). Inflammation and cancer. Nature *420*, 860-867. 10.1038/nature01322.

Davies, H., Bignell, G.R., Cox, C., Stephens, P., Edkins, S., Clegg, S., Teague, J., Woffendin, H., Garnett, M.J., Bottomley, W., et al. (2002). Mutations of the BRAF gene in human cancer. Nature *417*, 949-954. 10.1038/nature00766.

de Rubio, R.G., Ransom, R.F., Malik, S., Yule, D.I., Anantharam, A., and Smrcka, A.V. (2018). Phosphatidylinositol 4-phosphate is a major source of GPCR-stimulated phosphoinositide production. Sci Signal *11*. 10.1126/scisignal.aan1210.

Denoyelle, C., Abou-Rjaily, G., Bezrookove, V., Verhaegen, M., Johnson, T.M., Fullen, D.R., Pointer, J.N., Gruber, S.B., Su, L.D., Nikiforov, M.A., et al. (2006). Anti-oncogenic role of the endoplasmic reticulum differentially activated by mutations in the MAPK pathway. Nat Cell Biol *8*, 1053-1063. 10.1038/ncb1471.

DeWire, S.M., Ahn, S., Lefkowitz, R.J., and Shenoy, S.K. (2007). β-Arrestins and Cell Signaling. Annual Review of Physiology *69*, 483-510. 10.1146/annurev.physiol.69.022405.154749.

Dhanasekaran, N., and Dermott, J.M. (1996). Signaling by the G12 class of G proteins. Cellular Signalling *8*, 235-245. https://doi.org/10.1016/0898-6568(96)00048-4.

Diener-West, M., Reynolds, S.M., Agugliaro, D.J., Caldwell, R., Cumming, K., Earle, J.D., Hawkins, B.S., Hayman, J.A., Jaiyesimi, I., Kirkwood, J.M., et al. (2005). Second primary cancers after enrollment in the COMS trials for treatment of choroidal melanoma: COMS Report No. 25. Arch Ophthalmol *123*, 601-604. 10.1001/archopht.123.5.601.

DiGiacomo, V., Maziarz, M., Luebbers, A., Norris, J.M., Laksono, P., and Garcia-Marcos, M. (2020). Probing the mutational landscape of regulators of G protein signaling proteins in cancer. Sci Signal *13*. 10.1126/scisignal.aax8620.

Dixon, R.A., Kobilka, B.K., Strader, D.J., Benovic, J.L., Dohlman, H.G., Frielle, T., Bolanowski, M.A., Bennett, C.D., Rands, E., Diehl, R.E., et al. (1986). Cloning of the gene and cDNA for mammalian beta-adrenergic receptor and homology with rhodopsin. Nature *321*, 75-79. 10.1038/321075a0.

Dror, R.O., Arlow, D.H., Maragakis, P., Mildorf, T.J., Pan, A.C., Xu, H., Borhani, D.W., and Shaw, D.E. (2011). Activation mechanism of the beta2-adrenergic receptor. Proc Natl Acad Sci U S A *108*, 18684-18689. 10.1073/pnas.1110499108.

Duah, E., Teegala, L.R., Kondeti, V., Adapala, R.K., Keshamouni, V.G., Kanaoka, Y., Austen, K.F., Thodeti, C.K., and Paruchuri, S. (2019). Cysteinyl leukotriene 2 receptor promotes endothelial permeability, tumor angiogenesis, and metastasis. Proc Natl Acad Sci U S A *116*, 199-204. 10.1073/pnas.1817325115.

Dunham, A., and Beltrao, P. (2020). Exploring amino acid functions in a deep mutational landscape. bioRxiv, 2020.2005.2026.116756. 10.1101/2020.05.26.116756.

Dvash, E., Har-Tal, M., Barak, S., Meir, O., and Rubinstein, M. (2015). Leukotriene C4 is the major trigger of stress-induced oxidative DNA damage. Nature Communications *6*, 10112. 10.1038/ncomms10112.

Dziedzic, A., Miller, E., Saluk-Bijak, J., and Bijak, M. (2020). The GPR17 Receptor-A Promising Goal for Therapy and a Potential Marker of the Neurodegenerative Process in Multiple Sclerosis. Int J Mol Sci *21*. 10.3390/ijms21051852.

Elubous, K.A., Alebous, A.D., Abous, H.A., and Elubous, R.A. (2021). The Trends of Uveal Melanoma Research in the Past Two Decades and Future Perspectives. SN Compr Clin Med, 1-10. 10.1007/s42399-021-01068-y.

Feng, X., Degese, M.S., Iglesias-Bartolome, R., Vaque, J.P., Molinolo, A.A., Rodrigues, M., Zaidi, M.R., Ksander, B.R., Merlino, G., Sodhi, A., et al. (2014). Hippo-independent activation of YAP by the GNAQ uveal melanoma oncogene through a trio-regulated rho GTPase signaling circuitry. Cancer Cell *25*, 831-845. 10.1016/j.ccr.2014.04.016.

Foster, S.R., Hauser, A.S., Vedel, L., Strachan, R.T., Huang, X.P., Gavin, A.C., Shah, S.D., Nayak, A.P., Haugaard-Kedström, L.M., Penn, R.B., et al. (2019). Discovery of Human Signaling Systems: Pairing Peptides to G Protein-Coupled Receptors. Cell *179*, 895-908.e821. 10.1016/j.cell.2019.10.010.

Freundlieb, S., Schirra-Müller, C., and Bujard, H. (1999). A tetracycline controlled activation/repression system with increased potential for gene transfer into mammalian cells. J Gene Med *1*, 4-12. 10.1002/(sici)1521-2254(199901/02)1:1<4::Aid-jgm4>3.0.Co;2-y.

Goodman, O.B., Jr., Krupnick, J.G., Santini, F., Gurevich, V.V., Penn, R.B., Gagnon, A.W., Keen, J.H., and Benovic, J.L. (1996). Beta-arrestin acts as a clathrin adaptor in endocytosis of the beta2-adrenergic receptor. Nature *383*, 447-450. 10.1038/383447a0.

Gurevich, V.V., and Gurevich, E.V. (2019). GPCR Signaling Regulation: The Role of GRKs and Arrestins. Frontiers in Pharmacology *10*. 10.3389/fphar.2019.00125.

Gusach, A., Luginina, A., Marin, E., Brouillette, R.L., Besserer-Offroy, E., Longpre, J.M., Ishchenko, A., Popov, P., Patel, N., Fujimoto, T., et al. (2019a). Structural basis of ligand selectivity and disease mutations in cysteinyl leukotriene receptors. Nat Commun *10*, 5573. 10.1038/s41467-019-13348-2.

Gusach, A., Luginina, A., Marin, E., Brouillette, R.L., Besserer-Offroy, É., Longpré, J.M., Ishchenko, A., Popov, P., Patel, N., Fujimoto, T., et al. (2019b). Structural basis of ligand

selectivity and disease mutations in cysteinyl leukotriene receptors. Nat Commun *10*, 5573. 10.1038/s41467-019-13348-2.

Gutkind, J.S., Novotny, E.A., Brann, M.R., and Robbins, K.C. (1991). Muscarinic acetylcholine receptor subtypes as agonist-dependent oncogenes. Proc Natl Acad Sci U S A *88*, 4703-4707. 10.1073/pnas.88.11.4703.

Haga, K., and Haga, T. (1992). Activation by G protein beta gamma subunits of agonist- or light-dependent phosphorylation of muscarinic acetylcholine receptors and rhodopsin. J Biol Chem *267*, 2222-2227.

Hamilton, A., Faiferman, I., Stober, P., Watson, R.M., and O'Byrne, P.M. (1998). Pranlukast, a cysteinyl leukotriene receptor antagonist, attenuates allergen-induced early- and late-phase bronchoconstriction and airway hyperresponsiveness in asthmatic subjects. J Allergy Clin Immunol *102*, 177-183. 10.1016/s0091-6749(98)70083-1.

Harbour, J.W., Onken, M.D., Roberson, E.D., Duan, S., Cao, L., Worley, L.A., Council, M.L., Matatall, K.A., Helms, C., and Bowcock, A.M. (2010). Frequent mutation of BAP1 in metastasizing uveal melanomas. Science *330*, 1410-1413. 10.1126/science.1194472.

Harbour, J.W., Roberson, E.D., Anbunathan, H., Onken, M.D., Worley, L.A., and Bowcock, A.M. (2013). Recurrent mutations at codon 625 of the splicing factor SF3B1 in uveal melanoma. Nat Genet *45*, 133-135. 10.1038/ng.2523.

Hargrave, P.A., McDowell, J.H., Curtis, D.R., Wang, J.K., Juszczak, E., Fong, S.L., Rao, J.K., and Argos, P. (1983). The structure of bovine rhodopsin. Biophys Struct Mech *9*, 235-244. 10.1007/bf00535659.

Hata, Y., Butz, S., and Südhof, T.C. (1996). CASK: a novel dlg/PSD95 homolog with an N-terminal calmodulin-dependent protein kinase domain identified by interaction with neurexins. J Neurosci *16*, 2488-2494. 10.1523/jneurosci.16-08-02488.1996.

Hauser, A.S., Chavali, S., Masuho, I., Jahn, L.J., Martemyanov, K.A., Gloriam, D.E., and Babu, M.M. (2018a). Pharmacogenomics of GPCR Drug Targets. Cell *172*, 41-54 e19. 10.1016/j.cell.2017.11.033.

Hauser, A.S., Chavali, S., Masuho, I., Jahn, L.J., Martemyanov, K.A., Gloriam, D.E., and Babu, M.M. (2018b). Pharmacogenomics of GPCR Drug Targets. Cell *172*, 41-54.e19. https://doi.org/10.1016/j.cell.2017.11.033.

Heise, C.E., O'Dowd, B.F., Figueroa, D.J., Sawyer, N., Nguyen, T., Im, D.S., Stocco, R., Bellefeuille, J.N., Abramovitz, M., Cheng, R., et al. (2000). Characterization of the human cysteinyl leukotriene 2 receptor. J Biol Chem *275*, 30531-30536. 10.1074/jbc.M003490200.

Helgadottir, H., and Höiom, V. (2016). The genetics of uveal melanoma: current insights. Appl Clin Genet *9*, 147-155. 10.2147/tacg.S69210.

Henderson, R., and Unwin, P.N. (1975). Three-dimensional model of purple membrane obtained by electron microscopy. Nature *257*, 28-32. 10.1038/257028a0.

Hernandez-Segura, A., Nehme, J., and Demaria, M. (2018). Hallmarks of Cellular Senescence. Trends Cell Biol *28*, 436-453. 10.1016/j.tcb.2018.02.001.

Hitchman, T.D., Bayshtok, G., Ceraudo, E., Moore, A.R., Lee, C., Jia, R., Wang, N., Pachai, M.R., Shoushtari, A.N., Francis, J.H., et al. (2020). Combined Inhibition of Gαq and MEK Enhances Therapeutic Efficacy in Uveal Melanoma. Clinical Cancer Research, In press.

Ho, A.L., Musi, E., Ambrosini, G., Nair, J.S., Deraje Vasudeva, S., de Stanchina, E., and Schwartz, G.K. (2012). Impact of combined mTOR and MEK inhibition in uveal melanoma is driven by tumor genotype. PLoS One *7*, e40439. 10.1371/journal.pone.0040439.

Hu, G.-M., Mai, T.-L., and Chen, C.-M. (2017). Visualizing the GPCR Network: Classification and Evolution. Sci Rep *7*, 15495. 10.1038/s41598-017-15707-9.

Hu, H., Tian, M., Ding, C., and Yu, S. (2018). The C/EBP Homologous Protein (CHOP) Transcription Factor Functions in Endoplasmic Reticulum Stress-Induced Apoptosis and Microbial Infection. Front Immunol *9*, 3083. 10.3389/fimmu.2018.03083.

Huang, W., Masureel, M., Qu, Q., Janetzko, J., Inoue, A., Kato, H.E., Robertson, M.J., Nguyen, K.C., Glenn, J.S., Skiniotis, G., and Kobilka, B.K. (2020). Structure of the neurotensin receptor 1 in complex with β-arrestin 1. Nature *579*, 303-308. 10.1038/s41586-020-1953-1.

Hui, Y., Cheng, Y., Smalera, I., Jian, W., Goldhahn, L., Fitzgerald, G.A., and Funk, C.D. (2004). Directed vascular expression of human cysteinyl leukotriene 2 receptor modulates endothelial permeability and systemic blood pressure. Circulation *110*, 3360-3366. 10.1161/01.Cir.0000147775.50954.Aa.

Hulme, E.C., and Trevethick, M.A. (2010). Ligand binding assays at equilibrium: validation and interpretation. Br J Pharmacol *161*, 1219-1237. 10.1111/j.1476-5381.2009.00604.x.

Insel, P.A., Tang, C.M., Hahntow, I., and Michel, M.C. (2007). Impact of GPCRs in clinical medicine: monogenic diseases, genetic variants and drug targets. Biochim Biophys Acta *1768*, 994-1005. 10.1016/j.bbamem.2006.09.029.

Isberg, V., de Graaf, C., Bortolato, A., Cherezov, V., Katritch, V., Marshall, F.H., Mordalski, S., Pin, J.-P., Stevens, R.C., Vriend, G., and Gloriam, D.E. (2015). Generic GPCR residue numbers – aligning topology maps while minding the gaps. Trends in Pharmacological Sciences *36*, 22-31. https://doi.org/10.1016/j.tips.2014.11.001.

Jaakola, V.P., Griffith, M.T., Hanson, M.A., Cherezov, V., Chien, E.Y., Lane, J.R., Ijzerman, A.P., and Stevens, R.C. (2008). The 2.6 angstrom crystal structure of a human A2A adenosine receptor bound to an antagonist. Science *322*, 1211-1217. 10.1126/science.1164772.

Jones, E.M., Lubock, N.B., Venkatakrishnan, A.J., Wang, J., Tseng, A.M., Paggi, J.M., Latorraca, N.R., Cancilla, D., Satyadi, M., Davis, J.E., et al. (2020). Structural and functional

characterization of G protein-coupled receptors with deep mutational scanning. Elife *9*. 10.7554/eLife.54895.

Jones, T.R., Labelle, M., Belley, M., Champion, E., Charette, L., Evans, J., Ford-Hutchinson, A.W., Gauthier, J.Y., Lord, A., Masson, P., and et al. (1995). Pharmacology of montelukast sodium (Singulair), a potent and selective leukotriene D4 receptor antagonist. Can J Physiol Pharmacol *73*, 191-201. 10.1139/y95-028.

Kanaoka, Y., and Boyce, J.A. (2004). Cysteinyl leukotrienes and their receptors: cellular distribution and function in immune and inflammatory responses. J Immunol *173*, 1503-1510. 10.4049/jimmunol.173.3.1503.

Kanaoka, Y., Maekawa, A., and Austen, K.F. (2013). Identification of GPR99 protein as a potential third cysteinyl leukotriene receptor with a preference for leukotriene E4 ligand. J Biol Chem *288*, 10967-10972. 10.1074/jbc.C113.453704.

Kang, Y., Zhou, X.E., Gao, X., He, Y., Liu, W., Ishchenko, A., Barty, A., White, T.A., Yefanov, O., Han, G.W., et al. (2015). Crystal structure of rhodopsin bound to arrestin by femtosecond X-ray laser. Nature *523*, 561-567. 10.1038/nature14656.

Kapiteijn, E., Carlino, M., Boni, V., Loirat, D., Speetjens, F., Park, J., Calvo, E., Carvajal, R., Nyakas, M., Gonzalez-Maffe, J., et al. (2019). Abstract CT068: A Phase I trial of LXS196, a novel PKC inhibitor for metastatic uveal melanoma. Cancer Research *79*, CT068-CT068. 10.1158/1538-7445.Am2019-ct068.

Katopodis, P., Khalifa, M.S., and Anikin, V. (2021). Molecular characteristics of uveal melanoma and intraocular tumors. Oncol Lett *21*, 9. 10.3892/ol.2020.12270.

Katritch, V., Cherezov, V., and Stevens, R.C. (2013). Structure-function of the G protein-coupled receptor superfamily. Annu Rev Pharmacol Toxicol *53*, 531-556. 10.1146/annurev-pharmtox-032112-135923.

Katritch, V., Fenalti, G., Abola, E.E., Roth, B.L., Cherezov, V., and Stevens, R.C. (2014). Allosteric sodium in class A GPCR signaling. Trends Biochem Sci *39*, 233-244. 10.1016/j.tibs.2014.03.002.

Kenakin, T., Watson, C., Muniz-Medina, V., Christopoulos, A., and Novick, S. (2012). A simple method for quantifying functional selectivity and agonist bias. ACS Chem Neurosci *3*, 193-203. 10.1021/cn200111m.

Kim, K., Che, T., Panova, O., DiBerto, J.F., Lyu, J., Krumm, B.E., Wacker, D., Robertson, M.J., Seven, A.B., Nichols, D.E., et al. (2020). Structure of a Hallucinogen-Activated Gq-Coupled 5-HT(2A) Serotonin Receptor. Cell *182*, 1574-1588.e1519. 10.1016/j.cell.2020.08.024.

Kobayashi, H., Picard, L.P., Schönegge, A.M., and Bouvier, M. (2019). Bioluminescence resonance energy transfer-based imaging of protein-protein interactions in living cells. Nat Protoc *14*, 1084-1107. 10.1038/s41596-019-0129-7.

Koch, W.J., Inglese, J., Stone, W.C., and Lefkowitz, R.J. (1993). The binding site for the beta gamma subunits of heterotrimeric G proteins on the beta-adrenergic receptor kinase. J Biol Chem *268*, 8256-8260.

Krantz, B.A., Dave, N., Komatsubara, K.M., Marr, B.P., and Carvajal, R.D. (2017). Uveal melanoma: epidemiology, etiology, and treatment of primary disease. Clin Ophthalmol *11*, 279-289. 10.2147/opth.S89591.

Kühn, H., and Dreyer, W.J. (1972). Light dependent phosphorylation of rhodopsin by ATP. FEBS Lett *20*, 1-6. 10.1016/0014-5793(72)80002-4.

Kundu, K., Mann, M., Costa, F., and Backofen, R. (2014). MoDPepInt: an interactive web server for prediction of modular domain-peptide interactions. Bioinformatics *30*, 2668-2669. 10.1093/bioinformatics/btu350.

Kurland, L., Melhus, H., Karlsson, J., Kahan, T., Malmqvist, K., Ohman, P., Nyström, F., Hägg, A., and Lind, L. (2002). Polymorphisms in the angiotensinogen and angiotensin II type 1 receptor gene are related to change in left ventricular mass during antihypertensive treatment: results from the Swedish Irbesartan Left Ventricular Hypertrophy Investigation versus Atenolol (SILVHIA) trial. J Hypertens *20*, 657-663. 10.1097/00004872-200204000-00023.

Kweon, J., Jang, A.H., Shin, H.R., See, J.E., Lee, W., Lee, J.W., Chang, S., Kim, K., and Kim, Y. (2020). A CRISPR-based base-editing screen for the functional assessment of BRCA1 variants. Oncogene *39*, 30-35. 10.1038/s41388-019-0968-2.

Landis, C.A., Masters, S.B., Spada, A., Pace, A.M., Bourne, H.R., and Vallar, L. (1989). GTPase inhibiting mutations activate the alpha chain of Gs and stimulate adenylyl cyclase in human pituitary tumours. Nature *340*, 692-696. 10.1038/340692a0.

Lapadula, D., Farias, E., Randolph, C.E., Purwin, T.J., McGrath, D., Charpentier, T.H., Zhang, L., Wu, S., Terai, M., Sato, T., et al. (2019). Effects of Oncogenic Gα(q) and Gα(11) Inhibition by FR900359 in Uveal Melanoma. Mol Cancer Res *17*, 963-973. 10.1158/1541-7786.Mcr-18-0574.

Laporte, S.A., Oakley, R.H., Zhang, J., Holt, J.A., Ferguson, S.S., Caron, M.G., and Barak, L.S. (1999). The beta2-adrenergic receptor/betaarrestin complex recruits the clathrin adaptor AP-2 during endocytosis. Proc Natl Acad Sci U S A *96*, 3712-3717. 10.1073/pnas.96.7.3712.

Lee, C.W., Lewis, R.A., Corey, E.J., and Austen, K.F. (1983). Conversion of leukotriene D4 to leukotriene E4 by a dipeptidase released from the specific granule of human polymorphonuclear leucocytes. Immunology *48*, 27-35.

Lee, Y., Warne, T., Nehmé, R., Pandey, S., Dwivedi-Agnihotri, H., Chaturvedi, M., Edwards, P.C., García-Nafría, J., Leslie, A.G.W., Shukla, A.K., and Tate, C.G. (2020). Molecular basis of β-arrestin coupling to formoterol-bound β(1)-adrenoceptor. Nature *583*, 862-866. 10.1038/s41586-020-2419-1.

Lefkowitz, R.J. (2000). The superfamily of heptahelical receptors. Nat Cell Biol *2*, E133-136. 10.1038/35017152.

Leiserson, M.D., Wu, H.T., Vandin, F., and Raphael, B.J. (2015). CoMEt: a statistical approach to identify combinations of mutually exclusive alterations in cancer. Genome Biol *16*, 160. 10.1186/s13059-015-0700-7.

Liu, L., Wise, D.R., Diehl, J.A., and Simon, M.C. (2008). Hypoxic reactive oxygen species regulate the integrated stress response and cell survival. J Biol Chem *283*, 31153-31162. 10.1074/jbc.M805056200.

Liu, W., Chun, E., Thompson, A.A., Chubukov, P., Xu, F., Katritch, V., Han, G.W., Roth, C.B., Heitman, L.H., AP, I.J., et al. (2012). Structural basis for allosteric regulation of GPCRs by sodium ions. Science *337*, 232-236. 10.1126/science.1219218.

Lohse, M.J., Benovic, J.L., Codina, J., Caron, M.G., and Lefkowitz, R.J. (1990). beta-Arrestin: a protein that regulates beta-adrenergic receptor function. Science *248*, 1547-1550. 10.1126/science.2163110.

Lorenzen, E., Dodig-Crnkovic, T., Kotliar, I.B., Pin, E., Ceraudo, E., Vaughan, R.D., Uhlen, M., Huber, T., Schwenk, J.M., and Sakmar, T.P. (2019). Multiplexed analysis of the secretin-like GPCR-RAMP interactome. Sci Adv *5*, eaaw2778. 10.1126/sciadv.aaw2778.

Lotta, L.A., Mokrosiński, J., Mendes de Oliveira, E., Li, C., Sharp, S.J., Luan, J., Brouwers, B., Ayinampudi, V., Bowker, N., Kerrison, N., et al. (2019). Human Gain-of-Function MC4R Variants Show Signaling Bias and Protect against Obesity. Cell *177*, 597-607.e599. 10.1016/j.cell.2019.03.044.

Lu, Z.L., and Hulme, E.C. (1999). The functional topography of transmembrane domain 3 of the M1 muscarinic acetylcholine receptor, revealed by scanning mutagenesis. J Biol Chem *274*, 7309-7315.

Luginina, A., Gusach, A., Marin, E., Mishin, A., Brouillette, R., Popov, P., Shiriaeva, A., Besserer-Offroy, É., Longpré, J.-M., Lyapina, E., et al. (2019). Structure-based mechanism of cysteinyl leukotriene receptor inhibition by antiasthmatic drugs. Science Advances *5*, eaax2518. 10.1126/sciadv.aax2518.

Luttrell, L.M., and Lefkowitz, R.J. (2002). The role of beta-arrestins in the termination and transduction of G-protein-coupled receptor signals. J Cell Sci *115*, 455-465.

Luttrell, L.M., Roudabush, F.L., Choy, E.W., Miller, W.E., Field, M.E., Pierce, K.L., and Lefkowitz, R.J. (2001). Activation and targeting of extracellular signal-regulated kinases by beta-arrestin scaffolds. Proc Natl Acad Sci U S A *98*, 2449-2454. 10.1073/pnas.041604898.

Lynch, K.R., O'Neill, G.P., Liu, Q., Im, D.S., Sawyer, N., Metters, K.M., Coulombe, N., Abramovitz, M., Figueroa, D.J., Zeng, Z., et al. (1999). Characterization of the human cysteinyl leukotriene CysLT1 receptor. Nature *399*, 789-793. 10.1038/21658.

Lyons, J., Landis, C.A., Harsh, G., Vallar, L., Grünewald, K., Feichtinger, H., Duh, Q.Y., Clark, O.H., Kawasaki, E., Bourne, H.R., and et al. (1990). Two G protein oncogenes in human endocrine tumors. Science *249*, 655-659. 10.1126/science.2116665.

Machleidt, T., Woodroofe, C.C., Schwinn, M.K., Méndez, J., Robers, M.B., Zimmerman, K., Otto, P., Daniels, D.L., Kirkland, T.A., and Wood, K.V. (2015). NanoBRET--A Novel BRET Platform for the Analysis of Protein-Protein Interactions. ACS Chem Biol *10*, 1797-1804. 10.1021/acschembio.5b00143.

Maeda, S., Qu, Q., Robertson, M.J., Skiniotis, G., and Kobilka, B.K. (2019). Structures of the M1 and M2 muscarinic acetylcholine receptor/G-protein complexes. Science *364*, 552-557. 10.1126/science.aaw5188.

Magnusson, C., Ehrnström, R., Olsen, J., and Sjölander, A. (2007). An increased expression of cysteinyl leukotriene 2 receptor in colorectal adenocarcinomas correlates with high differentiation. Cancer Res *67*, 9190-9198. 10.1158/0008-5472.Can-07-0771.

Magnusson, C., Liu, J., Ehrnström, R., Manjer, J., Jirström, K., Andersson, T., and Sjölander, A. (2011). Cysteinyl leukotriene receptor expression pattern affects migration of breast cancer cells and survival of breast cancer patients. Int J Cancer *129*, 9-22. 10.1002/ijc.25648.

Magnusson, C., Mezhybovska, M., Lörinc, E., Fernebro, E., Nilbert, M., and Sjölander, A. (2010). Low expression of CysLT1R and high expression of CysLT2R mediate good prognosis in colorectal cancer. Eur J Cancer *46*, 826-835. 10.1016/j.ejca.2009.12.022.

Marchese, A., Paing, M.M., Temple, B.R., and Trejo, J. (2008). G protein-coupled receptor sorting to endosomes and lysosomes. Annu Rev Pharmacol Toxicol *48*, 601-629. 10.1146/annurev.pharmtox.48.113006.094646.

Martin, M., Maßhöfer, L., Temming, P., Rahmann, S., Metz, C., Bornfeld, N., van de Nes, J., Klein-Hitpass, L., Hinnebusch, A.G., Horsthemke, B., et al. (2013). Exome sequencing identifies recurrent somatic mutations in EIF1AX and SF3B1 in uveal melanoma with disomy 3. Nat Genet *45*, 933-936. 10.1038/ng.2674.

Matsuyama, M., Hayama, T., Funao, K., Kawahito, Y., Sano, H., Takemoto, Y., Nakatani, T., and Yoshimura, R. (2007). Overexpression of cysteinyl LT1 receptor in prostate cancer and CysLT1R antagonist inhibits prostate cancer cell growth through apoptosis. Oncol Rep *18*, 99-104.

Mizuno, N., and Itoh, H. (2009). Functions and regulatory mechanisms of Gq-signaling pathways. Neurosignals *17*, 42-54. 10.1159/000186689.

Mobbs, J.I., Belousoff, M.J., Harikumar, K.G., Piper, S.J., Xu, X., Furness, S.G.B., Venugopal, H., Christopoulos, A., Danev, R., Wootten, D., et al. (2021). Structures of the human cholecystokinin 1 (CCK1) receptor bound to Gs and Gq mimetic proteins provide insight into mechanisms of G protein selectivity. PLoS Biol *19*, e3001295. 10.1371/journal.pbio.3001295.

Mohammad Nezhady, M.A., Rivera, J.C., and Chemtob, S. (2020). Location Bias as Emerging Paradigm in GPCR Biology and Drug Discovery. iScience *23*, 101643. 10.1016/j.isci.2020.101643.

Moore, A.R., Ceraudo, E., Sher, J.J., Guan, Y., Shoushtari, A.N., Chang, M.T., Zhang, J.Q., Walczak, E.G., Kazmi, M.A., Taylor, B.S., et al. (2016). Recurrent activating mutations of G-protein-coupled receptor CYSLTR2 in uveal melanoma. Nat Genet *48*, 675-680. 10.1038/ng.3549.

Moos, M.P., Mewburn, J.D., Kan, F.W., Ishii, S., Abe, M., Sakimura, K., Noguchi, K., Shimizu, T., and Funk, C.D. (2008). Cysteinyl leukotriene 2 receptor-mediated vascular permeability via transendothelial vesicle transport. Faseb j *22*, 4352-4362. 10.1096/fj.08-113274.

Murai, J., Huang, S.Y., Das, B.B., Renaud, A., Zhang, Y., Doroshow, J.H., Ji, J., Takeda, S., and Pommier, Y. (2012). Trapping of PARP1 and PARP2 by Clinical PARP Inhibitors. Cancer Res *72*, 5588-5599. 10.1158/0008-5472.Can-12-2753.

Narula, J., Haider, N., Virmani, R., DiSalvo, T.G., Kolodgie, F.D., Hajjar, R.J., Schmidt, U., Semigran, M.J., Dec, G.W., and Khaw, B.A. (1996). Apoptosis in myocytes in end-stage heart failure. N Engl J Med *335*, 1182-1189. 10.1056/nejm199610173351603.

Nathans, J., and Hogness, D.S. (1983). Isolation, sequence analysis, and intron-exon arrangement of the gene encoding bovine rhodopsin. Cell *34*, 807-814. 10.1016/0092-8674(83)90537-8.

Neves, S.R., Ram, P.T., and Iyengar, R. (2002). G protein pathways. Science *296*, 1636-1639. 10.1126/science.1071550.

Nguyen, A.H., Thomsen, A.R.B., Cahill, T.J., 3rd, Huang, R., Huang, L.Y., Marcink, T., Clarke, O.B., Heissel, S., Masoudi, A., Ben-Hail, D., et al. (2019). Structure of an endosomal signaling GPCR-G protein-beta-arrestin megacomplex. Nat Struct Mol Biol *26*, 1123-1131. 10.1038/s41594-019-0330-y.

Ni, N.C., Yan, D., Ballantyne, L.L., Barajas-Espinosa, A., St Amand, T., Pratt, D.A., and Funk, C.D. (2011). A selective cysteinyl leukotriene receptor 2 antagonist blocks myocardial ischemia/reperfusion injury and vascular permeability in mice. J Pharmacol Exp Ther *339*, 768-778. 10.1124/jpet.111.186031.

Nielsen, C.K., Campbell, J.I., Ohd, J.F., Mörgelin, M., Riesbeck, K., Landberg, G., and Sjölander, A. (2005). A novel localization of the G-protein-coupled CysLT1 receptor in the nucleus of colorectal adenocarcinoma cells. Cancer Res *65*, 732-742.

Nishihara, E., Fukata, S., Hishinuma, A., Kudo, T., Ohye, H., Ito, M., Kubota, S., Amino, N., Kuma, K., and Miyauchi, A. (2006). Sporadic congenital hyperthyroidism due to a germline mutation in the thyrotropin receptor gene (Leu 512 Gln) in a Japanese patient. Endocr J *53*, 735-740.

Nygaard, R., Frimurer, T.M., Holst, B., Rosenkilde, M.M., and Schwartz, T.W. (2009). Ligand binding and micro-switches in 7TM receptor structures. Trends in Pharmacological Sciences *30*, 249-259. https://doi.org/10.1016/j.tips.2009.02.006.

Oakley, R.H., Laporte, S.A., Holt, J.A., Barak, L.S., and Caron, M.G. (1999). Association of beta-arrestin with G protein-coupled receptors during clathrin-mediated endocytosis dictates the profile of receptor resensitization. J Biol Chem *274*, 32248-32257. 10.1074/jbc.274.45.32248.

Olivetti, G., Abbi, R., Quaini, F., Kajstura, J., Cheng, W., Nitahara, J.A., Quaini, E., Di Loreto, C., Beltrami, C.A., Krajewski, S., et al. (1997). Apoptosis in the failing human heart. N Engl J Med *336*, 1131-1141. 10.1056/nejm199704173361603.

Ovchinnikov, Y.A. (1982). The complete amino acid sequence of visual rhodopsin. Bioorg Khim *8*, 1011-1014.

Pakos-Zebrucka, K., Koryga, I., Mnich, K., Ljujic, M., Samali, A., and Gorman, A.M. (2016). The integrated stress response. EMBO Rep *17*, 1374-1395. 10.15252/embr.201642195.

Palczewski, K., Kumasaka, T., Hori, T., Behnke, C.A., Motoshima, H., Fox, B.A., Le Trong, I., Teller, D.C., Okada, T., Stenkamp, R.E., et al. (2000). Crystal structure of rhodopsin: A G protein-coupled receptor. Science *289*, 739-745. 10.1126/science.289.5480.739.

Parish, A.J., Nguyen, V., Goodman, A.M., Murugesan, K., Frampton, G.M., and Kurzrock, R. (2018). GNAS, GNAQ, and GNA11 alterations in patients with diverse cancers. Cancer *124*, 4080-4089. 10.1002/cncr.31724.

Parma, J., Duprez, L., Van Sande, J., Cochaux, P., Gervy, C., Mockel, J., Dumont, J., and Vassart, G. (1993). Somatic mutations in the thyrotropin receptor gene cause hyperfunctioning thyroid adenomas. Nature *365*, 649-651. 10.1038/365649a0.

Pleskoff, O., Casarosa, P., Verneuil, L., Ainoun, F., Beisser, P., Smit, M., Leurs, R., Schneider, P., Michelson, S., and Ameisen, J.C. (2005). The human cytomegalovirus-encoded chemokine receptor US28 induces caspase-dependent apoptosis. Febs j *272*, 4163-4177. 10.1111/j.1742-4658.2005.04829.x.

Pohl, S.L., Birnbaumer, L., and Rodbell, M. (1971). The glucagon-sensitive adenyl cyclase system in plasma membranes of rat liver. I. Properties. J Biol Chem *246*, 1849-1856.

Pópulo, H., Soares, P., Rocha, A.S., Silva, P., and Lopes, J.M. (2010). Evaluation of the mTOR pathway in ocular (uvea and conjunctiva) melanoma. Melanoma Res *20*, 107-117. 10.1097/CMR.0b013e32832ccd09.

Rasmussen, S.G., Choi, H.J., Rosenbaum, D.M., Kobilka, T.S., Thian, F.S., Edwards, P.C., Burghammer, M., Ratnala, V.R., Sanishvili, R., Fischetti, R.F., et al. (2007). Crystal structure of the human beta2 adrenergic G-protein-coupled receptor. Nature *450*, 383-387. 10.1038/nature06325.

Reid, G.K., Kargman, S., Vickers, P.J., Mancini, J.A., Léveillé, C., Ethier, D., Miller, D.K., Gillard, J.W., Dixon, R.A., and Evans, J.F. (1990). Correlation between expression of 5-lipoxygenase-activating protein, 5-lipoxygenase, and cellular leukotriene synthesis. J Biol Chem *265*, 19818-19823.

Rius, M., Hummel-Eisenbeiss, J., and Keppler, D. (2008). ATP-dependent transport of leukotrienes B4 and C4 by the multidrug resistance protein ABCC4 (MRP4). J Pharmacol Exp Ther *324*, 86-94. 10.1124/jpet.107.131342.

Ross, E.M., and Gilman, A.G. (1977). Resolution of some components of adenylate cyclase necessary for catalytic activity. J Biol Chem *252*, 6966-6969.

Saier, L., and Peyruchaud, O. (2021). Emerging role of cysteinyl LTs in cancer. Br J Pharmacol. 10.1111/bph.15402.

Sakmar, T.P., Franke, R.R., and Khorana, H.G. (1989). Glutamic acid-113 serves as the retinylidene Schiff base counterion in bovine rhodopsin. Proc Natl Acad Sci U S A *86*, 8309-8313. 10.1073/pnas.86.21.8309.

Salim, T., Sand-Dejmek, J., and Sjölander, A. (2014). The inflammatory mediator leukotriene D_4 induces subcellular β-catenin translocation and migration of colon cancer cells. Exp Cell Res *321*, 255-266. 10.1016/j.yexcr.2013.10.021.

Samuelsson, B. (1983). Leukotrienes: mediators of immediate hypersensitivity reactions and inflammation. Science *220*, 568-575. 10.1126/science.6301011.

Sassone-Corsi, P. (2012). The cyclic AMP pathway. Cold Spring Harb Perspect Biol *4*, a011148. 10.1101/cshperspect.a011148.

Satapathy, S.R., and Sjölander, A. (2020). Cysteinyl leukotriene receptor 1 promotes 5-fluorouracil resistance and resistance-derived stemness in colon cancer cells. Cancer Lett *488*, 50-62. 10.1016/j.canlet.2020.05.023.

Savari, S., Liu, M., Zhang, Y., Sime, W., and Sjölander, A. (2013). CysLT(1)R antagonists inhibit tumor growth in a xenograft model of colon cancer. PLoS One *8*, e73466. 10.1371/journal.pone.0073466.

Scheerer, P., Park, J.H., Hildebrand, P.W., Kim, Y.J., Krauss, N., Choe, H.W., Hofmann, K.P., and Ernst, O.P. (2008). Crystal structure of opsin in its G-protein-interacting conformation. Nature *455*, 497-502. 10.1038/nature07330.

Schertler, G.F., Villa, C., and Henderson, R. (1993). Projection structure of rhodopsin. Nature *362*, 770-772. 10.1038/362770a0.

Shimada, I., Ueda, T., Kofuku, Y., Eddy, M.T., and Wüthrich, K. (2019). GPCR drug discovery: integrating solution NMR data with crystal and cryo-EM structures. Nat Rev Drug Discov *18*, 59-82. 10.1038/nrd.2018.180.

Singh, A.D., Turell, M.E., and Topham, A.K. (2011). Uveal melanoma: trends in incidence, treatment, and survival. Ophthalmology *118*, 1881-1885. 10.1016/j.ophtha.2011.01.040.

Slack, R.J., and Hall, D.A. (2012). Development of operational models of receptor activation including constitutive receptor activity and their use to determine the efficacy of the chemokine CCL17 at the CC chemokine receptor CCR4. Br J Pharmacol *166*, 1774-1792. 10.1111/j.1476-5381.2012.01901.x.

Slater, K., Heeran, A.B., Garcia-Mulero, S., Kalirai, H., Sanz-Pamplona, R., Rahman, A., Al-Attar, N., Helmi, M., O'Connell, F., Bosch, R., et al. (2020). High Cysteinyl Leukotriene Receptor 1 Expression Correlates with Poor Survival of Uveal Melanoma Patients and Cognate Antagonist Drugs Modulate the Growth, Cancer Secretome, and Metabolism of Uveal Melanoma Cells. Cancers (Basel) *12*. 10.3390/cancers12102950.

Spiegel, A. (2003). β-Arrestin--Not Just for G Protein-Coupled Receptors. Science *301*, 1338-1339. doi:10.1126/science.1089552.

Staus, D.P., Hu, H., Robertson, M.J., Kleinhenz, A.L.W., Wingler, L.M., Capel, W.D., Latorraca, N.R., Lefkowitz, R.J., and Skiniotis, G. (2020). Structure of the M2 muscarinic receptor-β-arrestin complex in a lipid nanodisc. Nature *579*, 297-302. 10.1038/s41586-020-1954-0.

Stenson, W.F. (1990). Role of eicosanoids as mediators of inflammation in inflammatory bowel disease. Scand J Gastroenterol Suppl *172*, 13-18. 10.3109/00365529009091903.

Stoddart, L.A., Johnstone, E.K.M., Wheal, A.J., Goulding, J., Robers, M.B., Machleidt, T., Wood, K.V., Hill, S.J., and Pfleger, K.D.G. (2015). Application of BRET to monitor ligand binding to GPCRs. Nat Methods *12*, 661-663. 10.1038/nmeth.3398.

Stoy, H., and Gurevich, V.V. (2015). How genetic errors in GPCRs affect their function: Possible therapeutic strategies. Genes Dis *2*, 108-132. 10.1016/j.gendis.2015.02.005.

Suknuntha, K., Yubolphan, R., Krueaprasertkul, K., Srihirun, S., Sibmooh, N., and Vivithanaporn, P. (2018). Leukotriene Receptor Antagonists Inhibit Mitogenic Activity in Triple Negative Breast Cancer Cells. Asian Pac J Cancer Prev *19*, 833-837. 10.22034/apjcp.2018.19.3.833.

Suomivuori, C.M., Latorraca, N.R., Wingler, L.M., Eismann, S., King, M.C., Kleinhenz, A.L.W., Skiba, M.A., Staus, D.P., Kruse, A.C., Lefkowitz, R.J., and Dror, R.O. (2020). Molecular mechanism of biased signaling in a prototypical G protein-coupled receptor. Science *367*, 881-887. 10.1126/science.aaz0326.

Sussman, T.A., Funchain, P., and Singh, A. (2020). Clinical Trials in Metastatic Uveal Melanoma: Current Status. Ocul Oncol Pathol *6*, 381-387. 10.1159/000508383.

Sutherland, E.W., and Rall, T.W. (1958). Fractionation and characterization of a cyclic adenine ribonucleotide formed by tissue particles. J Biol Chem *232*, 1077-1091.

Szegezdi, E., Logue, S.E., Gorman, A.M., and Samali, A. (2006). Mediators of endoplasmic reticulum stress-induced apoptosis. EMBO Rep *7*, 880-885. 10.1038/sj.embor.7400779.

Tao, Y.X. (2008). Constitutive activation of G protein-coupled receptors and diseases: insights into mechanisms of activation and therapeutics. Pharmacol Ther *120*, 129-148. 10.1016/j.pharmthera.2008.07.005.

Tao, Y.X., Abell, A.N., Liu, X., Nakamura, K., and Segaloff, D.L. (2000). Constitutive activation of G protein-coupled receptors as a result of selective substitution of a conserved leucine residue in transmembrane helix III. Mol Endocrinol *14*, 1272-1282. 10.1210/mend.14.8.0503.

Tattersfield, A.E., and Harrison, T.W. (2006). beta-Adrenoceptor polymorphisms: focus moves to long-acting beta-agonists. Am J Respir Crit Care Med *173*, 473-474. 10.1164/rccm.2512005.

Thompson, M.D., Hendy, G.N., Percy, M.E., Bichet, D.G., and Cole, D.E. (2014). G protein-coupled receptor mutations and human genetic disease. Methods Mol Biol *1175*, 153-187. 10.1007/978-1-4939-0956-8_8.

Trinquet, E., Fink, M., Bazin, H., Grillet, F., Maurin, F., Bourrier, E., Ansanay, H., Leroy, C., Michaud, A., Durroux, T., et al. (2006). D-myo-inositol 1-phosphate as a surrogate of D-myo-inositol 1,4,5-tris phosphate to monitor G protein-coupled receptor activation. Anal Biochem *358*, 126-135. 10.1016/j.ab.2006.08.002.

Tsai, M.J., Wu, P.H., Sheu, C.C., Hsu, Y.L., Chang, W.A., Hung, J.Y., Yang, C.J., Yang, Y.H., Kuo, P.L., and Huang, M.S. (2016). Cysteinyl Leukotriene Receptor Antagonists Decrease Cancer Risk in Asthma Patients. Sci Rep *6*, 23979. 10.1038/srep23979.

Ueda, H., Morishita, R., Itoh, H., Narumiya, S., Mikoshiba, K., Kato, K., and Asano, T. (2001). Galpha11 induces caspase-mediated proteolytic activation of Rho-associated kinase, ROCK-I, in HeLa cells. J Biol Chem *276*, 42527-42533. 10.1074/jbc.M102529200.

Van Raamsdonk, C.D., Bezrookove, V., Green, G., Bauer, J., Gaugler, L., O'Brien, J.M., Simpson, E.M., Barsh, G.S., and Bastian, B.C. (2009). Frequent somatic mutations of GNAQ in uveal melanoma and blue naevi. Nature *457*, 599-602. 10.1038/nature07586.

Van Raamsdonk, C.D., Griewank, K.G., Crosby, M.B., Garrido, M.C., Vemula, S., Wiesner, T., Obenauf, A.C., Wackernagel, W., Green, G., Bouvier, N., et al. (2010). Mutations in GNA11 in uveal melanoma. N Engl J Med *363*, 2191-2199. 10.1056/NEJMoa1000584.

Vanacker, H., Vetters, J., Moudombi, L., Caux, C., Janssens, S., and Michallet, M.C. (2017). Emerging Role of the Unfolded Protein Response in Tumor Immunosurveillance. Trends Cancer *3*, 491-505. 10.1016/j.trecan.2017.05.005.

Vaqué, J.P., Dorsam, R.T., Feng, X., Iglesias-Bartolome, R., Forsthoefel, D.J., Chen, Q., Debant, A., Seeger, M.A., Ksander, B.R., Teramoto, H., and Gutkind, J.S. (2013). A genome-wide RNAi screen reveals a Trio-regulated Rho GTPase circuitry transducing mitogenic signals initiated by G protein-coupled receptors. Mol Cell *49*, 94-108. 10.1016/j.molcel.2012.10.018.

Venkatakrishnan, A.J., Deupi, X., Lebon, G., Heydenreich, F.M., Flock, T., Miljus, T., Balaji, S., Bouvier, M., Veprintsev, D.B., Tate, C.G., et al. (2016). Diverse activation pathways in class A GPCRs converge near the G-protein-coupling region. Nature *536*, 484-487. 10.1038/nature19107.

Venkatakrishnan, A.J., Deupi, X., Lebon, G., Tate, C.G., Schertler, G.F., and Babu, M.M. (2013). Molecular signatures of G-protein-coupled receptors. Nature *494*, 185-194. 10.1038/nature11896.

Vogel, R., Mahalingam, M., Lüdeke, S., Huber, T., Siebert, F., and Sakmar, T.P. (2008). Functional role of the "ionic lock"--an interhelical hydrogen-bond network in family A heptahelical receptors. J Mol Biol *380*, 648-655. 10.1016/j.jmb.2008.05.022.

Vogelstein, B., Papadopoulos, N., Velculescu, V.E., Zhou, S., Diaz, L.A., Jr., and Kinzler, K.W. (2013). Cancer genome landscapes. Science *339*, 1546-1558. 10.1126/science.1235122.

Wang, J.K., McDowell, J.H., and Hargrave, P.A. (1980). Site of attachment of 11-cis-retinal in bovine rhodopsin. Biochemistry *19*, 5111-5117. 10.1021/bi00563a027.

Wang, M., and Kaufman, R.J. (2014). The impact of the endoplasmic reticulum protein-folding environment on cancer development. Nat Rev Cancer *14*, 581-597. 10.1038/nrc3800.

Welsch, D.J., Creely, D.P., Hauser, S.D., Mathis, K.J., Krivi, G.G., and Isakson, P.C. (1994). Molecular cloning and expression of human leukotriene-C4 synthase. Proc Natl Acad Sci U S A *91*, 9745-9749. 10.1073/pnas.91.21.9745.

Wenzel, S.E., and Kamada, A.K. (1996). Zileuton: the first 5-lipoxygenase inhibitor for the treatment of asthma. Ann Pharmacother *30*, 858-864. 10.1177/106002809603000725.

Wilden, U. (1995). Duration and amplitude of the light-induced cGMP hydrolysis in vertebrate photoreceptors are regulated by multiple phosphorylation of rhodopsin and by arrestin binding. Biochemistry *34*, 1446-1454. 10.1021/bi00004a040.

Wilden, U., Hall, S.W., and Kühn, H. (1986). Phosphodiesterase activation by photoexcited rhodopsin is quenched when rhodopsin is phosphorylated and binds the intrinsic 48-kDa protein of rod outer segments. Proc Natl Acad Sci U S A *83*, 1174-1178. 10.1073/pnas.83.5.1174.

Wiley, C.D., Brumwell, A.N., Davis, S.S., Jackson, J.R., Valdovinos, A., Calhoun, C., Alimirah, F., Castellanos, C.A., Ruan, R., Wei, Y., et al. (2019). Secretion of leukotrienes by senescent lung fibroblasts promotes pulmonary fibrosis. JCI Insight *4*. 10.1172/jci.insight.130056.

Wingler, L.M., Skiba, M.A., McMahon, C., Staus, D.P., Kleinhenz, A.L.W., Suomivuori, C.M., Latorraca, N.R., Dror, R.O., Lefkowitz, R.J., and Kruse, A.C. (2020). Angiotensin and biased analogs induce structurally distinct active conformations within a GPCR. Science *367*, 888-892. 10.1126/science.aay9813.

Wu, V., Yeerna, H., Nohata, N., Chiou, J., Harismendy, O., Raimondi, F., Inoue, A., Russell, R.B., Tamayo, P., and Gutkind, J.S. (2019). Illuminating the Onco-GPCRome: Novel G protein-

coupled receptor-driven oncocrine networks and targets for cancer immunotherapy. J Biol Chem *294*, 11062-11086. 10.1074/jbc.REV119.005601.

Wunder, F., Tinel, H., Kast, R., Geerts, A., Becker, E.M., Kolkhof, P., Hutter, J., Erguden, J., and Harter, M. (2010). Pharmacological characterization of the first potent and selective antagonist at the cysteinyl leukotriene 2 (CysLT(2)) receptor. Br J Pharmacol *160*, 399-409. 10.1111/j.1476-5381.2010.00730.x.

Xia, R., Wang, N., Xu, Z., Lu, Y., Song, J., Zhang, A., Guo, C., and He, Y. (2021). Cryo-EM structure of the human histamine H(1) receptor/G(q) complex. Nat Commun *12*, 2086. 10.1038/s41467-021-22427-2.

Xu, Y., Piston, D.W., and Johnson, C.H. (1999). A bioluminescence resonance energy transfer (BRET) system: Application to interacting circadian clock proteins. Proceedings of the National Academy of Sciences *96*, 151-156. 10.1073/pnas.96.1.151.

Yamauchi, J., Itoh, H., Shinoura, H., Miyamoto, Y., Hirasawa, A., Kaziro, Y., and Tsujimoto, G. (2001). Involvement of c-Jun N-terminal kinase and p38 mitogen-activated protein kinase in alpha1B-adrenergic receptor/Galphaq-induced inhibition of cell proliferation. Biochem Biophys Res Commun *281*, 1019-1023. 10.1006/bbrc.2001.4472.

Yamauchi, J., Nagao, M., Kaziro, Y., and Itoh, H. (1997). Activation of p38 mitogen-activated protein kinase by signaling through G protein-coupled receptors. Involvement of Gbetagamma and Galphaq/11 subunits. J Biol Chem *272*, 27771-27777. 10.1074/jbc.272.44.27771.

Yan, D., Stocco, R., Sawyer, N., Nesheim, M.E., Abramovitz, M., and Funk, C.D. (2011). Differential signaling of cysteinyl leukotrienes and a novel cysteinyl leukotriene receptor 2 (CysLT(2)) agonist, N-methyl-leukotriene C(4), in calcium reporter and beta arrestin assays. Mol Pharmacol *79*, 270-278. 10.1124/mol.110.069054.

Yang, D., Zhou, Q., Labroska, V., Qin, S., Darbalaei, S., Wu, Y., Yuliantie, E., Xie, L., Tao, H., Cheng, J., et al. (2021). G protein-coupled receptors: structure- and function-based drug discovery. Signal Transduction and Targeted Therapy *6*, 7. 10.1038/s41392-020-00435-w.

Young, D., Waitches, G., Birchmeier, C., Fasano, O., and Wigler, M. (1986). Isolation and characterization of a new cellular oncogene encoding a protein with multiple potential transmembrane domains. Cell *45*, 711-719. 10.1016/0092-8674(86)90785-3.

Zarzycka, B., Zaidi, S.A., Roth, B.L., and Katritch, V. (2019). Harnessing Ion-Binding Sites for GPCR Pharmacology. Pharmacol Rev *71*, 571-595. 10.1124/pr.119.017863.

Zhang, C., Srinivasan, Y., Arlow, D.H., Fung, J.J., Palmer, D., Zheng, Y., Green, H.F., Pandey, A., Dror, R.O., Shaw, D.E., et al. (2012). High-resolution crystal structure of human protease-activated receptor 1. Nature *492*, 387-392. 10.1038/nature11701.

Zhang, L., Xu, F., Chen, Z., Zhu, X., and Min, W. (2013). Bioluminescence Assisted Switching and Fluorescence Imaging (BASFI). The Journal of Physical Chemistry Letters *4*, 3897-3902. 10.1021/jz402128j.

Zhou, B., Hall, D.A., and Giraldo, J. (2019). Can Adding Constitutive Receptor Activity Redefine Biased Signaling Quantification? Trends Pharmacol Sci *40*, 156-160. 10.1016/j.tips.2019.01.002.

Zhou, X.E., He, Y., de Waal, P.W., Gao, X., Kang, Y., Van Eps, N., Yin, Y., Pal, K., Goswami, D., White, T.A., et al. (2017a). Identification of Phosphorylation Codes for Arrestin Recruitment by G Protein-Coupled Receptors. Cell *170*, 457-469.e413. 10.1016/j.cell.2017.07.002.

Zhou, X.E., He, Y., de Waal, P.W., Gao, X., Kang, Y., Van Eps, N., Yin, Y., Pal, K., Goswami, D., White, T.A., et al. (2017b). Identification of Phosphorylation Codes for Arrestin Recruitment by G Protein-Coupled Receptors. Cell *170*, 457-469 e413. 10.1016/j.cell.2017.07.002.